

# **Attrition of Spray-Dried Powders**

by

**Tina Mirzamohammadbonakdar**

Submitted in accordance with the requirements for the degree of

Doctor of Philosophy

The University of Leeds

The School of Chemical and Process Engineering

March 2016

The candidate confirms that the work submitted is her own, except those that are specifically detailed below, where the contributions of other authors are outlined. The candidate also confirms that appropriate credit has been given where reference has been made to the work of authors.

Chapter 5 of this thesis has already been submitted in the Journal of Powder Technology as a jointly authored paper. The article can be found using the following citation:

- ❖ Bonakdar, T., Ghadiri, M., Ahmadian, H., Martin de Juan, L., Xu, D., Tantawy, H. and Smith, D. (2015). Impact strength of placebo granules by impact testing. *Powder Technology*. Submitted.

All the experimental work has been done by myself and the manuscript has been written completely by myself. The co-authors have had a supervisory role, or industrial co-ordination of the project.

Chapter 6 of this thesis has already been published in the Journal of Powder Technology and International Journal of Pharmaceutic as jointly authored papers. The articles can be found using the following citation:

- ❖ Ali, M., Bonakdar, T., Ghadiri, M., and Tinke, A. (2015). Particle breakage in a scirocco disperser. *Powder Technology*. Vol. 285: 138-145

- ❖ Bonakdar, T., Ali, M., Dogbe, S., Ghadiri, M., and Tinke, A. (2016). A method for grindability testing using the scirocco disperser. *International Journal of Pharmaceutics*. Vol. 501: 65-74

The numerical simulation work based on CFD is the work of Dr Muzammil Ali. The impact testing of aspirin, sucrose and  $\alpha$ -lactose monohydrate has been done by Mr Selasi Dogbe. The experimental work on Scirocco for the second paper has been done by a training engineer at Janssen R&D (Beerse, Belgium). The raw data were passed on to me for the analysis and data interpretation. The other co-authors have had a supervisory role.

This copy has been submitted in the understanding that it is copyright material and that no quotation from the thesis may be published without proper acknowledgement.

## **Acknowledgements**

I have been fortunate enough to be surrounded by fantastically talented and knowledgeable people capable of guiding me along this route in my life. I would like to take this opportunity to express my great thanks to Professor Mojtaba Ghadiri for allowing me to join the Ghadiri Research Group, for his support and kindness and always devoting time in his very busy schedule. He has been supportive from both a technical and personal perspective.

I am also thankful for the helpful comments and friendship from colleagues at Procter and Gamble (Newcastle, UK), most notably, Mr David Smith, Dr Hossein Ahmadian, Dr Luis Martin de Juan, Dr Hossam Tantawy, Mr Simon Greener, Miss Tara Aziz and Dr Dan Xu. The financial support from Procter and Gamble is also gratefully appreciated.

It has been a pleasure to be a member of this research group, which has a collaborative and vibrant environment that has led to much friendship and enjoyment. I would particularly like to acknowledge the great help from Dr Colin Hare in useful discussions regarding this research. My thanks also goes to Dr Umair Zafar for all his help. Special thanks to Dr M. Pasha<sup>2</sup>; Massih for all his help, Mehrdad for being such a good friend, his help and always sharing the latest music through his £200 award-winning Philips headphones! Siwarote “Pom” Siriluck, thank you for always opening the window a liiiiittle and providing ventilation, and taking the wastes out of the office for the birds. Special thanks to

Selasi Dogbe for his great friendship and the times spent in emergency meetings on the future of human behaviour. I would like to thank the ever exponentially increasing Italian population in this research group. Dr Vincenzino Vivacqua, thank you for being a great friend, colleague and neighbour. I am not sure whether I should acknowledge the Tesco guy or not! Thanks to Fabio Fulchini for his amazing talent in cutting cheese. Cheers mate. Your roots will be in breakage, just like me. To whomever I have forgotten to mention the name, thank you.

Finally, this acknowledgement would be incomplete without the inclusion of those whom have been with me from the start. The love and infallible support of my family is wonderful to have. I would like to thank my parents for allowing me to realise my own potential. All the support they have provided me over the years was the greatest gift anyone has ever given me. I owe a lot to my parents, especially my mother who is my best best-friend. She has always been there for me, and listening to all my ranting and raving about everything I have faced during my PhD; and of course my sister, Elina, who is always reminding me of how lucky I am to have her as my younger sister!

*To My Dear Mother*

## **ABSTRACT**

Particle attrition in manufacturing plants handling particulate solids could cause processing as well as environmental problems, and lead to the degradation of product quality. Spray-dried powders are particularly prone to attrition because of their porous and often weak structure. In this thesis the mechanisms by which attrition takes place are addressed, taking account of particle size and structure and the portfolio of mechanical stresses. The evolution of structure during the spray drying process cannot be easily controlled but plays a pivotal role in defining particle strength. Spray-dried burkeite particles are a good example and have been used as a model porous powder to investigate the effect of structure on their strength and breakage propensity. The dominant prevailing stresses for such particles in a process plant are caused by collision. Therefore, the particles are subjected to well-defined stresses due to impact, and the change in the particle size distribution is determined by particle size analysis based on sieving. It is found that impact breakage of burkeite is affected by the structure, and some unexpected trends for breakage are observed; for a given impact velocity some smaller particle sizes break to a greater extent as compared with larger particles. This is attributed to uncontrollable variations of porosity (and hence particle envelope density) as a function of size. To study the effect of porosity on attrition of such particles, structure visualisation and analysis have been carried out by Scanning Electron Microscopy (SEM) and X-ray microtomography (XRT). SEM images show three levels of structure in a single particle of spray-dried burkeite. Based on the XRT results, the particle envelope density increases as particle size increases, and the

variation of envelope density influences the impact breakage. Once the relevant values of the envelope density are taken into account, then the trend of impact breakage data becomes unified, and the material mechanical properties of the particles can be inferred from the breakage results. The breakage of these particles has also been studied using the Scirocco disperser of Malvern Mastersizer 2000, as it is widely available, in contrast to the single particle impact rig. In this device, particles of different sizes accelerate to different velocities, and break to different extents. It is found that the shift in the specific surface area of different sizes of spray-dried burkeite particles can be related to the dimensionless group representing the breakage propensity, using the estimated impact velocity by CFD simulation. Following the successful outcome of this work, the approach was extended to determination of breakability of three other crystalline materials, aspirin, sucrose and  $\alpha$ -lactose monohydrate. The outcome indicates that the Scirocco disperser can be used as an assessment method for grindability testing of materials. The slope of the line obtained from the graph relating the shift in the specific surface area of the particles, reflecting breakage, to the particle size and density and impact velocity correlates well with that obtained from single particle impact testing. Therefore this method can be used to assess the grindability of the powders provided the impact velocity is first determined.

To elucidate the role of structure and interparticle bond strength, DEM simulation has been used to explore the effect of structure (porosity) on impact breakage of agglomerates, and to provide a better understanding of the effects of various parameters on agglomerate breakage. The effects of impact velocity, surface

energy, impact angle and porosity on agglomerate breakage have been analysed. It has been found that depending on the level of surface energy, there are different patterns of impact breakage. More porous agglomerates undergo a higher extent of breakage compared to the low porosity agglomerates. This is also the case when the breakage of agglomerates with low surface energy is compared to those with high surface energy. The agglomerate impact at normal target also results in higher breakage level compared to the impacting at inclined surfaces. This approach has great potential to be predictive of the effect of structure on the impact strength of agglomerates.

## Table of Contents

ABSTRACT.....	i
CHAPTER 1 INTRODUCTION.....	1
1.1 Background .....	3
1.2 Objectives and Structure of the Thesis.....	4
CHAPTER 2 LITERATURE REVIEW.....	8
2.1 Attrition.....	8
2.2 Modes of Breakage.....	10
2.2.1 Brittle Mode of Failure .....	11
2.2.2 Semi-Brittle Mode of Failure.....	11
2.2.3 Ductile Mode of Failure.....	12
2.3 Pattern of Breakage .....	14
2.3.1 Brittle Mode of Failure .....	16
2.3.2 Semi-Brittle Mode of Failure.....	17
2.4 Particle Breakage Assessment.....	21
2.4.1 Single Particle Impact Testing.....	21
2.5 Agglomerates .....	22
2.5.1 Bonding in Agglomerates .....	23
2.5.2 Agglomeration Process .....	24
2.5.3 Agglomerate Structure .....	25
2.5.4 Porous Agglomerates .....	26
2.5.5 Spray-Dried Powders .....	26
2.5.6 Morphological Changes during Spray-Drying.....	28
2.5.7 Mechanical Properties of Agglomerates.....	29

2.5.8	Modes of Agglomerate Breakage .....	31
2.5.9	Breakage Patterns of Agglomerates .....	32
2.5.10	Breakage Analysis .....	36
2.5.11	Computer Simulation of Agglomerate Breakage.....	38
2.6	Concluding Remarks .....	45
CHAPTER 3 MATERIALS AND CHARACTERISATION .....		47
3.1	Materials.....	47
3.2	Material Characterisation .....	53
3.2.1	Dynamic Vapour Sorption .....	53
3.2.2	Raman Spectroscopy.....	54
3.2.3	Thermal Gravimetric Analysis.....	55
3.2.4	Particle Density.....	56
3.3	Sample Preparation .....	56
3.3.2	Particle Size Distribution .....	59
3.4	Near-Mesh Particles .....	62
3.5	Representative Sample Mass.....	62
CHAPTER 4 ENVELOPE DENSITY .....		64
4.1	Introduction .....	64
4.2	Envelope Density Measurement Methods.....	65
4.3	Indirect Measurement Methods.....	65
4.3.1	Envelope Density Measurement Based On Volume Estimation .....	65
4.4	Direct Measurement Methods .....	76
4.4.1	GeoPyc .....	76
4.4.2	X-Ray Microtomography.....	78
4.4.3	Mercury Porosimetry .....	85

4.5	Concluding Remarks .....	87
	CHAPTER 5 IMPACT BREAKAGE .....	91
5.1	Introduction .....	91
5.2	Impact Testing .....	92
5.2.1	Preliminary Impact Tests .....	93
5.3	Representative Sample Mass .....	95
5.4	Impact Testing Using Near-Mesh Size Particles .....	97
5.5	Patterns of Breakage .....	101
5.6	Mode of Failure of Spray-Dried Burkeite Particles .....	110
5.6.1	Chipping .....	120
5.6.2	Fragmentation and Disintegration .....	125
5.6.3	Impact Strength of Clusters .....	131
5.7	Concluding Remarks .....	138
	CHAPTER 6 PARTICLE BREAKAGE IN THE SCIROCCO DISPERSER .....	140
6.1	Background .....	140
6.2	Experimental Work Using the Scirocco Disperser .....	143
6.3	Grindability Assessment .....	154
6.3.1	Single Particle Impact Breakage Parameter .....	164
6.4	Concluding Remarks .....	166
	CHAPTER 7 SIMULATION .....	168
7.1	Introduction .....	168
7.2	Generation of Agglomerates .....	169
7.2.1	Simulations of Agglomerates .....	170
7.2.2	Time-Step Integration .....	170
7.2.3	Hertz Normal Contact Model .....	171

7.2.4	Hertz-Mindlin (no slip) Tangential Contact Model .....	172
7.3	JKR Elastic-Adhesion Normal Contact Model .....	172
7.3.1	Primary Particles .....	174
7.3.2	Forming an Agglomerate .....	176
7.3.3	Relaxation Step .....	176
7.3.4	Adhesive Bonding Model .....	178
7.3.5	Effect of Factory Geometry .....	179
7.3.6	Effect of Factory Size .....	181
7.4	Impact Strength of Agglomerates .....	181
7.4.1	Damage Ratio.....	181
7.4.2	Effect of Surface Energy on Agglomerate Impact Strength .....	182
7.4.3	Effect of Impact Angle on Agglomerate Impact Strength .....	183
7.4.4	Effect of Porosity on Agglomerate Impact Strength.....	188
7.5	Analysis of Impact Results.....	191
7.6	Concluding Remarks .....	195
	CHAPTER 8 OVERALL CONCLUSIONS AND FUTURE WORK.....	197
8.1	Conclusions .....	197
8.2	Future Work .....	200
	REFERENCES.....	203
	Appendix A .....	215
	Appendix B .....	221

## List of Figures

Figure 1-1. Schematic diagram of the project plan .....	5
Figure 2-1. Illustration of radial (A G Evans and Wilshaw, 1976), median and lateral cracks (Salman et al., 2004).....	12
Figure 2-2. Material flaw during a ductile failure (Briscoe, 1992) .....	13
Figure 2-3. Patterns of breakage (Papadopoulos, 1998).....	15
Figure 2-4. Schematic patterns of agglomerate breakage (Subero, 2001b) .....	35
Figure 2-5. The qualitative dependence of the observed pattern of breakage with the impact velocity and solid fraction (Subero and Ghadiri, 2001).....	36
Figure 2-6. Simulated system; (a) before impact, (b) after impact, fines are attached on the carrier surface .....	41
Figure 2-7. Simulated agglomerates with yellow colour showing small primary particles, blue large primary particles, and grey the bonds (Spetl et al., 2015) .....	42
Figure 3-1. SEM image of a single particle of spray-dried burkeite .....	49
Figure 3-2. SEM image of the surface of a spray-dried burkeite particle .....	50
Figure 3-3. Internal structure of a single particle of spray-dried burkeite.....	51
Figure 3-4. Clusters inside a spray-dried burkeite particle.....	51
Figure 3-5. Crystalline structure of the clusters .....	52
Figure 3-6. DVS analysis of spray-dried burkeite particles .....	54
Figure 3-7. Raman spectroscopy test on spray-dried burkeite particles.....	54
Figure 3-8. TGA analysis of spray-dried burkeite particles .....	55
Figure 3-9. Schematic diagram of splitting and blending procedure .....	58
Figure 3-10. Cumulative percentage undersize of burkeite particles by manual and mechanical sieving.....	61
Figure 3-11. Near mesh size particle (Allen, 1990) .....	62

Figure 4-1. Schematic diagram of the QICPIC (Sympatec, Germany) image analysis device .....	71
Figure 4-2. Some images captured by QICPIC during analysis of 1000 $\mu\text{m}$ particles.....	72
Figure 4-3. A picture of 850 $\mu\text{m}$ particles spread by vibratory table .....	73
Figure 4-4. Sample preparation for XRT scan using a very small quantity of sample .....	79
Figure 4-5. First XRT scan on 850 $\mu\text{m}$ burkeite particles (small sample mass), using Nanotom XRT machine at University of Leeds .....	80
Figure 4-6. Sample preparation for XRT scan (using 3 g of 850 $\mu\text{m}$ near-mesh burkeite particles) .....	81
Figure 4-7. XRT scan on 850 $\mu\text{m}$ burkeite particles (representative sample mass), using XRT machine at University of Nottingham .....	82
Figure 4-8. (a) Scan of a bed of burkeite particles before removing the glass container; (b) scan of a bed of the particles after removing the glass container .....	83
Figure 4-9. (a) A slice of the raw data of the bed scan for 850 $\mu\text{m}$ particles; (b) A slice of the particles bed after filling the internal porosity of the particles.....	84
Figure 4-10. Mercury porosimetry results for 300-425 $\mu\text{m}$ burkeite particles.....	86
Figure 5-1. Single particle impact rig (Samimi et al., 2003).....	92
Figure 5-2. The extent of breakage, $R^*$ , as a function of impact velocity for different sieve size cuts.....	94
Figure 5-3. Extent of breakage, $R^*$ , as a function of different impact velocities for near-mesh particles .....	97
Figure 5-4. SEM image of possible impact zone after impacting 850 $\mu\text{m}$ near-mesh particle at 4 m/s .....	99
Figure 5-5. SEM image of the surface of impacted 850 $\mu\text{m}$ near-mesh particle at 4 m/s.....	99
Figure 5-6. Bulk density variations of different near-mesh particle sizes at different impact conditions .....	100
Figure 5-7. Patterns of breakage for 212 $\mu\text{m}$ particles .....	102

Figure 5-8. Patterns of breakage for 250 $\mu\text{m}$ particles .....	103
Figure 5-9. Patterns of breakage for 500 $\mu\text{m}$ particles .....	104
Figure 5-10. Patterns of breakage for 600 $\mu\text{m}$ particles .....	105
Figure 5-11. Patterns of breakage for 850 $\mu\text{m}$ particles .....	106
Figure 5-12. Patterns of breakage for 1000 $\mu\text{m}$ particles .....	107
Figure 5-13. Transition velocity from chipping to fragmentation for different particle sizes of spray-dried burkeite.....	108
Figure 5-14. Transition velocity from fragmentation to disintegration for different particle sizes of spray-dried burkeite .....	108
Figure 5-15. Extent of breakage, $R^*$ , as a function of impact velocity for different particle sizes of burkeite for chipping regime .....	110
Figure 5-16. Nano-Crush test device.....	111
Figure 5-17. Nano-Crush test on 850 $\mu\text{m}$ particles by controlling the depth at 40 $\mu\text{m}$ .....	112
Figure 5-18. SEM images with different magnifications of 850 $\mu\text{m}$ particle after Nano-Crush test at 40 $\mu\text{m}$ crushing depth .....	113
Figure 5-19. Nano-Crush test on 850 $\mu\text{m}$ particles by controlling the depth at 50 $\mu\text{m}$ .....	114
Figure 5-20. Different magnifications SEM images of 850 $\mu\text{m}$ particle after Nano-Crush test at 50 $\mu\text{m}$ crushing depth .....	115
Figure 5-21. Failure of the 850 $\mu\text{m}$ particle by Nano-crush test at the crushing depth of 60 $\mu\text{m}$ .....	116
Figure 5-22. SEM images of 850 $\mu\text{m}$ near-mesh particle failure by Nano-Crush test at the crushing depth of around 60 $\mu\text{m}$ .....	117
Figure 5-23. Failure of the 850 $\mu\text{m}$ near-mesh particle by Nano-crush test at the crushing depth of around 100 $\mu\text{m}$ .....	118
Figure 5-24. SEM images of 850 $\mu\text{m}$ near-mesh particle failure by Nano-Crush test at the crushing depth of around 100 $\mu\text{m}$ .....	119
Figure 5-25. Extent of breakage, $R^*$ , as a function of $V^2$ for chipping regime ....	121

Figure 5-26. Extent of breakage, $R^*$ , as a function of $DV^2$ for the data corresponding to the chipping regime .....	122
Figure 5-27. Extent of breakage, $R^*$ , as a function of $\rho DV^2$ with the slope representing $\alpha H/K_c^2$ , showing data unification.....	123
Figure 5-28. Transition velocity from no-breakage to chipping as a function of $D^2\rho^{-0.5}$ .....	125
Figure 5-29. Breakage analysis of 212 $\mu\text{m}$ near-mesh particles for impact velocities corresponding to fragmentation and disintegration regimes.....	126
Figure 5-30. Breakage analysis of 250 $\mu\text{m}$ near-mesh particles for impact velocities corresponding to fragmentation and disintegration.....	127
Figure 5-31. Breakage analysis of 500 $\mu\text{m}$ near-mesh particles for impact velocities corresponding to fragmentation and disintegration.....	128
Figure 5-32. Breakage analysis of 600 $\mu\text{m}$ near-mesh particles for impact velocities corresponding to fragmentation and disintegration.....	129
Figure 5-33. Breakage analysis of 850 $\mu\text{m}$ near-mesh particles for impact velocities corresponding to fragmentation and disintegration.....	129
Figure 5-34. Breakage analysis of 1000 $\mu\text{m}$ near-mesh particles for impact velocities corresponding to fragmentation and disintegration.....	130
Figure 5-35. SEM image of clusters inside a spray-dried burkeite particle .....	131
Figure 5-36. SEM image of clusters which the spray-dried burkeite particles are made of .....	132
Figure 5-37. SEM image of clusters within a spray-dried burkeite particle .....	132
Figure 5-38. Several broken clusters after impacting at 50 m/s .....	134
Figure 5-39. Broken clusters after impact at 50 m/s .....	134
Figure 5-40. High magnification of the broken clusters after impacting at 50 m/s .....	135
Figure 5-41. Extent of breakage, $R^*$ , for impacting the clusters inside the spray-dried burkeite particles at different impact velocities.....	136
Figure 6-1. Schematic diagram of the Scirocco disperser .....	141

Figure 6-2. Particle size distribution for different near-mesh particle sizes at 300 kPa nozzle pressure .....	145
Figure 6-3. Impact velocity of burkeite particles as a function of nozzle pressure for density of 1200 kg/m <sup>3</sup> .....	146
Figure 6-4. Relative shift in the specific surface area of burkeite as a function of impact velocity in Scirocco disperser.....	149
Figure 6-5. Calculation of debris size distribution based on the distribution of feed and broken materials.....	151
Figure 6-6. Relative change in the specific surface area as a function of $\alpha\eta(\frac{\rho_f d_{f,v}}{\rho_d d_{d,v}})$ .....	153
Figure 6-7. Correction of size distribution data for some of the reported results, e.g. 160-180 $\mu\text{m}$ feed size of sucrose .....	156
Figure 6-8. Relative shift in size distribution of 224-250 $\mu\text{m}$ of aspirin at different nozzle pressures .....	157
Figure 6-9. Relative shift in size distribution of 224-250 $\mu\text{m}$ of sucrose at different nozzle pressures .....	158
Figure 6-10. Relative shift in size distribution of 224-250 $\mu\text{m}$ of $\alpha$ -lactose monohydrate at different nozzle pressures .....	159
Figure 6-11. Relative shift in the specific surface area of aspirin as a function of impact velocity in Scirocco disperser.....	160
Figure 6-12. Relative shift in the specific surface area of sucrose as a function of impact velocity in Scirocco disperser.....	161
Figure 6-13. Relative shift in the specific surface area of $\alpha$ -lactose monohydrate as a function of impact velocity in Scirocco disperser.....	161
Figure 6-14. Shift in the specific surface area of aspirin, sucrose and lactose particles as a function of $\rho_{f,d} d_{f,v} V^2 (d_{f,v}/d_{d,v})$ .....	163
Figure 7-1. Schematic force-overlap response of JKR model (Pasha, 2013).....	173
Figure 7-2. An agglomerate made by EDEM simulation.....	179
Figure 7-3. Agglomerates made with primary particles generated using two different geometries; (a) box; (b) sphere .....	180

Figure 7-4. Damage ratio as a function of impact velocity for agglomerates with different cohesive interparticle forces .....	182
Figure 7-5. Schematic of different impact angles .....	183
Figure 7-6. Damage ratio as a function of impact velocity for the same agglomerates (surface energy of 3 J/m <sup>2</sup> ) at different impact angles	184
Figure 7-7. Damage ratio as a function of impact velocity for the same agglomerates (surface energy of 0.5 J/m <sup>2</sup> ) at different impact angles .....	185
Figure 7-8. Damage ratio as a function of impact velocity for the same agglomerates (surface energy of 1 J/m <sup>2</sup> ) at different impact angles	185
Figure 7-9. Damage ratio as a function of impact velocity for normal component of impact velocity, impacting the same agglomerates (surface energy of 3 J/m <sup>2</sup> ) at different impact angles .....	186
Figure 7-10. Damage ratio as a function of impact velocity for normal component of impact velocity, impacting the same agglomerates (surface energy of 0.5 J/m <sup>2</sup> ) at different impact angles .....	187
Figure 7-11. Damage ratio as a function of impact velocity for normal component of impact velocity, impacting the same agglomerates (surface energy of 1 J/m <sup>2</sup> ) at different impact angles .....	187
Figure 7-12. Damage ratio as a function of impact velocity for two agglomerates with different levels of porosity and surface energy of 0.5 J/m <sup>2</sup> .....	189
Figure 7-13. Damage ratio as a function of impact velocity for two agglomerates with different levels of porosity and surface energy of 3 J/m <sup>2</sup> .....	190
Figure 7-14. Damage ratio as a function of $\Gamma^{-5/3}$ for agglomerates with different surface energies .....	192
Figure 7-15. Side view of force distribution after impacting at 0.5 m/s for agglomerates with (a): 0.5 J/m <sup>2</sup> ; (b) 3 J/m <sup>2</sup> .....	193
Figure 7-16. Damage ratio as a function of $V^2$ for agglomerates with different surface energies .....	194

## List of Tables

Table 3-1. Mass percentage of burkeite particles in different sieve cuts obtained from manual and mechanical sieving .....	60
Table 4-1. Density measurement results based on the projected-area measured diameter by G3 for different near mesh size particles .....	67
Table 4-2. Density measurement results based on volume calculated by near-mesh size for different particle sizes .....	68
Table 4-3. Envelope density measurement of quartz sand using volume estimation method by near-mesh sizes .....	69
Table 4-4. Error analysis on the effect of sample mass on envelope density of burkeite by estimating the mean diameter using QICPIC, and number of particles using vibratory table .....	74
Table 4-5. Envelope density measurement results based on volume calculated by QICPIC for different near-mesh particle sizes .....	75
Table 4-6. Density measurement by GeoPyc for 500, 600, 850 and 1000 $\mu\text{m}$ near-mesh burkeite particles .....	77
Table 4-7. Envelope density and internal porosity measurement using XRT .....	85
Table 4-8. Comparison of envelope density measurement results obtained by different methods for burkeite particles reported in $\text{kg}/\text{m}^3$ for different near-mesh particle sizes .....	88
Table 5-1. Error analysis on representative sample mass for impact testing at 8 m/s using 500 $\mu\text{m}$ particles .....	96
Table 5-2. Transition velocity from no-breakage to chipping for different near-mesh particle sizes .....	124
Table 5-3. Breakage data of impacting the clusters at different impact velocities.....	137
Table 6-1. The characteristics sizes $d_{10}$ , $d_{50}$ and $d_{90}$ of the particle size distribution of the feed particles (given by Spraytec) and of the broken particles (given by Mastersizer 2000) in $\mu\text{m}$ for different nozzle pressures .....	144
Table 6-2. The SSA of the feed particles ( $\text{SSA}_0$ ) and broken particles for different near-mesh particle sizes at different nozzle gauge pressures .....	148
Table 6-3. Matreial properties of aspirin, sucrose and $\alpha$ -lactose monohydrate .....	164

Table 6-4. The ratio of slopes for each two materials .....	165
Table 7-1. Size and number of generated primary particles.....	175
Table 7-2. Material properties of primary particles used for the simulation.....	175
Table 7-3. Particle-particle and particle-wall properties used in simulation.....	176
Table 7-4. Comparison of different parameters before and after relaxation step.....	177

## Nomenclature

### *Latin Characters*

$b$	Fitting parameter for Weibull distribution	-
$D$	Particle size	m
$\bar{d}_{d,v}$	Average size (volumetric basis) of the debris	m
$d_{f,v}$	A measure of feed particle size	m
$\bar{d}_{f,v}$	Average size (volumetric basis) of the feed material	m
$E$	Young's modulus	Pa
$E^*$	Reduced Young's modulus	Pa
$f_c$	Pull-off force	N
$F_{fr}$	Fragmentation force	N
$f_{Mat}$	Material properties	g/Jm
$F_n$	Normal contact force	N
$G$	Shear modulus	Pa
$H$	Hardness	Pa
$K_1$	Fitting parameter for Weibull distribution	-
$K_c$	Fracture toughness	MPam <sup>1/2</sup>
$K_r$	Fracture efficiency	-
$M$	Mass	G
$m$	A measure of the spread of strength	-
$m_{de}$	Mass of debris	g
$m_f$	Mass of feed particles	g
$m_m$	Mass of mother particles	g
$n$	Number of repeats	-
$N$	Number of particles	-
$N_u$	Number of unbroken particles	-
$R$	Radius of the particle	m
$R^-$	Attrition calculated assuming lost material is mother particles	%
$R^+$	Attrition calculated assuming lost material is debris	%
$R^*$	Attrition calculated from collected materials	%
$S$	Probability of breakage	-
$S_d$	Surface area of debris	m <sup>2</sup>
$S_f$	Surface area of feed material	m <sup>2</sup>
$SE$	Standard error	-
$SSA_0$	Specific surface area of feed material	m <sup>2</sup> /g
$T_R$	Rayleigh time-step	s
$V$	Impact velocity	m/s
$V_0$	Velocity below which there is no breakage	m/s
$V_{ch}$	Transition velocity from plastic deformation to chipping	m/s
$V_{fr}$	Transition velocity from chipping to fragmentation	m/s

$V_p$	Average volume of a single particle	$m^3$
$W_m$	Kinetic energy from impact	J
$W_k$	Single particle mass specific impact energy	J/g
$W_{k,min}$	Minimum kinetic energy which causes breakage	J/g
$We$	Weber Number	-
$We'$	Modified Weber Number	-
$Z$	Flaw density	-

### ***Greek Characters***

$\alpha$	Proportionality factor in Ghadiri and Zhang model	-
$\beta$	Proportionality factor for shift in specific surface area calculation	-
$\Gamma$	Surface energy	$J/m^2$
$\Gamma_f$	Fracture surface energy	$J/m^2$
$\gamma$	Surface energy	$m^2/g$
$\Delta$	Damage ratio	-
$\Delta SSA$	Specific surface area of debris	$m^2/g$
$\delta$	Normal overlap	m
$\varepsilon$	Interstitial bed voidage	-
$\varepsilon_p$	Average porosity of each near-mesh size particle	-
$\eta$	Breakage propensity	-
$\rho$	Density	$kg/m^3$
$\rho_b$	Bulk density	$kg/m^3$
$\rho_d$	Envelope density of debris	$kg/m^3$
$\rho_e$	Envelope density	$kg/m^3$
$\rho_f$	Envelope density of feed particles	$kg/m^3$
$\rho_t$	True density	$kg/m^3$
$\sigma$	Standard deviation	-
$\sigma_A$	Applied stress	Pa
$\sigma_s$	A characteristic strength	Pa
$\nu$	Poisson's ratio	-
$\psi_d$	Sphericity shape factor of debris	-
$\psi_f$	Sphericity shape factor of feed material	-

## CHAPTER 1 INTRODUCTION

For manufacturing plants handling particulate solids, it is important to understand particle attrition, as it is one of the most common problems they might face. Attrition can have a major impact on powder quality, safety, reliability and economic implications. Attrition in manufacturing plants commonly occurs in pneumatic conveying lines by particles sliding on the walls and impacting at bends (Frye and Peukert, 2004; Frye and Peukert, 2005; H. Kalman, 2000; Salman et al., 2002; T et al., 2003; Chapelle et al., 2004), inside rotating drums, where particles may experience bulk shear deformation and impact, depending on the flow regime and drum fill (Grant and Kalman, 2001), in fluidised beds (Boerefijn et al., 2000; Bentham et al., 2004), and in filling and discharge from storage units and moving beds (Couroyer et al., 1999; Ghadiri et al., 2000).

In this work, the powders of study are produced by spray-drying. Such powders are particularly prone to attrition because of their porous structure. It is well known that the operating conditions of the spray drying towers can have a significant effect on the powder mechanical strength and friability. Powders moving through the plant can experience different types of stresses, causing undesirable attrition (Ahmadian and Ghadiri, 2007). However, the breakage of spray-dried particles and the effect of formulation on the evolved structure and strength are not fully understood. In order to evaluate the attrition propensity of powders under laboratory conditions a portfolio of stresses, simulating plant conditions, should be applied.

The present work addresses the changes in particle size distribution (PSD) of spray-dried burkeite particles, which are chosen as a model material, subjected to well-defined stresses due to impact. The breakage of the particles under different levels of impact stresses is studied and analysed. Due to spray-drying operating conditions, there is variation of porosity as a function of size, which in fact causes envelope density changes with particle sizes. Use of different visualisation methods such as Scanning Electron Microscopy (SEM) and X-ray microtomography (XRT) is made to investigate the envelope density variation as a function of size.

Recently, the use of DEM simulation has also become very popular, as it provides a fast method to explore the effects of different parameters on strength of the particles. The DEM simulation of porous agglomerates is carried out to understand the effects of porosity, impact angle, interface energy and impact velocity on the impact breakage of agglomerates.

The results of simulation along with the experimental work provide a broader understanding of breakage behaviour of particles. The achievements of this work will also help related industries to avoid the conditions which result in undesirable particle attrition, e.g. designing pneumatic conveying lines, cyclones and other items of equipment, where particles experience mechanical stress by impact. Therefore, by improvement in their design of units of operations, the possible problems arising from particle attrition can be reduced.

## 1.1 Background

Laundry detergent powders undergo notable attrition in manufacturing plants. It is well known that the operating conditions of the spray drying process and subsequent powder transportation have a major impact on the powder characteristics. It is, therefore, highly desirable to quantify the attrition propensity of detergent powders by applying a portfolio of stresses which simulate plant conditions. Ahmadian (2008) specified the range of impact velocities and shear stresses prevailing in a ‘generic’ manufacturing plant. Segovia-Torres (2012) started her PhD research programme on analysis of the extent of attrition of laundry detergent powders produced with different levels of porosity, subjected to the simulated stress conditions at the University of Leeds. She subjected the powder samples to impact and bulk shear deformations and quantified the extent of breakage, observing surprising data trends.

For impact testing, in some cases small particles broke to a larger extent as compared to large particles, and some samples with high ‘nominal’ porosity broke less than the ones with a lower porosity. Segovia-Torres (2012) also carried out some attrition testing in a shear cell and observed that in some cases shear deformations led to particle growth due to agglomeration, instead of size reduction.

In view of Segovia-Torres’s work on laundry detergent powder posing difficulties due to complexity of the formulation and uncertainty in porosity across the particle size distributions, it was suggested that further work should be focussed on a simpler model system, such as burkeite, with more control on the porosity of the powder in the manufacturing process, and so began this PhD study on attrition of spray-dried powders

with the main focus on spray-dried burkeite particles. The same difficulties were faced, i.e. the small particles break to the higher extent compared to the large particles at some impact velocities. It was found that the impact breakage was affected by the structure, which caused some unexpected trends in particle breakage. To explain these trends, the structure of the spray-dried powders needs to be analysed. For this purpose, a visualisation study using X-ray microtomography and structure analysis was deemed to be needed.

## **1.2 Objectives and Structure of the Thesis**

The overall objective of this project is to gain a detailed understanding of the impact breakage of spray-dried burkeite particles, and also the influence of the structure on the impact breakage of agglomerates, from both qualitative and quantitative points of view. For this purpose, a combination of experimental work and numerical simulation is used. The schematic diagram of the project plan is shown in Figure 1-1.

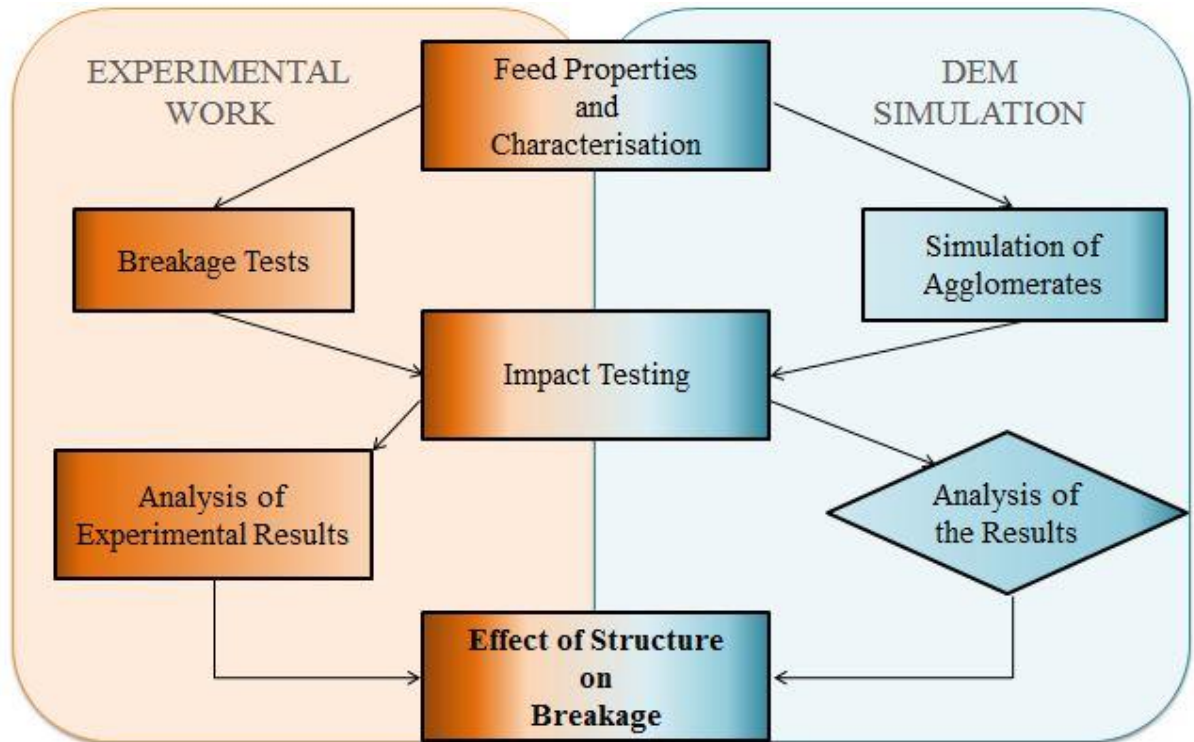


Figure 1-1. Schematic diagram of the project plan

A more detailed description of the contents of each chapter is outlined below:

**Chapter 2** A comprehensive review of the literature dealing with the particle attrition, failure modes and patterns of breakage is presented first. The breakage analysis for each pattern of breakage is described afterwards. A literature review on agglomerates, their breakage and modes of failure is then given. Understanding of breakage of porous agglomerates and spray-dried particles will then be presented. Finally, a review of computer simulation of agglomerates and their breakage is given.

**Chapter 3** In this chapter, the selected material for the experimental part of the work is described. Different tests used for material characterisation, as well as sample preparation are also presented.

**Chapter 4** As part of material characterisation, envelope density of different sizes of the particles needs to be quantified. Various methods are used to measure the envelope density of the particles as a function of size. In this chapter, a full description is given for each measurement technique. The results are then compared, and justifications of the selected method to carry out the work are given.

**Chapter 5** In this chapter, particle breakage of spray-dried burkeite particles is investigated using the single particle impact rig. The breakage of the particles is analysed depending on their patterns of breakage. The impact breakage results along with the envelope density of the particles are used to estimate the mechanical properties of the material.

**Chapter 6** In continuation of the previous chapter, the impact breakage of particles is studied using the Scirocco disperser of the Malvern Mastersizer 2000, as compared to single particle impact rig test, as it is widely available. The method is then applied to other crystalline structure materials. A good match is obtained between slope of the line obtained from Scirocco testing and that of the single particle impact testing. The results show that the Scirocco disperse can also be used as a grindability test method to assess the grindability of different materials.

**Chapter 7** This chapter begins with an introduction to the numerical simulation technique used in this work. Different steps used to generate an agglomerate as well as the bonding model are then described. The impact breakage of agglomerates under different impact conditions is presented. The effects of porosity, impact angle, impact velocity and surface energy on the breakage results are also shown.

**Chapter 8** In this chapter, general conclusions of the work are given. Some ideas are also presented as a future plan to continue this research.

## CHAPTER 2 LITERATURE REVIEW

In this chapter, several pieces of work on particle breakage are reviewed. Different concepts such as mode of failure and patterns of breakage are described. Some models used for breakage analysis are shown. A part of the chapter is focused on agglomerate breakage. DEM simulation has been used by many researchers to provide a better understanding of influential parameters on agglomerate breakage.

### 2.1 Attrition

Understanding particle breakage is a key factor in order to improve product quality in manufacturing plants handling particulate solids. Breakage has a major impact on powder quality and on a number of process operation features, such as reliability, safety, environmental impacts as well as economic implications. Powders moving through plants can experience different types of stresses, most commonly impact and shear stresses, causing undesirable attrition. The properties of particulate solids may change as a result of attrition, such as size distribution, shape, surface area and bulk density. These could have significant influence on product attributes. Bemrose and Bridgwater (1987) have studied the factors which affect particle attrition such as material properties, environmental and contact conditions. Density, Young's modulus, hardness, fracture toughness, porosity, shape, size and surface roughness are examples of material properties that influence particle attrition. Temperature, humidity, fluid pressure and fluid viscosity are some environmental conditions which can affect the attrition of the particles. Contact conditions depend on the particles examined individually or as bulk. The contact conditions such as contact area, angle, friction and

contact force can be considered for a single particle, and shear stress, shear strain, bed height and consolidation stress for bulk of materials.

Particle breakage has been investigated extensively in the literature; nevertheless the definition of various terms used to describe the particle breakage is often misleading. There are different terms used to describe particle breakage, such as attrition, wear, chipping and fragmentation. Attrition refers to any unintentional breakage of particulate solids (Bemrose and Bridgwater, 1987). Any surface damage of the particles which can be caused by erosion (by impacting a surface with a velocity) or abrasion (by sliding against the surface) is called wear. Shipway and Hutchings (1993b) reviewed the wear mechanisms. Chipping is caused by sub-surface lateral cracks initiating and developing during unloading, leading to removal of a small volume from a particle surface. The size of the chips removed is significantly smaller than the initial size of the particle (Ghadiri and Zhang, 2002). If the particles split into several smaller parts (by propagation of radial and median cracks), it is referred to as fragmentation. During fragmentation, a small amount of debris may also be produced (Ghadiri and Zhang, 2002).

Common places where attrition occurs are: in the pneumatic conveying lines by particles sliding on the walls and impacting at bends (Frye and Peukert, 2004); inside a rotating drums where particles may experience bulk shear deformation and impact depending on the flow regime and drum fill (Grant and Kalman, 2001); and in fluidised beds, where Boerefijn et al. (2000) and Bentham et al. (2004) have studied the attrition of particles in the jetting region (the work of Boerefijn et al. (2000) was focused on the high jet velocities in the distributor region causing intense inter-particle collisions).

Particle breakage might occur by impact, compression and sliding depending on the stressing conditions, material properties and environmental conditions during discharge from the bin by producing a network of strong contact forces.

Breakage of granules and agglomerates is not extensively classified by the definition of particle failure described above. Granules may undergo damage by other mechanisms such as disintegration. An extensive review on agglomerate breakage has been reported by Reynolds et al. (2005) and characterisation of granule strength by Bika et al. (2001). The classification of agglomerate failure is discussed further in section 2.5.

## **2.2 Modes of Breakage**

Applying a stress to a particle could result in deformation, which is initially elastic (non-permanent) and could be followed by plastic (permanent) deformation (Thornton and Ning, 1998) and initiation and propagation of cracks. The type of cracks is dependent on the mode of failure, which is categorised as brittle, semi-brittle and ductile. A particle failing in a brittle failure mode experiences extensive elastic deformation, but limited plastic deformation before failure due to crack propagation. Conversely, in the case of ductile mode of failure, the material experiences extensive plastic deformation. This may lead to failure by rupture (ductile tearing) rather than crack propagation. For the semi-brittle failure mode, the material experiences extensive elastic and plastic deformations, which cause crack propagation that is initiated from the plastic contact zone (Ghadiri and Zhang, 2002).

### **2.2.1 Brittle Mode of Failure**

A material with the brittle mode of failure is naturally strong, but its strength depends on the pre-existing internal and surface flaws. Shipway and Hutchings (1993 a, b) found that for the contact deformation with a low compliance (stiff) the internal tensile stresses are larger than the circumferential tensile hoop stresses; hence the internal tensile stress causes crack propagation. In contrast, in contact deformation with a high compliance (soft material), the circumferential tensile stresses are high as compared with the internal tensile stresses, which lead to the formation of orange-segment fragments ( Shipway and Hutchings, 1993a, 1993b). However, a predictive analysis of breakage is difficult as information on the size and number density of flaws in the particles is not generally available.

Brittle failure has been observed by Arbiter et al. (1969) for sand-cement, Salman and Gorham (2000) for soda-lime glass sphere, Rumpf and Schönert (1972) and Schönert (2004) for glass, Papadopoulos (1998) for porous silica, Wu et al. (2004) for plaster particles, Subero-Couroyer et al. (2005) and Antonyuk et al. (2005) for  $\gamma$ -alumina beads.

### **2.2.2 Semi-Brittle Mode of Failure**

In this mode of failure, the brittle fracture occurs at the boundaries of a plastically deformed zone. Chipping and wear are the results of the lateral crack propagation, whilst radial and median vent cracks are responsible for fragmentation (Ghadiri and Zhang, 2002). The stress field in this failure mode is very different compared with the elastic deformation. The plastic zone is under hydrostatic pressure causing tensile

circumferential hoop stresses at the boundary of plastic region leading to the formation of radial and median vent cracks during the loading cycle (Lawn and Wilshaw, 1975). During the unloading process, the elastically deformed region relaxes and the residual energy forms tensile stresses along the plastic boundary. Sub-surface lateral cracks are commonly formed as a result of the tensile stress (Hagan and Swain, 2001). In semi-brittle failure mode, cracks are initiated from the plastic zone, and hence the pre-existing flaws may not affect the failure, and hence the pattern of crack propagation is associated with local plastic deformation (Evans and Wilshaw, 1976). Radial, median and lateral cracks are shown schematically in Figure 2-1.

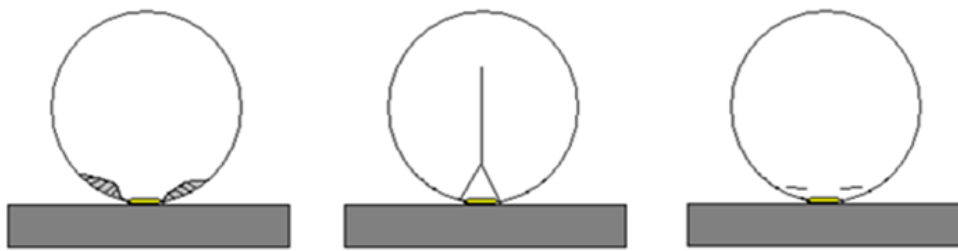


**Figure 2-1. Illustration of radial (A G Evans and Wilshaw, 1976), median and lateral cracks (Salman et al., 2004)**

Semi-brittle mode of failure has been observed by Zhang and Ghadiri (2002) for sodium chloride and potassium chloride, Papadopoulos (1998), Salman et al. (2003), Gorham et al. (2003) and Chaudhri (2004) for impact breakage of polymethyl methacrylate (PMMA) spheres and Antonyuk et al. (2006) for a synthetic zeolite.

### **2.2.3 Ductile Mode of Failure**

This mode of failure occurs through substantial plastic deformation of the material. Metals and some soft materials such as some polymers are mostly damaged under this mode of failure. Material properties and the method of loading are two important factors which affect the process of particle failure. The two dominant mechanisms of material removal in this failure mode are ploughing and cutting which are shown in Figure 2-2 (Briscoe, 1992).

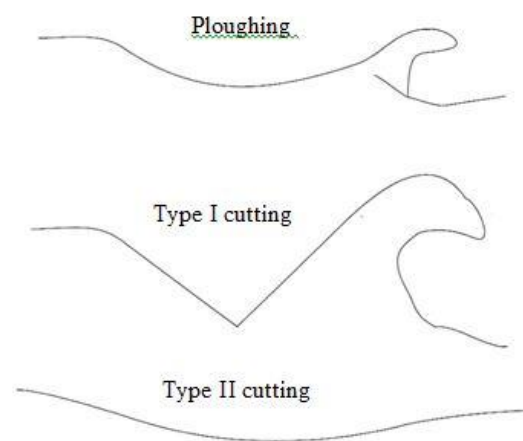


Figure 2-2. Material flow during a ductile failure (Briscoe, 1992)

For ductile mode of failure, Antonyuk et al. (2005) observed dominant plastic deformation for sodium benzoate granules. The ductile failure mode for the impact of weak agglomerates, made of lactose powders was reported by Ning et al. (1997). The agglomerates underwent extensive plastic deformation and clusters were detached from the plastic zone. The same approach has been observed by Samimi et al. (2003), who tested soft detergent based agglomerates using quasi-static, single and bulk particle compression. They observed microscopic ductile behaviour for the agglomerate having

a binder, due to the elongation and rupture of the binder ligaments within the crack opening. (Meenan et al., 1997). Yu et al. (2004, 2003) also carried out research on the ductile deformation of ceramics.

### **2.3 Pattern of Breakage**

The most common causes of particle attrition are chipping and fragmentation. Sub-surface lateral cracks are responsible for the chipping, and as they extend, the removal of small chips from the particle occurs. There is a minimum force required to plastically deform the particle and bring the onset of chipping. Beyond a threshold force, radial cracks will extend further towards the centre of the particle and cause fragmentation (Hare et al., 2009).

In order to analyse the breakage results, it is important to identify different patterns of breakage, e.g. chipping, fragmentation and disintegration. Papadopoulos (1998) studied the changing trend of the size distribution curve with impact velocity based on the work of Schumann (1940). Using this approach the breakage patterns can be separated based on the trend of the curves obtained by plotting the cumulative percentage undersize as a function of normalised size. The breakage patterns are classified into chipping, fragmentation and disintegration depending on the shape of the curves as shown in Figure 2-3.

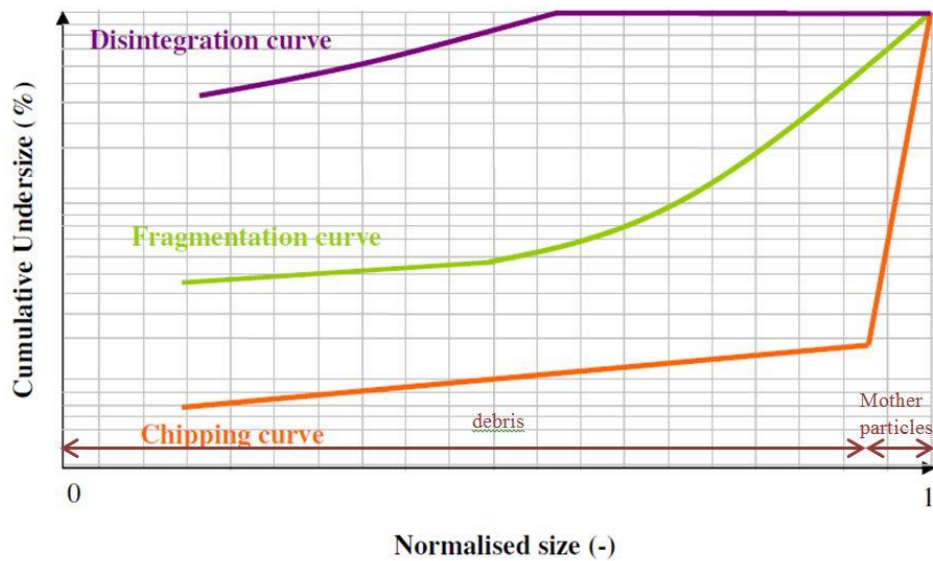


Figure 2-3. Patterns of breakage (Papadopoulos, 1998)

Definitions of the size of debris and mother particles are not straight forward, as the chips tend to have very irregular shapes and so their sieve size is not easily defined. The same applies to the size of the mother particles. However, a common approach to assess the fraction of debris generated through chipping is to consider a cut-off sieve size above which only mother particles are expected, and below which the particles are considered as debris. This cut-off size is typically taken as two sieve size cut below the lower size of the feed particles (Ahmadian and Ghadiri, 2007; Kwan et al., 2004).

In quantifying the particle breakage, there are some material losses due to manual handling, which causes uncertainty in analysing the extent of breakage. Ghadiri and Zhang (2002) defined limits of breakage based on whether the lost material could be attributed to the mother particles or to debris. In the former case the extent of breakage is defined by  $R^-$ , and in the latter case it is defined by  $R^+$ .  $R^*$  is defined based on the collected materials, i.e. ignoring the losses.

$$R^- = \frac{m_{de}}{m_f} \times 100\% \quad \text{Eq. (2-1)}$$

$$R^+ = \frac{m_f - m_m}{m_f} \times 100\% \quad \text{Eq. (2-2)}$$

$$R^* = \frac{m_{de}}{m_m + m_{de}} \times 100\% \quad \text{Eq. (2-3)}$$

where  $m_{de}$ ,  $m_f$  and  $m_m$  are the mass of debris, feed and mother particles, respectively.

### 2.3.1 Brittle Mode of Failure

Due to lack of information on the size and position of flaws in a particle, a deterministic analysis of particle breakage for the brittle mode of failure is difficult. Thus to characterise the breakage in this failure mode, the empirical determination of the crushing strength would be the only way. For this mode of failure, Weibull analysis could be used to fit the experimental observations (Weibull, 1951). It gives the probability of breakage ( $S$ ) as a function of the applied stress ( $\sigma_A$ ). These fitting parameters,  $z$ ,  $\sigma_s$  and  $m$  represent flaw density, a characteristic strength and a measure of the spread of strength, respectively (Weichert, 1988).

$$S = 1 - \exp\left[-z\left(\frac{\sigma_A}{\sigma_s}\right)^m\right] \quad \text{Eq. (2-4)}$$

The Weibull equation has been modified by Vogel and Peukert (2003) to describe the impact breakage.

$$S = 1 - \exp[-f_{Mat}D(W_k - W_{k,min})] \quad \text{Eq. (2-5)}$$

The parameters  $f_{Mat}$  and  $W_{k,min}$  are two fitting parameters in this equation and reflect the material properties and the minimum kinetic energy which causes breakage,

respectively.  $D$  is the particle size and  $W_k$  denotes single particle mass specific impact energy.  $f_{Mat}$  represents the resistance to breakage of the particle against the applied load  $W_k$  (Vogel and Peukert, 2005). Similar work has also been done by (Salman et al., 1995), who related the fraction of unbroken particles to the impact velocity by the use of Weibull analysis.

### 2.3.2 Semi-Brittle Mode of Failure

The most important mechanical properties for the semi-brittle failure mode are hardness, Young's modulus and fracture toughness. 'Hard' materials undergo less plastic deformation compared with 'soft' materials, but store greater residual strain energy; therefore they have more tendencies to generate lateral cracks than the soft materials. For the semi-brittle materials, chipping occurs by sub-surface lateral cracks, and fragmentation by radial and median vent cracks (Ghadiri and Zhang, 2002). Chipping and fragmentation are analysed further below.

#### 2.3.2.1 Plastic Deformation – Chipping Transition

Transitions of plastic deformation to chipping and chipping to fragmentation play an important role in understanding of particles breakage. Considering the role of different types of cracks is important as well. The critical transition velocity for plastic deformation-chipping is given below, which indicates that the critical transition velocity is proportional to the inverse of the square of particle size (Ghadiri, 1997).

$$V_{ch} \propto \left(\frac{K_C}{H}\right)^4 \frac{E}{H^{1/2}} \rho^{-1/2} D^{-2} \quad \text{Eq. (2-6)}$$

where  $V_{ch}$  is the transition velocity from plastic deformation to chipping,  $H$  and  $K_c$  are hardness and fracture toughness, respectively.  $E$  is Young's modulus,  $\rho$  is the envelope density and  $D$  is a volume-based characteristic particle size.

### 2.3.2.2 Chipping

The formation of sub-surface lateral cracks due to surface damage is one of the important processes of material removal. This process is generally referred to as chipping. Ghadiri and Zhang (2002) proposed a model for the calculation of the volume of debris formed as a result of impact damage based on the depth and length of the lateral cracks. The volume fraction of debris is defined as the ratio of volume of chips to the volume of original particles. The calculation of this volume fraction leads to a dimensionless group, which describes the attrition propensity due to chipping,  $\eta$ :

$$\eta = \frac{\rho V^2 D H}{K_c^2} \quad \text{Eq. (2-7)}$$

where  $D$  is a linear dimension of the particle,  $V$  is the impact velocity and  $\rho$  is the particle density. Toughness,  $K_c$ , and hardness,  $H$ , of the particles affect the characteristics of lateral cracks.

There are other models, reported in the literature, used to analyse the particle breakage under indentation by chipping. Evans and Wilshaw (1976) analysed the material removal rate expected from lateral fracture, and showed that the chipping volume is proportional to a group of parameters as shown below:

$$\eta = \frac{\rho D V^{12/5}}{K_c^{3/2} H^{1/2}} \quad \text{Eq. (2-8)}$$

However, this expression is not dimensionless. The above-mentioned model is developed for low impact velocities and quasi-static single particles. Bika et al. (2001) compared the above model with the model of (Ghadiri and Zhang, 1992), and showed that the work of Ghadiri and Zhang (1992) shows different dependency of  $\eta$  on impact velocity, hardness and fracture toughness compared to the presented model by Eq. (2-8) (Bika et al., 2001; Ghadiri and Zhang, 2002).

Gahn and Mersmann (1997) analysed the fractional loss of the material under impact. They used the energy balance approach assuming the kinetic energy from impact transformed into plastic work. Based on this model,

$$\eta = \frac{2}{3} \frac{H^{2/3} K_r W_m^{4/3}}{G \Gamma_f} \quad \text{Eq. (2-9)}$$

where  $K_r$  is the fracture efficiency,  $G$  is the shear modulus,  $\Gamma_f$  is the fracture surface energy and  $W_m$  is the kinetic energy from impact. It is assumed that a cone-shaped particle impacts to the target, and the volume of the fragment is equal to the removed volume from the cone.

### 2.3.2.3 Chipping-Fragmentation Transition

Considering impact damage, the threshold velocity of fragmentation is a function of hardness, density, fracture toughness and the size of the plastic zone in the semi-brittle failure mode. It is observed that the dependence of the critical transition velocity  $V_{fr}$  on the particle size  $D$  is similar to that of plastic deformation-chipping (Ghadiri, 1997).

$$V_{fr} \propto \left(\frac{K_c}{H}\right)^4 H^{1/2} \rho^{-1/2} D^{-2} \quad \text{Eq. (2-10)}$$

where  $V_{fr}$  is the transition velocity from chipping to fragmentation.

#### 2.3.2.4 Fragmentation

Formation of fragments occurs when the radial and median cracks are extended to the full length of the particles, leading to the loss of integrity of the structure. However, there is no theory which can relate the product size distribution to the material properties and stress conditions in a predictive way. Ghadiri and Zhang (2002) proposed a relationship to estimate the force for fracture of a sphere of diameter  $D$  based on indentation fracture. The fragmentation force ( $F_{fr}$ ) for crack extension is given by:

$$F_{fr} \propto K_c^{4/3} D^{4/3} H^{-1/3} \quad \text{Eq. (2-11)}$$

Salman et al. (1995) proposed an empirical model to quantify the probability of breakage by counting the number of unbroken particles after impact testing. In this model the number of unbroken particles ( $N_u$ ) is described as a function of impact velocity ( $V$ ) using a two-parameter cumulative Weibull distribution ( $K_1$  and  $b$ ), as given by Eq. (2-12):

$$N_u = 100 \exp\left[-\left[\frac{V}{K_1}\right]^b\right] \quad \text{Eq. (2-12)}$$

where  $K_1$  is considered as a parameter representing the average strength of a given particle size under a specific loading condition, as it is related to the velocity at which the probability of damage is 36.8% or  $100/e$ . The parameter  $b$  is considered as

Weibull modulus and is linked to the slope of the curve, and it represents a distribution of strengths for the population of particles.

It should be noted that both equations above have a lower limit of particle size validity. The limit comes from an ultimate particle size below which the particles cannot be fractured at all, and they can only undergo plastic deformation, irrespective of impact velocity. Kendall (1978), Puttick (1980) and Hagan (1981) developed some models for this limit. These models are based on the energy requirements for crack propagation.

## **2.4 Particle Breakage Assessment**

There are a number of test methods to evaluate the breakage of the particles, whether singly or in bulk. Impact (Boerefijn et al., 1998; Subero and Ghadiri, 2001; Samimi et al., 2003; Samimi et al., 2004; Antonyuk, Khanal, Jørgen Tomas, et al., 2006; H Kalman, 2000), wear (Hutchings, 1993), side crushing (Beekman, 2000; Beekman et al., 2003; Adams et al., 1994; Cheong et al., 2005) and indentation (Elwazri et al., 2009) are some of the test methods used for single particles. According to Ghadiri *et al.* (2000), these methods have relatively well-defined conditions and can be used to study the influence of stress field and materials properties on particle breakage; however, due to simplicity of these methods, they are not fully representative of industrial conditions.

### **2.4.1 Single Particle Impact Testing**

The single particle impact test is a dynamic test method, in which the particles are accelerated and impacted to a normal or oblique target. This has been extensively used as a test method to study the breakage behaviour of particles under impact conditions by Salman *et al.* (2003, 1995) to study the breakage of fertiliser and alumina

agglomerates, respectively. Arbiter *et al.* (1969) used free fall impact to study the breakage behaviour of sand-cement agglomerates. Breakage patterns of lactose agglomerates was investigated by Ning *et al.* (1997) and Boerefijn *et al.* (1998). Also materials such as sodium chloride crystals (Yuregir *et al.*, 1986), sand (Lecoq *et al.*, 2003), and detergents (Samimi *et al.*, 2004) have been tested in this way. Tomas *et al.* (1999) and Khanal *et al.* (2004) have used the approach for impact testing of large concrete balls. Ghadiri and co-workers have developed an impact tester to study the breakage of particles (Samimi *et al.*, 2003; Yuregir *et al.*, 1986).

The oblique impact of granules has been investigated by Salman *et al.* (2003) and Samimi *et al.* (2004). Salman *et al.* (2003) found that the breakage decreases as the impact angle decreases from normal. However, Samimi *et al.* (2004) found that by decreasing the impact angle, the extent of breakage increased. The breakage of granules by oblique impact shows contrasting trends and still needs further investigation in order to be fully understood.

Repeated impact testing has been used to investigate the effects of fatigue using different impact test devices (Beekman, 2000; Pitchumani *et al.*, 2004). Particle breakage has been analysed by both quantitative and qualitative methods. Ning *et al.* (1997) have used single particle impact tests coupled with high speed video recording to observe initiation and propagation of cracks.

## **2.5 Agglomerates**

Agglomerates are made of primary particles bonded together. The primary particles may be made of a single or different components, in the case of a mixture, the

agglomerate structure could contain the materials mixed randomly together, or it could be layered. A type of bonding is usually used in the agglomerates. All these possibilities show a great variation in structure, and so their breakage behaviour can be quite different from each other and from single particles too. As a consequence, this has led to much research to characterise the breakage of agglomerates, with the application of computer modelling in many cases.

Despite the complexity of the breakage behaviour of the agglomerates, the agglomerated products have some advantages over their un-agglomerated constituents. They are less prone to segregation as the size and density in principle can be controlled. They can be formed from a range of components with different concentration. It is usually helpful in pharmaceutical industries for active ingredients where their dose size cannot be accurately controlled in any other ways. Another advantage is that agglomerates can be made to increase the solubility in liquids, as their porous structure allows liquid ingress and also the binders can be chosen in a way that they dissolve in the liquid (Mullier et al., 1991).

### **2.5.1 Bonding in Agglomerates**

The binding mechanisms of agglomeration can be classified into solid bridges (such as partial melting, re-crystallisation during drying, etc), adhesion and cohesion forces, surface tension and capillary pressure (such as liquid bridges), attraction forces between solids (such as molecular forces, electric forces and magnetic forces) and interlocking bonds (Reynolds et al., 2005; Rumpf, 1958).

### 2.5.2 Agglomeration Process

Agglomeration (or granulation) is referred to as the formation of larger entities from particulate solids by either sticking particles together due to short range physical forces between the particles or using binders or some materials to form a material bridge between the solid surfaces by adhere physically or chemically (Pietsch, 2008). Agglomeration (or granulation) can be achieved in a number of ways, such as in a high-shear mixer, fluidised bed operation and spray-drying process (Huntington, 2004). However, there are other techniques to form an agglomerate. For instance, Ku et al. (2015) studied binderless agglomerate formation using auto-granulation of fine titania powder under vibration. Their approach was used to promote agglomerate growth by controlling the vibration conditions. Fine powders are poor in flowability and they have the affinity to agglomerate due to cohesion. The size of the agglomerates was analysed as a function of frequency and amplitude of the vibration. However, the maximum size of the agglomerates is affected by the balance between cohesive energy of the particles and the disruptive energy of the vibration. After forming different agglomerates at different vibration conditions, they analysed the internal structure of the agglomerates by providing a cross-section of them. They found that there is a core-rim microstructure for all the agglomerates regardless of their formation conditions. The results showed that the equilibrium size of the agglomerates increases as the vibrational intensity increases. A higher power and energy of vibration would also give rise to formation of larger and stronger agglomerates.

The agglomeration process using spray-drying is described in section 2.5.5.

### **2.5.3 Agglomerate Structure**

There is a direct relation between the structure of an agglomerate and the agglomeration process and parameters. Therefore, any change in the structure of the agglomerates is achieved by manipulating the agglomeration process. There is extensive work reported in the literature by Ennis et al. (1991), Gutsch et al. (1995), Keningley et al. (1997), Müller and Löffler (1996), Juslin and Yliruusi (1996), Litster et al. (1998) on the process of agglomerate growth and evolution of structure. At a basic level, the structure of the agglomerates is defined using general terms, such as porosity/ void fraction or its complimentary solid/ packing fraction (Rumpf, 1958; Karihaloo, 1979; Rice, 1996). These parameters can also be related to envelope density and co-ordination number of agglomerate (Smith et al., 1930; Manegold et al., 1931; Meissner et al., 1964). However, recently more analytic tools are available to study the structure of the agglomerates such as X-ray microtomography approach, through which a wide range of structural features such as distribution of pore size and its position can be determined.

#### **2.5.3.1 X-Ray Microtomography**

X-ray microtomography (XRT) is a technique to non-destructively characterise material microstructure in three dimensions at a micrometre level spatial resolution. This has been used to study the structure of the agglomerates due to its high resolution and ability to acquire the three-dimensional information (Fu et al., 2006). XRT scans allow the user to visualise the internal and microstructural details of the agglomerates. Material atomic mass and the energy of X-ray affect the intensity values associated with different features of the scanned images (Eggermont et al., 1981; Stock, 1999), which by the quality of scan and differentiation between the materials can be affected.

Moreno-Atanasio et al. (2010) used the combination of X-ray microtomography and computer simulation for analysis of granular and porous materials. Rahmanian et al. (2009) has also reported characterisation of granule structure using XRT. Golchert et al. (2004) also used X-ray microtomography to characterise the structure of actual granules. They used DEM simulation to analyse the effect of agglomerate shape and structure on breakage patterns during compression. For the first time, they studied the failure of the agglomerates with a wide size distribution of primary particles in a random structure. These all show the capability of XRT to provide more information on the structure of particles, leading to an understanding of the breakage behaviour of them.

#### **2.5.4 Porous Agglomerates**

Due to the complex structure of porous agglomerates, it is challenging to analyse their breakage behaviour by experimental work. In contrast, computational simulation has been found as a helpful tool, which provides a better understanding of the effects of different parameters on the breakage behaviour of porous agglomerates, and it is described in section 2.6.1.1. One of the good examples of porous agglomerate is spray-dried powders such as milk, detergent and coffee powders.

#### **2.5.5 Spray-Dried Powders**

Spray-dried powders have an agglomerate structure. Spray-drying is the transformation of a feed material in a fluid or slurry state into a dried particulate form by spraying the feed into a hot drying gas (Masters, 1991). Different techniques are used in the spray-drying process to achieve a desired product. The spray-drying system can be classified

into two main categories: co-current and counter-current. In a co-current spray-dryer the air moves in the same direction as the spray, with both usually entering at the top of the drying chamber and leaving through the bottom. In the counter-current spray-drying tower, the system operates with the spray and air moving in opposite directions. The latter is mainly used for manufacturing detergent powders. It is well known that the operating conditions of the spray drying towers such as slurry flow rate, air inlet temperature and atomizing pressure can have a significant effect on the powder mechanical strength, porosity and hence friability of the particles. The structure of the particles is also affected by operating conditions.

Detergent washing powders are a good example of spray-dried powders. Conversion of detergent slurries to dry powders by spray drying is an important step in the production of detergent powders (Masters, 1991). In the past, the spray drying method using phosphate based materials (sodium triphosphate) was a common method in the production of builders of detergent powders. However, as they were not environmentally friendly materials, they have been replaced by zeolites, sodium carbonate and sodium sulphate salts (Meenan et al., 1997). Yangxin et al. (2008) listed six group of components which laundry detergent powders generally contain builders (used to remove calcium ions to soften water), surfactants, enzymes, fillers, bleaching agents and additives such as fabric softening clay and brighteners. The strength of the builder plays an important role in the strength of the detergent washing powders. These particles are particularly prone to attrition because of their porous and weak structure.

### 2.5.6 Morphological Changes during Spray-Drying

Understanding the drying kinetics of single droplets with different sizes provides some information on phenomena associated with spray-drying operations such as the morphology of the particles. Most of the studies are based on the classical theories rather than experimental outcomes (Adhikari et al., 2000; Walton, 2000). The behaviour of the particles can be explained partially by heat and mass transfer theories, and some part of it through morphological changes of liquid single droplet to dried solid. Some design parameters, such as diameter and height of the chamber, might help to propose a link between drier design and product quality (Dolinsky, 2001; Ferrari et al., 1989; Hecht and King, 2000). Walton (2000) in his work showed that the morphology of final product is related to drying conditions.

Drying conditions (such as temperature), size and geometry of the chamber and the atomising device are the factors which need to be taken into account before spray-drying process. However some researchers consider the atomisation as the most critical step (Allen and Bakker, 1994; Furuta et al., 1994; Oakley, 1994). The overall quality of the operation can be determined by the size distribution of spray, size of the atomiser, particle trajectory and velocity inside the chamber (Chawla, 1994). Digital image analysis is used in evaluating the particle size, formation of crust, shrinkage phenomena, inflation, blow-up holes, etc. For this purpose, different methods such as stereo, light, scanning electron microscopy (SEM) and confocal microscopy can be used (Aguilera and Stanley, 1999; Kaláb et al., 1995). Stereo optical microscopy is a method used for three-dimensional visualisation at low resolution. Light microscopy is very similar to SEM, and both are used to assess morphological changes related to

drying. However, SEM provides a higher resolution, and is more appropriate to observe the structures with a greater depth. Confocal microscopy is used to obtain optical sectioning of the particle at different levels beneath the surface.

(Alamilla-Beltrán et al., 2005) showed that the size and shape variation of particles during drying depend on the moisture content of the materials as well as the operating temperature. Final products tend to have smaller particle sizes, when the drying is done at low temperatures, while for intermediate and high temperatures the final products are quite large (with around 100% inflation with respect to the initial atomised droplet). Formation of thick and irregular crust mainly occurs at low temperature (70-110°C). Understanding morphology-temperature relationship plays an important role on prediction of size distribution, moisture content, density and strength of the particles (Alamilla-Beltrán et al., 2005).

### **2.5.7 Mechanical Properties of Agglomerates**

The mechanical behaviour of agglomerates is of interest to different industries, as it is a critical issue for production and performance depending on the applications, i.e. dispersion, granulation, compaction and drying. Despite the importance of this topic, there are fewer studies on it compared to single particles. As mentioned before, agglomerates are assemblies of primary particles. One of the most important factors that makes the agglomerate characterisation complex is its porosity, which is a key structural feature. The main aim of mechanical testing of materials is to determine their strength. Strength appears a simple concept, but in practice it is very difficult to define and measure it. Here, the strength is defined as the stress at which a material begins to deform plastically, or in some cases it can develop macroscopic damage. The failure

point in fact depends on the distributed microstructure, i.e. porosity and cracks (Bika et al., 2001).

The yield stress is one of the main measures of strength. There are different measurement techniques, and the results are highly dependent on the loading condition. Indentation probably is one of the most common methods for assessing the yield stress. Various types of indentors can be used depending on the application, such as Vickers (square base diamond pyramid), Brinell (sphere), Knoop (rhombohedral diamond pyramid), etc. A load is applied, and the indenter would slowly be penetrated into the surface of the specimen to a strain of typically 8-10 % (Bika et al., 2001). The applied load divided by the projected area of impression made by indenter on the surface of the particle multiplied by each indenter unique shape factor would give hardness number,  $H$ . In principal, hardness is a function of elastic modulus, Poisson's ratio and yield strength. The big advantage of this hardness measurement method is its simplicity, and it can easily be applied on the surface of the agglomerates. Indentation on the surface of the agglomerate can be easily done if the size of the indenter should be large enough compared to the characteristic size of the particles and pores. However, the issue of selectivity should be also considered, i.e. in case of polycrystalline structure agglomerates, the indentation might be done on one of the phases or at grain boundaries or on other microstructural features, giving rise to misleading measured values.

The indentation method can also be used to measure Young's modulus (Oliver and Pharr, 1992; Sneddon, 1965) and fracture toughness (Evans and Wilshaw, 1976). The main issue is that it requires a smooth and pore-free surface in order to trace the radial crack propagation to calculate the fracture toughness. Overall, the results are strongly

dependent on the load, rate and environmental conditions, and the reported results are not an absolute value of Young's modulus for the material.

### **2.5.8 Modes of Agglomerate Breakage**

The modes of breakage for single particles have well been established; particles may fail through chipping or fragmentation. However the definitions of these terms do not lend themselves well to the mechanisms of agglomerate failure; this is largely due to non-uniformity in granule structures; however, several classifications of breakage modes for agglomerates have been proposed. Subero and Ghadiri (2001) investigated breakage patterns of agglomerates of approximately 30 mm diameter, formed by glass ballotini bonded with bisphenol-based epoxy resin, the breakage patterns found were local damage, local damage and oblique fracture, local damage and diametrical fracture, and multiple fragmentation. Mishra and Thornton (2001) classified agglomerate breakage through the modes of fracture, fragmentation, disintegration, and total disintegration. Using numerical simulations of orthogonal agglomerate impact with a wall, their work showed that at high velocities, denser agglomerates failed through fragmentation, whereas less dense agglomerates failed through disintegration. Intermediately packed agglomerates showed a shift from disintegration failure mode to fragmentation, when the number of contacts was increased (without changing solid fraction) beyond a threshold value. Reynolds et al. (2005) identified 12 different breakage patterns for solid, wet, and binderless granules. This highlights the variation in granule breakage, but also the need for a uniform breakage pattern classification procedure, such as that existing for single particles (i.e. chipping, disintegration, and fragmentation).

Due to the complexity of the agglomerates structure arising from many factors, such as primary particle size distribution, void fraction, density and inter-particle bond characteristics, a full breakage map of agglomerates is not yet established. However, the failure mode of agglomerates can macroscopically be covered by the three classical modes of failure. Boerefijn et al. (1998) observed the ductile mode of failure macroscopically in disintegration of weak agglomerates bonded by van der Waals forces. Subero and Ghadiri (2001) studied patterns of failure of large agglomerates of glass ballotini bonded together using a brittle glue. This is described in detail in the next section.

### **2.5.9 Breakage Patterns of Agglomerates**

Subero and Ghadiri (2001) found several breakage patterns of agglomerate materials: localised damage on the contact point, fragmentation by propagation of various cracks into the agglomerate body or extensive disintegration. Overall, the agglomerates can break in different patterns depending on their properties and loading conditions, leading to various failure modes. This refers strictly to the macroscopic failure presented by the whole agglomerate, rather than the failure of individual interparticle bonds (Ning et al., 1997; Subero, 2001b; Ge and Schmauder, 1995). In terms of the breakage of individual inter-particle bonds, two different forms of failure have been observed: internal (cohesive) and interfacial (adhesive). The internal breakage produces irregular surfaces due to crack jumping, whilst in the interfacial failure, clean and smooth fracture surfaces can be observed (Subero and Ghadiri, 2001).

Agglomerate failure is sensitive to the structure and interparticle bond characteristics. Hence, the pattern and mode of failure are more complex than the continuum solid

particles. If the bond is stronger than the primary particles, it is likely that the cracks propagate through the primary particles themselves. However, the bond is commonly weaker than the particles and hence agglomerate failure is through bond breakage. This is the case under consideration below, reviewing the work in the literature. The work of Subero and Ghadiri (2001) showed the various patterns of breakage of agglomerates at both macro-scale level, i.e. agglomerate breakage, and micro-scale level, i.e. interparticle bond breakage. Agglomerates with well-defined bond properties and void distributions were prepared using die casting. This technique has a good control on the structure of the agglomerates, i.e. void number, void size and bond properties.

As mentioned before, glass ballotini were used in this work as the constituent primary particles, and bisphenol-based epoxy resin as the bonding material. The particles were mixed with ammonium nitrate salt granules before moulding. After curing to produce strong bonds, the agglomerates were cooled for a while at room temperature, and then washed with water to dissolve the salt particles in water to produce large cavities in the structure. The agglomerates were then dried. Different number and size of the macrovoids could be produced in this way providing agglomerates with different structures ready for impact testing.

The observation of the shapes of fragments can help to elucidate the fracture pattern. Subero and Ghadiri (2001) reported two main types of breakage due to impact: localised and distributed damage. The localised damage was observed near the impact area. Generally, the zone around the impact point broke into very small fragments. In some cases for the high impact velocity, the debris generated flowed out of the impact zone.

In some occasions, clusters were also produced near the impact zone. The level of size reduction depended on the macro-void number/size. For the clusters with a high macro-void number/size, a visible reduction of their dimension in the direction of impact was observed. For agglomerates containing macro-voids the impact zone was very weak, and disintegrated into very small fragments. In this case, the stresses cannot be propagated into the agglomerate to cause fracture.

The second type of breakage is the fragmentation of agglomerates, which can be identified by large planar cracks, and the splitting of the agglomerate into a small number of relatively large clusters. In this pattern of breakage three types of cracks were observed: oblique, median and secondary cracks. On some occasions, both oblique and meridian cracks cause fragmentation and as a result of that multiple fragmentations can be observed.

Subero and Ghadiri (2001) proposed that for the majority of the patterns of breakage of agglomerates, the semi-brittle mode of failure can be considered, because in their case the damage initiated from the impact zone and propagated into the body of the agglomerate, rather than any crack propagating. Different patterns of breakage are described schematically in Figure 2-4.

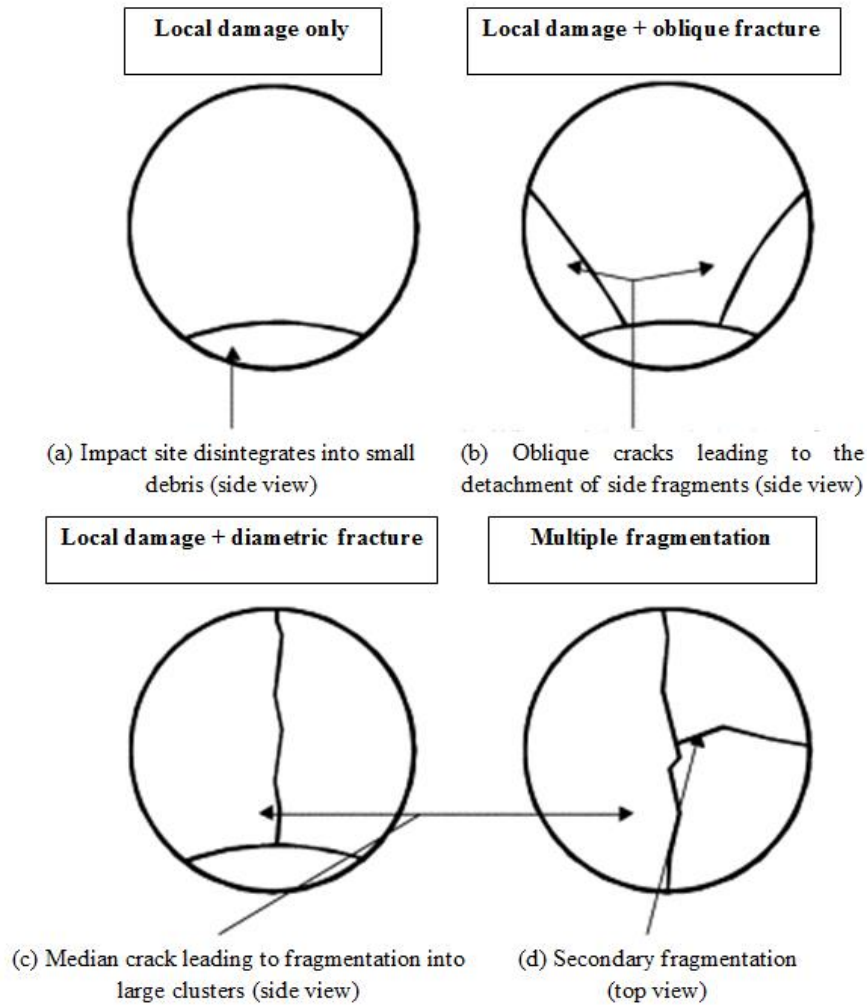


**Figure 2-4. Schematic patterns of agglomerate breakage (Subero, 2001b)**

It is clear from the above that a multitude of cracking patterns prevails in breakage of agglomerates, depending on the impact velocity and macro-void size/number. The fragmentation pattern is more dominant, with increasing impact velocity and also the size of macro-voids. Therefore, both fragmentation and localised damage can be observed at high

velocities. A regime map of agglomerate breakage has been proposed by Subero and Ghadiri (2001) and this is reproduced as Figure 2-5 below.

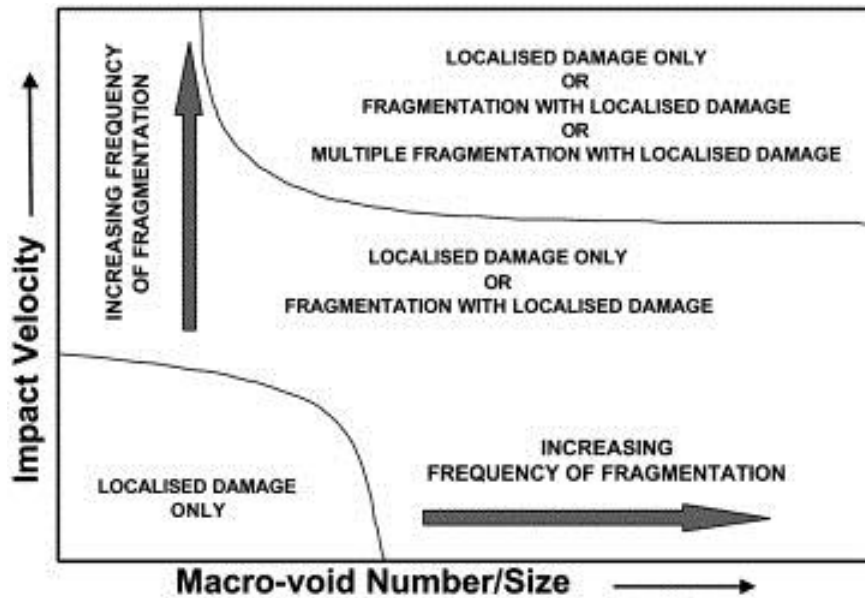


Figure 2-5. The qualitative dependence of the observed pattern of breakage with the impact velocity and solid fraction (Subero and Ghadiri, 2001)

### 2.5.10 Breakage Analysis

In order to analyse the breakage results of a bonded agglomerate, the concept of damage ratio can be used, which is defined as the number of broken interparticle bonds divided by the total number of bonds present in the agglomerate. It is a measure of extent of damage and is related to the Weber number,  $We$ , according to (Kafui and Thornton, 1993):

$$We = \frac{\rho V^2 D}{\Gamma} \quad \text{Eq. (2-13)}$$

where  $\rho$ ,  $D$  and  $\Gamma$  are the primary particle density, diameter and surface energy and  $V$  is the impact velocity. The breakage propensity parameter given by Eq. (2-4),  $\eta$ , can be related to Weber number, as  $K_c$  can be related to the surface energy  $\Gamma$  by the use of Linear Elastic Fracture Mechanics. For instance,  $K_c = 2E\Gamma(1 - \nu^2)$  for the case of plane strain ( $\nu$  is Poisson's ratio), which follows:

$$\eta \propto \frac{\rho V^2 D}{\Gamma} \times \frac{H}{E} \quad \text{Eq. (2-14)}$$

The form  $H/E$  is attributed to the elastic-plastic deformation characteristics of the agglomerate. When the simulation results are interpreted in the form of fractional loss per impact, Thornton et al. (1995) reported that at low impact velocities, corresponding to the chipping regime, the fractional loss per impact varies linearly with the Weber number, which is in agreement with the model of Ghadiri and Zhang (2002).

To model agglomerate breakage, Moreno-Atanasio and Ghadiri (2006) explored a simple case where the energy expended to break the bonds was linearly related to the incident kinetic energy. Considering the work spent to break a bond, they found that the damage ratio,  $\Delta$ , is given by:

$$\Delta \propto \frac{\rho V^2 D}{\Gamma} \times \left(\frac{ED}{\Gamma}\right)^{2/3} \quad \text{Eq. (2-15)}$$

Clearly the Weber number and other dimensionless groups such as  $ED/\Gamma$  influence the breakage of agglomerates, as demonstrated by the numerical simulations of Moreno-Atanasio and Ghadiri (2006). More extensive work is required to describe the breakage characteristics of agglomerates with binders of different failure properties.

### 2.5.11 Computer Simulation of Agglomerate Breakage

There are different ways in which the strength of agglomerates has been defined. Rumpf (1962) defined the strength of agglomerates as the force needed to break all the interparticle contacts simultaneously. According to the work of Kendall (1988), the strength of agglomerates has been defined based on the resistance of crack propagation using the linear elastic fracture mechanics.

Computational modelling and simulation have been extensively used to analyse the breakage behaviour of the agglomerates. The Distinct Element Method (DEM) is a numerical technique which is used for the investigation of the mechanics of granular materials. Kafui and Thornton (1993) used DEM to simulate two dimensional (2-D) particle motions in the impact breakage of agglomerates. Later, the three dimensional (3-D) particle motion of agglomerate breakage was simulated by Subero et al. (1999). One of the advantages of using DEM is its versatility. There is a possibility to change any material property without affecting the others. The other advantage of DEM is that the effect of impact on the number of broken interparticle contacts can be quantified.

In Subero's work (Subero, 2001a), primary particles were generated randomly in a confined spherical space. Different physical properties such as density, size distribution, elastic modulus and Poisson's ratio were assigned to the primary particles at the generation time. As in most cases the bond is weaker than the primary particles and agglomerate failure is through bond breakage, the primary particles were considered non-breakable. To bring the particles together and generate the agglomerate, a centripetal force field was applied.

To simulate agglomerates with a porous structure, macro-voids were generated in the agglomerates by removing the primary particles from random locations within the agglomerate. The macro-voids were produced after generating the agglomerates. The number and size of the macro-voids were varied to produce agglomerates with different structures. To evaluate the breakage of agglomerates by simulation, the generated agglomerates were impacted at different velocities. The damage mainly occurred at the impact site, and a number of particles were detached from the original agglomerates; however some damage, albeit insignificant, could be observed in the rest of the agglomerates as well.

For the simple case of auto-adhesive primary particles, where the interparticle adhesion follows the JKR model (Johnson et al., 1971), extensive work has been reported in the literature based on the development of the Distinct Element Analysis of agglomerates by Thornton and his co-workers (Thornton et al., 1999; Thornton et al., 2004). The effects of interface energy, impact angle and agglomerate morphology have been investigated by DEA by Subero et al. (1999), Moreno et al. (2003) and Golchert et al. (2004), respectively. Kafui and Thornton (1993), Moreno-Atanasio and Ghadiri (2006b), Schubert et al. (2005), and Antonyuk et al. (2006) have simulated the impact damage of agglomerates on collision with a wall by the Distinct Element Method. DEM simulation has also been widely used to study the impact breakage of agglomerates (Ghadiri and Moreno-Atanasio, 2007; Thornton and Liu, 2004; Subero et al., 1999). The research results showed that interparticle properties as well as primary particles properties, such as size, Young's modulus play important roles in agglomerate strength. Mechanistic models have also been used to relate the interface energy between the

particle to breakage behaviour of agglomerates (Moreno-Atanasio and Ghadiri, 2006; Thornton and Yin, 1991).

In a recent work, Nguyen and Rasmuson (2015) studied the breakage and adhesion regime map for the normal impact of loose agglomerates with a spherical target (as shown in Figure 2-6). Their case study was dry powders for inhalation. The particles are first disintegrated and then adhered onto the carrier particles. The structure of these particles should be in a way that they are strong enough to survive during handling and loose enough to be dispersed for inhalation (Jones and Price, 2006; De Boer et al., 2012). They made several agglomerates with different levels of interface energy between fines-fines  $\Gamma_{1-1}$ , and also fines-carrier  $\Gamma_{1-2}$ . The agglomerate was then impacted at a spherical target. The fragments produced due to impact were distinguished using a clustering algorithm (Daszykowski and Walczak, 2010), and the size of the clusters was normalised with the original size of the agglomerate. Different levels of interface energy would give rise to various packing densities. However in this study the agglomerates have the same packing density.

In order to analyse the breakage results, they suggested that a combination of damage ratio, proposed by Moreno-Atanasio (2003), and the ratio of cohesion to adhesion strength make it feasible to relate the impact behaviour of agglomerates to particle properties. The damage ratio,  $\Delta$ , has been described previously in section 2.6.10, and the ratio of  $\frac{\Gamma_{1-1}}{\Gamma_{1-2}}$  shows the cohesion strength to the adhesion strength. Plotting  $\Delta$  as a function of  $\frac{\Gamma_{1-1}}{\Gamma_{1-2}}$  would result in a map construct in which different regimes are shown based on the daughter fragments from the breakage event.

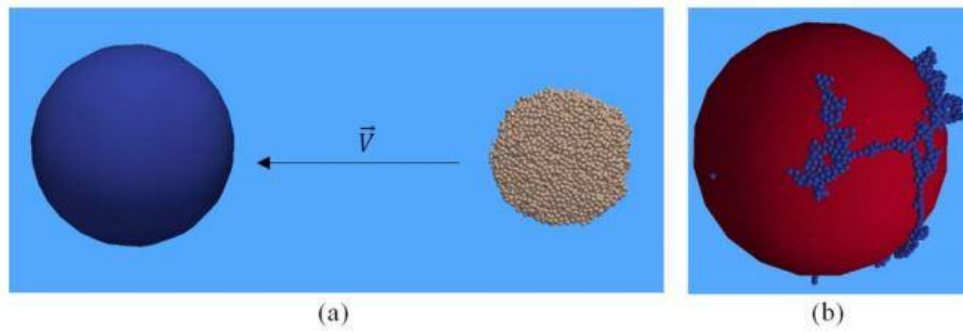
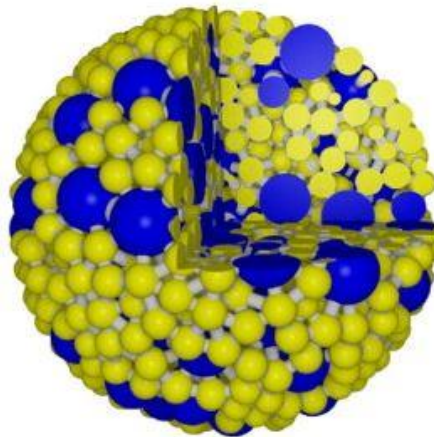


Figure 2-6. Simulated system; (a) before impact, (b) after impact, fines are attached on the carrier surface

(Nguyen et al., 2015)

Other pieces of research work on DEM simulation of agglomerate breakage investigated the effects of impact angle, agglomerate size, impact velocity and material properties on the fracture behaviour of agglomerates due impact, such as work of (Potapov and Campbell, 1996; Thornton et al., 1999; Samimi et al., 2004; Salman et al., 2003; Antonyuk, Khanal, Jürgen Tomas, et al., 2006). The bonding model has been found to have a significant effect on the breakage behaviour of agglomerates (Metzger and Glasser, 2012). Morphology is another influential factor on agglomerate breakage, i.e. loose agglomerates behave differently compared to dense agglomerates (Subero, 2001a). The effect of agglomerate shape has also been investigated using the DEM simulation of breakage of cylindrical, spherical and cubical agglomerates (Thornton and Liu, 2004). On the other hand, the shape of the primary particles can be influential on the agglomerate breakage results (Balakrishnan et al., 2010; Rong et al., 2013; Wolff et al., 2013). One of the most important factors affecting the agglomerate breakage is microstructural effects, such as porosity. Spetl et al. (2015) evaluated the mechanical behaviour of spherical bonded agglomerates, in which the microstructure is specified using a dense packing of spheres that are bonded together, with stochastic model-based

microstructure using DEM simulation. A stochastic simulation refers to a simulation in which the evolution of variables, that can be changed stochastically (randomly) with certain probabilities, is traced. The agglomerates were generated using two primary particle sizes with different mixing ratios. A very loose random packing density (~56%) was used. Bonds were applied to connect particles with a gap distance below a certain threshold (Dosta et al., 2013). The particle-particle and particle-wall interactions were described using the soft sphere contact model. The Hertz theory was used to calculate the normal component of force, and the model of Mindlin and Deresiewicz (1953) was used for the tangential component. The stochastic model was used to vary the ratios of primary particles to form different agglomerates. Special care was taken to obtain comparable agglomerate microstructures even for different mixing ratios, which was done by controlling the volume of bonds and primary particles. The total porosity and diameter of agglomerate is always the same, for all testing conditions. One of the agglomerates formed, using the above-mentioned conditions, is shown in Figure 2-7.



**Figure 2-7. Simulated agglomerates with yellow colour showing small primary particles, blue large primary particles, and grey the bonds (Spettl et al., 2015)**

The agglomerates were then crushed by compression between two steel plates at constant speed. The load-displacement curves were plotted. The number of broken bonds and size of the fragments were also monitored to analyse the breakage results for different agglomerates, and to track the effects of bonds and primary particles on agglomerate strength. The results show that there is a linear relationship between number of broken bonds and the breakage energy, which is as expected. They also tracked the size of the first and second largest fragments produced after breakage. Surprisingly, there is no relation between size of the fragments and the mixing ratios (Spetl et al., 2015).

The type of bonding used in the agglomeration system plays an important role in defining the strength of the particles. It is very critical to choose a realistic bonding model in the agglomerate simulation, in order to obtain more accurate and comparable results with experimental work.

Brown et al. (2014) developed a new bonding contact model based on the Timoshenko beam theory, which considers shear, axial and bending behaviour of a bond. Use of a beam element is based on the assumption of linking the centre of the particles in a bonded contact (Schneider et al., 2010; André et al., 2012; Carmona et al., 2008; D'addetta et al., 2002). The newly developed bonding model, which is referred to as the Timoshenko Beam Bond Model (TBBM), provides a more realistic representation of cemented granular materials. The failure of cementitious materials occurs through crack initiation and propagation. Therefore, reliability of DEM simulation for these materials is highly dependent on the contact laws acting on the bonds, and this model has the ability of bond breakage. Another advantage of this bonding model is that it can

represent different deformable structures such as shells or frames, by which deformation of both particle and boundaries can be analysed using DEM simulation.

The interaction of the spherical particles can occur at either bonded or non-bonded contacts. A non-bonded contact such as Hertz-Mindlin contact law is based on a spring-dashpot arrangement (DEM-Solutions, 2015; Johnson, 1987). However, for a bonded contact model a virtual bond element is considered to exist between the particles kept by each other. In both cases, they resist shear and compressive forces. The difference is that the bonded contact type can also resist bending, twisting and tensile forces. For Timoshenko beam bond model, the bond is assumed as a rigid feature connecting the centres of each two particles, by which the bond has the same six degrees of freedom as particles. Although there are different parameters in this bonding model, such as bond Young's modulus, Poisson's ratio, compressive strength, tensile strength, shear strength and radius multiplier, which need to be defined, most of them can be kept constant, and a few need to be modified in order to produce concrete behaviour. This model is used to represent the elastic behaviour of a deformable structure for both particle and deformable boundaries using the same DEM simulation (Brown et al., 2014).

Overall, making use of the right type of the bonding contact model leads to more realistic results produced by simulation. This in fact depends on the application of the simulated process. The JKR bonding model is used for simulating agglomerates formed by adhesive forces. Simulation of the auto-granulation process is a good application of using the JKR model (Ku et al., 2015; Johnson et al., 1971). On the other hand, the use of rigid bonds such as Timoshenko beam bond model is made to simulate cement-like structures with deformable boundaries (Brown et al., 2014).

Despite all of the work done on the analysis of the breakage behaviour of agglomerates, much still needs to be done to provide a better understanding of the underlying causes of variation in breakage behaviour of different agglomerates. Computer simulations by the Distinct Element Method have provided further insight into how agglomerates break under quasi-static and dynamic conditions.

## 2.6 Concluding Remarks

Attrition is a serious problem in manufacturing plants handling weak and friable powders. Surface damage and body fragmentation of such particles need to be fully understood in order to mitigate the extent of attrition, as it affects the quality of the product. Analysis of breakage behaviour of different materials is also useful for designing various units of operations such as cyclones, pneumatic lines and other items of equipment, where particles experience mechanical stresses.

The mechanisms of attrition depend on the formation of various types of cracks, which in turn depend on the mode of failure, i.e. brittle, semi-brittle and ductile. There is some work reported in the literature for well-defined structures, such as crystalline solids. However, the information is sparse for spray-dried and agglomerated structures. The breakage of agglomerates has been the subject of several studies, where the effects of interparticle bond characteristics and structure have been investigated. Nevertheless, the prediction of the mode of failure of agglomerates is far more complex compared to continuous solid particles.

The above issue becomes more challenging when it comes to porous agglomerates. Some of the known characterisation methods, such as nano-indentation, have some

limitation for such particles. Spray-dried powders are a good example of porous agglomerates. The structure of these particles can be affected by operating conditions. Therefore, it is essential to characterise the structural differences of such particles as a function of size. For this purpose, different methods, such as X-ray microtomography, have been found to be useful. Several pieces of work on breakage analysis of these particles have been reported in the literature showing the complexity of their breakage behaviour.

The behaviour of agglomerates and non-agglomerated porous materials is affected by parameters such as density, agglomerate size, primary particle size, and interparticle bond strength. Although in reality characterisation of internal stresses in some cases is very complicated, the numerical simulation has been found as a powerful tool to provide a good knowledge on different factors affecting the failure of the agglomerates. However, it should be noted that using accurate parameters such as a proper bonding contact model is very critical in order to obtain more realistic results. There are different bonding models such as the JKR and Timoshenko beam bond model which can be used depending on the different applications. However, a better characterisation of bond failure is still needed to develop a contact model, which can then be used in simulations, and subsequently validated by experimental work. It in fact needs a more precise control of structure and interparticle bond properties in order to investigate their role in affecting the strength of complex structures and to help develop realistic models for simulations.

## CHAPTER 3 MATERIALS AND CHARACTERISATION

Powder characterisation is an essential step in the goal of understanding the behaviour of powders in different processes. Therefore, it is not a trivial task. In this chapter, a description of the materials used for the experimental work is provided. The purity and features of the materials have been tested using different methods such as Raman spectroscopy, Thermogravimetric Analysis (TGA) and Dynamic Vapour Sorption (DVS). The results show that burkeite is the only salt formed during spray-drying. Some information on the methods used for sample preparation and particle size distribution measurement are also described.

### 3.1 Materials

Synthetic detergent washing powders are most commonly produced by spray-drying, and conversion of detergent slurries to dry powders by spray drying is an important step in the production of detergent powders (Masters, 1991). Most of the detergent compositions contain deterative active ingredients. Such ingredients usually make the particles 'sticky', causing serious issues in their flowability. However, in order to eliminate this effect, a 'bulking agent' in the form of separate particles is usually added to the composition. Some examples of bulking agents are sulphates, zeolite, carbonates, clays and silicates. Both carbonate and silicate affect the pH of the wash liquor, with a negative influence on cleaning performance. Clay can damage the fabrics by changing the colour or causing deposition on the fabrics. Sulphates have been found to be one of the best bulk agents, as it is pH neutral. However, because of its high bulk density it

easily sinks as it is added to the water, causing sedimentation. Hence using sulphate along with other components would be a good option (Tantawy and Martinez-Guzman, 2014).

Spray-dried burkeite particles are used in this work as a model material as they are a good example of a complex porous structure. They are highly porous and friable and hence prone to undergo attrition even under gentle handling. Burkeite is a co-crystal of sodium sulphate and sodium carbonate, and it has the general form  $\text{Na}_4\text{SO}_4(\text{CO}_3)_i(\text{SO}_4)_{1-i}$ . The particles of interest here have been produced at Procter and Gamble Technical Centre, Newcastle Innovation Centre (NIC), Longbenton, UK by spray-drying of a slurry of the mixture of the two salts. Sodium carbonate and sodium sulphate were added to water in a proportion to produce a slurry of burkeite with some excess sodium sulphate. The slurry was then atomised in a spray drying tower to produce dried porous particles of burkeite.

Generally, in spray-drying of detergent washing powders, as drying proceeds, a crust is formed and the crystals within the droplets form clusters. During the drying process, the surface of the particle becomes dry and the wet core shrinks inside the particle, and the spray-dried particle is formed (Meenan et al., 1997; Sano and Keey, 1982; Audu and Jeffreys, 1975). However, for spray-drying of burkeite particles at P&G, no clear procedure has been reported regarding drying, and the formation of the particles still needs to be understood. The hypothesis is that the outer layer is dried faster than the inner part of the particle. Based on the observation of Dr Dan Xu at P&G there are some crystals of burkeite (around 10-12  $\mu\text{m}$ ) in the tank, during slurry preparation.

Therefore, there is crystal growth inside each particle during drying of the droplet, which in fact results in formation of the clusters, as will be shown later on.

The potential application of these particles is as additives to use them as carrier/ filler of surfactants for detergent washing powders; therefore it is critical to explore the strength of the particles under different levels of stresses. Scanning Electron Microscopy (SEM) of a single particle of spray-dried burkeite is shown in Figure 3-1. The particle has an agglomerate structure. As mentioned before, the outer layer of the particle is dried first. During the drying process of the inner part, there is a possibility that the water vapour escapes from the particle through holes formed on the surface, presumably by eruption. The holes on the surface of the particle are also observed in Figure 3-1.

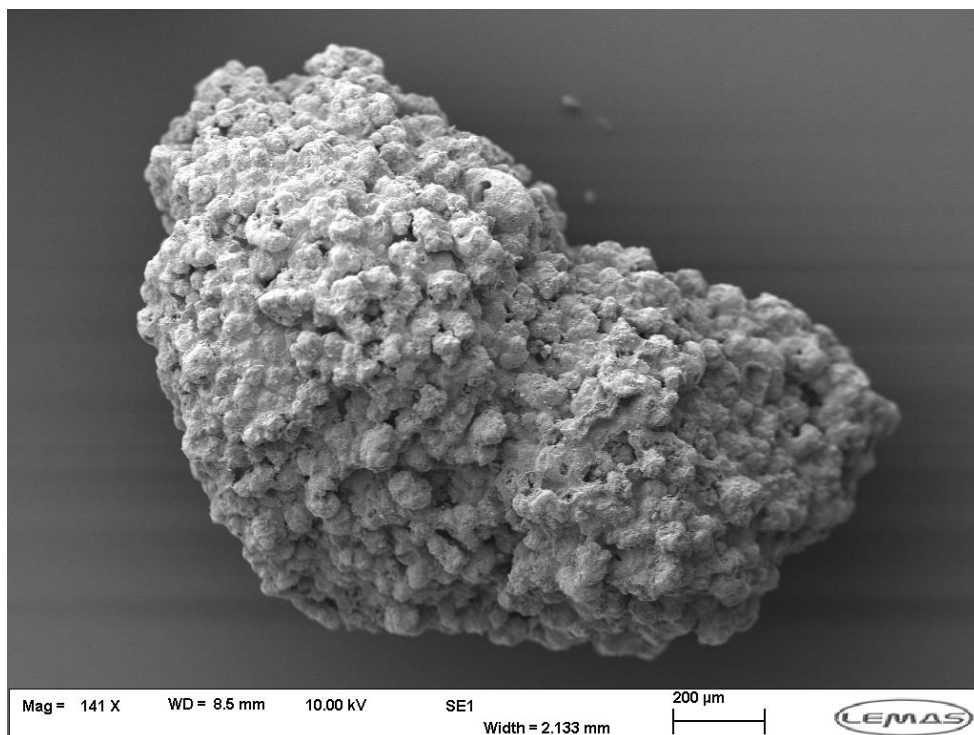


**Figure 3-1. SEM image of a single particle of spray-dried burkeite**

A higher magnification of the SEM image of the particles shows a kind of skin on some part of the particle surface, as shown in Figure 3-2. This type of skin exists on some of the particles, which could be formed during drying of the outer layer of the particle. Debris are also observed on the surface of the particles as shown in Figure 3-2. A single particle has been chosen from a container of the sample to be observed under SEM. However, due to the weak and friable structure of the particles, they can easily break even during handling and produce dust/ debris, which might stick to the surface of the other particles.

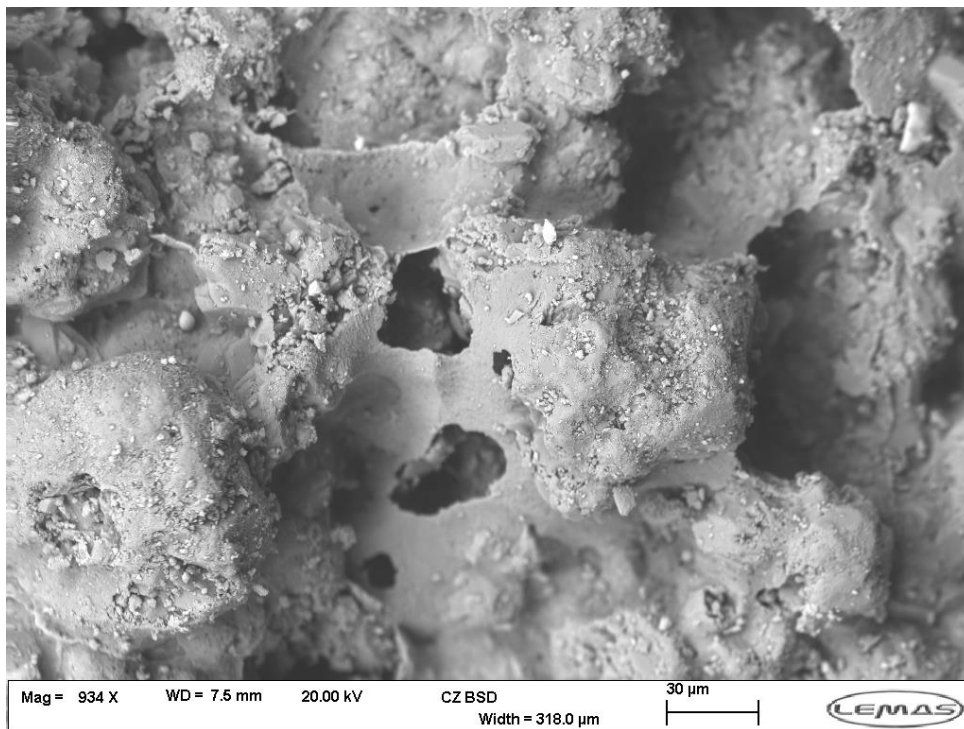


**Figure 3-2. SEM image of the surface of a spray-dried burkeite particle**

To see the internal structure, a single particle was mounted on an SEM stub using a speckle of glue. The particle was then cut with a sharp knife on a plane, exposing the internal structure. The SEM images with different magnifications are shown in Figures 3-3 to 3-5.

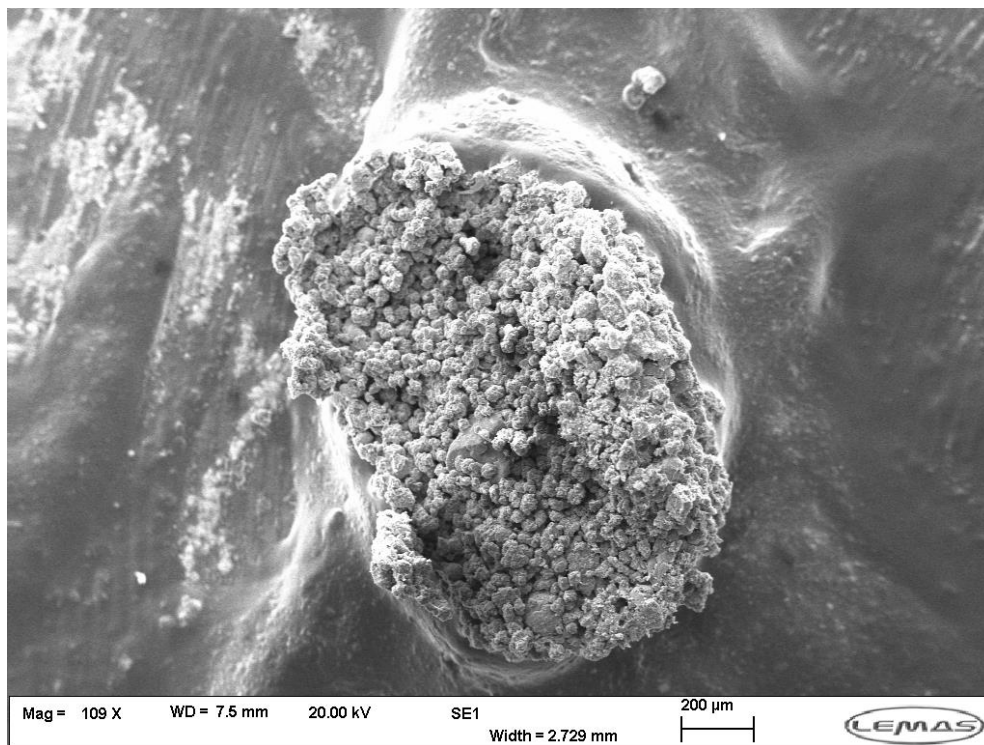


Figure 3-3. Internal structure of a single particle of spray-dried burkeite

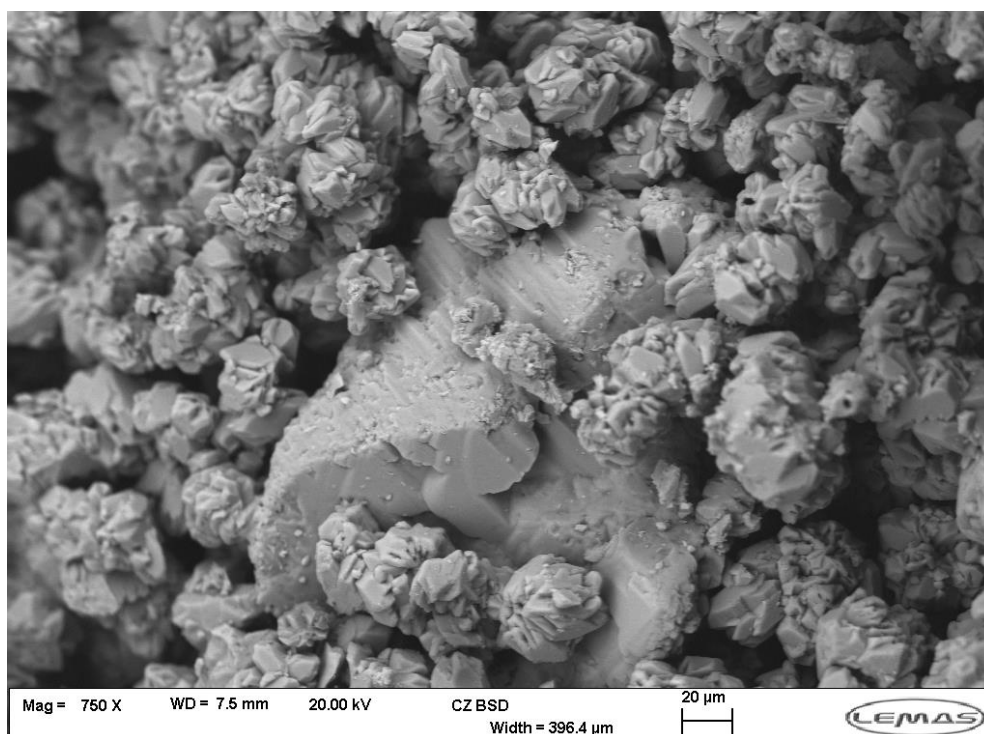
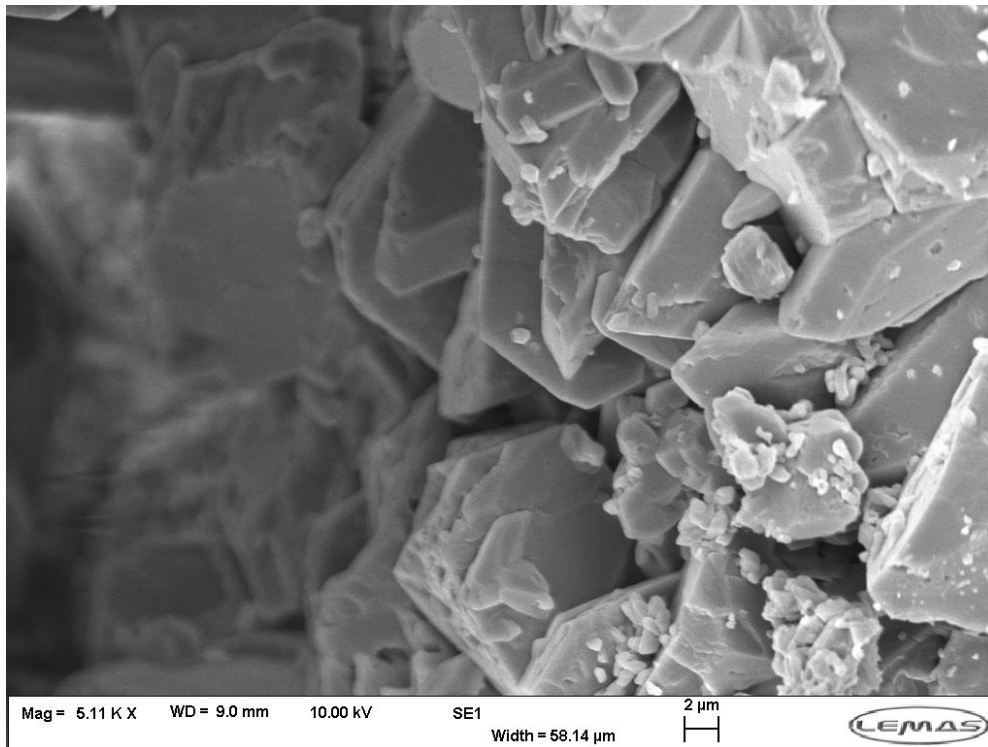


Figure 3-4. Clusters inside a spray-dried burkeite particle



**Figure 3-5. Crystalline structure of the clusters**

The SEM images clearly show three different levels of structure in a single particle of spray-dried burkeite. Each individual particle has an agglomerate structure, which is made of a number of clusters (Figure 3-3), and the gap between the clusters forms the porosity inside the particles. Each cluster has several crystals stuck to each other (Figure 3-4), which has been shown in a higher magnification in Figure 3-5. The large feature observed in Figure 3-4 is undissolved sodium sulphate, which exists in some particles.

As it shall be seen later, the clusters are loosely bonded together. The crystals forming each cluster are bonded together much more strongly. The study on analysis of the strength of the clusters and particles is shown in Chapter 5.

## 3.2 Material Characterisation

Due to the nature of the spray-drying, the material properties which are porosity-dependent would vary depending on the production conditions. Therefore the material properties reported in the literatures for spray-dried burkeite particles cannot be used in this work. However, different methods have been used to prove purity of the particles.

The produced spray-dried burkeite particles are then tested using different methods such as Raman spectroscopy and Dynamic Vapour Sorption at P&G, NIC (UK) to assess if burkeite is the only salt formed in the process (Xu and Martin de Juan, 2014).

### 3.2.1 Dynamic Vapour Sorption

Dynamic Vapour Sorption (DVS) is a gravimetric technique to measure how much and how quickly a solvent can be absorbed by a sample (Mackin et al., 2002). The test was carried out by P&G after producing spray-dried burkeite particles by placing them into a container in the DVS device which is surrounded by a temperature controlled cabinet. Water was used as the vapour. All the experiments were done at 30°C. The results are shown in Figure 3-6, which indicates that burkeite particles do not absorb any moisture in the above-mentioned conditions. BP in Figure 3-6 refers to blown powder which has been used in comparison with burkeite.

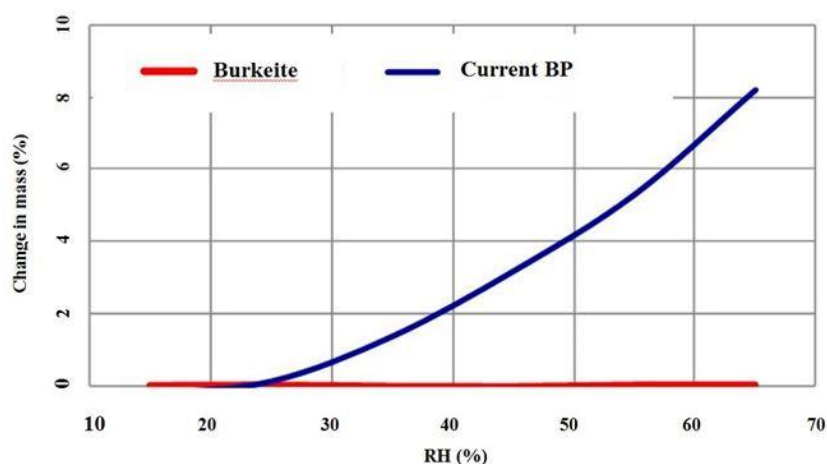


Figure 3-6. DVS analysis of spray-dried burkeite particles

### 3.2.2 Raman Spectroscopy

Raman spectroscopy is a spectroscopic technique to identify samples molecular structure. The light used in this technique might be reflected, absorbed or scattered in some manner. The interaction of molecular vibrations with the laser light causes the energy of the laser photons to be shifted up or down (Smith and Dent, 2005). The Raman test has been done by Tara Aziz at P&G, NIC (UK) to characterise the produced spray-dried burkeite particles at their site. The results are shown in Figure 3-7.

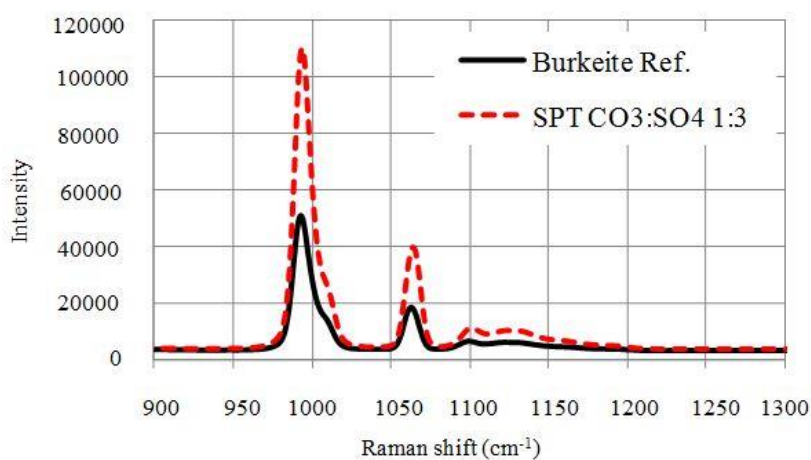


Figure 3-7. Raman spectroscopy test on spray-dried burkeite particles

The peaks are in agreement with the peaks of the reference burkeite, showing that the produced particles at P&G are pure burkeite.

### 3.2.3 Thermal Gravimetric Analysis

Thermal Gravimetric Analysis (TGA) was also used to check the moisture-content of the particles. The results are shown in Figure 3-8.

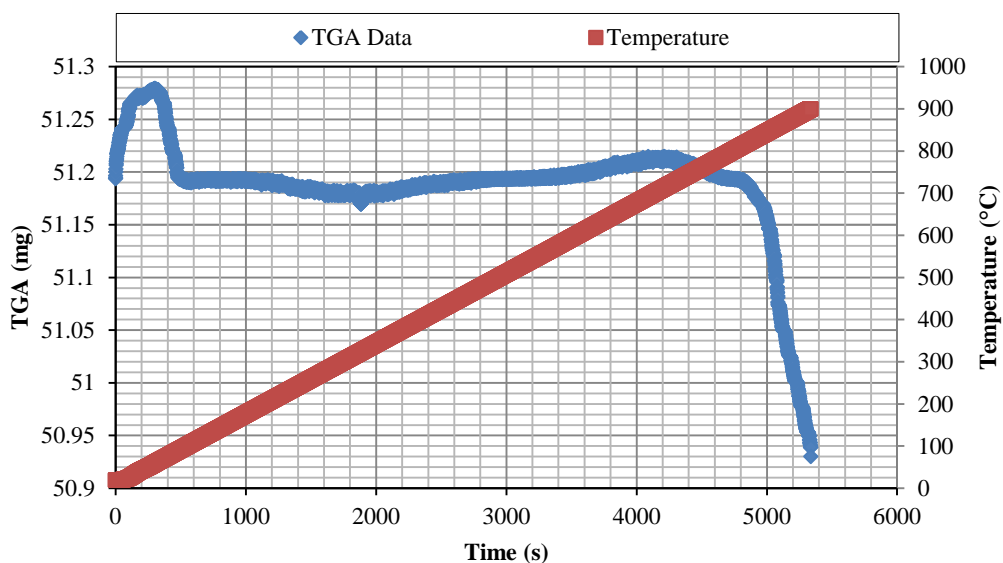


Figure 3-8. TGA analysis of spray-dried burkeite particles

Based on the results shown by TGA test, the spray-dried burkeite particles have been heated up to around 900°C, and the reported result does not show any excess water or hydrate form inside the particles. The observed peak at the beginning of the curve is due to some artefacts of the TGA device. However, the trend is still reliable. The trend shows a fairly straight line up to around 750°C, indicating no changes in the material. However, there is a mass loss as a function of temperature from 750°C to 900°C, showing decomposition of burkeite at this range of temperature.

### 3.2.4 Particle Density

Based on the results of Raman spectroscopy, the material used in this work is pure burkeite. Therefore the skeleton (true) density of the particles is  $2670 \text{ kg/m}^3$ , as reported in the literature (Anon, 2015). However, the spray-dried burkeite particles are porous. Therefore the envelope density of the particles needs to be evaluated. Due to the nature of spray-drying procedure, it is very challenging to control the envelope density of different particle sizes. Different operating conditions, such as air inlet temperature and slurry flow rate, might affect the structure of the particles. According to some observations reported by Dr Dan Xu at P&G, NIC (UK), there are some crystals (around 10-20  $\mu\text{m}$ ) already formed in the tank. Therefore, as the slurry is atomised in the tower, a number of the crystals might be in droplets, which can also affect the structure (density) of the particles. Hence it is critical to measure the envelope density of different particle sizes of spray-dried burkeite powder. Various measurement methods have been used for this purpose, and they are fully described in chapter 4. In order to study the structural differences as a function of size, it is important to use as narrow size distribution as possible. Therefore, a new design of experiments has been used to produce narrow size distribution of the particles.

## 3.3 Sample Preparation

It is critical to use a representative sample mass in order to produce statistically reliable results (Bash, 2015). Therefore, the first step of sample preparation is to split the sample into sub-samples with desired quantities.

### 3.3.1.1 Sample Splitting Method

The spray-dried burkeite powders used in this work were produced by Procter and Gamble, NIC (UK) and provided in 15 kg batches. In order to obtain a representative sample for particle size distribution measurement, each batch had to be divided to small quantities, which were appropriate for sieving. Therefore sample splitting was carried out using a riffler (Retsch, UK). As the quantity of the initial batch is quite large, blending is needed after each splitting step to make sure that each split sample is representative of the original batch of the sample (John et al., 2009).

Sample splitting of a large batch of burkeite starts with splitting the sample into two samples, and each split sample would be again split into two other sub-samples. The blending procedure now is done by combining two samples of each split category as shown in Figure 3-9.

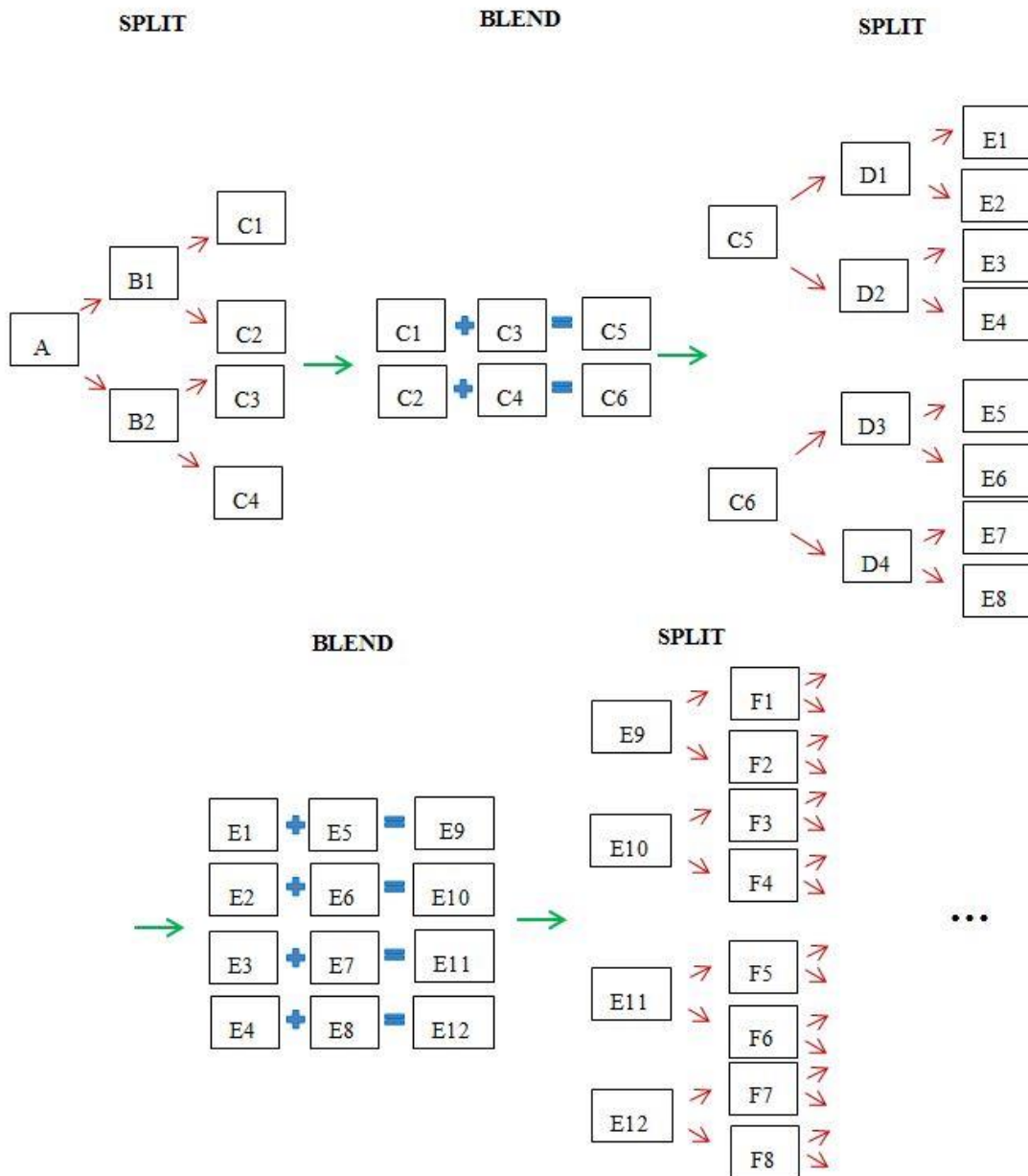


Figure 3-9. Schematic diagram of splitting and blending procedure

The splitting and blending procedure were continued until obtaining a small sample, the splitting by itself would be then done to reach the quantity required for the experiment. Combination of splitting and blending assures the split sample to be totally representative of the main batch.

### 3.3.2 Particle Size Distribution

The spray-dried burkeite particles are highly porous and friable and hence prone to undergo attrition even under gentle handling. So handling of the particles for sieve analysis itself could give rise to attrition. Sieving was carried out by two different methods of sieving: mechanical sieving and hand (manual) sieving. British standard sieve sizes were used for both sieving methods. Mechanical sieving has been done for 15 seconds, using an interval of 1 s and amplitude of 0.5 mm. Hand sieving was carried out based on the method described by Allen (1990). For this purpose the smallest aperture sieve should be placed on a catch pan. An appropriate quantity of sample would be placed on the mesh. The sieve should be slightly inclined approximately  $45^\circ$  to the horizontal. A cylindrical piece of wood (or the heel of the hand) is used to tap on the sieve. The sieve should be rotated  $1/8$  of a turn every 25 raps. The process is repeated until less than 0.2% of the original sample passes through the sieve. The residues would then be transferred to the larger sieve mesh opening. This method is repeated for a chosen range of sieve apertures and the subsequent residual weights collected. Hand sieving compared to mechanical sieving is very time consuming. However it provides a better control on sieving procedure when weak particles are used. The mass percentage and cumulative size distribution of the materials are shown in Table 3-1 and Figure 3-10, respectively, for both manual and mechanical sieving.

**Table 3-1. Mass percentage of burkeite particles in different sieve cuts obtained from manual and mechanical sieving**

<b>Particle size (<math>\mu\text{m}</math>)</b>	<b>Mass percentage (%) obtained from hand sieving</b>	<b>Mass percentage (%) obtained from mechanical sieving</b>
<125	11.10	26.92
125-150	3.28	
150-180	9.62	
180-212	8.65	
212-250	7.89	9.62
250-300	8.52	9.76
300-355	7.29	10.82
355-425	7.77	9.87
425-500	7.51	7.40
500-600	10.48	9.33
600-710	7.81	7.35

710-850	5.61	5.03
850-1000	3.53	3.18
>1000	0.93	0.70

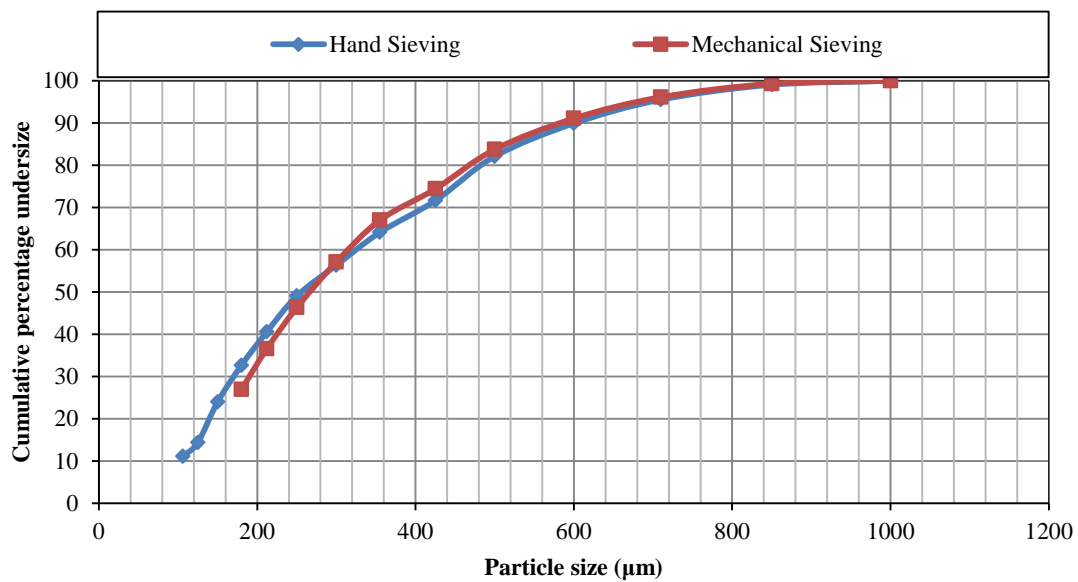


Figure 3-10. Cumulative percentage undersize of burkeite particles by manual and mechanical sieving

The comparison of results shows that the mass percentage of small particles resulting from hand sieving is more than the mechanical sieving, although the size distribution curves obtained from both methods almost overlap. Based on the above observation, it has been decided to use hand sieving as a main sieving method, as hand sieving gives more control on sieving procedure. A careless mechanical sieving by choosing a large

quantity of sample mass will cause the mesh openings to be blinded, which will in fact result in a wrong measurement of size distribution. However, this is not an issue in manual sieving, as the sieves are frequently checked and brushed to avoid this problem.

### 3.4 Near-Mesh Particles

Near-mesh size particles have been prepared by sieving the particles and retrieving only those caught in the mesh opening of the sieve by gentle brushing (Figure 3-11).

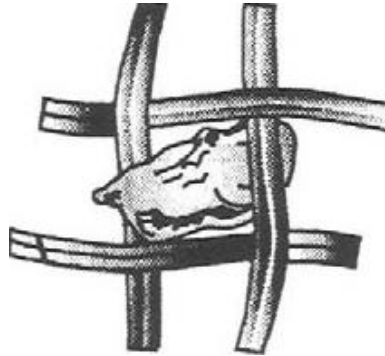


Figure 3-11. Near mesh size particle (Allen, 1990)

Different near-mesh particle sizes were prepared using the above method, and used for structural differences evaluation, as is described in the next chapter.

### 3.5 Representative Sample Mass

To produce statistically reliable results it is critical to use a representative sample mass (Bash, 2015). Error analysis has been done to explore the effect of sample mass on reliability and accuracy of the experiments outcomes such as envelope density measurement and impact breakage results. The standard error, SE, of different number of repeats is calculated using the Equation below.

$$SE = \frac{\sigma}{\sqrt{n}} \qquad \text{Eq. (3-1)}$$

where  $\sigma$  is the standard deviation and  $n$  is the number of repeats.

Standard error is viewed as the standard deviation of the error in the sample mean with respect to the true mean. Standard error analysis has been carried out for all the experiments in this work to choose a minimum representative sample mass required to run the tests, and hence produce reliable results.

## CHAPTER 4 ENVELOPE DENSITY

In order to provide a better understanding of the effect of porosity and structure on the impact strength of the spray-dried burkeite particles, the structural differences (density variation) as a function of particle size needs to be evaluated. In this chapter, different methods of envelope density measurement of burkeite particles, such as GeoPyc (Micrometrics, USA), X-ray microtomography (XRT), mercury porosimetry, etc, have been described. Some other methods have also been used to measure the volume of the particles, such as G3 Morphologi, QICPIC (Sympatec, Germany) and near-mesh sizing, which will be then used to calculate their envelope density. The advantages and disadvantages of each method are investigated in this chapter. Most of the methods show variation of envelope density with size. Among all the methods, the envelope densities obtained from QICPIC and XRT seem to be more realistic, as they account for particle shape.

### 4.1 Introduction

Envelope density is defined as the ratio of mass to volume of the particles including all the open and closed pores. Measurement of particle mass is straight forward. However that of particle volume can be difficult and different measurement methods could give different results. Thus the determination of envelope density is not straight forward as will be seen in the following sections. Based on the results of the previous work, there are structural differences as a function of size for spray-dried particles. Therefore, a good knowledge of envelope density is needed to understand the effect of structure (envelope density) on the strength of the particles.

## 4.2 Envelope Density Measurement Methods

There are some known methods to measure the envelope density of the particles, such as GeoPyc (Micrometrics, USA) and mercury porosimetry. However, envelope density measurement of very weak and friable materials is a challenge. In order to explore the envelope density of spray-dried burkeite particles and its variation with size, different methods have been used, such as GeoPyc, X-ray microtomography, mercury porosimetry and volume-estimation methods. These methods are classified into two main categories, indirect and direct, and are fully described below.

## 4.3 Indirect Measurement Methods

Indirect measurement methods are referred to the methods by which parameters involved in envelope density are estimated rather than measured, and based on the estimated values, the envelope density is then calculated. Based on the definition of envelope density, estimating the volume of a known mass would result in an estimate of the envelope density. Therefore different techniques of estimating particle volume are evaluated in this section.

### 4.3.1 Envelope Density Measurement Based On Volume Estimation

According to the definition of envelope density, if the average volume of a particle can be estimated, it can be then used to calculate its envelope density,  $\rho_e$ . This requires the number of particles of a given mass to be known.

$$\rho_e = \frac{M}{N \times V_p} \quad \text{Eq. (4-1)}$$

where  $N$  is the number of particles for a given mass,  $M$ , and  $V_p$  is the average volume of a single particle.

The main challenge is to estimate the average volume of the particles. There are different methods to estimate the particle size by which the volume could be estimated, such as G3 Morphologi, QICPIC, etc.

#### **4.3.1.1 G3 Morphologi**

G3 Morphologi measures the projected features of the particles lying on their maximum plane of stability, using the technique of static image analysis. In order to measure the envelope density, the average mass and volume of a good number of particles need to be measured. The G3 can measure the number of particles easily, but particle volume of the particles can only be estimated. A measure of particle size is the projected-area diameter of the particles given by G3, from which the average volume can be estimated. Assuming a spherical shape for the particles, the envelope density measurement results are shown in Table 4-1.

**Table 4-1. Density measurement results based on the projected-area measured diameter by G3 for different near mesh size particles**

<b>Nominal Near-Mesh Particle Size (<math>\mu\text{m}</math>)</b>	<b>Mass (g)</b>	<b>Mean Diameter Obtained by G3 (<math>\mu\text{m}</math>)</b>	<b># Particles</b>	<b>Envelope Density (<math>\text{kg/m}^3</math>)</b>
500	0.1083	605	1022	916
600	0.1091	637	757	1065
850	0.1636	917	317	1278
1000	0.2021	1193	220	1035

The burkeite particles are nearly spherical in overall shape as they are produced by spray-drying, but with asperities. Nevertheless using the G3, and basing the calculation on the projected-area diameter, the particle volume is overestimated as the particles tend to lie on their maximum stable plane. Hence it is most likely that the envelope density is underestimated. Despite the shortcoming of the approach, there is a clear variation of the envelope density with size.

Alternatively the envelope density calculations can be based on the volume calculated by the actual mesh size of the particles as shown in Table 4-2, as the particle shape is reasonably equiaxed.

**Table 4-2. Density measurement results based on volume calculated by near-mesh size for different particle sizes**

<b>Nominal Near-Mesh Particle Size (<math>\mu\text{m}</math>)</b>	<b>Mass (g)</b>	<b>Volume (<math>\text{m}^3</math>)</b>	<b># Particles</b>	<b>Envelope density (<math>\text{kg}/\text{m}^3</math>)</b>
500	0.1083	$6.54 \times 10^{-11}$	1022	1619
600	0.1091	$1.13 \times 10^{-10}$	757	1274
850	0.1636	$3.21 \times 10^{-10}$	317	1604
1000	0.2021	$5.23 \times 10^{-10}$	220	1756

In this case a larger envelope density is obtained as compared to using G3 Morphologi for size analysis. The error is associated with assuming spherical shape and size based on the mesh opening size. Apart from the assumption on the shape of the particles, the main issue is that in both cases a very low sample mass has been used, as the G3 measurement area has been designed for a low quantity of materials, and the time to give a measurement is very long, and running different number of repeats is time consuming. For such particles, there is a possibility of density variation even within a narrow size. Clearly, both methods show variations of the envelope density with size, and most likely describe the limits of the envelope density, with the actual value lying somewhere in between the two. The envelope density varies with size, but to what extent the near-mesh method gives a realistic estimate needs to be further ascertained. Therefore, it is interesting to find out how this method works for a material with known density and without any density variation as a function of size. A non-porous material is a good candidate, as in this case the envelope density and true density are the same.

Therefore quartz sand has been chosen to be tested using the near-mesh method. Sufficient quantities of 300  $\mu\text{m}$  and 600  $\mu\text{m}$  near-mesh particles have been prepared by manual sieving. As the particles are non-porous, therefore the envelope density and true density ( $2648 \text{ kg/m}^3$ ) should be the same. Three repeats have been done on density measurement of quartz sand, and the results are shown in Table 4-3. The reported densities are averages of three repeats.

**Table 4-3. Envelope density measurement of quartz sand using volume estimation method by near-mesh sizes**

<b>Nominal Near-Mesh Particle Size (<math>\mu\text{m}</math>)</b>	<b>Mass (g)</b>	<b>Envelope density (<math>\text{kg/m}^3</math>)</b>
300	0.4	2708
600	1.7	2656

As the results show, volume estimation method using the near-mesh size of the particles works for quartz sand. Furthermore, there is no variation of density within different sizes of the particles; therefore even by using a low quantity sample mass of the material a good agreement can be reached between the measured value and the actual value of envelope density. It could also be that the sand particles are roughly equiaxed, i.e. they do not have consistently one dimension larger than the other one. However, for particles such as spray-dried burkeite, which there is density variation even within a narrow size of the particles, it is suggested to use a minimum representative sample mass for each measurement, as well as considering the shape factor to account for departure from spherical shape.

#### 4.3.1.2 QICPIC

The QICPIC (Sympatec, Germany) instrument is based on dynamic image analysis of particles. Particle projection is recorded whilst flowing in a view cell and analysed to determine various characteristic dimensions, e.g. equivalent circle projected-area diameter. Depending on the suspension medium and flow condition in the view cell, particles may present their projection either at random orientation or a preferred orientation. In some cases, different dispersion pressures can be applied to disperse the particles before size measurement step. However, for weak and friable materials such as spray-dried burkeite particles, the free-fall condition is used. In these measurements particle image is recorded under gravity at low velocity, so the orientation is random. Therefore, it gives the measure of mean diameter for non-spherical particles at random orientations. The schematic diagram of the QICPIC measurement device is shown in Figure 4-1.

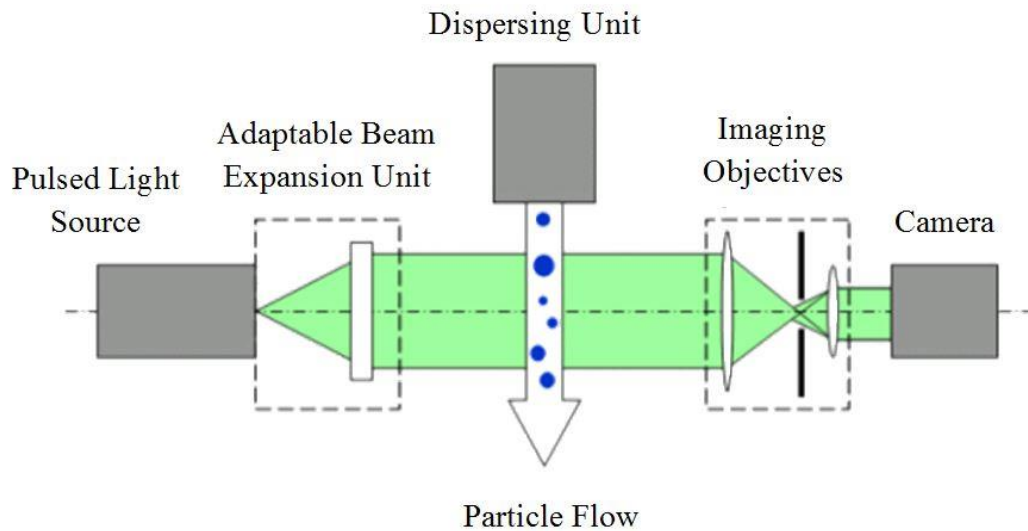


Figure 4-1. Schematic diagram of the QICPIC (Sympatec, Germany) image analysis device

The frame rate and feeder vibration rate are adjusted automatically by the device, which provides the best setting to capture most of the particles. However, the number of particles reported by QICPIC is not accurate, as there is a possibility of double-counting or missing the particles during image capturing. Some images of 1000  $\mu\text{m}$  near-mesh particles captured by QICPIC are shown in Figure 4-2. The characteristic dimension of the particles has been reported as EQPC, Feret, etc. EQPC is the diameter of a circle that has the same area as the projection area of the particles. Feret is not a diameter in its actual sense but the common basis of a group of sizes which is defined as the distance between two tangents to the contour of the particle in a well-defined orientation. Maximal and minimal Feret diameters are the largest and smallest distances found based on the above-mentioned approach after consideration of all possible orientations.

	EQPC Aspect ratio	1062 $\mu\text{m}$ 0.772		EQPC Aspect ratio	1235 $\mu\text{m}$ 0.773
	EQPC Aspect ratio	1205 $\mu\text{m}$ 0.774		EQPC Aspect ratio	980 $\mu\text{m}$ 0.788
	EQPC Aspect ratio	1015 $\mu\text{m}$ 0.791		EQPC Aspect ratio Image number	1066 $\mu\text{m}$ 0.791 96
	EQPC Aspect ratio	1068 $\mu\text{m}$ 0.794		EQPC Aspect ratio	950 $\mu\text{m}$ 0.796

Figure 4-2. Some images captured by QICPIC during analysis of 1000  $\mu\text{m}$  particles

Aspect ratio has also been reported in Figure 4-2, which is a measure of particle shape, and is defined as the ratio of the minimum to the maximum Feret diameter. The values of aspect ratio clearly show that the assumption of spherical particles is not correct (the particles are assumed to be spherical if the aspect ratio is above 0.95). It hence explains the larger value obtained by sieve size approach compared to G3 Morphologi.

The particle mean diameter (volume basis) at random orientations has now been estimated by QICPIC. However, as it was mentioned before, the number of the particles reported by QICPIC is not accurate. Therefore, a different method is used to estimate the number of particles, and calculate the envelope density of spray-dried burkeite. In order to count the number of particles for a given mass used in QICPIC, the particles are spread using a vibratory table, pictures are taken from the particles, and the number of particles are analysed using ImageJ software.



**Figure 4-3. A picture of 850 µm particles spread by vibratory table**

In order to produce reliable results, it is critical to analyse a representative sample mass of the particles. Therefore error analysis was carried out to explore the effect of sample mass on envelope density results. For this purpose, the above approach has been followed on various sample quantities with different number of repeats, e.g. six repeats have been done using 1 g of 850 µm near-mesh burkeite particles. For each test, the number of particles has been measured using vibratory table. The envelope density has then been calculated. The standard deviation and standard error (using Eq. 3-1) of the envelope density measurements have been calculated for the first two repeats, then for the first three and so on. The same approach was then repeated using 2 g and 3 g of sample. The results of standard error analysis show that as the sample quantity increases, a smaller number of repeats are needed in order to get an acceptable standard deviation and standard error, which in fact shows the importance of representative sample mass on error associated with the obtained results. Comparison of standard errors of different number of repeats for different sample mass quantities shows that as the mass quantity increases the standard error and standard deviation decrease, although the envelope density values are very close between using 1 g and 3 g of sample.

**Table 4-4. Error analysis on the effect of sample mass on envelope density of burkeite by estimating the mean diameter using QICPIC, and number of particles using vibratory table**

Nominal Near-Mesh Particle Size ( $\mu\text{m}$ )	Test Number	Mass (g)	Number of Particles	Envelope Density ( $\text{kg/m}^3$ )	Standard Deviation (cumulative)	Standard Error (cumulative)
850	1	1.05	2482	1318	-	-
850	2	1.04	2324	1394	53.63	37.92
850	3	1.01	2317	1366	38.31	22.12
850	4	1.09	2366	1396	36.14	18.07
850	5	1.01	2339	1347	32.74	14.64
850	6	1.04	2422	1342	30.64	12.51
850	1	2.09	4806	1355	-	-
850	2	2.07	4683	1381	18.21	12.88
850	3	2.05	4761	1345	18.69	10.79
850	1	3.11	7123	1359	-	-
850	2	3.12	7127	1362	2.08	1.47

The final results of envelope density measurement by estimating the average volume of the particles using QICPIC and minimum representative sample mass (3 g of sample for

850 and 1000  $\mu\text{m}$  particles, and 2 g of sample for 212, 250, 500 and 600  $\mu\text{m}$  particles) are shown in Table 4-5.

**Table 4-5. Envelope density measurement results based on volume calculated by QICPIC for different near-mesh particle sizes**

Nominal Near-Mesh Particle Size ( $\mu\text{m}$ )	Projected-Area Diameter at Random Orientation ( $\mu\text{m}$ )	Particle Volume $\times 10^{+6}$ ( $\text{m}^3$ )	Envelope Density ( $\text{kg}/\text{m}^3$ )
212	246	7.8	1028
250	277	11.1	1346
500	571	97.5	1131
600	680	164.6	1134
850	976	486.8	1361
1000	1197	898	1015

Based on the results shown in Table 4-5, there appears to be no clear trend in envelope density changes as a function of size. Surprisingly, the envelope density of 500  $\mu\text{m}$  and 600  $\mu\text{m}$  are very close. This is also the case for 250  $\mu\text{m}$  and 850  $\mu\text{m}$  particles.

## 4.4 Direct Measurement Methods

GeoPyc, X-ray microtomography and mercury porosimetry are referred to as direct measurement methods of envelope density.

### 4.4.1 GeoPyc

The GeoPyc (Micromeritics, USA) follows a unique displacement measurement technique that uses a proprietary quasi-fluid medium composed of small ( $\sim 50 \mu\text{m}$ ) rigid spherical particles having a high degree of flowability, which is called DryFlo. The sample is placed in a bed of DryFlo, which is agitated and gently consolidated. The GeoPyc instrument collects the displacement data, performs the calculations, and displays or prints the results. The instrument also reports percentage porosity and specific pore volume when absolute density information (density excluding pore and small cavity volume) is entered. Near-mesh particle sizes of 500, 600, 850 and 1000  $\mu\text{m}$  have been tested by GeoPyc, and each measurement test has been repeated three times, and the reported envelope density is the average value. The results are shown in Table 4-6.

Table 4-6. Density measurement by GeoPyc for 500, 600, 850 and 1000  $\mu\text{m}$  near-mesh burkeite particles

Nominal Near-Mesh Particle Size ( $\mu\text{m}$ )	Average Mass (g)	Average Density ( $\text{kg}/\text{m}^3$ )	Standard Deviation	Average Volume ( $\text{mm}^3$ )
500	0.0167	551	0.0622	30.3
600	0.019	745	0.0263	25.4
850	0.015	563	0.0389	26.6
1000	0.0154	671	0.0979	23

Observation of Scanning Electron Microscope (SEM) images of the burkeite particles before the test (Figure 3-1) shows that for some particles, parts of the surface layers have fallen off. Consequently the Dry Flo powders could go through those larger than  $50 \mu\text{m}$  openings, which adversely affect the results of the envelope density. However, it should give rise to larger estimated envelope density, while the opposite is observed in the reported results here. Moreover, GeoPyc is not a right measurement device for particles with a non-smooth surface and small irregularities on the surface, as the DryFlo particles are not able to cover all the irregularities of the surface, therefore the volume covered by DryFlo would be over-estimated, which leads to underestimating the envelope density of the particles. Furthermore, the quantity of the material used in GeoPyc is very low, therefore it is not recommended for envelope density measurement of particles with density variations even within a narrow size range, as the results would not be representative of the whole sample. Based on the manual of GeoPyc

(Micromeritics, USA), the particle size should exceed 2 mm for the best results (Analyzer, n.d.), which is not the case here.

#### 4.4.2 X-Ray Microtomography

X-ray microtomography (XRT) is a powerful technique used to visualise the internal and microstructural details of the particles. It provides useful information on their shape and size. Due to its ability of visualisation and size measurement, it can be used to measure bulk density of a given mass of particles. Interstitial voidage (gaps between the particles) in a particle bed can also be measured using visualisation and image processing techniques. The acquired information can then be used to calculate the envelope density of the particles based on the equation below,

$$\rho_e = \frac{\rho_b}{(1-\varepsilon)} \quad \text{Eq. (4-2)}$$

where  $\rho_e$  and  $\rho_b$  are the envelope density of individual particles and the bulk density of the particle bed, respectively, and  $\varepsilon$  is the interstitial bed voidage, i.e. the fraction of bed volume occupied by gaps between the particles.

In this work, X-ray microtomography was carried out using a Nanotom X-ray computed tomography instrument (GE Phoenix, Wunstorf, Germany). A bed of the spray-dried burkeite particles (around 0.5 g) was scanned using at a micrometre level spatial resolution. VGStudio software was then used for reconstruction of the images. The post-processing task was done using Avizo Fire software to obtain the particle volume.

As a very first attempt, a small mass of particles was scanned. The sample used for scan is shown in Figure 4-4.



**Figure 4-4. Sample preparation for XRT scan using a very small quantity of sample**

The resolution of the scan was 8  $\mu\text{m}$  using a very small quantity of 850  $\mu\text{m}$  particles. However, the quality of scan was poor (as shown in Figure 4-5). The ring artifacts observed in the scanned images are concentric rings superimposed on the tomographic slices due to non-uniformly calibrated detector elements as well as the presence of dead pixels on detector.

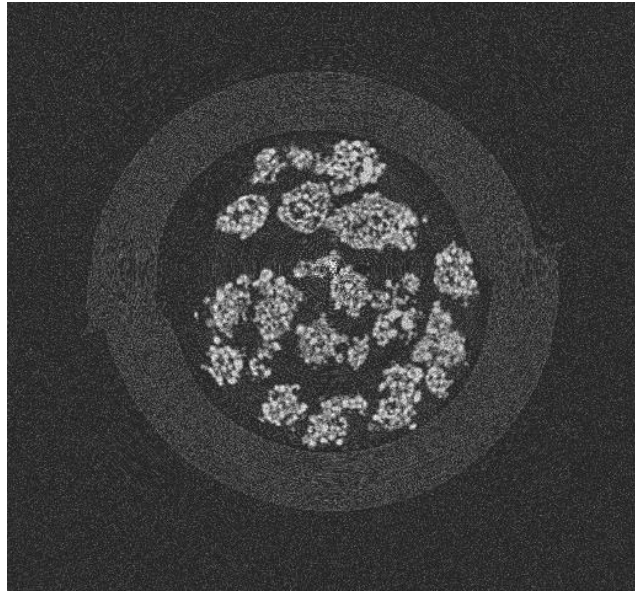


**Figure 4-5. First XRT scan on 850  $\mu\text{m}$  burkeite particles (small sample mass), using Nanotom XRT machine at University of Leeds**

In order to obtain accurate results, reduction of the artefacts and noise is needed for the post-processing of the images. Applying a good filtration is a key point at this step, which takes a lot of time.

Considering the importance of a representative sample mass on reliability and accuracy of the measurement results, a new attempt was made using a minimum representative sample mass (based on error analysis) for each scan, 2 g for small particle sizes (212, 250, 500 and 600  $\mu\text{m}$ ) and 3 g for large particles (850 and 1000  $\mu\text{m}$ ) as shown in Figure 4-6.



**Figure 4-6. Sample preparation for XRT scan (using 3 g of 850  $\mu\text{m}$  near-mesh burkeite particles)**

The new scans were done at the University of Nottingham, using the same XRT machine, as the XRT machine at the University of Leeds was out of service. However, the quality of scans was better compared to those at Leeds, as the problem of the dead zones of the detector was not present. A slice of the scanned image for 850  $\mu\text{m}$  particles is shown in Figure 4-7.

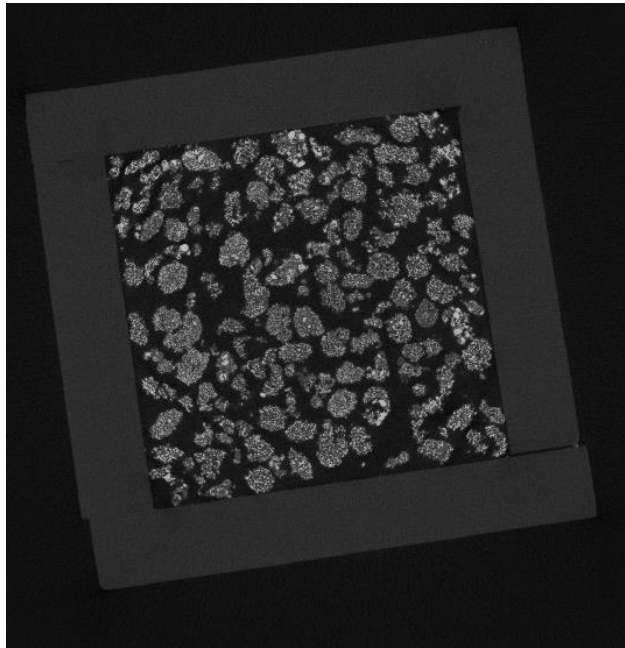


**Figure 4-7. XRT scan on 850 µm burkeite particles (representative sample mass), using XRT machine at University of Nottingham**

The resolutions of the scans obtained for 212 µm particles (using 2 g of sample) and 1000 µm particles (using 3 g of sample) were 12 µm and 17 µm, respectively. In order to get a better resolution of the scan using a large quantity of the materials, a multiple-scan can be taken of a bed of the material, and they can be merged together during reconstruction step. However, due to the time and cost of the scans, this approach has not been used here. The resolution level of the scan can cause some errors in the envelope density measurement results. The error arising from the resolution of the scans is reported later on in this section.

The image processing analysis was carried out by calculating the volume of the bed. The information on the bed volume as well as mass of the sample was used to calculate the bulk density. A scan of the bed of particles is shown in Figure 4-8a. At the first step, the glass container has been removed from the scans, as shown in Figure 4-8b.

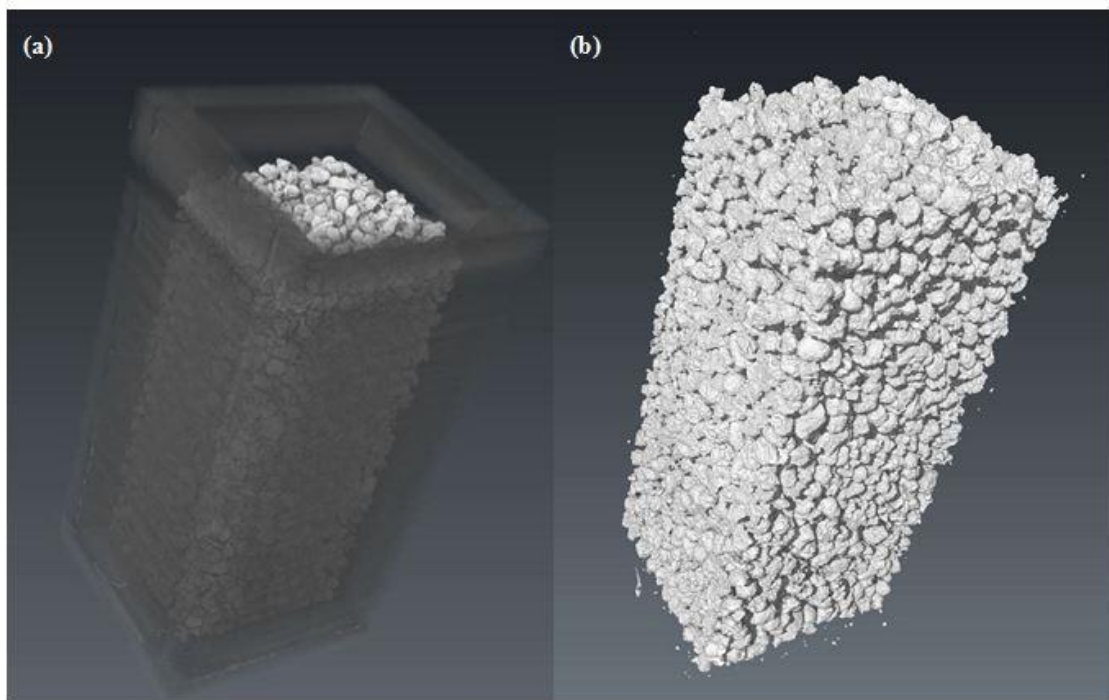


**Figure 4-8. (a) Scan of a bed of burkeite particles before removing the glass container; (b) scan of a bed of the particles after removing the glass container**

In order to calculate the interstitial voidage, the voidage inside the particles needs to be filled in the post-processing step. The approach has been shown in 2D in Figure 4-9, however the calculations are done in 3D.

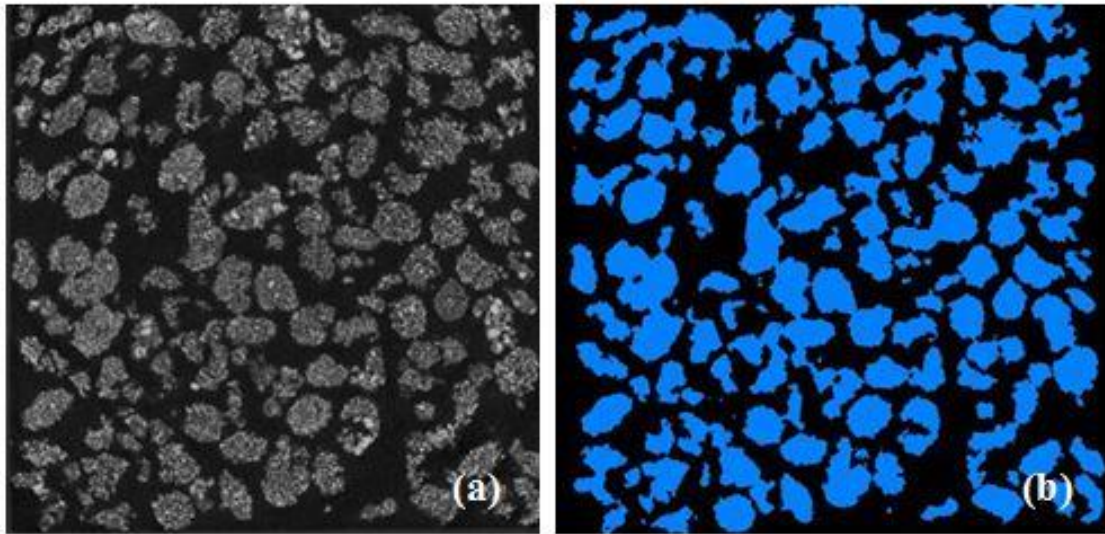


**Figure 4-9. (a) A slice of the raw data of the bed scan for 850  $\mu\text{m}$  particles; (b) A slice of the particles bed after filling the internal porosity of the particles**

The black colour in Figure 4-9a represents air in the system, and the light grey shows the particles. In Figure 4-9b the air inside the particles is removed (the blue colour shows the filled particles), and the interstitial voidage is calculated for the bed of particles. The envelope density of different sizes of the burkeite particles has been calculated using the above approach. Based on the envelope density, the average porosity of the particles is also calculated using Eq. (4-3).

$$\rho_e = \rho_t(1 - \varepsilon_p) \quad \text{Eq. (4-3)}$$

where  $\rho_t$  is true density of burkeite, 2673 kg/m<sup>3</sup>, and  $\varepsilon_p$  is the average porosity of each near-mesh size of spray-dried burkeite particles. The measured data are presented in Table 4-7.

Table 4-7. Envelope density and internal porosity measurement using XRT

Particle size ( $\mu\text{m}$ )	Bulk density ( $\text{kg}/\text{m}^3$ )	Envelope Density ( $\text{kg}/\text{m}^3$ )	$\epsilon_p$ (%)
212	803	899	65
250	761	1077	58
500	654	1181	54
600	619	1273	50
850	597	1382	46
1000	565	1339	48

Comparison of the envelope density measurement results for different particle sizes obtained from X-ray microtomography clearly shows that the envelope density changes with particle size, and mainly increases as the particle size is increased, except the largest particle size (1000  $\mu\text{m}$ ), where its value is even smaller than 850  $\mu\text{m}$  particles. The 1000  $\mu\text{m}$  particles are likely to have formed from the coalescence and agglomeration of smaller drying droplets. If we consider the increasing trend of density with particle size to also prevail for 1000  $\mu\text{m}$  particles, then the difference between the *expected* value of density of 1000  $\mu\text{m}$  particle and its actual measured value is slightly larger than the variations due to errors associated with the XRT analysis (2.4% for the latter). This implies there are real structural differences between particle sizes.

#### 4.4.3 Mercury Porosimetry

Mercury porosimetry is a well-known method, widely used to measure the envelope density of the particles. However the minimum representative sample mass required for

testing is an important issue which needs to be considered. The sample quantity used in mercury porosimetry is in the sub-gram range, but this is only suitable for fine powders. For the particle size range of interest here, a much larger quantity will be required, e.g. around 2 g for 500  $\mu\text{m}$  particle size. Therefore each measurement test uses insufficient material for it to be representative of the particles. Based on the mentioned reasons, the mercury porosimetry does not seem to be a suitable measurement method in this work. However, as P&G (NIC, UK) had a mercury porosimeter, they did a test on 300-425  $\mu\text{m}$  sieve cut of burkeite particles. Based on the mercury porosimetry results, the envelope density of this sieve cut has been estimated as 1700  $\text{kg}/\text{m}^3$ , and the curve reported by the device is shown in Figure 4-10.

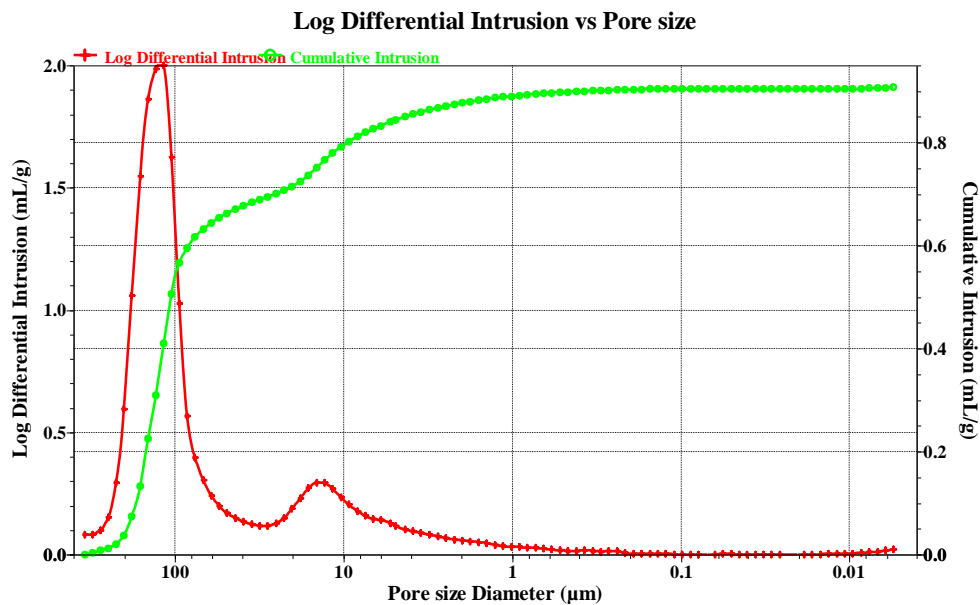


**Figure 4-10. Mercury porosimetry results for 300-425  $\mu\text{m}$  burkeite particles**

The reported result from mercury porosimetry differs notably from those obtained by other methods. This is unlikely to have arisen from the particle size distribution, because the XRT and QICPIC methods do not show such drastic variation with size. It

is therefore likely that other factors contributed to the difference, e.g. the issue of using minimum representative sample mass.

#### **4.5 Concluding Remarks**

The envelope density measurement results obtained from different methods such as GeoPyc, particle volume estimation methods and X-ray microtomography have been compared and shown in Table 4-8.

**Table 4-8. Comparison of envelope density measurement results obtained by different methods for burkeite particles reported in  $\text{kg/m}^3$  for different near-mesh particle sizes**

Nominal Near-Mesh Particle Size ( $\mu\text{m}$ )	Direct Methods		Indirect Methods		
	GeoPyc	XRT	G3 Morphologi	Near-Mesh	QICPIC
212	-	899	-	-	1028
250	-	1077	-	-	1346
500	552	1181	916	1619	1131
600	747	1273	1065	1274	1134
850	563	1382	1278	1604	1361
1000	667	1339	1035	1756	1015

GeoPyc is not a suitable method for envelope density measurement of spray-dried burkeite particles. The DryFlo particles cannot cover all the irregularities of the surface of the particles, therefore the volume of the particles is over-estimated, and in turn it causes underestimation of the envelope density of the particles. In using GeoPyc the difficulty of using the minimum representative sample mass is also an issue. This

method works quite well for particles larger than 2 mm with smooth surfaces, without any density variation within a narrow size of the particles.

X-ray microtomography is used to scan a bed of the particles (using a representative sample mass). This method provides the opportunity to visualise the three-dimensional view of the particles. The interstitial voidage of the bed is calculated by removing the glass container, filling the porosities inside the particles, and calculating the ratio of the air within the bed to the total volume of the particle bed. The only shortcoming of this method is the resolution of the scan when a large mass of particles is used, and hence the *expected* value can be different from the actual measured value.

Use of different volume estimation methods is made in order to find a simple method to estimate the envelope density of the weak particles such as spray-dried burkeite. G3 Morphologi measures the maximum projected-area diameter of the particles; therefore it is not a suitable measurement method for estimating particle volume of non-spherical particles. However, the advantage of using G3 is that the number of the particles for a given mass can be calculated and reported by the software. The disadvantage of this method is that in order to analyse a minimum representative sample mass of the particles, the measurement takes time and it is slow. Alternatively, the actual diameter of near-mesh particles based on the sieve size is used to estimate the average volume of the particles. The envelope density obtained by this method is larger than that obtained by G3 Morphologi. The near-mesh size, as obtained by sieving, actually represents the second largest size of the particles, thereby underestimating the particle volume. Therefore, the dynamic image analysis method has been used to measure the projected area equivalent circle diameter of the particles at random orientation, from which the

particle volume is estimated. This method is considered to be a more realistic representative of the mean diameter amongst other methods, i.e. G3 Morphologi and near-mesh techniques. However, as mentioned before, there is the possibility of double counting or missing the particles using QICPIC, therefore the number of the particles counted by the device is not accurate. Hence, another approach can be used here to give a better estimate of number of particles within a given sample mass. For this purpose the particles are spread on a sheet, using a vibratory table, and the number of particles is measured by the use of image analysis software. The acquired information on the number of particles using this approach with the average volume of the particles by QICPIC provides a simple method to estimate the envelope density of different particle sizes.

Amongst all the measurement methods, volume estimation using QICPIC and XRT seem to be the most realistic methods, as they both consider the effect of particle shape. Comparison of these two methods shows agreement for envelope densities of 500  $\mu\text{m}$  and 850  $\mu\text{m}$  particles, although the trend of envelope density changes as a function of size is different between these two methods. The envelope density values obtained from XRT will be used in this work.

## CHAPTER 5      IMPACT BREAKAGE

In this chapter the impact strength of spray-dried burkeite particles under different impact conditions is studied. The breakage patterns are then identified for each impact condition, as a different type of analysis needs to be applied for each pattern of breakage. Explaining the breakage results requires some information on mode of failure of the particles. For this purpose, the particles are tested under quasi-static conditions to explore their failure under such conditions. The analyses are then carried out considering the structural variations (reflected by the envelope density differences), which provide a better understanding on impact breakage behaviour of the particles.

### 5.1 Introduction

Spray-dried burkeite particles in the manufacturing plants experience different impact stresses as they are going through different units of operation such as chutes, slide valves, pneumatic lines, etc. In order to study the impact attrition of spray-dried burkeite, the particles are subjected to different levels of impact stresses, and the change in particle size distribution is determined by particle size analysis based on sieving. However, different patterns of breakage need to be identified at different impact conditions, as a different analysis should be done for each pattern of breakage. For instance, particle failure through chipping is completely different to that of disintegration. A good knowledge of different modes of failure is needed to choose a right theory to describe the breakage results. The information on the structural differences as a function of size is used here to analyse the breakage behaviour of the

particles. The outcome of the analysis also provides some information on material mechanical properties of the particles.

## 5.2 Impact Testing

The single particle impact rig test used for the experiments is the modified design of the single particle impact apparatus originally developed by Yüregir et al. (1987). The particles are fed from the top of the rig, and impacted to a flat rigid target at different impact velocities by changing the vacuum pressure. The impact velocity is measured by time of flight of particles passing by two photodiodes. The time is then used by the software in the PC to calculate the particle velocity (see Figure 5-1).

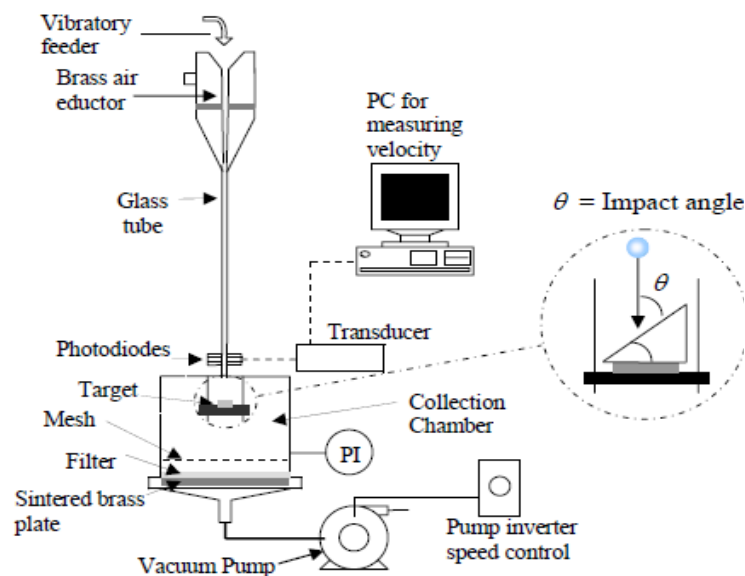
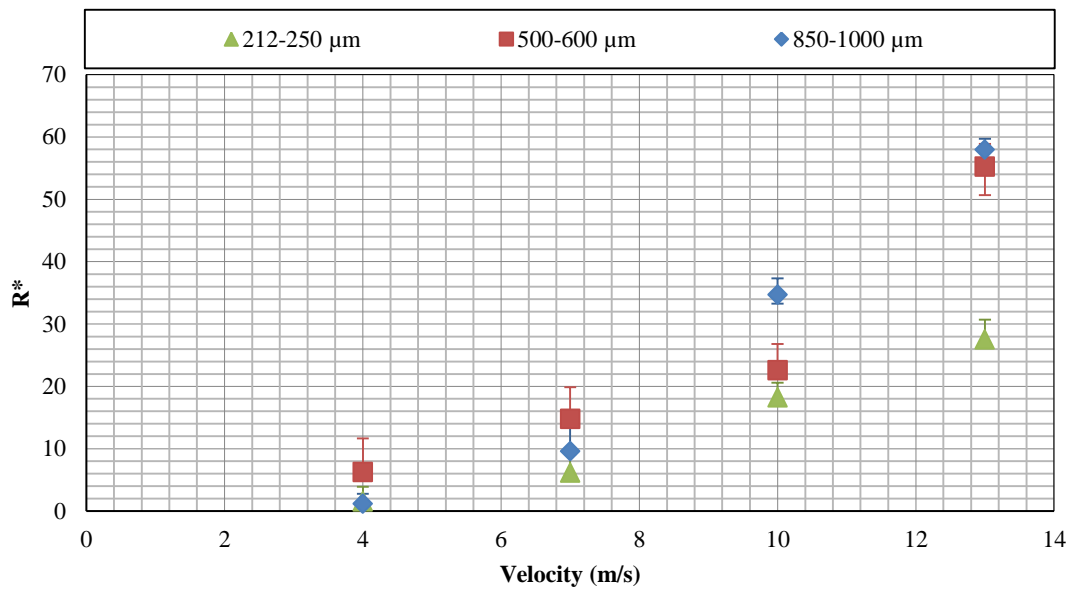


Figure 5-1. Single particle impact rig (Samimi et al., 2003)

Particles are collected after impact testing, and sieved by two sieve sizes below the lower feed size. The particles passing through this sieve are categorised as debris, and the rest of the particles as mother particles. The results are expressed in terms of the extent of breakage using the equation (2-7).

### 5.2.1 Preliminary Impact Tests

The preliminary tests were done on the first batch of spray-dried burkeite particles sent by P&G (NIC, UK) to University of Leeds. The quantity of the first batch was very small. Therefore, a small number of impact tests were done before receiving the main batch of the samples. Three different sieve sizes, 212-250  $\mu\text{m}$ , 500-600  $\mu\text{m}$  and 850-1000  $\mu\text{m}$  were prepared by manual sieving, and the experiments were carried out by impacting them at four different impact velocities: 4, 7, 10 and 13 m/s. The extent of breakage as a function of particle size is shown in Figure 5-2. The error bars shown in the graph are based on  $R^-$  and  $R^+$ , which indicate a small loss of debris from the collected mass. The mother particles were sufficiently large for all to be recovered from the collection chamber.



**Figure 5-2.** The extent of breakage,  $R^*$ , as a function of impact velocity for different sieve size cuts

As the results show, at 4 m/s impact velocity the extent of breakage corresponding to 212-250  $\mu\text{m}$  particles almost overlaps with 850-1000  $\mu\text{m}$  particles, and at 7 m/s impact velocity the largest particle sizes (850-1000  $\mu\text{m}$ ) break less than 500-600  $\mu\text{m}$  particles, which is in contradiction with the expected trend that large particles break to a greater extent than small particles.

There could be different factors involved in causing the anomalies. The most important one is the minimum representative sample mass. As it has been shown in the previous chapter, the quantity of sample plays an important role in results of the experiments, particularly for the particles which there are structural variations even within a narrow size of them. Therefore an error analysis needs to be carried out to find the minimum sample mass required to produce statistically reliable results. Another factor, which can cause discrepancy, is the structural differences of the particles between the three sieve cuts. As shown in the previous chapter, the envelope density of the particles varies

between different particle sizes, which in this case the particle sizes should be chosen as narrow as possible in order to be able to study the impact breakage and structural differences as a function of size. Experimental error might also be involved in the observed anomalies. Therefore, a new set of tests was carried out by considering the mentioned issues.

### **5.3 Representative Sample Mass**

It takes a lot of effort to prepare near-mesh particles, and hence the sample supply is limited. Therefore the minimum sample mass to obtain statistically reliable experimental results should be established. The sample preparation approach as presented in the previous chapter has been used here. Around 2 g of 500  $\mu\text{m}$  burkeite particles are impacted at 8 m/s using the single particle impact rig. The extent of breakage has then been calculated. Five different repeats are done using the same conditions. The standard deviation and standard error have been calculated on a cumulative basis, i.e. for first two tests, first three tests, and so on. The sample mass has then been increased to 4 g, and two repeats have been done under the same impact conditions. The standard deviation and standard error have been calculated for these two repeats. Based on the reported results in Table 5-1, a larger sample quantity and number of repeats give rise to a lower standard error. The results of standard error analysis using 500  $\mu\text{m}$  particles are shown in Table 5-1.

Table 5-1. Error analysis on representative sample mass for impact testing at 8 m/s using 500  $\mu\text{m}$  particles

Nominal Near-Mesh Particle Size ( $\mu\text{m}$ )	Number of Test	Mass (g)	$R^*$ (-)	Standard Deviation (cumulative)	Standard Error (cumulative)
500	1	2.57	0.43	-	-
500	2	2.29	0.47	0.065	0.046
500	3	2.26	0.49	0.055	0.031
500	4	2.36	0.47	0.053	0.026
500	5	2.14	0.47	0.048	0.021
500	1	4.17	0.48	-	-
500	2	4.17	0.48	0.003	0.002

Based on the error analysis results and considering the practicality of producing near-mesh size particles, it was decided to use at least 2 g of sample for small particles (212, 250, 500 and 600  $\mu\text{m}$ ), and 3 g of sample for large particles (850 and 1000  $\mu\text{m}$ ). The decision on minimum sample mass for large particle sizes was made based on the error analysis results reported in the previous chapter, which showed that at least 3 g of sample was needed for large particles.

## 5.4 Impact Testing Using Near-Mesh Size Particles

New impact breakage tests were carried out for 212  $\mu\text{m}$ , 250  $\mu\text{m}$ , 500  $\mu\text{m}$ , 600  $\mu\text{m}$ , 850  $\mu\text{m}$  and 1000  $\mu\text{m}$  of near mesh size particles by impacting the particles at 2, 3, 4, 6, 8, 11, 14 and 18 m/s. The range of impact velocities has been chosen based on the PhD work of Ahmadian (2008), who showed that the range of the impact velocities in a generic detergent powder manufacturing plant is usually between 2 to 20 m/s. It should be noted that these new tests were done on the new batch of burkeite particles. These particles are weaker than the previous batch, and they easily break even at the lowest impact velocity.

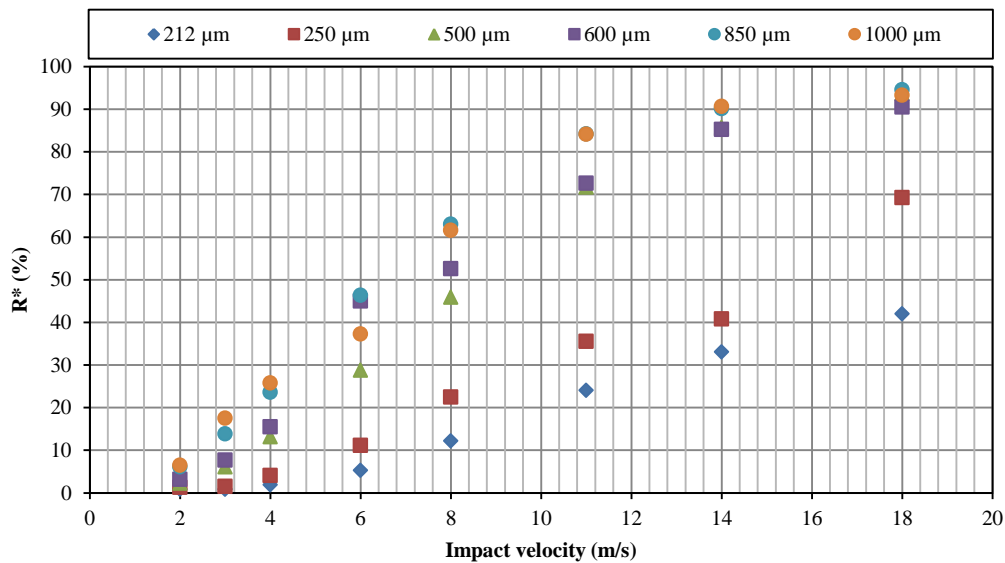


Figure 5-3. Extent of breakage,  $R^*$ , as a function of different impact velocities for near-mesh particles

Large particles generally break to larger extents, but there are anomalies in the trends shown in Figure 5-3. Overall, the data points corresponding to the extent of breakage are very close, but nevertheless the same unexpected trend as observed in the

preliminary impact testing prevails here; i.e. at 6 m/s the largest particles, 1000  $\mu\text{m}$ , break less than the 600  $\mu\text{m}$  and 850  $\mu\text{m}$  particles. It is generally expected that the larger particles break to a greater extent than the smaller ones.

However, using the term of extent of breakage,  $R^*$ , and the basis of its calculation are valid for the chipping regime. Therefore, in order to provide a more precise analysis, different patterns of breakage, chipping, fragmentation and disintegration, need to be separated first, and then studied separately. The procedure for identifying different patterns of breakage has been fully described in section 2-3.

The particles after impact have also been observed using a Scanning Electron Microscope. As an example, the SEM images of an 850  $\mu\text{m}$  particle after impact at 4 m/s are shown in Figures 5-4 and 5-5. Figure 5-4 shows a small section of the surface of a single particle after impact testing, where the impact has presumably taken place. A flat surface is observed in this figure, which is considered to be the impacted area. In Figure 5-5, the damage can be seen on the surface of another particle, and a part of the surface layer has fallen off. Debris and small chips are observed inside the broken surface skin.

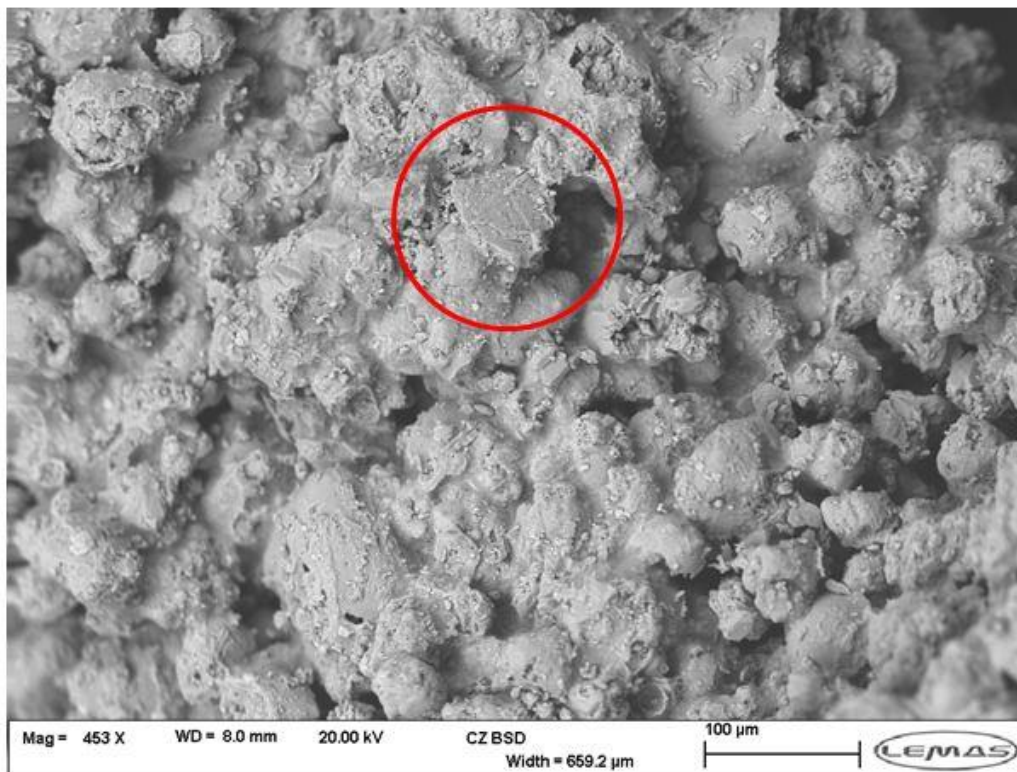


Figure 5-4. SEM image of possible impact zone after impacting 850 μm near-mesh particle at 4 m/s

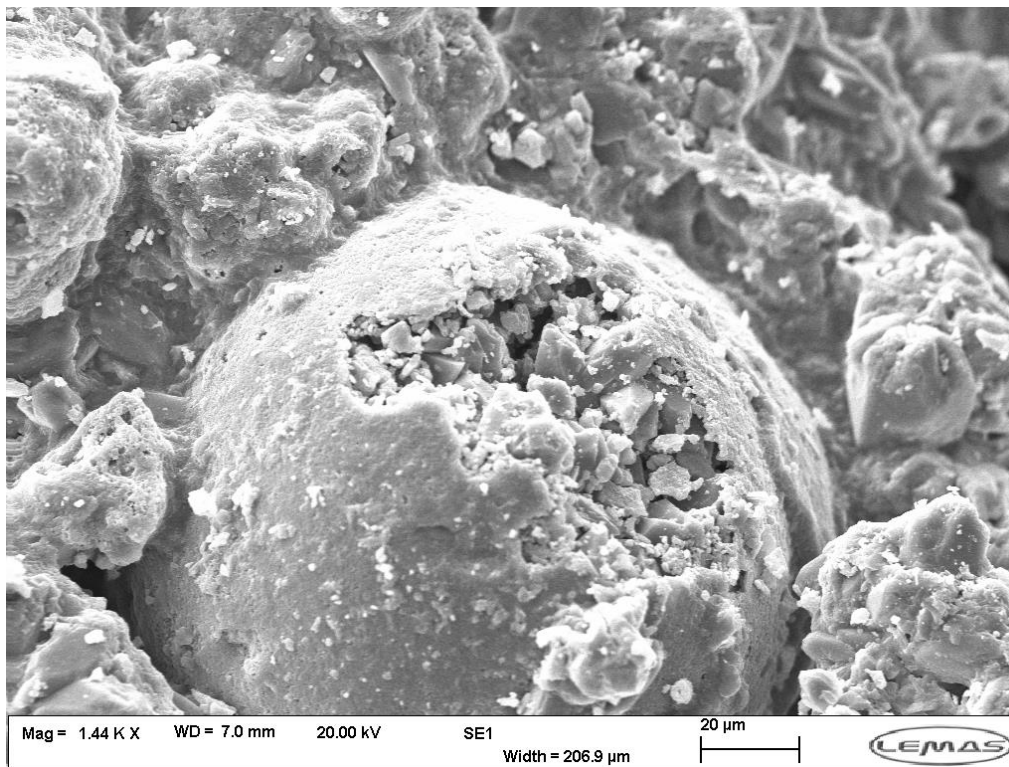
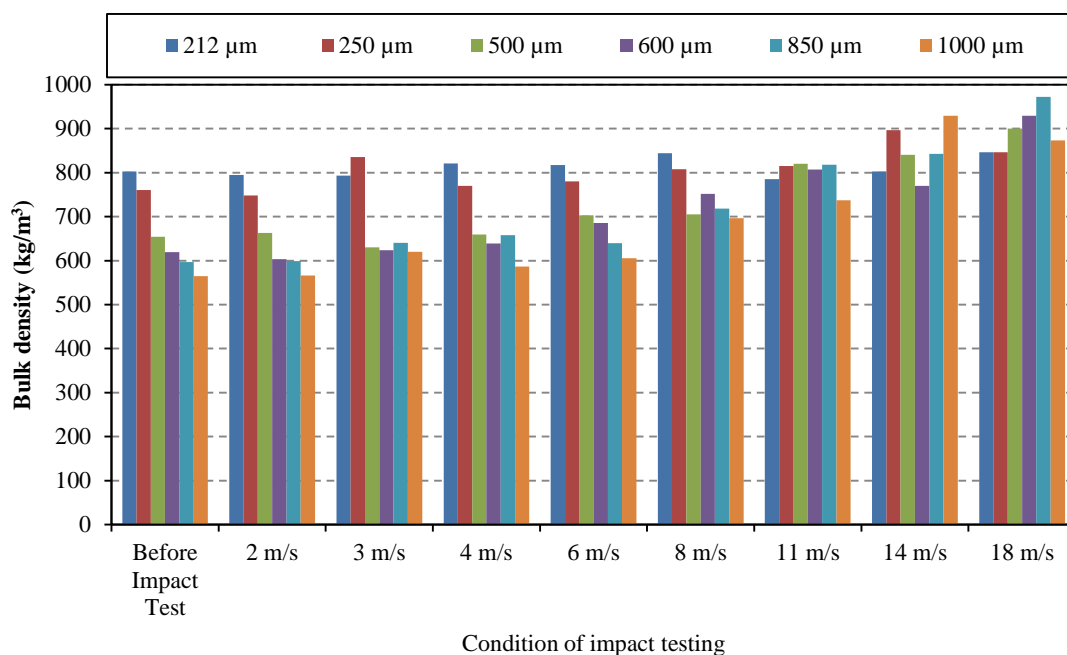


Figure 5-5. SEM image of the surface of impacted 850 μm near-mesh particle at 4 m/s

The particles are collected after impact to carry out the breakage analysis. The bulk density of the particles at different impact conditions has been measured to explore how the volume of the particles changes after breakage. It should be noted that bulk density is container dependent. Therefore in order to compare the results, the bulk density of all the particles after and before impact has been measured using the same container without any tapping. The results are shown in Figure 5-6.



**Figure 5-6. Bulk density variations of different near-mesh particle sizes at different impact conditions**

There is a significant reduction in bulk densities of different near-mesh particle sizes before impact. This behaviour is in agreement with what has been obtained by X-ray microtomography, as the particle size increases, the interstitial voidage between the particles also increases, which in fact leads to the lower bulk density and higher envelope density. However, the reason of increase in interstitial voidage values by increasing the particle sizes is not clear. As the impact velocity increases, the difference

between the bulk densities becomes smaller. This can be attributed to the breakage behaviour of the particles. Spray-dried burkeite particles consist of several crystal clusters with gaps in between them, resulting in different values of porosity for different particle sizes. However, as the particles break by impacting at different impact velocities, they disintegrate into these clusters (it will be fully described later). The structure of the particles collapses and now the bulk is mainly made of crystal clusters present within the particles. Therefore, the difference between the bulk densities at high impact velocities becomes less significant compared to those before impact, as there is a better packing between clusters than single particles and the clusters pack more densely than in the spray-dried particles.

## 5.5 Patterns of Breakage

In order to analyse the breakage data, it is critical to identify different patterns of breakage such as chipping, fragmentation and disintegration for different impact conditions. Papadopoulos (1998) studied the changing trend of the broken particles size distribution curve with impact velocity based on the work of Schumann (1940). The same approach was used here to identify different patterns of breakage for each near-mesh size of burkeite particles and different impact velocities. According to Schumann's presentation, the cumulative percentage undersize of broken particles is plotted as a function of normalised size, i.e. the size of the broken particles divided by the feed size. This is shown in Figure 5-7 for 212  $\mu\text{m}$  near-mesh size feed particles.

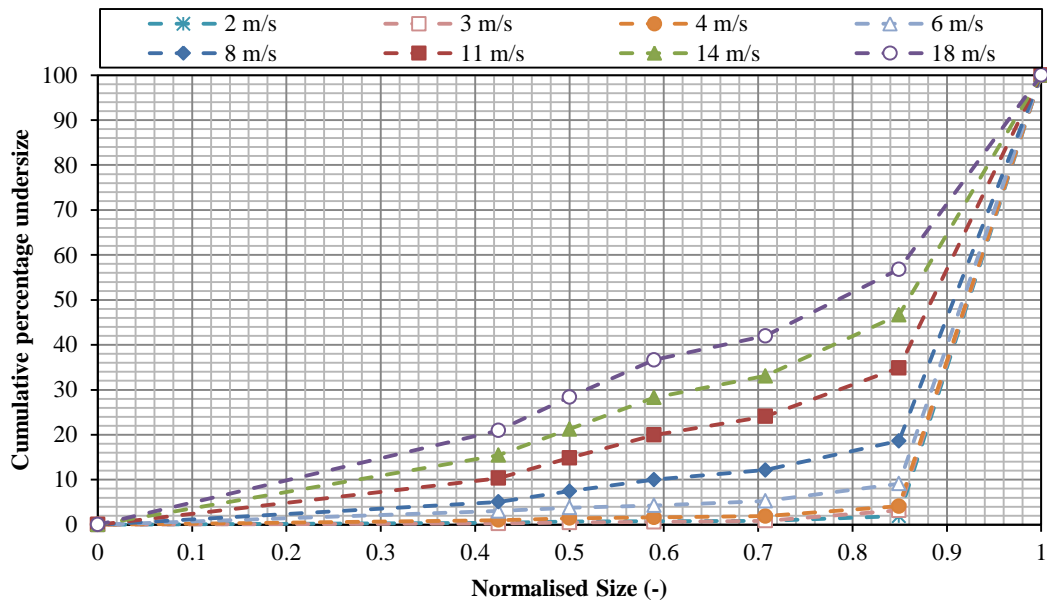


Figure 5-7. Patterns of breakage for 212  $\mu\text{m}$  particles

The results show a gradual shift from chipping regime to fragmentation regime. If we consider the dominant patterns of breakage for 212  $\mu\text{m}$  near-mesh particles, then the particle breakage in the range 2-8 m/s could be categorised as chipping and above that as fragmentation. Obviously, there should be a transition velocity, and in this case it is in the range 8-11 m/s. The transition velocity is inversely proportional to the square of particle size as shown by Eq. (2-10), so larger particles would undergo fragmentation at much lower velocity and this is described below.

The patterns of particle breakage for 250  $\mu\text{m}$  near-mesh size feed particles are shown in Figure 5-8.

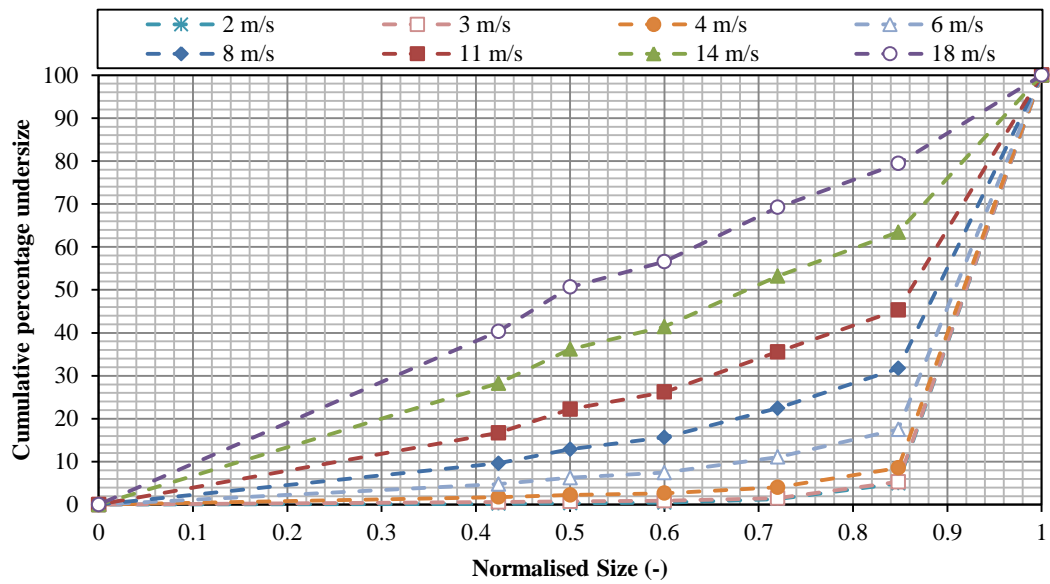


Figure 5-8. Patterns of breakage for 250  $\mu\text{m}$  particles

Clearly, a gradual shift in particle size distribution is observed here indicating a transition from chipping to fragmentation as the impact velocity is increased, but as the feed particle size is larger, the transition occurs at a lower velocity range, in this case between 6-8 m/s. The fragmentation regime is observed for data obtained from 8-18 m/s impact velocity. At 18 m/s full fragmentation occurs, giving almost a straight line, which shows the presence of broken particles in all size classes.

The patterns of particle breakage for 500  $\mu\text{m}$  near-mesh size feed particles are shown in Figure 5-9.

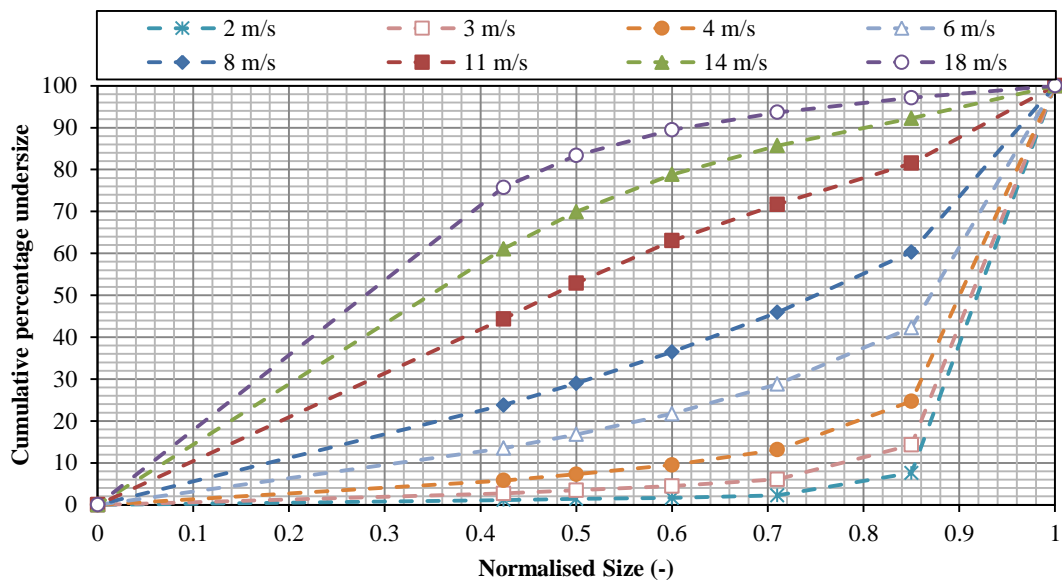


Figure 5-9. Patterns of breakage for 500  $\mu\text{m}$  particles

The results show a gradual shift from chipping to fragmentation and then from fragmentation to disintegration. However, considering the dominant patterns of breakage for this feed size particles, the particle breakage in the range 1-4 m/s could be categorised as chipping, 6-11 m/s as fragmentation, and above 14 m/s as disintegration. Therefore the transition velocity from chipping to fragmentation is between 4 to 6 m/s, and the transition velocity from fragmentation to disintegration is between 11 to 14 m/s.

The patterns of particle breakage for 600  $\mu\text{m}$  near-mesh feed sizes are shown in Figure 5-10.

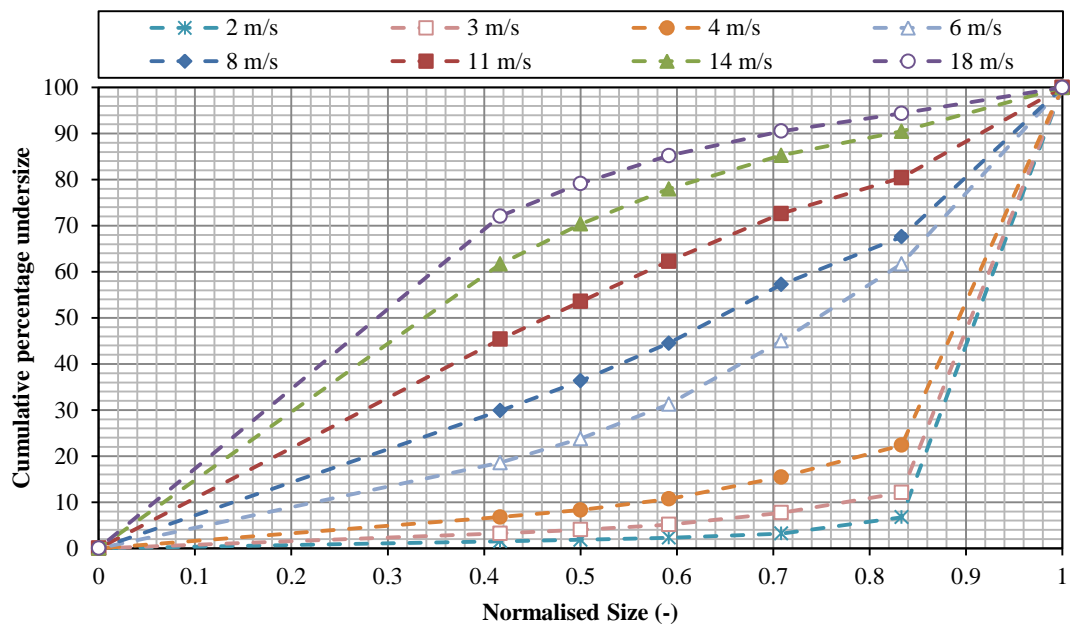


Figure 5-10. Patterns of breakage for 600  $\mu\text{m}$  particles

Transitions from both chipping to fragmentation and from fragmentation to disintegration occurs in the same velocity range as 500  $\mu\text{m}$  near-mesh feed size particles, i.e. 4-6 m/s and 11-14 m/s, respectively. However, the exact transition velocity might be slightly different for 500 and 600  $\mu\text{m}$  near-mesh particles.

The patterns of breakage for 850  $\mu\text{m}$  near-mesh feed size particles are shown in Figure 5-11.

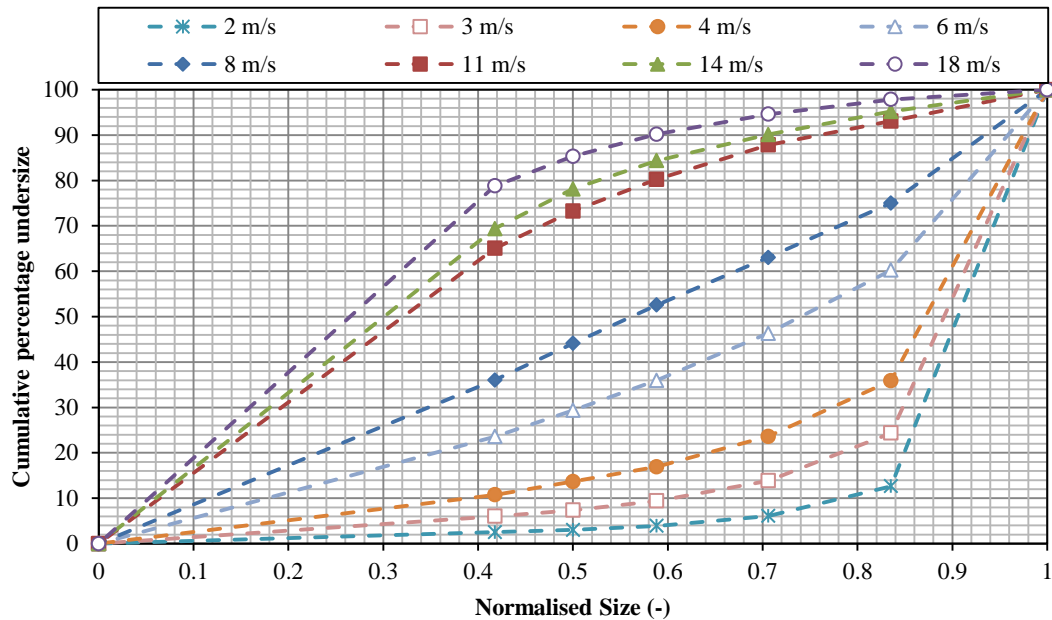


Figure 5-11. Patterns of breakage for 850  $\mu\text{m}$  particles

The results show a similar pattern as for the two smaller sizes. The particle breakage in the range 2-4 m/s could be categorised as chipping, 6-8 m/s as fragmentation, and above 11 m/s as disintegration. The transition velocities from chipping to fragmentation and from fragmentation to disintegration are in the range of 4-6 m/s and 8-11 m/s, respectively.

The dominant patterns of breakage for 1000  $\mu\text{m}$  near-mesh feed size particles are shown in Figure 5-12.

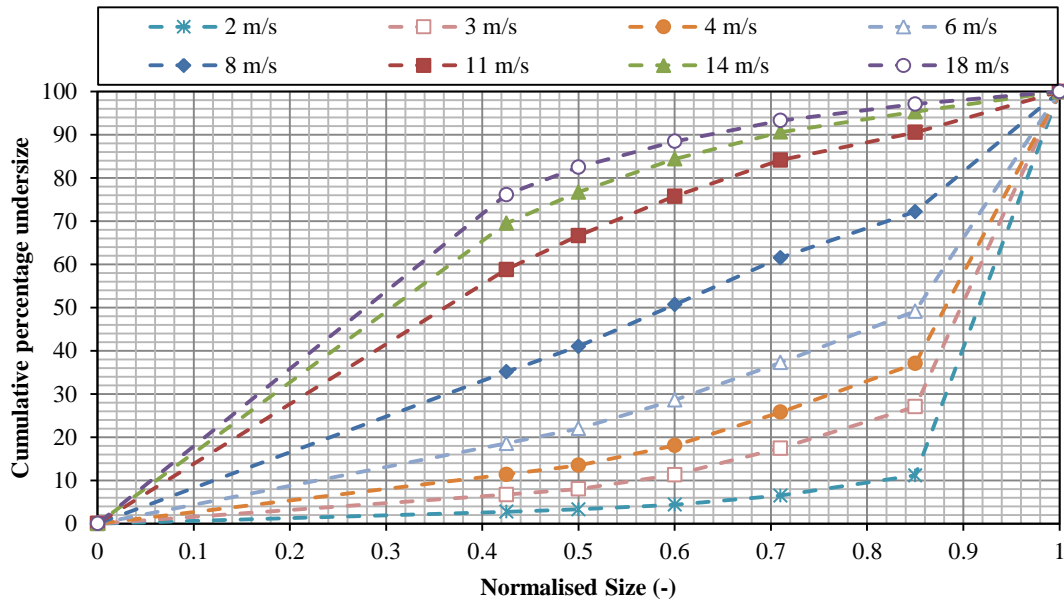


Figure 5-12. Patterns of breakage for 1000  $\mu\text{m}$  particles

Similar to the previous three particle size cases, a gradual shift in particle size distribution is observed here too. The transition velocity ranges from chipping to fragmentation and from fragmentation to disintegration for 1000  $\mu\text{m}$  particles are as the same as those for 850  $\mu\text{m}$  particles. However, the exact transition velocities might be different. Based on the results shown in Figure 5-12, the particle breakage in the range 2-4 m/s is categorised as chipping, 6-8 m/s as fragmentation, and above 11 m/s as disintegration.

Based on the above analyses, the transition velocities from chipping to fragmentation and from fragmentation to disintegration for different particle sizes have been summarised and are shown in Figures 5-13 and 5-14, respectively.

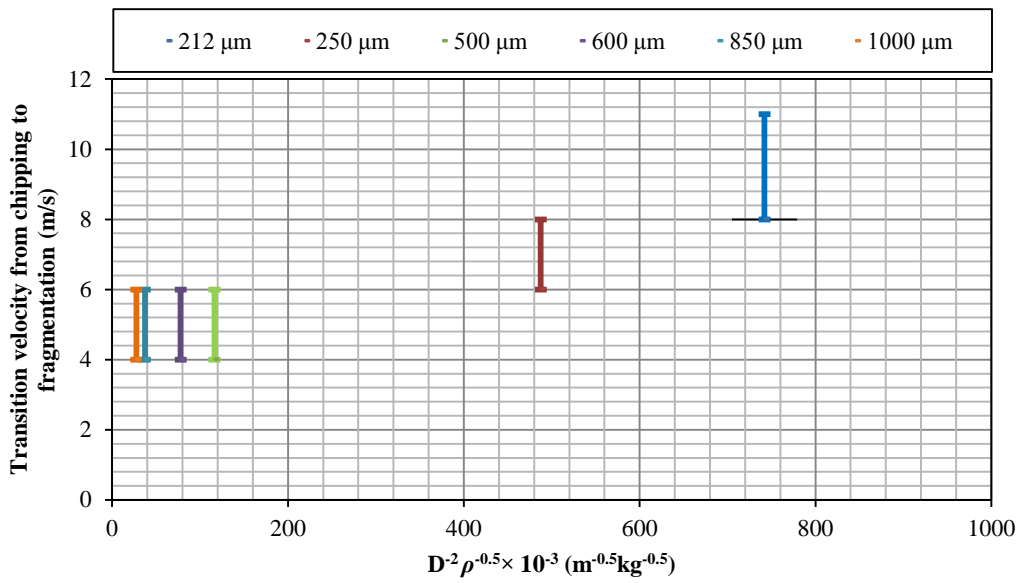


Figure 5-13. Transition velocity from chipping to fragmentation for different particle sizes of spray-dried burkeite

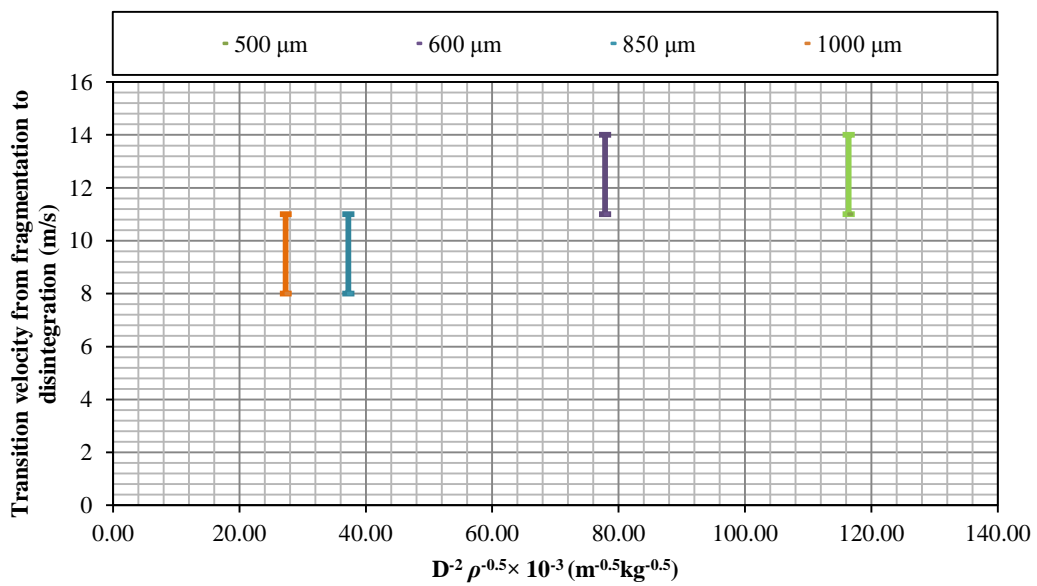


Figure 5-14. Transition velocity from fragmentation to disintegration for different particle sizes of spray-dried burkeite

The results of Figure 5-13 are in agreement with Eq. (2-10), as they show that the transition velocities are inversely proportional to the square of particle size as well as

square root of envelope density. However, based on this equation the transition velocity is very sensitive to  $K_c$  and  $H$ , i.e. transition velocity from chipping to fragmentation is a function of  $(K_c/H)^4$ , which has been assumed to be constant for different particle sizes.

The calculated transition velocities in this work are based on this inadequate assumption, as there was not any information available on hardness and fracture toughness of different particle sizes of spray-dried burkeite. Based on Figure 5-13, as the particle sizes increase, the particles undergo fragmentation/ disintegration at lower velocities. Some of the results show the same transition velocity ranges for two different particle sizes, i.e. the chipping to fragmentation transition velocity of both 500  $\mu\text{m}$  and 600  $\mu\text{m}$  near-mesh feed size particles is in the range of 4 to 6 m/s. This is most likely the consequence of variations in the structure reflected by the envelope density. Although, the transition velocity range is the same, the exact transition velocities for these two particle sizes might be different.

The transition velocities from fragmentation to disintegration have been also plotted as a function of  $D^{-2} \rho^{-0.5}$ , as shown in Figure 5-14. However, there is no reported equation for transition velocity from fragmentation to disintegration in the literature.

The data corresponding to each pattern of breakage can now be separated. For example, for particle breakage in the chipping regime, the extent of breakage,  $R^*$ , is shown as a function of impact velocity for different particle sizes in Figure 5-15.

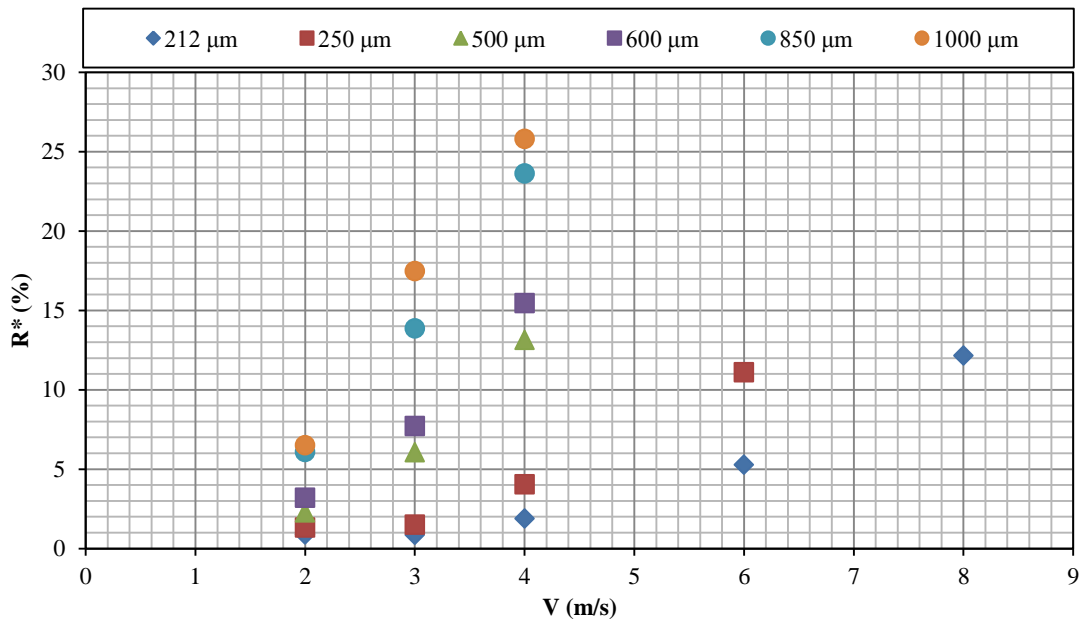


Figure 5-15. Extent of breakage,  $R^*$ , as a function of impact velocity for different particle sizes of burkeite for chipping regime

Clearly  $R^*$  increases with the impact velocity and particle size. However, a theory is needed to explain the breakage results, and it depends on the mode of failure.

## 5.6 Mode of Failure of Spray-Dried Burkeite Particles

As described in the literature review chapter, it is not easy to define the mode of failure of agglomerates. Due to non-uniformity of the agglomerate structure, the definition of modes of failure does not lend themselves well to the mechanisms of agglomerate failure. Nevertheless, the failure mode of agglomerates can *macroscopically* be covered by the three classical modes of failure; semi-brittle, brittle and ductile failure mode, as described in section 2.6.8.

In order to explore the mode of failure of spray-dried burkeite particles, they were tested under quasi-static conditions. For this purpose, a Nano-Crush test device was used (Figure 5-16). The device is used for determining the crushing strength of a specimen, and it can be operated either based on load or depth of deformation. A single particle is placed on the disc under the tip of the indenter; the other settings would be controlled by using the Nano-Crush software. All the results reported by the software of the device correspond to loading curve, and with the setting of the current device the unloading curve is not shown as an output of the measurements. Therefore in order to obtain some information on the mode of failure, SEM images were taken after the tests.



**Figure 5-16. Nano-Crush test device**

A good number of 850  $\mu\text{m}$  near-mesh particles were tested using this device, by controlling the depth of deformation. The particles were placed in a way that they are completely stable before running the test. The tests were then carried out at two different conditions: (i) controlling the depth and stopping the test at a certain depth

before failure of the particles, (ii) stopping the test after particle failure is observed. For each test, at least five repeats have been done in order to make the results more reliable. Scanning Electron Microscopy was used to observe the particles and any possible cracks.

The first set of tests was done by controlling the depth of crushing at 40  $\mu\text{m}$ . The load-displacement curve is reported by the software as shown below:

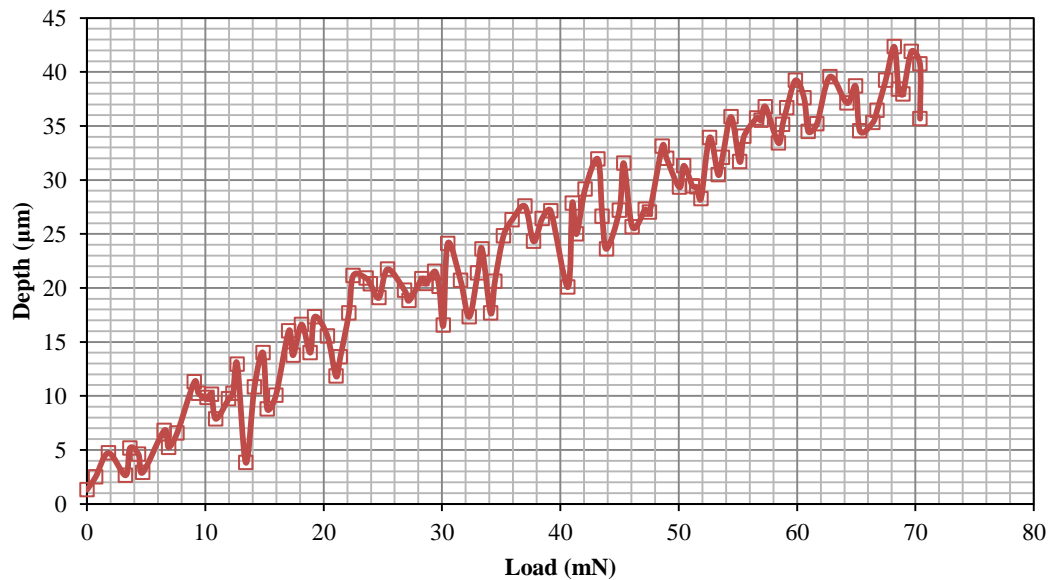


**Figure 5-17. Nano-Crush test on 850  $\mu\text{m}$  particles by controlling the depth at 40  $\mu\text{m}$**

The test was stopped at around 40  $\mu\text{m}$  crushing depth before the particle completely failed. The SEM image of the above particle is shown in Figure 5-18.

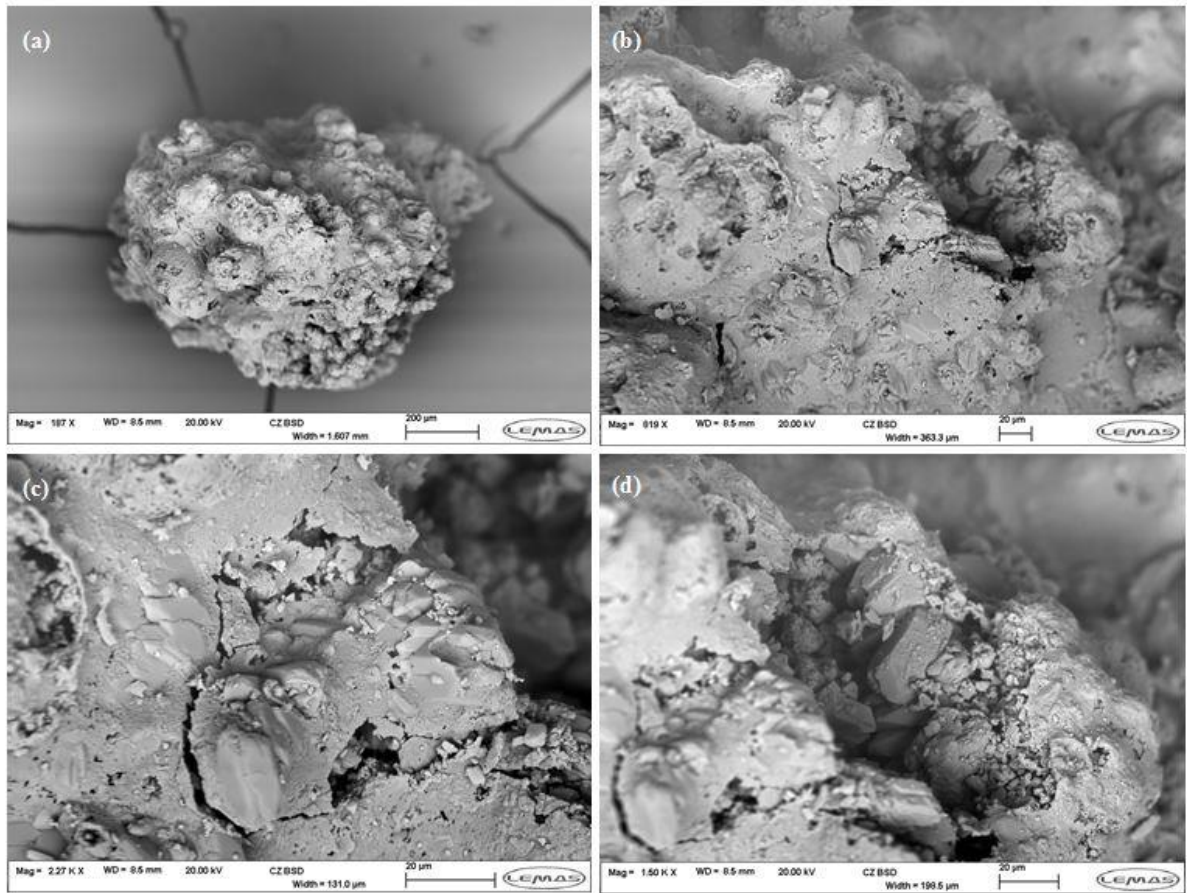


**Figure 5-18. SEM images with different magnifications of 850 μm particle after Nano-Crush test at 40 μm crushing depth**

Figure 5-18a is a top view of the particle. As observed in Figure 5-18b, there are cracks on the crushing zone, which is clearer in higher resolution SEM images, Figures 5-18c and 5-18d.

The second test was done by stopping the test at 50 μm crushing depth. The typical load-displacement curve as well as SEM images of the tests at this condition are shown in Figures 5-19 and 5-20.

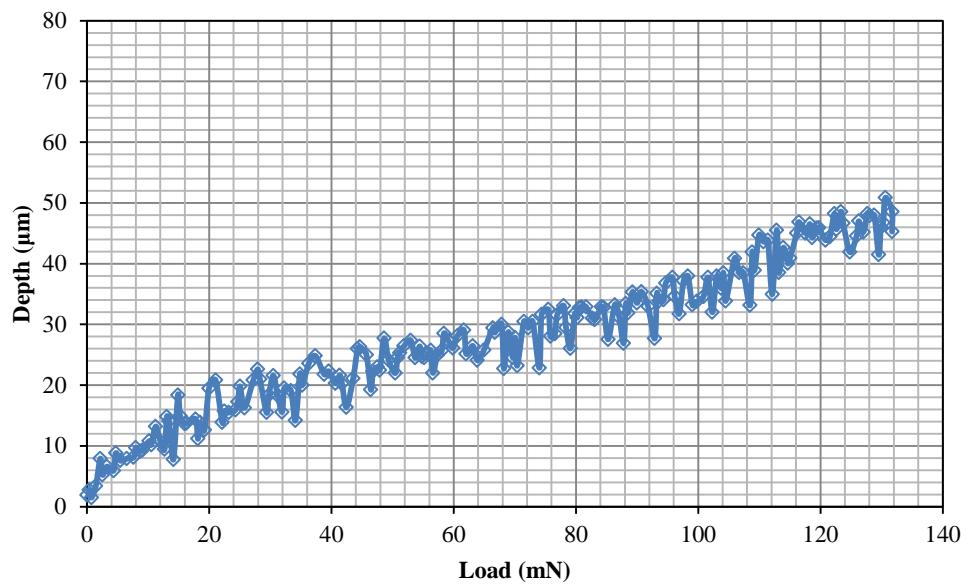
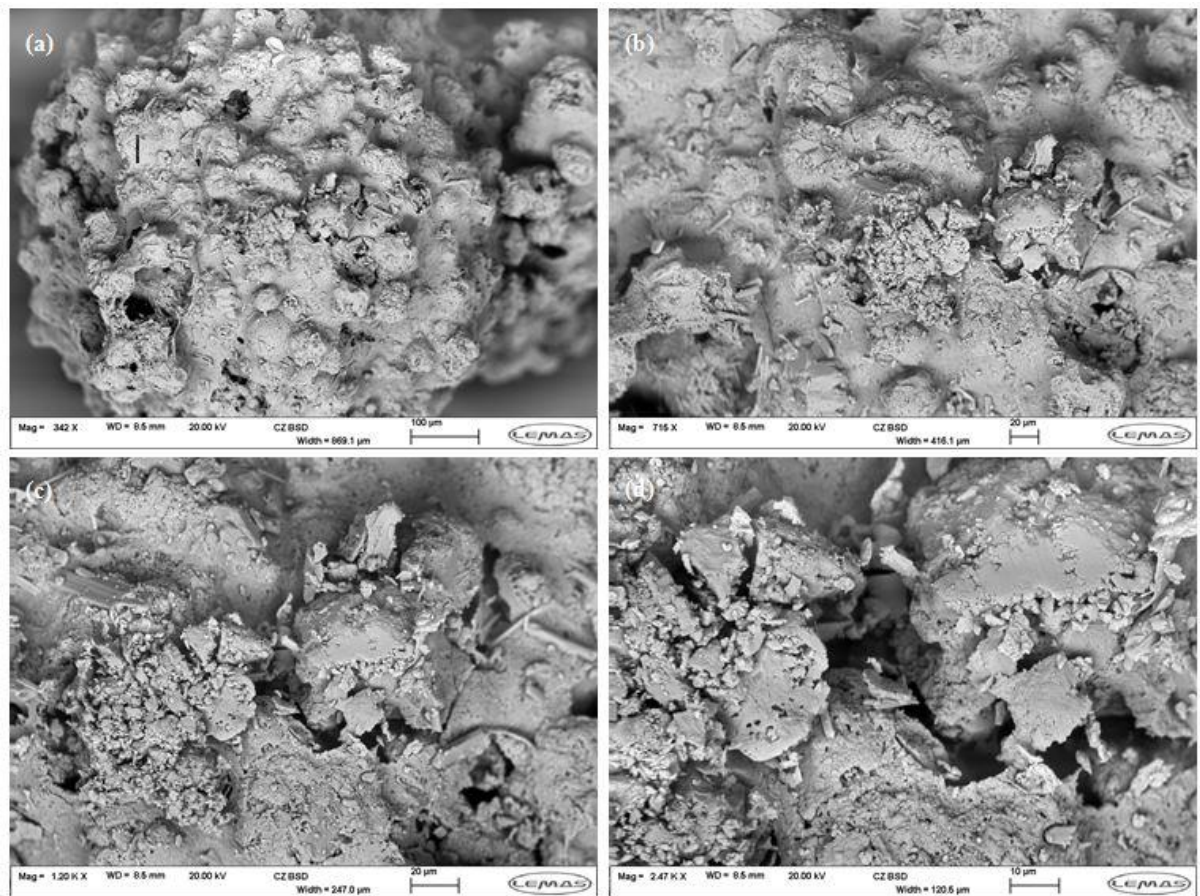


Figure 5-19. Nano-Crush test on 850 µm particles by controlling the depth at 50 µm



**Figure 5-20. Different magnifications SEM images of 850  $\mu\text{m}$  particle after Nano-Crush test at 50  $\mu\text{m}$  crushing depth**

The top view of the particle has been shown in Figure 16a. In a higher magnification SEM image, Figure 5-20b, a flat surface is observed, which could possibly be the crushing zone. A crack is seen in higher magnification images, as shown in Figure 5-20c and 5-20d.

The second type of test is to stop the test after the particle has completely failed. The failure of the particle is clearly observed when there is a big jump in the load-displacement curve. The tests have been done on 850  $\mu\text{m}$  particles. Some examples of particle failure under this test condition are shown below.

In the first example, the particle failure occurs at depth of around 60  $\mu\text{m}$ . The test is stopped as soon as the jump is observed in order to avoid the particle to be fully crushed. The load-displacement curve and SEM images of the particle are shown in Figures 5-21 and 5-22.

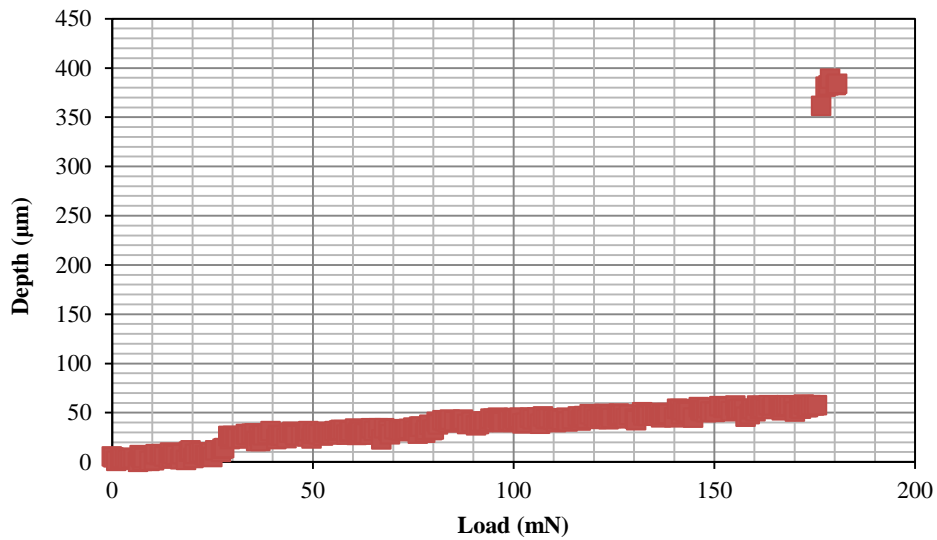


Figure 5-21. Failure of the 850  $\mu\text{m}$  particle by Nano-crush test at the crushing depth of 60  $\mu\text{m}$

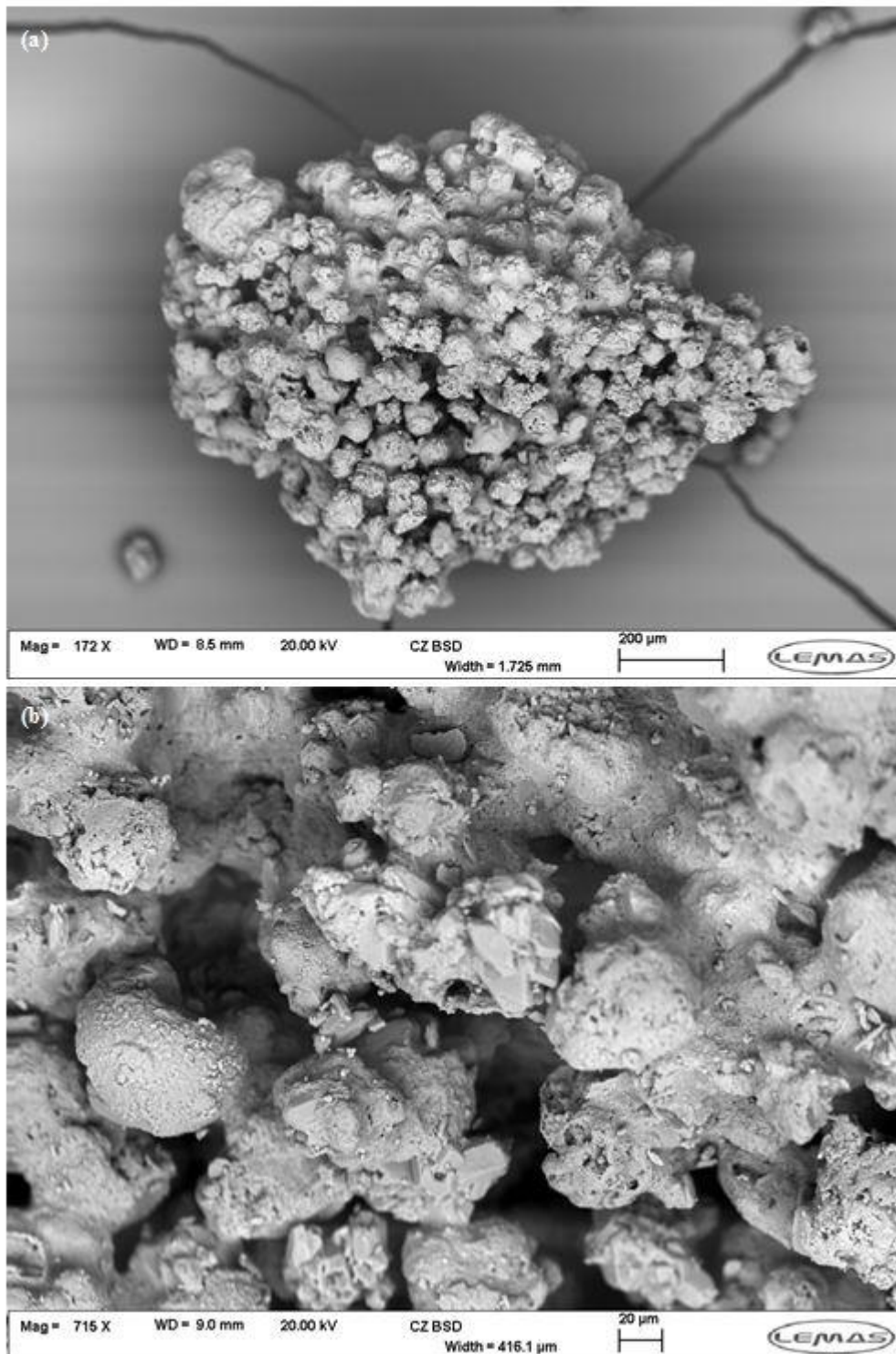
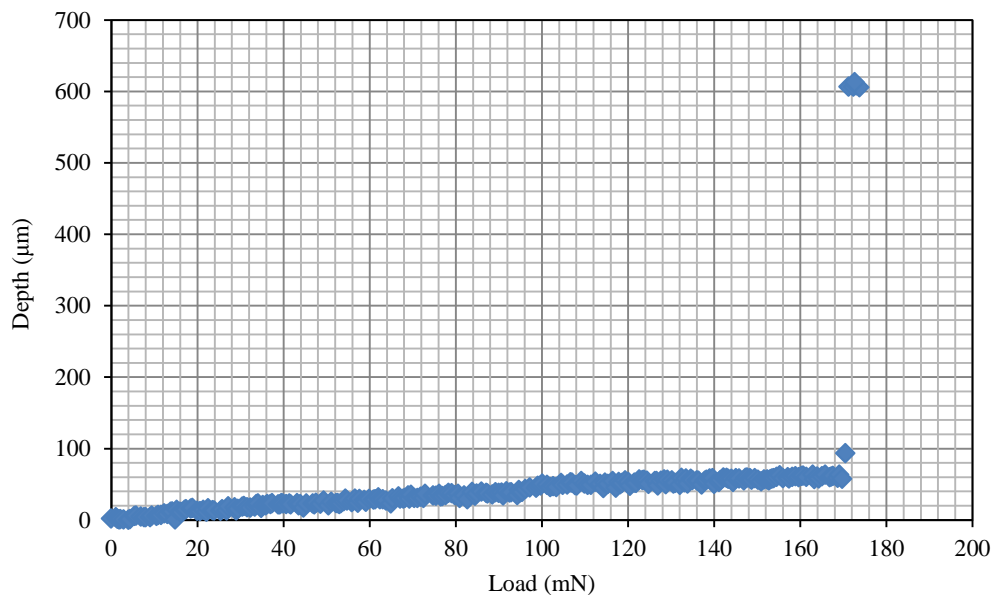


Figure 5-22. SEM images of 850  $\mu\text{m}$  near-mesh particle failure by Nano-Crush test at the crushing depth of around 60  $\mu\text{m}$

Based on the SEM images shown in Figure 5-22, a crack is observed in the middle of the particle, and presumably it has vertically gone all the way along the particle. However, due to existence of cavities and pores inside the particles, the direction of the crack is not clear.

In the second example, the particle failed at a depth of around 100  $\mu\text{m}$ . The results and SEM images are shown in Figures 5-23 and 5-24.



**Figure 5-23. Failure of the 850  $\mu\text{m}$  near-mesh particle by Nano-crush test at the crushing depth of around 100  $\mu\text{m}$**

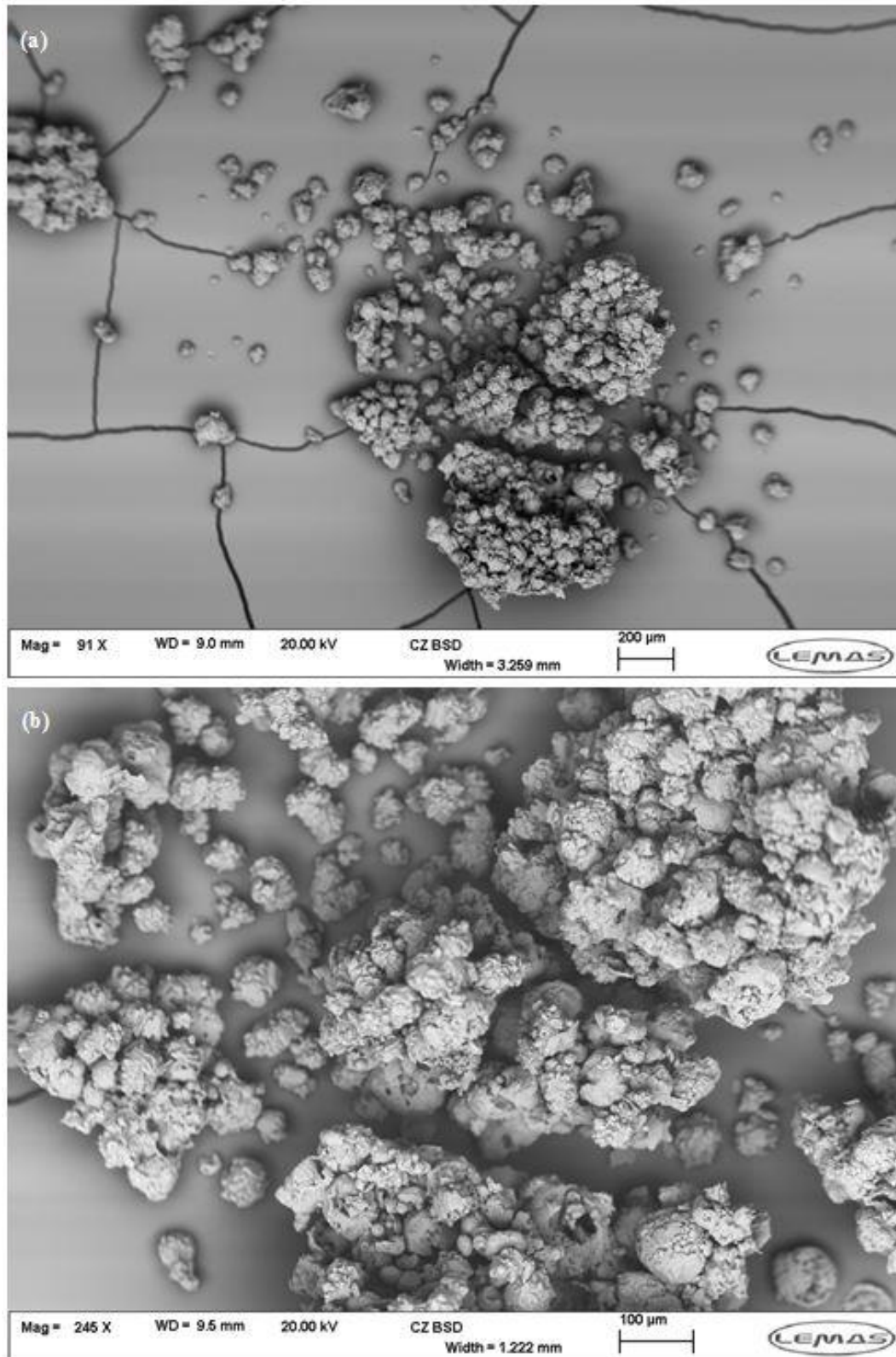


Figure 5-24. SEM images of 850 µm near-mesh particle failure by Nano-Crush test at the crushing depth of around 100 µm

In this case the particle has disintegrated into several pieces, as observed in Figure 5-24a and 5-24b.

Overall, the existence of pores and cavities inside the spray-dried burkeite particles makes any firm conclusion on the failure mode difficult. In some cases, the cavities inside the particles act as flaws, and the failure is more similar to brittle failure mode. However, this is not always the case, and flattening of the contact is also observed in some cases, where crack propagation is developed from the crushing zone. Based on the Nano-Crush tests and observed results, a clear mode of failure cannot be concluded for spray-dried burkeite particles.

The analysis of both brittle and semi-brittle modes of failure has been described in section 2.2. Based on that information, the models of Ghadiri and Zhang (2002) and Vogel and Peukert (2003) both show the same trend in terms of dependency on particle velocity and size for the case where the extent of breakage is small. Therefore, regardless of the mode of failure of burkeite particles under impact, the breakage analysis can be carried out in terms of dependence on particle size and impact velocity.

### **5.6.1 Chipping**

The analysis reported below is based on the semi-brittle mode of failure, therefore the model of Ghadiri and Zhang (2002) will be used. However, the breakage propensity parameter obtained in this way can also be considered as the material parameter of the model of Vogel and Peukert (2003), as both represent the slope of the line of the extent of breakage as a function of  $DV^2$  (see chapter 2).

According to the model of Ghadiri and Zhang (2002), the extent of breakage follows a square of velocity relationship. The extent of breakage is expressed as a function of  $V^2$  to see if such a dependence holds, and is shown in Figure 5-25.

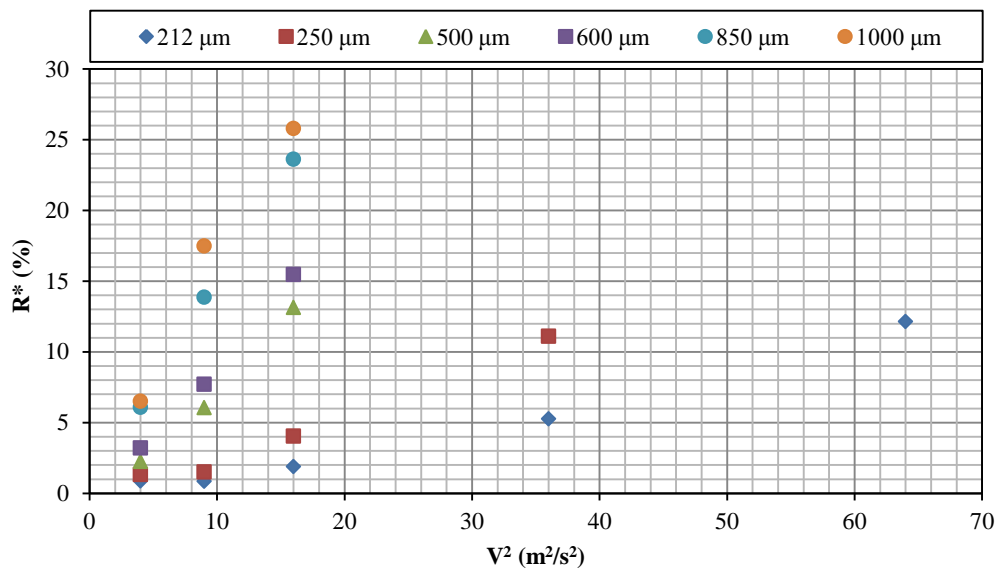


Figure 5-25. Extent of breakage,  $R^*$ , as a function of  $V^2$  for chipping regime

A linear trend is clearly observed when the extent of breakage is plotted as a function of  $V^2$  for each near-mesh feed particle size. However, the extent of breakage is also a function of particle size. Therefore, by considering both effects of particle size and impact velocity, the extent of breakage,  $R^*$ , for the chipping regime has been plotted as a function of  $DV^2$ , as shown in Figure 5-26.

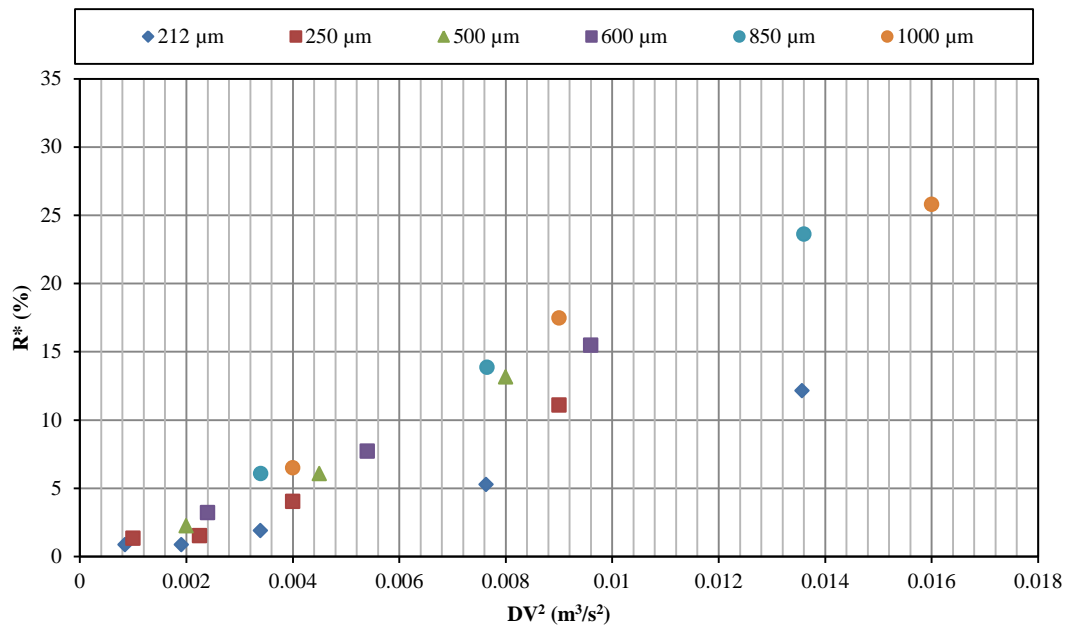


Figure 5-26. Extent of breakage,  $R^*$ , as a function of  $DV^2$  for the data corresponding to the chipping regime

Clearly some unification of the extent of breakage,  $R^*$ , as a function of  $DV^2$  is achieved as expected. However, there is scatter in the data and this is likely to have arisen from differences in the structure of the particles amongst different particle sizes, i.e. the variations in the envelope density and mechanical properties, such as  $H$  and  $K_c$  according to Eq. (2-6). Therefore the envelope density variations as a function of size (as reported in chapter 4) need to be used as part of the analysis. This is shown in Figure 5-27, where the extent of breakage is expressed as a function of  $\rho DV^2$ .

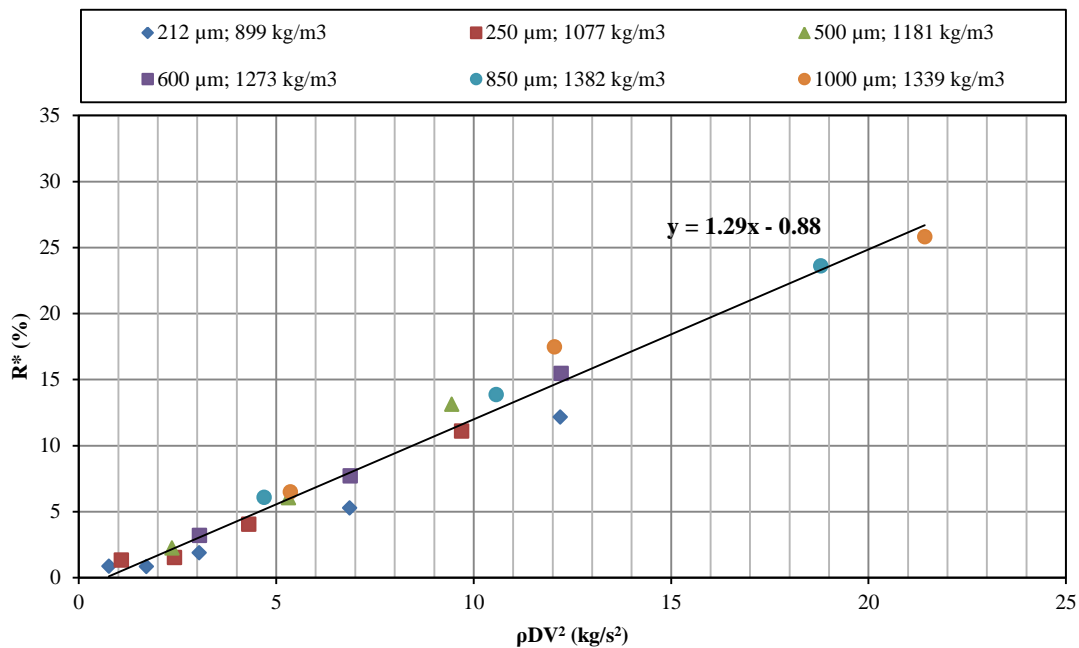


Figure 5-27. Extent of breakage,  $R^*$ , as a function of  $\rho DV^2$  with the slope representing  $\alpha H/K_c^2$ , showing data unification

Clearly a much better unification than that shown in Figure 5-27 is obtained for a wide range of particle sizes and impact velocities by accounting for the actual envelope densities. The slope of the line is a lumped parameter representing the mechanical properties of the material,  $H/K_c^2$ . Interestingly, considering the intercept of the fitted line with abscissa, there is a minimum impact velocity for a given particle size below which there is no/ little breakage. The transition velocity from no breakage to chipping for different near-mesh particle sizes is shown in Table 5-2.

**Table 5-2. Transition velocity from no-breakage to chipping for different near-mesh particle sizes**

Particle size ( $\mu\text{m}$ )	Transition velocity from no breakage to chipping (m/s)
212	1.9
250	1.6
500	1.1
600	0.9
850	0.8
1000	0.7

As described in the Literature Review Chapter, The transition velocity from no breakage to chipping is proportional to the inverse of the square of the particle size. Therefore, the transition velocities have also been plotted as a function of  $D^{-2}\rho^{-0.5}$ , as shown in Figure 5-28. The increasing trend of transition velocities by increasing the  $D^{-2}\rho^{-0.5}$  is in agreement with Eq (2-6).

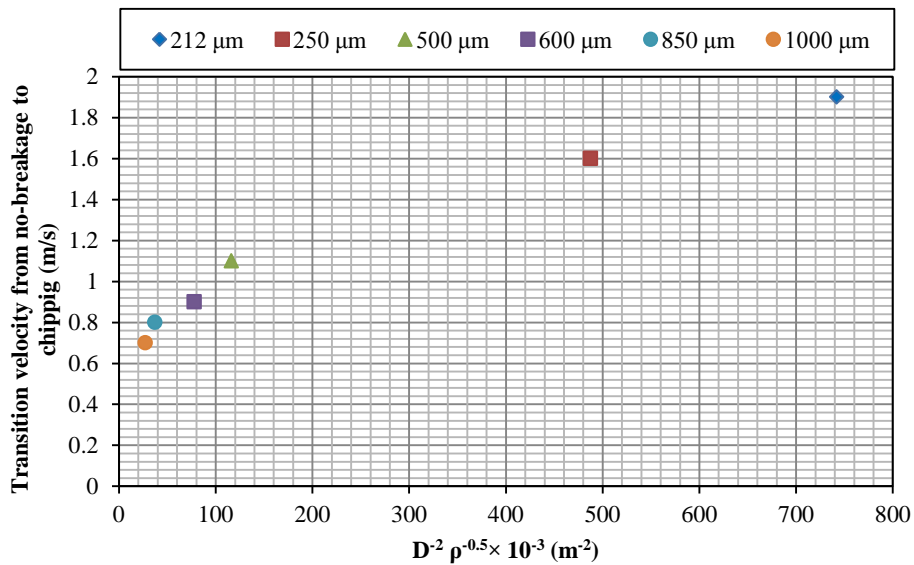


Figure 5-28. Transition velocity from no-breakage to chipping as a function of  $D^{-2}\rho^{-0.5}$

This information is very useful for designing pneumatic conveying lines, cyclones and other items of equipment, where particles experience mechanical stress by impact.

### 5.6.2 Fragmentation and Disintegration

Full sieve analyses have been done on the data for fragmentation and disintegration regimes. The impact velocities corresponding to these two regimes have been identified using Schumann's plot. The collected particles after impact testing have been sieved up to five sieve cuts below the feed size, and the mass fraction for each sieve has been determined. The results are shown in Figure 5-29.

For the closest sieve size cut to the feed size, i.e. 180-212  $\mu\text{m}$ , the data corresponding to 11 m/s have the largest frequency percentage. For smaller sieve size cuts, the largest fraction of broken particles is related to the highest impact velocity, i.e. around 20% are

smaller than 90  $\mu\text{m}$  at 18 m/s, while at 11 m/s just 10% of the feed particles are broken to less than 90  $\mu\text{m}$ . As will be shown later, the fraction less than 90  $\mu\text{m}$  contains the individual clusters of crystals adhered to each other. These have a relatively narrow size distribution.

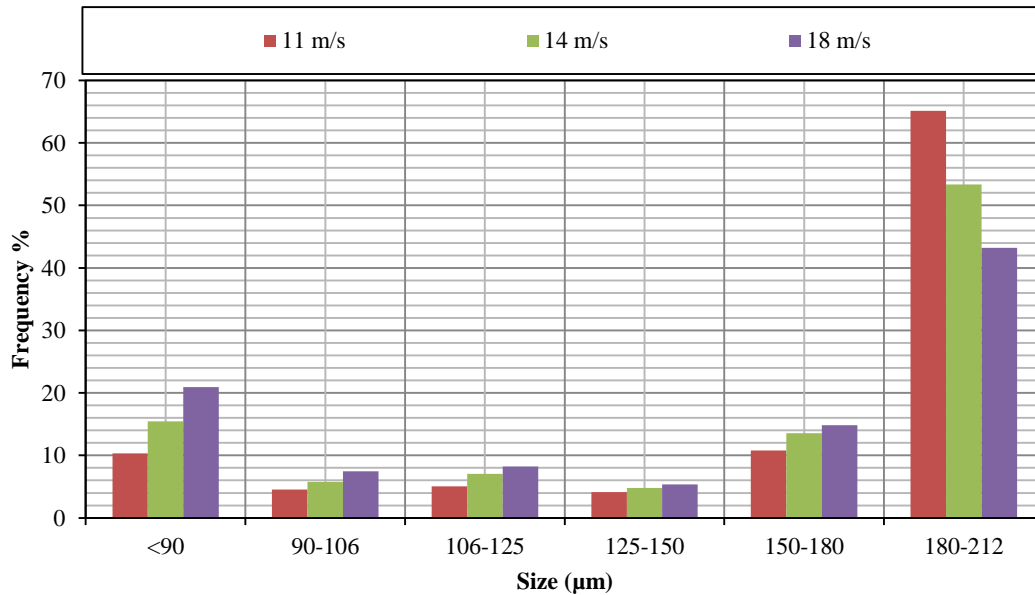


**Figure 5-29. Breakage analysis of 212  $\mu\text{m}$  near-mesh particles for impact velocities corresponding to fragmentation and disintegration regimes**

The same trend as 212  $\mu\text{m}$  near-mesh particles is observed for 250  $\mu\text{m}$  particles (as shown in Figure 5-30). However the fractions of broken particles within 180-212  $\mu\text{m}$  sieve cut are almost the same for all the impact velocities.

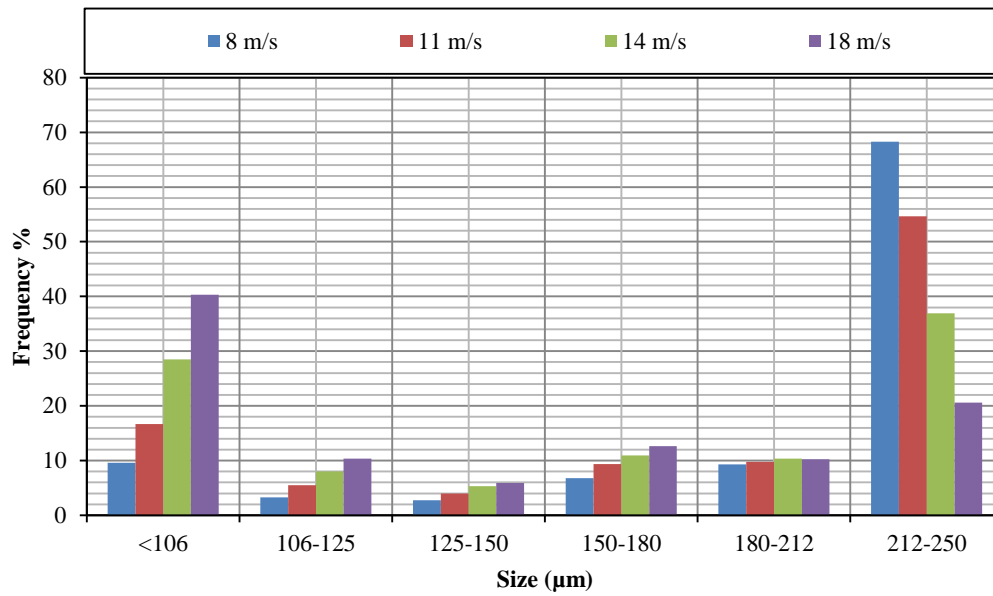


**Figure 5-30. Breakage analysis of 250  $\mu\text{m}$  near-mesh particles for impact velocities corresponding to fragmentation and disintegration**

The trend of the data corresponding to fragmentation and disintegration for impacting 500  $\mu\text{m}$  feed particles (as shown in Figure 5-31) seems to be different compared to the two previous near-mesh particles, 212 and 250  $\mu\text{m}$ . The fraction of broken particles for the largest and smallest sieve cuts is as expected.

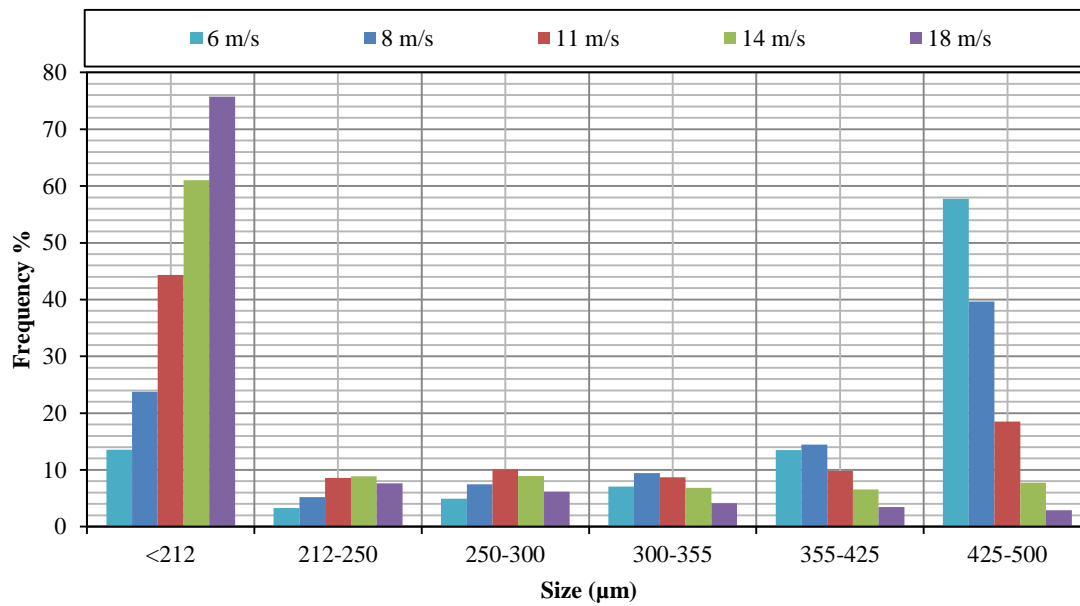


**Figure 5-31. Breakage analysis of 500 µm near-mesh particles for impact velocities corresponding to fragmentation and disintegration**

For 600 µm near-mesh feed particles, the impacted particles at 6 m/s and 8 m/s almost produce the same fraction of broken particles mass within the largest sieve cut. However, the fraction of broken particles for the smallest size cut is as expected.

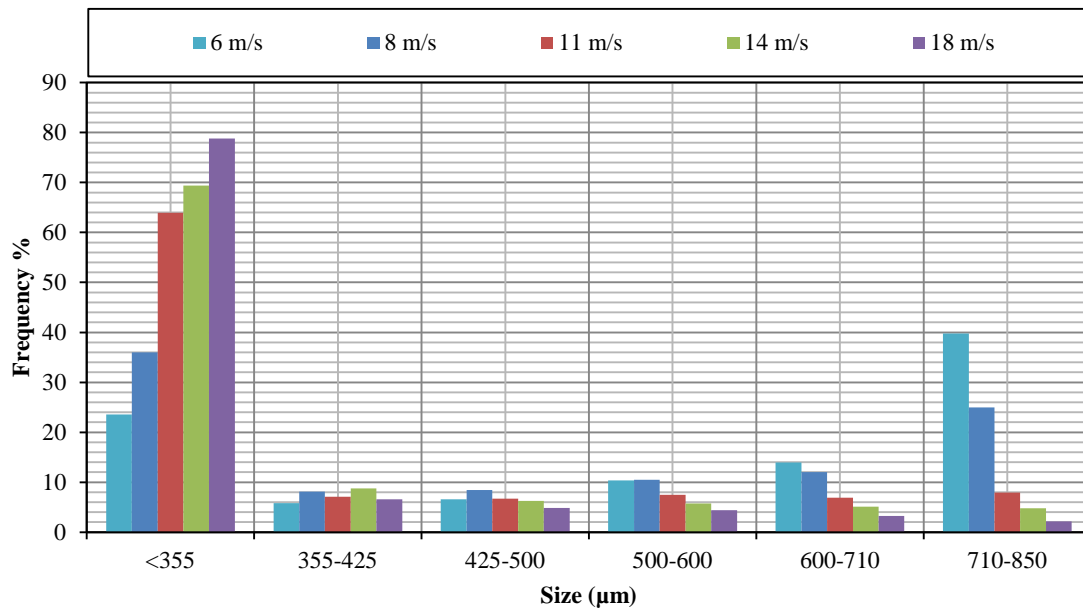


**Figure 5-32. Breakage analysis of 600  $\mu\text{m}$  near-mesh particles for impact velocities corresponding to fragmentation and disintegration**

The same trend as the previous near-mesh feed particle size is observed for 850  $\mu\text{m}$  particles. The highest fraction of broken particles within the largest sieve cut corresponds to the lowest impact velocity, however the opposite is observed for the smallest sieve cut, i.e. 80% of feed particles are broken to less than 355  $\mu\text{m}$  after impact at 18 m/s, while this is around 24% for impacting at 6 m/s.

The same expected trend as 850  $\mu\text{m}$  particles is observed for the data corresponding to fragmentation and disintegration after impacting 1000  $\mu\text{m}$  near-mesh particles as shown in Figure 5-34.

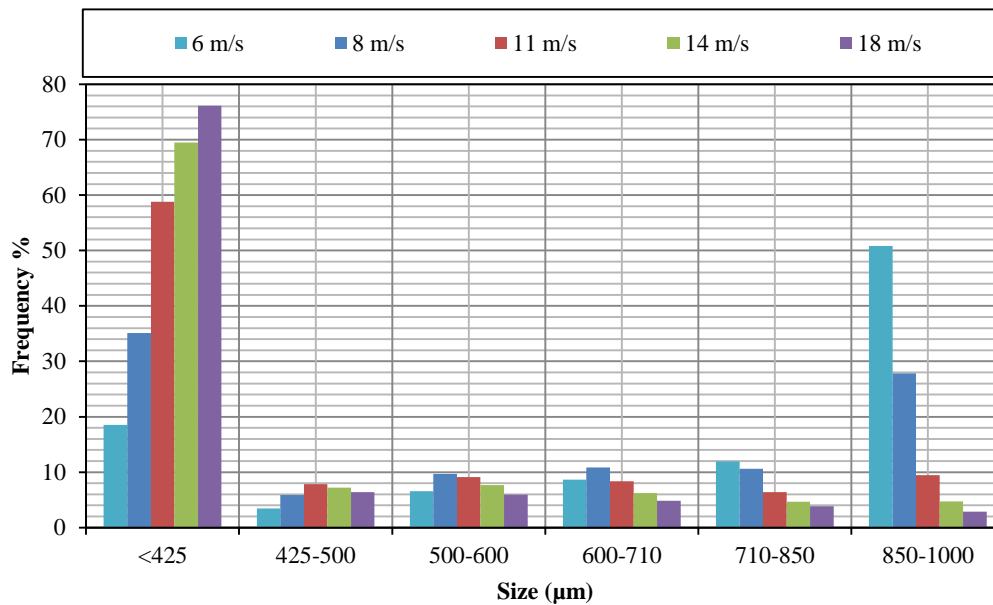


**Figure 5-34. Breakage analysis of 1000  $\mu\text{m}$  near-mesh particles for impact velocities corresponding to fragmentation and disintegration**

Sieve analysis can be carried out for smaller sieve sizes if the quantity of feed materials is large enough (at least 10 g), otherwise for a large number of sieves there is a risk of losing the particles when a small mass quantity is used. This information can be used to develop breakage function. Fragmentation and disintegration of spray-dried burkeite particles at different impact velocities produce plenty of fragments and fine particles depending on the impact velocity. As is shown in Figure 3-4, each spray-dried burkeite particle is made of clusters. When the particles go through the disintegration regime, they break down into these little clusters. Spray-dried burkeite particles are very weak and friable, and as the breakage results show, they can go under extensive breakage even at low impact velocities. However, it is not clear whether the clusters inside the particle are as weak as the particle itself or not. Hence, an experiment has been

designed to explore the strength of the clusters within the particle, and it is described below.

### 5.6.3 Impact Strength of Clusters

The first step before carrying out the experiments is to produce enough quantity of clusters. For this purpose, a sufficient quantity of the burkeite particles was placed in a plastic bag, and rubbed by hand to break the particles. The broken particles were then sieved and the particles within 45-53  $\mu\text{m}$  were separated, as they are roughly the same size as clusters based on SEM images taken from internal structure of burkeite (Figure 3-3). The sieved particles were then observed under SEM to be compared with Figure 3-4. Some SEM images of the clusters, produced using this approach, are shown in Figures 5-35 to 5-37.

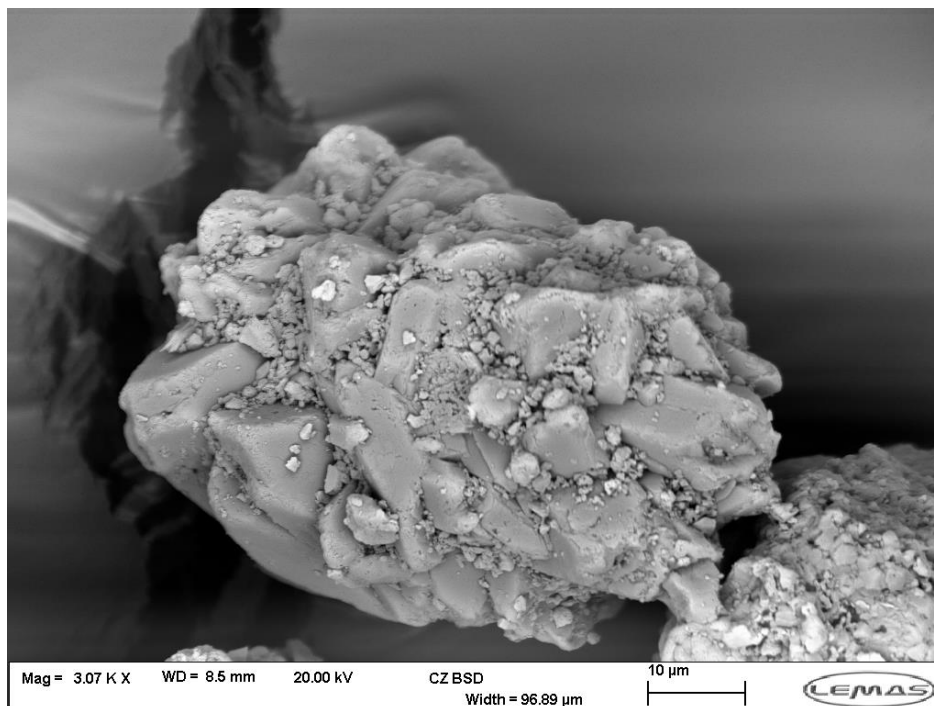


Figure 5-35. SEM image of clusters inside a spray-dried burkeite particle

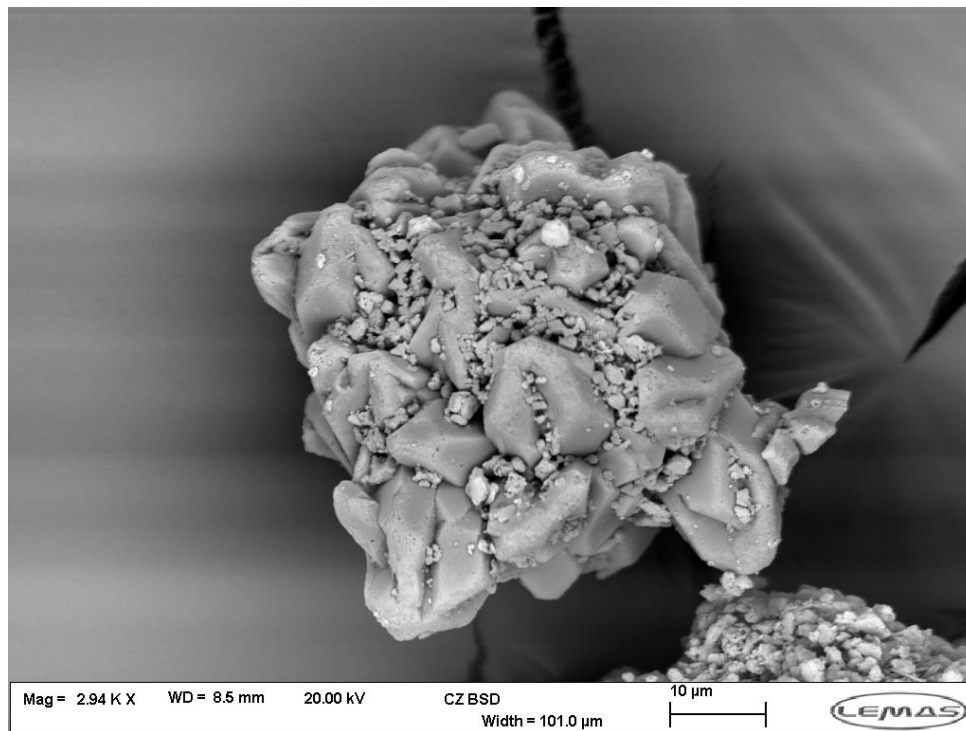


Figure 5-36. SEM image of clusters which the spray-dried burkeite particles are made of

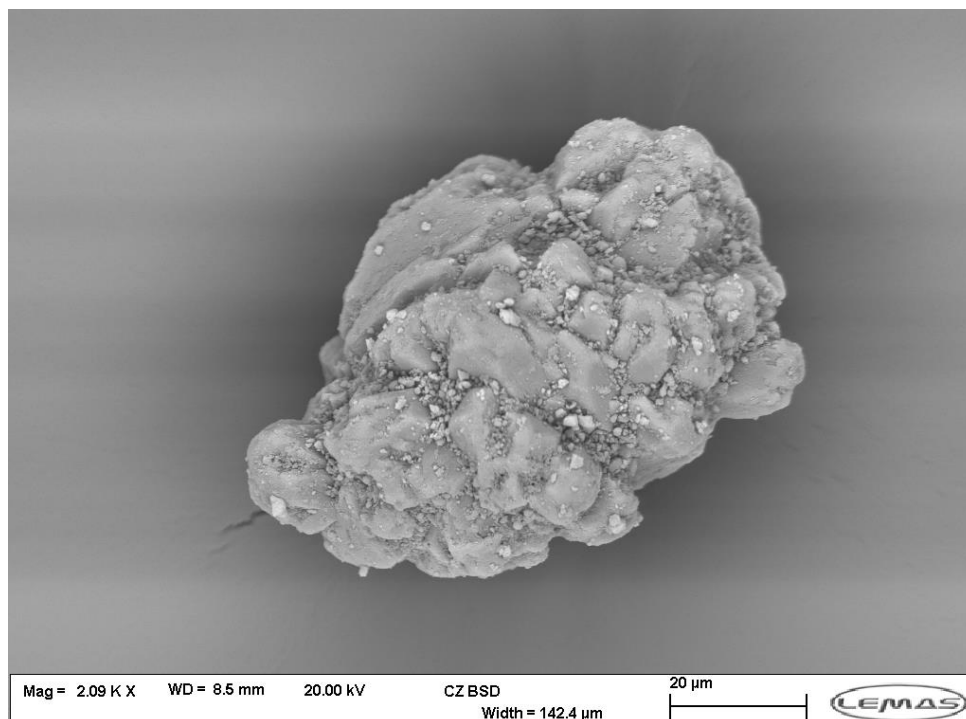


Figure 5-37. SEM image of clusters within a spray-dried burkeite particle

The clusters were then impacted at four different impact velocities, 18, 30, 50 and 60 m/s. It should be noted that single particle impact rig is better to be used for particles larger than 200  $\mu\text{m}$ , as the sensor cannot measure the time of flight for very small particle sizes. However, the vacuum pressures required to provide the mentioned impact velocities for the particles in the 45-53  $\mu\text{m}$  size range have been extrapolated using the information of larger sizes. The minimum impact velocity for these experiments was chosen to be equal to the maximum impact velocity used for impacting the spray-dried burkeite particles, as the clusters are expected to be stronger than the single particles. Some of the broken clusters are shown in Figure 5-38. These clusters have been collected after impact at 50 m/s, and observed by SEM. In a higher magnification, the broken clusters are shown in Figure 5-39, indicating that the clusters might break through breakage of the intercrystalline bonds. In some cases, the breakage of each individual crystal might result in breakage of the cluster, and hence producing debris, as shown in Figure 5-40.

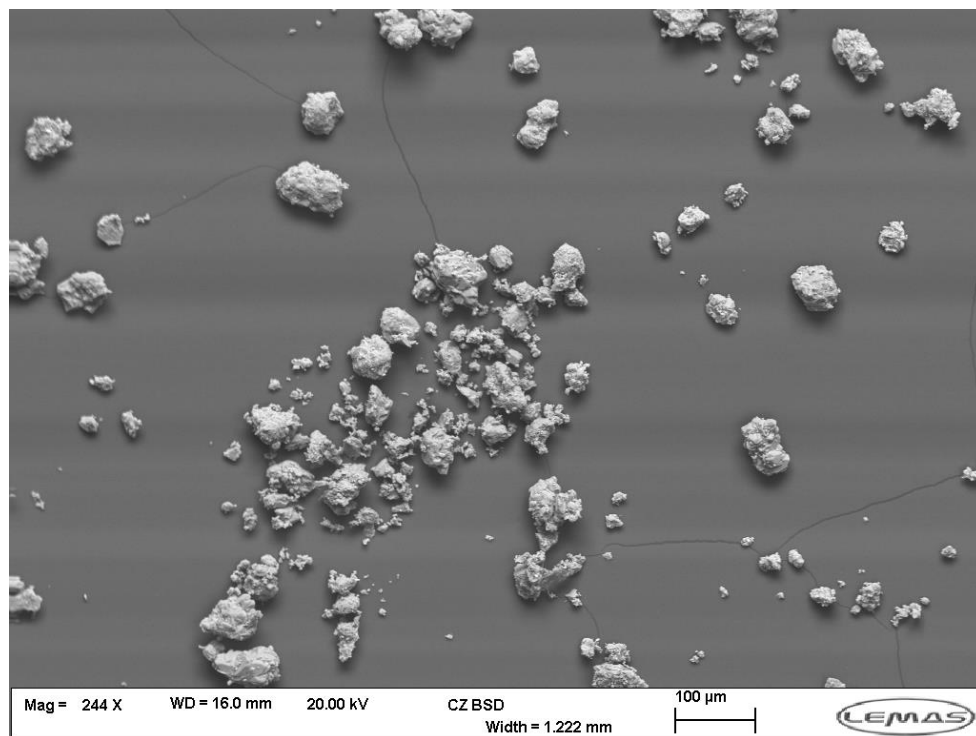


Figure 5-38. Several broken clusters after impacting at 50 m/s

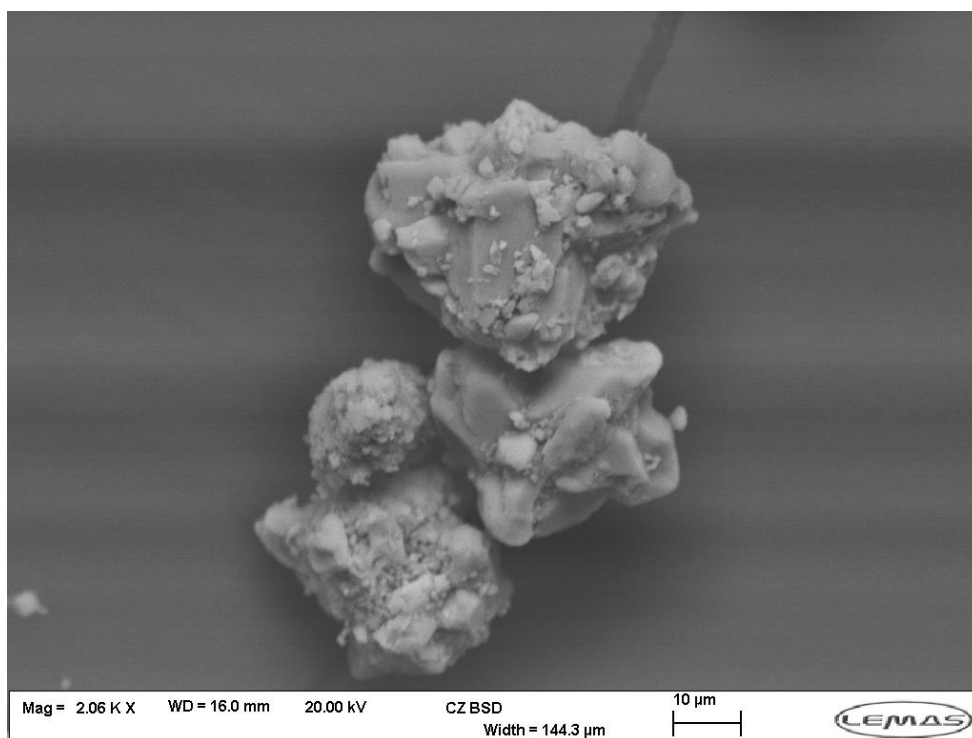
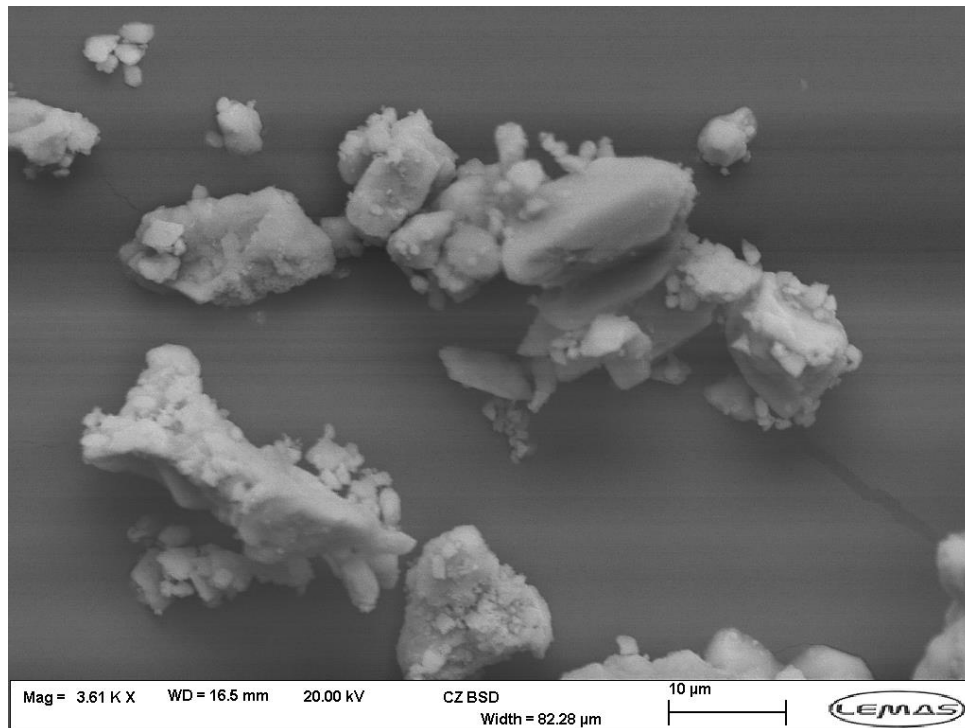
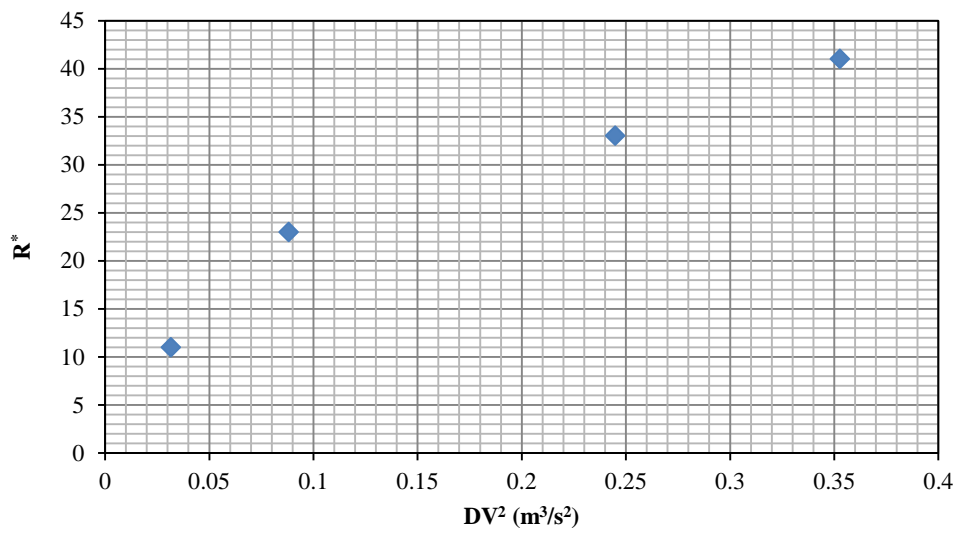


Figure 5-39. Broken clusters after impact at 50 m/s



**Figure 5-40. High magnification of the broken clusters after impacting at 50 m/s**

The impacted particles were then collected and the debris was separated using the sieve 37.5  $\mu$ m, which is two sieve sizes below the lower feed size. The broken particles did not seem to be cohesive. The extent of breakage was calculated and is shown in Figure 5-38. Three repeats were done for each impact velocity. The error bars have not been shown in the graph, as they are smaller than the legends: the full data are given in Table 5-3, instead.



**Figure 5-41. Extent of breakage,  $R^*$ , for impacting the clusters inside the spray-dried burkeite particles at different impact velocities**

Table 5-3. Breakage data of impacting the clusters at different impact velocities

Feed size ( $\mu\text{m}$ )	Number of test	R* (%) at 18 m/s	R* (%) at 30 m/s	R* (%) at 50 m/s	R* (%) at 60 m/s
45-53	1	11	22	34	42
45-53	2	12	24	31	40
45-53	3	11	23	34	41
	<b>Average R* (%)</b>	11	23	33	41
	<b>STDEV</b>	0.006	0.010	0.018	0.010
	<b>CV (%)</b>	5.09	4.35	5.73	2.44

The comparison of the extent of breakage of clusters at 18 m/s with the spray-dried particles at the same impact velocity shows that the clusters break less than the single particle. The extent of breakage for clusters at 18 m/s is around 11%. For large particles (850  $\mu\text{m}$ ) this is up to 95 %, and for small particles (212  $\mu\text{m}$ ) it is 40%. The low extent of breakage in the case of clusters as compared to the spray-dried burkeite particles could be attributed to either the size of the clusters (the small particle sizes are expected to undergo less breakage than large particle sizes) or the strength of the clusters. Considering the former, the extent of breakage for small spray-dried particles (i.e. the same size as clusters) can be extrapolated using the information from Figure 5-27. The extrapolation results show that for a particle with a size of around 50  $\mu\text{m}$ , the extent of

breakage at 18 m/s should be around 50%. Clearly, what has been obtained for the clusters is much lower than that. Therefore, clusters are clearly stronger than individual particles.

## 5.7 Concluding Remarks

Impact attrition of spray-dried burkeite particles has been studied by applying different impact stresses typical of those prevailing in a manufacturing plant. Burkeite is very weak and friable; hence it is prone to breakage even at low impact velocities. The impact tests were carried out using a minimum representative sample mass, which has been identified and used for all the impact tests in order to produce reliable and accurate results.

The impact tests indicate some structural differences for different particle sizes such as envelope density variations as a function of size, which are attributed to spray-drying processes and conditions. Therefore different measurement methods have been tested to explore the envelope density of different particle sizes. Among all the methods, the data from X-ray microtomography have been used as values for the envelope density of different particle sizes. XRT is one of the methods which takes account of shape of the particles, and hence it provides a better estimate of the average volume of the particles, which has a direct influence on the measured envelope density. The results show that the envelope density generally increases with particle size, although the underlying mechanism giving rise to these variations is unknown but it could be attributed to spray-drying processes. The measured values have been used to analyse the breakage data.

Different patterns of breakage have been identified for various impact conditions. The analysis gives information on the transition velocity ranges from chipping to fragmentation and from fragmentation to disintegration. It has been found that a good unification of breakage data may be obtained for the chipping regime using the measured envelope densities and the extent of breakage for the chipping regime. It also gives information about the transition velocity from no breakage to chipping, as well as material mechanical properties responsible for particle breakage.

The data corresponding to fragmentation and disintegration regimes have been studied by full sieve analysis. However, due to using a low quantity sample mass, the sieving has been carried out down to five sieve cuts below the feed size. In the case of using a larger quantity of sample mass, the sieve analysis can be continued further down to provide some information on fraction of broken particles with small sizes. As the particles go through fragmentation and disintegration regimes, the agglomerates break down to crystalline structure clusters. The evaluation of the impact strength of these clusters shows that they are much stronger than the spray-dried particles. These clusters are made of crystals stuck to each other. Side crushing of the clusters showed that the intercrystalline bond is very strong. SEM observations show how they break. The clusters within the spray-dried parties are loosely bound to each other, rubbing an assembly together produces these clusters. In order to increase the inter-cluster bond strength, it is possible to add binders, which in fact will increase the strength of the spray-dried particles.

## **CHAPTER 6      PARTICLE BREAKAGE IN THE SCIROCCO DISPERSER**

The impact breakage results of spray-dried burkeite particles have been analysed using the single particle impact rig, as for the particle breakage that is sensitive to strain rate, impact testing is the most appropriate method. However, this rig is not a commercially available device. In contrast, dry powder dispersers, such as the Scirocco disperser of the Malvern Mastersizer 2000, are widely available, and can be used for this purpose, provided particle impact velocity is known.

In this chapter, the breakage analysis of spray-dried burkeite particles as they go through the Scirocco disperser is reported. The same approach has also been applied to three other crystalline structures to explore how the method works for non-porous materials. Based on the results obtained, this method is suggested as a simple assessment method for grindability testing of different materials.

### **6.1 Background**

Particle size analysis is one of the key procedures in various industries handling and/or producing products in particulate form, as it provides some information about consistency in process performance as well as product attributes. This can be done using different techniques. Currently, particle sizing by laser light diffraction is one of the most common methods. The size measurement can be done under either wet or dry dispersion condition. For the latter, different air pressures are used to disperse the particles using a Venturi eductor configuration, and a good example of this type of

disperser units is the Scirocco disperser used in the Malvern Mastersizer 2000. A schematic diagram of the Scirocco disperser is shown in Figure 6-1.

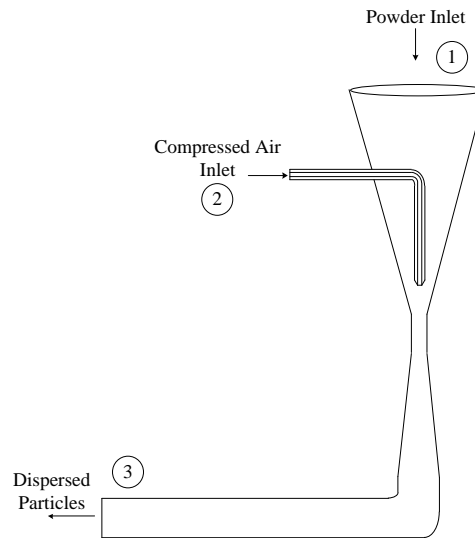


**Figure 6-1. Schematic diagram of the Scirocco disperser**

In the Scirocco disperser, a high pressure air is supplied to the air inlet (port 2), which results in a high velocity jet of air at the nozzle tip. The particles are slowly fed to the top inlet of the disperser (port 1) and get rapidly accelerated as they interact with the high velocity air jet stream. The dispersion of particles takes place as they impacts at the elbow. The dispersed particles exit from the outlet (port 3) and are presented to the laser light for laser diffraction measurements.

As the particles are accelerated by an air jet, they are impacted on the container walls and L-bend. There are two different categories of particles; for fine and cohesive powders the dispersion/collision energy might be inadequate to properly disperse them and some clusters may survive. Calvert et al. (2009) have done a review of different dispersion methods used in the laser diffraction technique. Recently Calvert et al. (2013) investigated the dispersion of cohesive powders and related the dispersion

efficiency to the powder flowability as described by the cohesive powder flow function. In contrast, for weak and friable powders, the wall collisions may lead to undesirable particle breakage. In both cases the particle sizing is affected.

There is no extensive work on the breakage of weak powders as a function of nozzle pressure using these dispersers in the literatures, although there is full awareness and concern about particle breakage during dispersion. Therefore breakage of spray-dried burkeite particles in the Scirocco disperser has been studied to provide some information on breakage of weak particles in these dispersers, and a better understanding of the breakage behaviour of burkeite particles. However, the length of the Scirocco disperser is not long enough for the particles to reach their terminate velocities. Therefore the impact velocity of different particle sizes in the elbow needs to be evaluated.

Ali et al. (2015) in their work showed that CFD simulation can be used to calculate the impact velocity of the particles at the L-bend of the Scirocco disperser. They carried out three dimensional multiphase Computational Fluid Dynamic simulations of the Scirocco disperser and analysed the air flow field, following which particle trajectories and impact velocities were calculated using an Eulerian-Lagrangian approach. The calculated velocities were based on the first impact on the L-bend, and are used in this work, combined with the experimental work to analyse the breakage behaviour of the spray-dried burkeite particles in the Scirocco disperser.

## 6.2 Experimental Work Using the Scirocco Disperser

Six near-mesh sizes were chosen to carry out the experimental work; 212, 250, 500, 600, 850, 1000  $\mu\text{m}$ . Each particle size was fed into the Scirocco disperser at a rate meeting the minimum obscuration requirement for particle size analysis by laser diffraction. A sensitivity analysis was carried out to find out the optimum vibratory feed rate as well as the minimum mass required to provide an adequate obscuration (4 to 8 %).

Five different dispersion air pressures were used to disperse the particles; 100, 150, 200, 250 and 300 kPa (corresponding to 1, 1.5, 2, 2.5 and 3 barg). The size distribution was measured by laser diffraction method using Mastersizer 2000, and the specific surface area (SSA) of the dispersed and broken particles was calculated based on the particle size distribution and density of the particles, and reported by the software of Mastersizer 2000. However, a different method needs to be used in order to measure the SSA and size distribution of the feed particles, as the particles are weak and friable and in order to avoid the results being affected by particle breakage in the Scirocco disperser of Mastersizer 2000, a use of another device has been made. This was done using Spraytec laser diffraction analyser of Malvern. The measurements were done by gently pouring the particles under free-fall condition to measurement zone of the Spraytec. Under such condition almost no breakage takes place and hence the measured size distribution and SSA are attributed to the feed particles.

The characteristic sizes  $d_{10}$ ,  $d_{50}$  and  $d_{90}$  of the PSD for the nozzle pressures used in this work are summarised in Table 6-1.

**Table 6-1. The characteristics sizes  $d_{10}$ ,  $d_{50}$  and  $d_{90}$  of the particle size distribution of the feed particles (given by Spraytec) and of the broken particles (given by Mastersizer 2000) in  $\mu\text{m}$  for different nozzle pressures**

Size ( $\mu\text{m}$ )	212			250			500			600			850			1000		
Pressure (kPa)	$d_{10}$	$d_{50}$	$d_{90}$															
<b>Feed</b>	180	228	288	215	282	374	385	530	718	440	584	757	464	628	801	527	1014	1105
<b>100</b>	35	107	308	34	91	239	39	94	235	44	120	284	45	126	353	43	127	355
<b>150</b>	30	94	269	30	91	270	39	88	205	43	93	239	43	105	309	44	110	316
<b>200</b>	21	82	208	22	78	205	34	78	178	37	84	205	40	97	275	39	104	309
<b>250</b>	17	79	203	21	74	179	29	75	158	34	79	178	33	88	236	38	95	275
<b>300</b>	14	71	178	15	71	157	22	71	157	30	75	157	34	82	206	33	87	233

Based on the results reported in the Table 6-1, there is a shift in the particle size distribution curves, as the nozzle pressure is increased, which indicates particle breakage. At high pressures, roughly similar debris sizes have been obtained for all the particle sizes. This is due to particle disintegration into constituting crystal clusters/aggregates forming the spray-dried burkeite particles as shown in the previous chapter. At low nozzle pressures, the trend of the particle size distribution change is not

monotonous as the particles undergo fragmentation, and the size of the fragments depends on different factors such as feed size, impact velocity and structure of the particles.

As an example, the size distributions of different particle sizes having passed through the Scirocco at the highest nozzle pressure (300 kPa) are shown in Figure 6-2. The rest of the data for all nozzle pressures are shown in the Appendix A (pages 215-220).

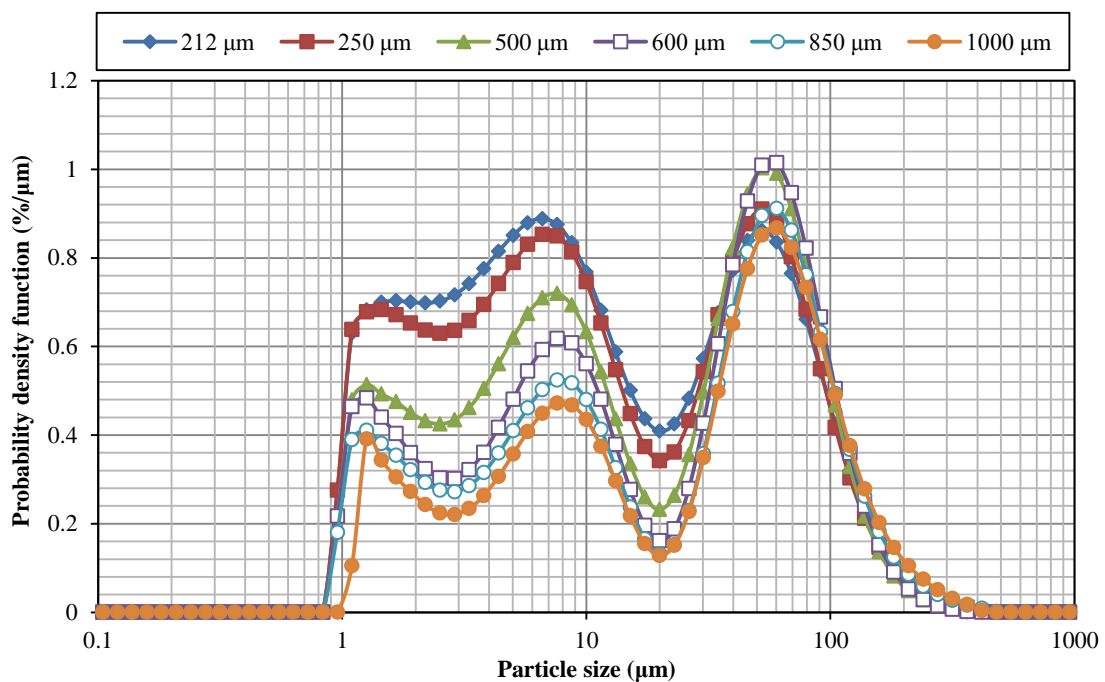


Figure 6-2. Particle size distribution for different near-mesh particle sizes at 300 kPa nozzle pressure

The size distribution of broken particles at 300 kPa is bimodal, with the first mode showing the size of the clusters as most particles are disintegrated into crystal clusters forming the particles. It can be clearly seen that for a given nozzle pressure, the small particles break to the higher extent than large particles, and produce more debris.

As previously mentioned, the impact velocities of the particles at various nozzle pressures were calculated by CFD simulation by Ali et al. (2015), who reported the impact velocities of spray-dried burkeite particles in the Scirocco disperser when different nozzle pressures were applied. The first impact in the elbow of the Scirocco disperser has been considered, for which the velocity is the highest, responsible for breakage. The impact velocity as a function of nozzle pressure for different particle sizes is shown in Figure 6-3.

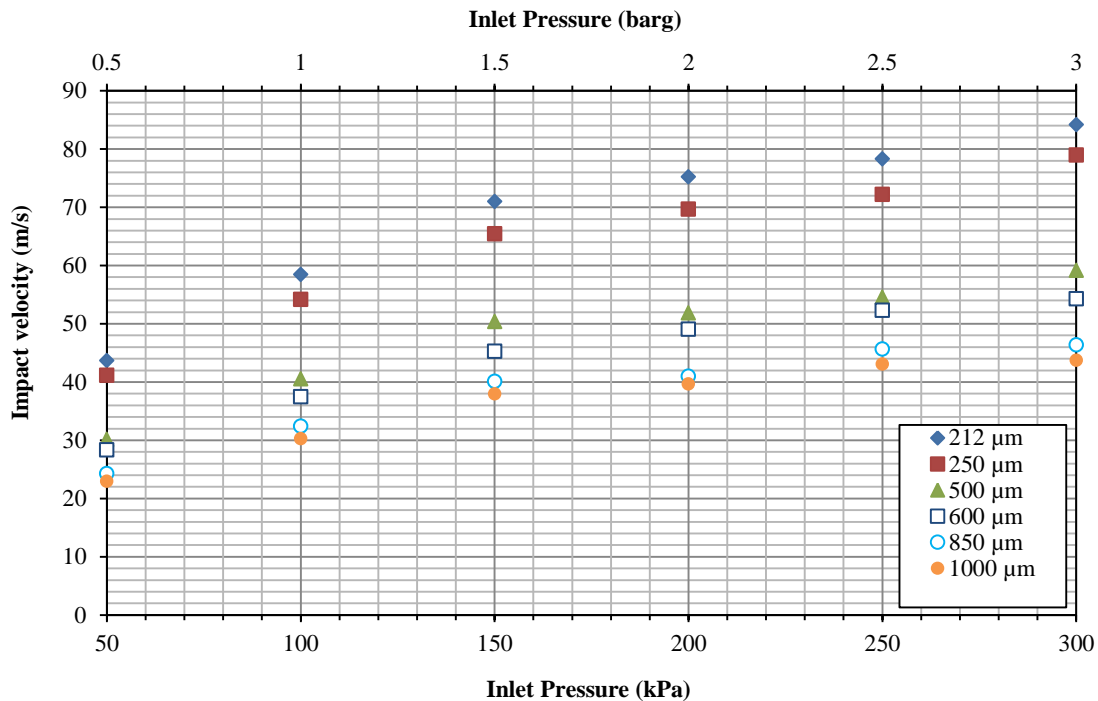


Figure 6-3. Impact velocity of burkeite particles as a function of nozzle pressure for density of  $1200 \text{ kg/m}^3$

(Ali et al., 2015)

As expected, by increasing the inlet pressure the impact velocity of the particles at the L-bend also increases. The simulation results show that for a constant nozzle pressure, smaller particles have higher impact velocities compared to the larger particles. The results shown in Figure 6-3 have been calculated based on the same envelope density

for all the particle sizes. However, it was previously shown that there was a variation in the envelope density of the particles as a function of size. Therefore the impact velocities used for breakage analysis are calculated based on the envelope density of each near-mesh size particle using CFD simulation by Ali et al. (2015).

The specific surface area, SSA, of the feed particles as well as that of the broken particles are derived from the PSD and envelope density of the particles, given by Mastersizer 2000. The values as a function of nozzle pressure are given in Table 6-2.

The  $SSA_0$  was measured by Spraytec.

**Table 6-2. The SSA of the feed particles ( $SSA_0$ ) and broken particles for different near-mesh particle sizes at different nozzle gauge pressures**

		SSA ( $m^2/kg$ )					
		212 ( $\mu m$ )	250 ( $\mu m$ )	500 ( $\mu m$ )	600 ( $\mu m$ )	850 ( $\mu m$ )	1000 ( $\mu m$ )
	Pressure (kPa)						
Spraytec	Feed	29.76	20.19	9.91	8.30	5.27	4.68
Malvern Mastersizer 2000	100	109.22	97.02	75.59	57.99	51.57	53.58
	150	138.31	114.88	85.35	74.08	60.37	61.21
	200	176.23	148.49	112.81	95.68	70.68	66.32
	250	197.31	157.28	128.35	109.55	94.13	83.57
	300	227.63	182.45	143.97	119.93	98.87	92.83

Based on the results reported in Table 6-2, as the nozzle pressure is increased, the SSA of the particles increases due to breaking.

The specific surface area of the particles reported by Malvern Mastersizer 2000 at different impact velocities is used to calculate the shift in the specific surface area,  $\Delta SSA$ . This is normalised with respect to the initial specific surface area,  $SSA_0$  (relative

shift) and plotted as a function of impact velocity for the spray-dried burkeite particles as shown in Figure 6-4.

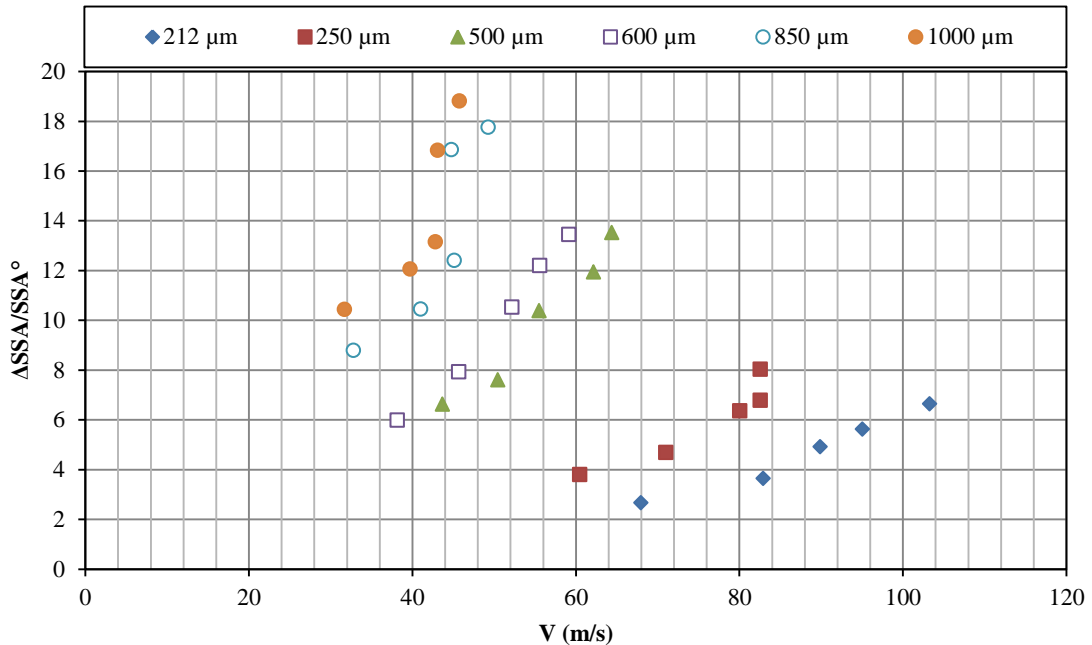


**Figure 6-4. Relative shift in the specific surface area of burkeite as a function of impact velocity in Scirocco disperser**

A family of curves is observed for spray-dried burkeite particles with clear trends for the effect of impact velocity and particle size. At a constant impact velocity, the larger particle sizes tend to break more than the smaller ones.

As has been fully described in the previous chapter, it is assumed that the test material used here fails through the semi-brittle failure mode. Therefore, the same model is used as the one for analysis of single particle impact breakage results. The equation below is the model of Ghadiri and Zhang (2002) as given in Eq. (2-7), modified by adding subscripts to  $d$  and  $\rho$ , which refer to feed material.

$$R^* = \alpha\eta = \alpha \frac{\rho_f d_{f,v} H}{K_c^2} V^2 = C \rho_f d_{f,v} V^2 \quad \text{Eq. (6-1)}$$

where  $d_{f,v}$  is a measure of feed particle size (on a volumetric basis),  $\rho_f$  is the envelope density of feed particles.

$R^*$  is expressed on a gravimetric basis, but using Malvern Mastersizer 2000, the particle size distribution is characterised by laser diffraction and expressed on a volumetric basis. So it is necessary to relate the shift in particle size distribution to  $R^*$ . As the breakage process could produce a wide size distribution, it is more convenient to express  $R^*$  in terms of the relative change in the specific surface area. Considering the definition of  $R^*$ , the mass fraction of debris can be expressed by Equation (6-2).

$$R^* = \alpha\eta = \frac{n_d \rho_d \left(\frac{\pi}{6} \bar{d}_{d,v}^3\right)}{n_f \rho_f \left(\frac{\pi}{6} \bar{d}_{f,v}^3\right)} \quad \text{Eq. (6-2)}$$

where  $\rho_f$  and  $\rho_d$  are the density of feed particles and debris, respectively.  $n_f$  and  $n_d$  are the number of feed particles and debris, respectively.  $\bar{d}_{f,v}$  is the average size (volumetric basis) of the feed material, and  $\bar{d}_{d,v}$  is average size of the debris, which is calculated based on the particle size distribution after Scirocco testing, as qualitatively shown in Figure 6-5 and described below. The size distribution of the debris is obtained from the shaded area, from which the volume-weighted arithmetic mean size,  $\bar{d}_{d,v}$ , and the relative shift in the specific surface area ( $\Delta SSA / SSA_0$ ) are calculated.

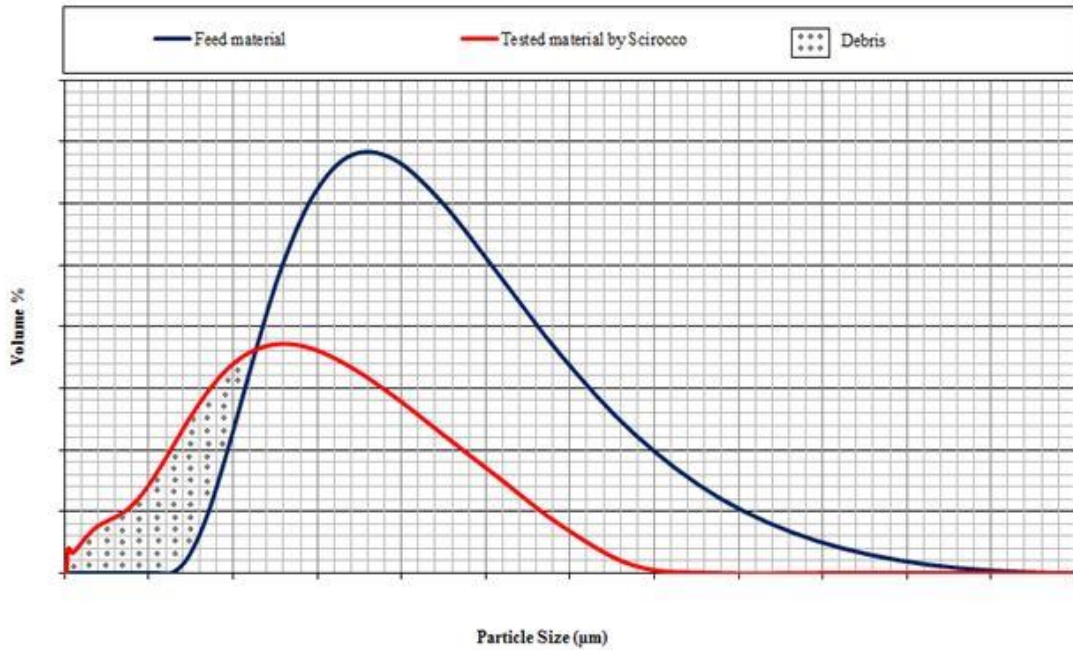


Figure 6-5. Calculation of debris size distribution based on the distribution of feed and broken materials

Conversion of Eq. (6-2) to the surface area basis requires  $\bar{d}_{f,v}$  and  $\bar{d}_{d,v}$  to be expressed in terms of the surface-area equivalent diameters. This can be done by the use of sphericity shape factor,  $\psi$ , defined as the ratio of the surface area of the volume-equivalent sphere ( $\pi d_v^2$ ) to the actual particle-surface area:  $n_d \pi \bar{d}_{d,v}^2 = \psi_d S_d$  and  $n_f \pi \bar{d}_{f,v}^2 = \psi_f S_f$ . Therefore:

$$\frac{\rho_d \bar{d}_{d,v}}{\rho_f \bar{d}_{f,v}} \times \frac{\psi_d S_d}{\psi_f S_f} = \alpha \eta \quad \text{Eq. (6-3)}$$

where  $S_d$  and  $S_f$  are the surface area of debris and feed material, respectively.  $\psi_d$  and  $\psi_f$  are the sphericity shape factor of debris and feed particles, respectively. The ratio  $S_d/S_f$  represents the relative shift in the surface area, i.e.

$$\frac{S_d}{S_f} = \frac{\Delta SSA}{SSA_0} \quad \text{Eq. (6-4)}$$

where  $\Delta SSA$  is specific surface area of debris and  $SSA_0$  is the specific surface area of the feed material. Therefore, by converting the extent of breakage (gravimetric basis) to the relative shift in the surface area:

$$\alpha \frac{\rho_f \bar{d}_{f,v} V^2 H}{K_c^2} \times \frac{\rho_f \bar{d}_{f,v}}{\rho_d \bar{d}_{d,v}} \times \frac{\psi_f}{\psi_d} = \frac{\Delta SSA}{SSA_0} \quad \text{Eq. (6-5)}$$

For simplicity, it is assumed that the feed materials and broken particles both have a similar shape factor. Therefore  $\frac{\psi_f}{\psi_d}$  is considered as unity, and Eq. (6-5) is converted to Equation 6-6 below

$$\alpha \eta \times \frac{\rho_f \bar{d}_{f,v}}{\rho_d \bar{d}_{d,v}} = \frac{\Delta SSA}{SSA_0} \quad \text{Eq. (6-6)}$$

The spray-dried burkeite particles are highly porous, due to the gap between the clusters. The debris and crystal clusters are formed as a matter of breakage. Therefore the envelope density of the debris is higher than that of spray-dried particles. The envelope density of the debris,  $\rho_d$ , has been estimated by extrapolation of the data using the measured density of different particle sizes by XRT and the average size of the debris. The results of the surface area ratio, as measured by laser diffraction in Mastersizer 2000, are now plotted as a function of  $\alpha \eta \left( \frac{\rho_f \bar{d}_{f,v}}{\rho_d \bar{d}_{d,v}} \right)$  in Figure 6-6 for the chipping regime.

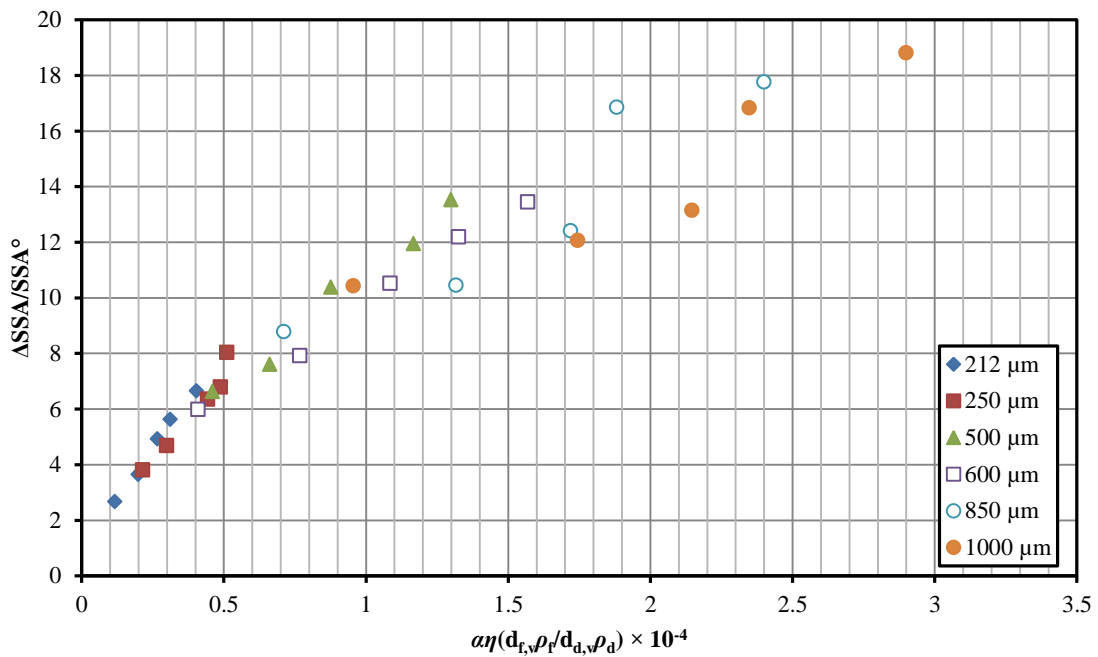


Figure 6-6. Relative change in the specific surface area as a function of  $\alpha\eta\left(\frac{\rho_f \bar{d}_{f,v}}{\rho_d \bar{d}_{d,v}}\right)$

By characterising the breakage propensity of the particles by single particle impact testing and evaluating their impact velocity by CFD, it is found that a remarkable unification of breakage data is obtained when the relative change in the surface area for different particle sizes is expressed as a function of the dimensionless group representing the breakage propensity,  $\eta$ , based on the impact velocity in the Scirocco. However, it remains to be seen how universal this approach can be by applying it to a wide range of materials. If successful, it actually provides a very simple but powerful way to analyse the impact breakage propensity and, hence, grindability of particulate solids. This is addressed in the following section.

### 6.3 Grindability Assessment

In the continuation of the above work, three crystalline organic solids (non-porous) were chosen to assess the Scirocco disperser as a grindability test method. The advantage of using this device is that it is widely available, and dispersed particles are presented to the laser light immediately for particle size measurement and analysis, hence reducing the time and effort required for measuring the size distribution of the impacted particles.

For this purpose, crystals of aspirin, sucrose and  $\alpha$ -lactose monohydrate ( $\alpha$ -LM) were used as model test materials in view of their relevance to the pharmaceutical industry. In fact the interest in this work emanated from a pharmaceutical company that wished to adopt the above approach for grindability testing. So the experimental work of dispersion and sieving was carried out by the pharmaceutical company and the analysis presented below was carried out by the author. The same approach used for the spray-dried burkeite particles is applied here. The narrow size distribution of the test particles was prepared using a combination of British Standard and DIN sieve sizes: 80-90  $\mu\text{m}$ , 112-125  $\mu\text{m}$ , 160-180  $\mu\text{m}$  and 224-250  $\mu\text{m}$  for  $\alpha$ -lactose monohydrate, 160-180  $\mu\text{m}$ , 224-250  $\mu\text{m}$ , 400-425  $\mu\text{m}$  and 600-630  $\mu\text{m}$  for sucrose, and 224-250  $\mu\text{m}$ , 400-425  $\mu\text{m}$  and 600-630  $\mu\text{m}$  for aspirin. Each sieve fraction was then fed into the Scirocco disperser at a rate meeting the minimum obscuration requirement for particle size analysis by laser diffraction. The experiments were carried out at eight different nozzle pressures, i.e. 50, 100, 150, 200, 250, 300, 350 and 400 kPa (corresponding to 0.5, 1, 1.5, 2, 2.5, 3, 3.5 and 4 barg).

Using a very small mass quantity is one of the advantages of using the Scirocco disperser to evaluate the grindability of the particles, as the sample availability could be a critical issue (i.e. 1-2 g depending on the particle size). The particle size distribution after impact was measured using the Mastersizer 2000 and the specific surface area (SSA) of the particles was calculated using the surface mean diameter,  $d_{3,2}$ . However, when fine and coarse particles are present in the dispersion, the Malvern Mastersizer 2000 system sometimes is not able to report the right size distribution, as will be shown below. This issue was with Malvern Instruments. Therefore a small correction was applied to a small number of the size distribution curves as described below and shown in Figure 6-7. The size distribution curve at the 0.1 barg (feed materials) has been taken as reference PSD. The rest of the distribution curves for higher nozzle pressures were then compared to the curve with the next lower pressure. For example, the data of dispersing feed particles with the size of 160-180  $\mu\text{m}$  of sucrose have been checked using the above approach. The curve corresponding to 0.1 barg shows the size distribution of the feed particles. The next dispersion pressure is 0.5 barg. The size distribution curves for both 0.1 and 0.5 barg are shown in Figure 6-7. It is expected that the particles going through the Scirocco disperser at 0.5 barg are smaller than the feed particles or at most the same size (if they do not break). However, the size distribution curve at 0.5 barg shows a slightly larger volume fraction for particles in its tail end compared to feed particles. This problem might happen for the particle types which are aggregated, but it is not the case here. Therefore the data corresponding to 0.5 barg nozzle pressure have been corrected by changing the volume percentage of the particles in each bin class if needed. For this purpose, the volume percentage of 0.5 barg data in each top bin size moving down from the upper end is compared to that of 0.1 barg. If it

has a larger value compared to the feed size, the value is reduced to a lower value. Careful attention is needed, as by changing the data in each size class the data of other size classes are also changed. This procedure was then continued up to the mode size data point until the overlap disappearing. However, the issue after each correction is that the summation of the volume percentages is not 100 anymore. Therefore the data are re-scaled and plotted (as shown in the re-scale graph of Figure 6-7) to meet this condition. In the case of Figure 6-7, only these size classes needed to be corrected, and for other cases a similar number prevailed. The new  $d_{3,2}$  was then calculated based on re-scaled data, and was used to determine the SSA of the particles. As mentioned before, the above problem is observed for a small number of the results of sucrose and  $\alpha$ -lactose monohydrate, where the extent of breakage was so small that the PSD consisted mainly of the mother particles and some dust.

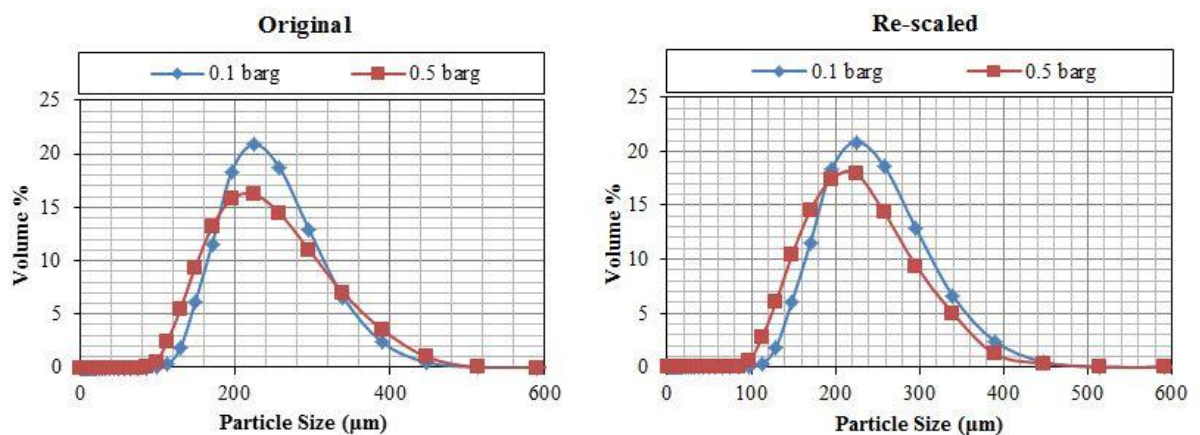


Figure 6-7. Correction of size distribution data for some of the reported results, e.g. 160-180  $\mu\text{m}$  feed size of sucrose

In the next step after calculating the corrected value of SSA for different particle sizes, the relative change in the specific surface area due to particle breakage needs to be

calculated, for which the specific surface area of the feed ( $SSA_o$ ) is required. These crystalline materials are stronger than the spray-dried burkeite particles, therefore the  $SSA_o$  was taken to be the SSA obtained at the lowest possible pressure applied to the nozzle for each sieve fraction, which is 10 kPa (0.1 barg), thus assuming that no breakage took place at this pressure.

The particle size distributions of aspirin, sucrose and  $\alpha$ -lactose monohydrate particles for the feed size of 224-250  $\mu\text{m}$ , having passed through the Scirocco at different nozzle pressures, are shown in Figures 6-8 to 6-10 as typical examples. The rest of the data for all sieve fractions are shown in the Appendix A.

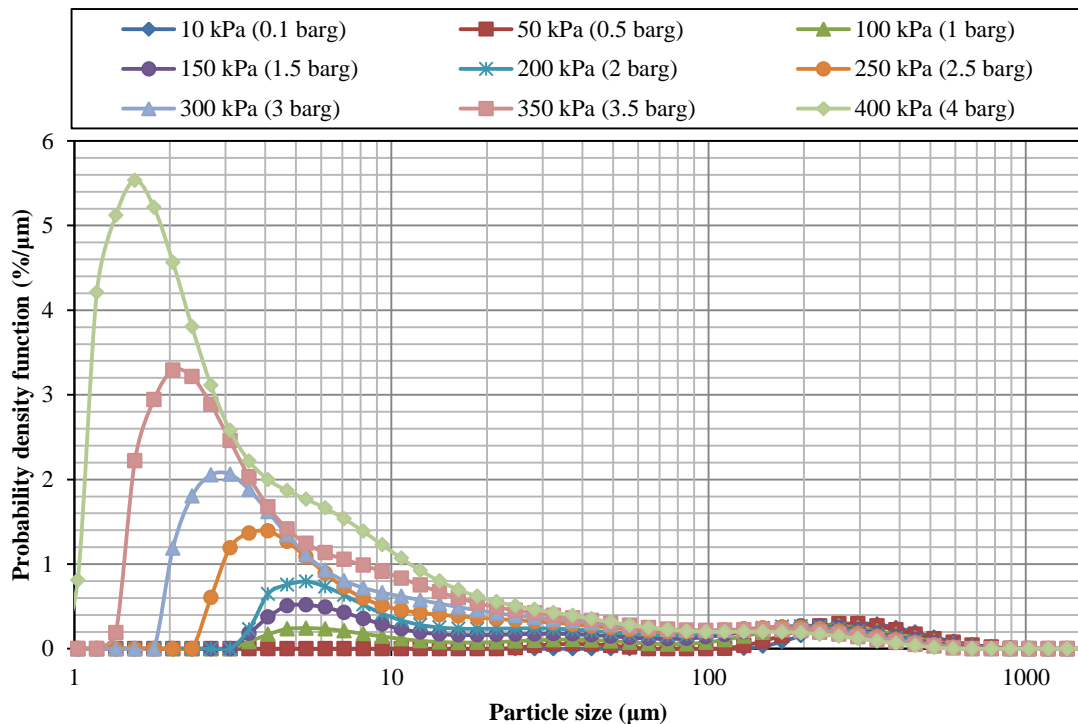


Figure 6-8. Relative shift in size distribution of 224-250  $\mu\text{m}$  of aspirin at different nozzle pressures

The data for 50 kPa (0.5 barg) almost overlap with 10 kPa (0.1 barg), without much breakage. The formation of debris first appears at 100 kPa (1 barg), which leads to a bimodal particle size distribution. As the nozzle pressure increases, the average size of debris decreases. The higher air pressures give rise to larger impact velocities in the Scirocco disperser, shifting the particle size distributions to the left.

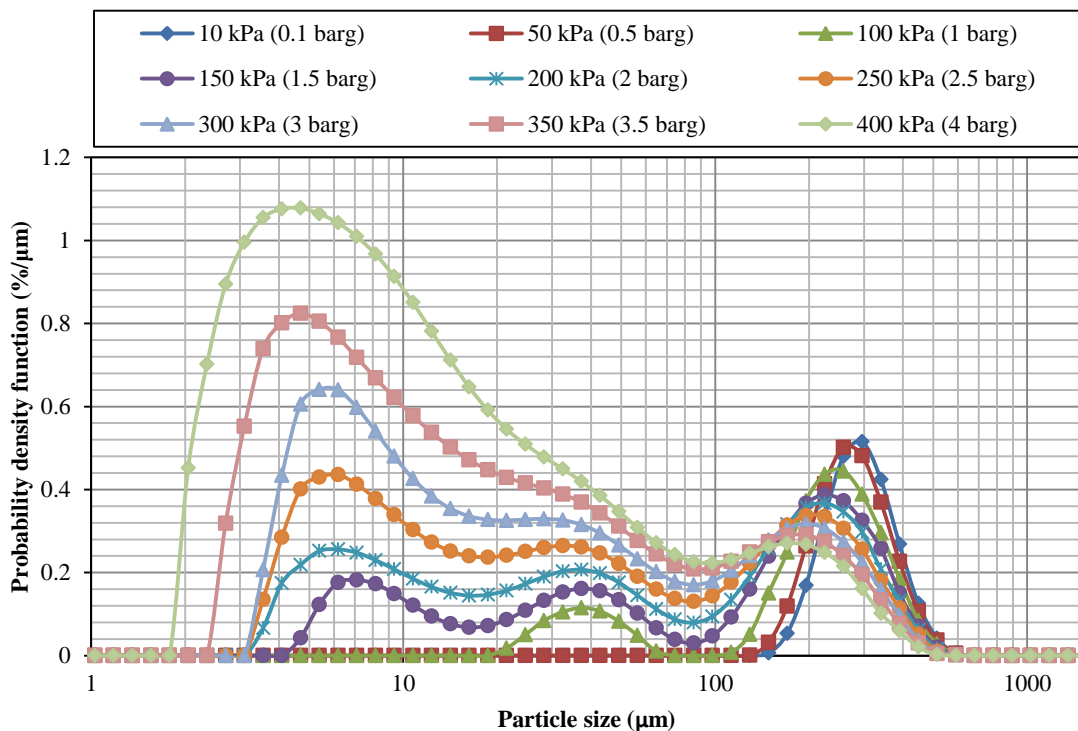


Figure 6-9. Relative shift in size distribution of 224-250  $\mu\text{m}$  of sucrose at different nozzle pressures

Despite the particles having a narrow size distribution, laser diffraction gives a relatively large span, e.g. referring to the case of sucrose in Figure 6-9, a range from nearly 150-550  $\mu\text{m}$  is obtained for the size 224-250  $\mu\text{m}$  (see 0.1 barg). For sucrose, 50 kPa (0.5 barg) gives some fragments with a slight shift to smaller sizes compared to 10 kPa (0.1 barg). The formation of debris is observed at 100 kPa (1 barg). Increasing the nozzle pressure then leads to a shift in particle size distribution to the left. The average

diameter of debris produced during the tests decreases as the nozzle pressure increases. Comparing Figures 6-8 and 6-9 shows that for the same nozzle pressure and feed size of materials, aspirin particles tend to break more than sucrose particles.

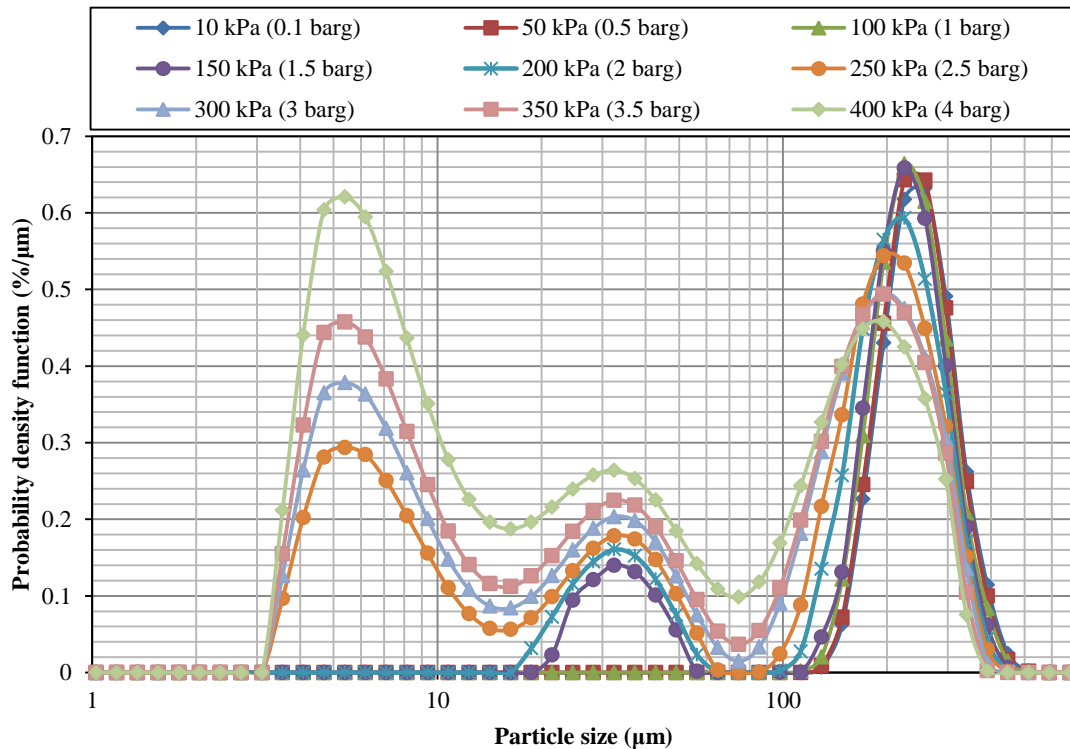
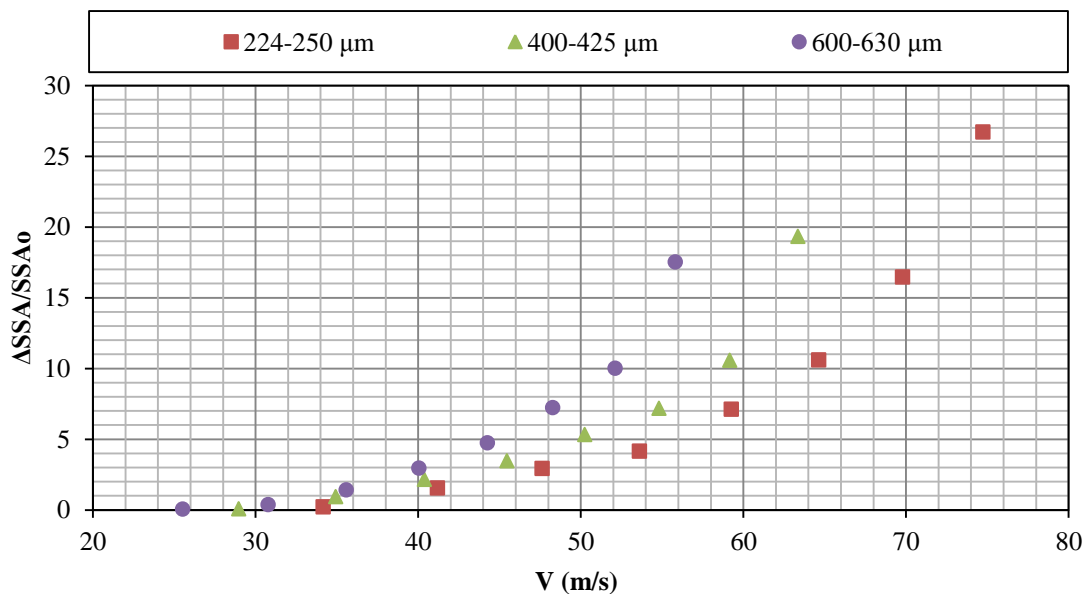


Figure 6-10. Relative shift in size distribution of 224-250  $\mu\text{m}$  of  $\alpha$ -lactose monohydrate at different nozzle pressures

For lactose, 50 kPa (0.5 barg) almost overlaps with 10 kPa (0.1 barg), i.e. almost no breakage. A slight shift in particle size distribution to the left and formation of fragments are observed for 100 kPa (1 barg). The formation of debris occurs at higher pressures (150 kPa), compared to the two other test materials. More debris with smaller sizes is produced when the nozzle pressure is increased. Comparison of Figures 6-8 to 6-10 shows that, at a constant nozzle pressure, aspirin breaks more than sucrose, and sucrose breaks more than lactose for a given particle size.

The same approach has been used here to calculate the impact velocity of the particles in the elbow. The specific surface area of the particles reported by the Malvern Mastersizer 2000 at different impact velocities is used to calculate the shift in the specific surface area,  $\Delta SSA$ , and the relative shift in the specific surface area of the particles is plotted as a function of impact velocity for the test materials, as shown in Figures 6-11 to 6-13.



**Figure 6-11. Relative shift in the specific surface area of aspirin as a function of impact velocity in Scirocco disperser**

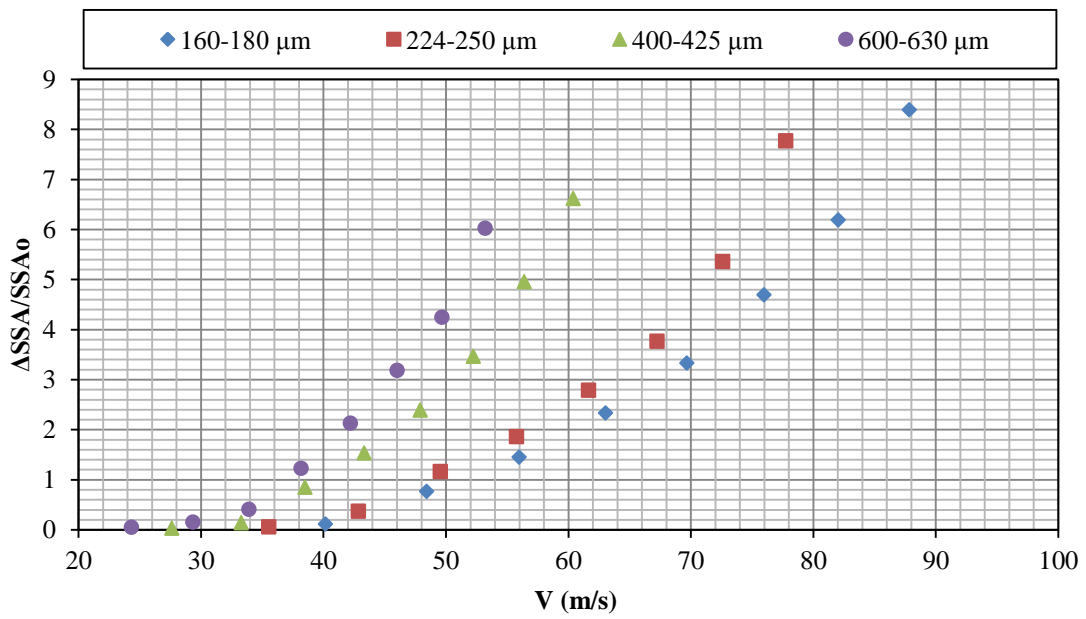


Figure 6-12. Relative shift in the specific surface area of sucrose as a function of impact velocity in Scirocco disperser

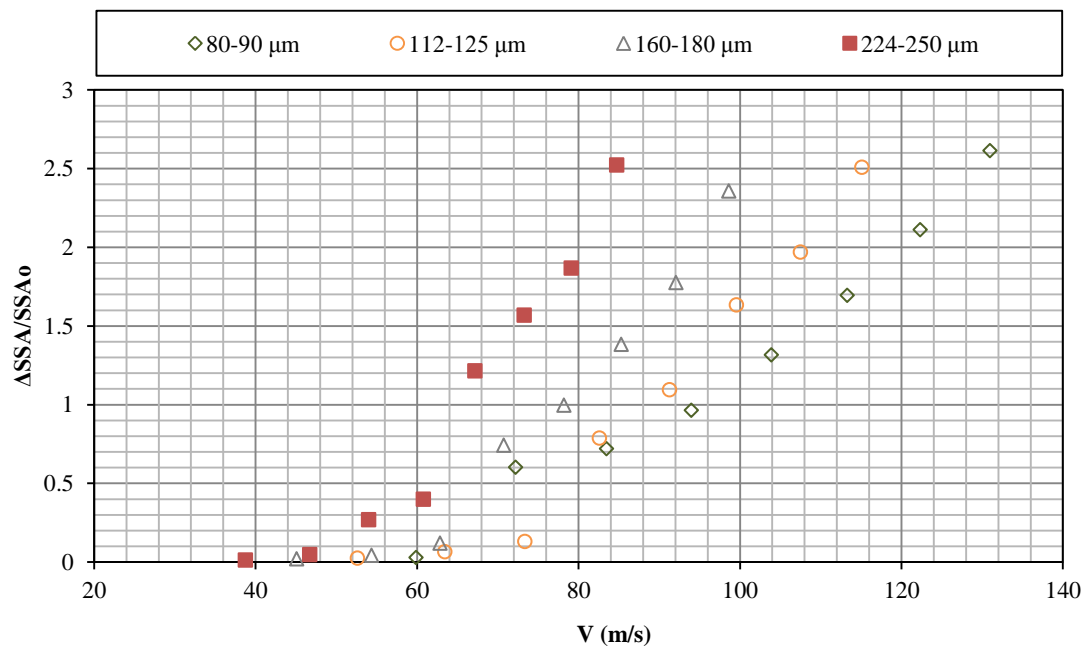


Figure 6-13. Relative shift in the specific surface area of α-lactose monohydrate as a function of impact velocity in Scirocco disperser

Similar to spray-dried burkeite, a family of curves is observed for all the test materials with clear trends for the effect of impact velocity and particle size. At a constant impact velocity, the larger particle sizes have a larger relative shift of the specific surface area, which in fact shows that they break more than the smaller particles.

The analysis of breakage results has been carried out using Eq. (6-5). The characterisation of the ratio of sphericity of feed material to debris requires extensive work and it has not been attempted here. In the first instance this is considered as a constant. Hence Eq. (6-5) can be presented as below:

$$\beta \frac{\rho_f \bar{d}_{f,v} V^2 H}{K_c^2} \times \frac{\rho_f \bar{d}_{f,v}}{\rho_d \bar{d}_{d,v}} = \frac{\Delta SSA}{SSA^0} \quad \text{Eq. (6-7)}$$

where  $\beta$  is a new proportionality factor corresponding to  $\alpha \frac{\psi_f}{\psi_d}$ .

The relative shift in the specific surface area can now be plotted as a function of  $\rho_f \bar{d}_{f,v} V^2 \left( \frac{\rho_f \bar{d}_{f,v}}{\rho_d \bar{d}_{d,v}} \right)$  for all the three test materials, as shown in Figure 6-14. For crystalline solids, the envelope density is not expected to change as particles undergo size reduction, so  $\rho_d = \rho_f$ . This was not the case for spray-dried burkeite particles.

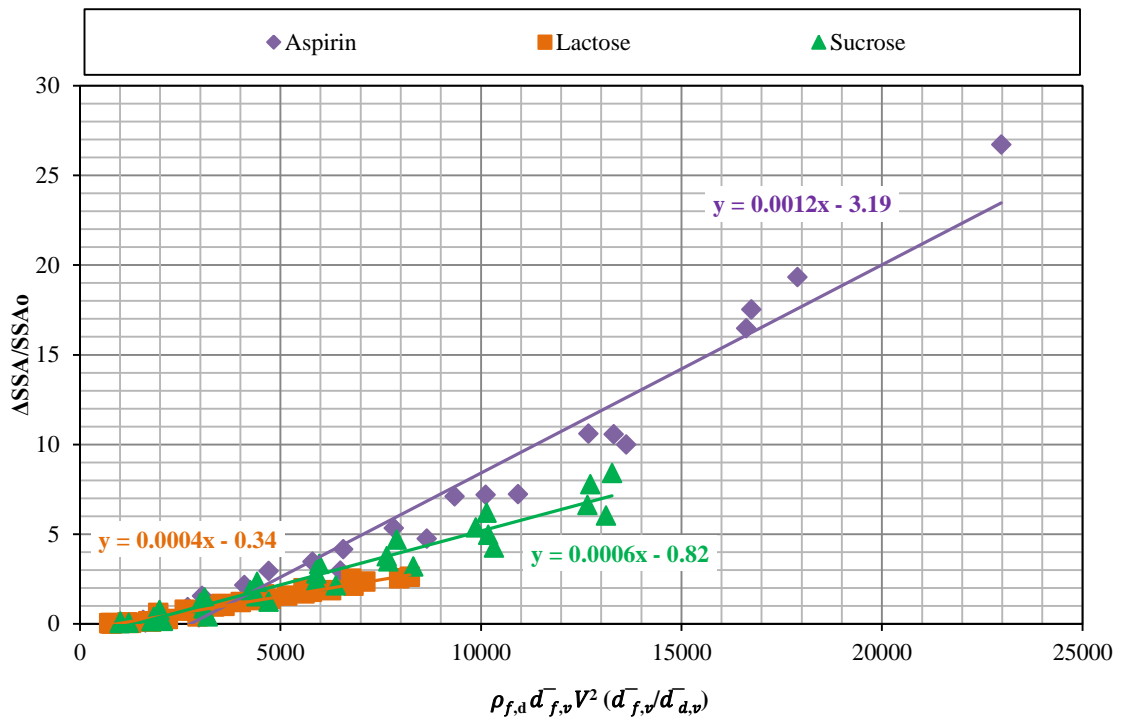


Figure 6-14. Shift in the specific surface area of aspirin, sucrose and lactose particles as a function of  $\rho_{f,d} \bar{d}_{f,v} V^2 (\bar{d}_{f,v} / \bar{d}_{d,v})$

For each test material a good unification of breakage data is obtained for the particle sizes and inlet nozzle pressures tested. Moreover, the slope of the lines,  $\beta H/K_c^2$ , reflects the ease with which the particles break in the Scirocco disperser, and is thus expected to correlate with similar data obtained by the single particle impact breakage method, provided interparticle interaction in the Scirocco disperser does not affect the rate of breakage. Furthermore, the intercept of each line gives the impact velocity for a given particle size below which the particles would not break. This provides a design rule for mitigating particle breakage in pneumatic conveying lines.

### 6.3.1 Single Particle Impact Breakage Parameter

Experiments have been carried out by various research workers in the past in which  $\alpha H/K_c^2$ , the breakability index of Eq. (2-6) has been determined from the slope of the line of  $R^*$  as a function of  $\rho_f \bar{d}_{f,v} V^2$  (Ali *et al.*, 2015). The material mechanical properties of aspirin, sucrose and  $\alpha$ -lactose monohydrate have been obtained using the same approach. The most recent analysis is summarised in Table 6-3.

**Table 6-3. Material properties of aspirin, sucrose and  $\alpha$ -lactose monohydrate**

Material	Density (kg/m <sup>3</sup> )	$\alpha H/K_c^2$
Aspirin	1397	0.050
Sucrose	1587	0.026
$\alpha$ -LM	1520	0.017

The slopes of the two lines of particle breakage obtained by Scirocco testing and from single particle impact testing, as given in Figure 6-14 and Table 6-1, should be correlated as they both reflect the impact damage. The larger they are, the easier the particles break. Therefore, the ratio of the slopes for the same set of materials should be comparable. This is shown in Table 6-4.

Table 6-4. The ratio of slopes for each two materials

Material	Ratio of slopes from single particle impact testing	Ratio of slopes from Scirocco testing
<i>Aspirin/Sucrose</i>	1.9	2.0
<i>Sucrose/Lactose</i>	1.5	1.5
<i>Aspirin/Lactose</i>	2.9	3.0

As the comparison shows, a very good match is observed between the ratio of mechanical properties obtained by the Scirocco disperser and by the single particle impact tester. The ratios show the relative ease of breakability of one material compared to another. For instance, the ratio of the slopes for sucrose to  $\alpha$ -lactose monohydrate is 1.5, which shows that sucrose breaks 1.5 times easier than  $\alpha$ -lactose monohydrate. This information can be used to evaluate the grindability of different materials. Considering that the mass required to be tested in the Scirocco is very low, the method is attractive for cases where the sample supply is scarce, e.g. new active pharmaceutical ingredients in the pharmaceutical industry.

## 6.4 Concluding Remarks

Particles of different sizes accelerate to different velocities in the Scirocco disperser and break to different extents. For spray-dried burkeite particles, even the lowest nozzle pressure causes notable particle breakage. By characterising the breakage propensity by single particle impact testing and evaluating the impact velocity by CFD, it is found that a remarkable unification of breakage data may be obtained when the relative change in the surface area for different particle sizes is expressed as a function of the dimensionless group representing the breakage propensity,  $\eta$ , based on the impact velocity in the Scirocco, obtained from the CFD simulations.

Considering that the mass required to be tested in the Scirocco is very low, the method is attractive for cases where the sample supply is scarce, e.g. new active pharmaceutical ingredients in pharmaceutical industry. Therefore an attempt was made using three crystalline structures (aspirin, sucrose and  $\alpha$ -lactose monohydrate) to explore how universal this approach can be, and to evaluate the suitability of the Scirocco disperser as a grindability test device. The impact velocities of three test materials, i.e. aspirin, sucrose and  $\alpha$ -lactose monohydrate, for a range of particle sizes have been calculated for eight nozzle pressures. The impact velocity of particles increases almost linearly initially with increasing the nozzle pressure, but the rate of increase slows down at high pressures.

The relative increase in the specific surface area of the particles with respect to the initial value following impact in the Scirocco disperser shows a linear dependence on  $\rho_f \bar{d}_{f,v} V^2 \left( \frac{\rho_f \bar{d}_{f,v}}{\rho_d \bar{d}_{d,v}} \right)$ . The slope of the fitted line reflects particle breakage propensity and



correlates well with  $\alpha H/K_c^2$  obtained by single particle impact testing. Therefore, this method can be used to evaluate the grindability of powders and grains, provided the particle impact velocity is first determined.

## CHAPTER 7 SIMULATION

The characterisation of internal stresses in the case of complex structures, such as spray-dried burkeite particles, is not possible by experimental methods. In contrast, the numerical simulations by Distinct Element Method provide a basis for sensitivity analysis of factors affecting the strength and failure of agglomerates.

In this chapter, DEM simulation is used to study the impact breakage of agglomerates and influential parameters on the agglomerate impact strength. DEM simulation has been found as a fairly fast method to provide a better understanding of the factors affecting the agglomerate breakage. Simulations have been carried out using EDEM software (DEM Solutions, Edinburgh, UK). The agglomerates with different structures are formed using interparticle bonding based on the JKR model, and impacted under various impact conditions.

### 7.1 Introduction

Agglomerates may be formed in various ways and their mechanical strength depends on many factors due to the degree of freedom afforded by the primary particle properties and their interactions. Weak agglomerates formed for example by spray-drying are prone to attrition, which has adverse effects on product quality, ability to process, dust formation and explosion hazards. Therefore it is highly desirable to develop a predictive ability for agglomerate breakage.

Agglomerate structure has a strong influence on its strength (Subero and Ghadiri, 2001). The failure of the agglomerates under quasi-static and impact behaviour can be

completely different, and for the latter the effects of impact velocity and impact angle have not been fully understood yet. For some structures, the strength mainly depends on the normal component of the impact velocity, and for some others it also depends on the tangential component. However, the factors making the differences are not clearly known yet.

The use of the Distinct Element Method (DEM) has become very common recently, as it provides a better understanding of the effects of different parameters on the impact strength of the agglomerates. Depending on the type of contact model used for bonding of the primary particles in the agglomerate, the strength of the bond or the contact forces might influence the agglomerate strength. In this work DEM simulation is used to analyse the effect of agglomerate structure on the impact strength of agglomerates. The agglomerates are made using elastic spheres bonded together using the Johnson-Kendall-Roberts (JKR) model (Johnson et al., 1971). The particles with two different structures (levels of porosity) are impacted on different targets (with different impact angles) and at different impact velocities. The level of contact adhesive force is then changed to explore the effect of surface energy on impact strength of the agglomerates. This enables the underlying causes of variations in the impact angle and velocity to be clarified.

## **7.2 Generation of Agglomerates**

In this section, different steps of agglomerate preparation are described. Details of the contact models, various parameters and material properties used in the simulation are given. The impact breakage analysis methods are also described.

### 7.2.1 Simulations of Agglomerates

At the beginning of the simulation work,  $PFC^{3D}$  software (Itasca Consulting Group, USA) was used to generate the agglomerates. However, it turned out to be very slow for the number of particles used in the simulation, as the time-step which can be used in  $PFC^{3D}$  is very small and increasing the time step would result in the software crashing. Therefore the simulations were switched to and carried out using EDEM, which is much faster than  $PFC^{3D}$ . The main advantage of using  $PFC^{3D}$  over EDEM is ease of control at the particle removing stage, whilst this becomes more complicated in EDEM software. However, EDEM is more user friendly compared to  $PFC^{3D}$ , because of its Graphical User Interface (GUI).

### 7.2.2 Time-Step Integration

In a particulate system, there are a number of particles, which displace independently from one another and interact only at contact points. Movement of a particle in the system is affected by different parameters such as forces and torques originated from contacts with its immediate neighboring particles. However, disturbance propagation from particles far away from a specific particle can also affect its movement. In order to avoid this effect in DEM, the particle displacement is calculated after a very short time-step. The time-step is chosen in a way that the disturbance is not propagated from each particle farther than its immediate neighbouring particles (Cundall and Strack, 1979).

The speed of the disturbance wave is estimated using Rayleigh surface wave propagation, which uses physical properties of the particles. In order to prevent numerical instability and ensure realistic force transmission rates in an assembly, the

time chosen in the simulation must be smaller than the Rayleigh time,  $T_R$ , required for the stress wave to travel from the contact point to a point on the opposite side on the particle surface, which is described by Eq. (7-1),

$$T_R = \frac{\pi R (\frac{\rho}{G})^{1/2}}{0.1631\nu + 0.8766} \quad \text{Eq. (7-1)}$$

where  $R$  and  $\rho$  are the radius and density of the particle,  $G$  is the shear modulus, and  $\nu$  is Poisson's ratio of the particle.

A fraction of the Rayleigh time-step is usually used in the simulations. For dense systems with a coordination number above 4, a typical time-step of  $0.2T_R$  is used. For a lower coordination number, using  $0.4T_R$  is appropriate. The critical time-step for an assembly with various material type particles is chosen based on the smallest one among those determined for different material properties (Ning and Ghadiri, 2006). The time-step chosen in this work is based on  $0.2T_R$ .

### 7.2.3 Hertz Normal Contact Model

The Hertz model is one of the most common contact models used in DEM (Hertz, 1882) The normal contact force,  $F_n$ , between two perfectly elastic spheres in contact is calculated based on the equation below (Thornton and Ning, 1998; H.R. Hertz, 1882),

$$F_n = \frac{4}{3} E^* R^{*2} \delta^{\frac{3}{2}} \quad \text{Eq. (7-2)}$$

where  $\delta$  is the normal overlap,  $E^*$  and  $R^*$  are the reduced Young's modulus and reduced radius, and they are calculated based on equations 7-3 and 7-4, respectively.

$$E^* = \left( \frac{1-\nu_1^2}{E_1} + \frac{1-\nu_2^2}{E_2} \right) \quad \text{Eq. (7-3)}$$

where  $E_1$  and  $E_2$  are Young's moduli of the particles in contact, and  $\nu_1$  and  $\nu_2$  are Poisson's ratio of the particles in contact.

$$R^* = \left( \frac{1}{R_1} + \frac{1}{R_2} \right)^{-1} \quad \text{Eq. (7-4)}$$

where  $R_1$  and  $R_2$  are radii of the particles in contact.

#### 7.2.4 Hertz-Mindlin (no slip) Tangential Contact Model

Based on the theory of Mindlin and Deresiewicz (1953), the Hertz-Mindlin contact model has been developed which is a nonlinear contact formulation (Cundall, 1989). This is a tangential model for perfectly elastic contacts proposed by Mindlin (1949), which does not consider the existing hysteresis effects in Mindlin and Deresiewicz (1953), and neglects the effects of micro-slip (Mindlin, 1949). The Hertz-Mindlin (no slip) contact model is used here at the beginning part of the simulations. However, when it comes to apply the contact bonding model, the Hertz model is replaced by the JKR model, as described below.

### 7.3 JKR Elastic-Adhesion Normal Contact Model

The Johnson-Kendall-Roberts (JKR) model is used to apply a contact adhesive force between the particles. The level of the adhesion force is varied by changing the surface energy of the particles. In the JKR theory, it is assumed that the attractive forces operate within the contact area and they are zero outside this region. The JKR model gives a larger contact area compared to the Hertz model due to adhesion, and there is an

outer annular region, which experiences tensile stresses (Thornton and Yin, 1991). The schematic diagram of the force-overlap response of the JKR model is shown in Figure 7-1.

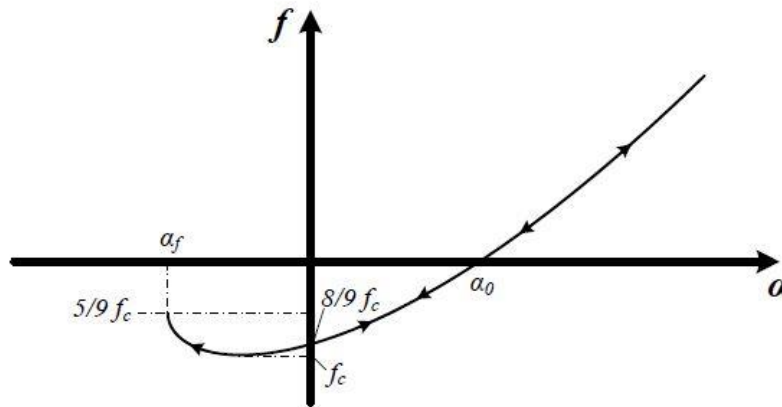


Figure 7-1. Schematic force-overlap response of JKR model (Pasha, 2013)

Considering that Hertz and JKR analyses are valid for low impact velocities, where the stress transmission time through the particle is much shorter than the impact time, the following case is applicable.

As the schematic shows, when two particles move towards each other and come into contact the force between them is reduced to  $8/9 f_c$  (Thornton and Ning, 1998), where  $f_c$  refers to the pull-off force (it will be described later on). This is due to van der Waals attractive forces. The particles velocities are then reduced to zero; by then the loading stage is complete and the contact force reaches a maximum value. During the velocity reduction step, part of the kinetic energy is radiated into the substrate as elastic waves. The next stage is the recovery stage, in which the spheres move in the opposite

directions. A part of the work used in the loading stage would be now recovered. The recovery stage is completed when the overlap,  $\alpha_f$ , becomes zero; at this stage the particles are still adhered. The contact breaks at a negative overlap and at this point the contact force is  $5/9 f_c$  (Ning, 1995).

The maximum tensile force experienced by the contact is called the pull-off force.

$$f_c = \frac{3}{2}\pi R^* \Gamma \quad \text{Eq. (7-5)}$$

where  $\Gamma$  is the interface energy.

### 7.3.1 Primary Particles

As a first attempt, the primary particles were generated in a factory with cubical (box) geometry with a length of 20 mm. Six different types of primary particles were defined. All types have the same material properties; however, they vary in size and number. One of the limitations of EDEM software is that the particles cannot be removed based on their ID number unless a custom code is used. However, there is a possibility of removing the particles based on particle type. This now explains the reason for generating the primary particles of the same material as different particle types based on their sizes. The details of size and number of generated particles are shown in Table 7-1.

**Table 7-1. Size and number of generated primary particles**

Particle type	A	B	C	D	E	F
Diameter of primary particle ( $\mu\text{m}$ )	150	200	250	300	350	400
Number of primary particles	700	700	800	1000	600	500

This work has been carried out to qualitatively study the effect of various parameters on impact strength of agglomerates. Therefore the material properties used for the simulations are not corresponding to spray-dried burkeite particles. The material properties used in the simulations are shown in Table 7-2 and 7-3. The shear modulus has been chosen to be small in order to speed up the simulation.

**Table 7-2. Material properties of primary particles used for the simulation**

Properties	Primary particles	Wall
Poisson's ratio	0.3	0.3
Shear modulus (GPa)	0.1	0.1
Density ( $\text{kg/m}^3$ )	2600	7800

Table 7-3. Particle-particle and particle-wall properties used in simulation

Properties	Particle - Particle	Particle - Wall
Coefficient of restitution	0.3	0.4
Coefficient of static friction	0.35	0.35
Coefficient of rolling friction	0.01	0.01

### 7.3.2 Forming an Agglomerate

After generating the primary particles, a centripetal force is applied in order to bring all the particles together and form an agglomerate. The applied force depends on the size of the particles, as well as their distance from the centre. The force is calculated according to Newton's second law of motion; hence a value is given to the acceleration. To start,  $10 \text{ m/s}^2$  is defined as the acceleration value. The higher the acceleration value, the faster the particles move towards the centre. The full code used for the body force contact model is shown in Appendix B (pages 221-223).

### 7.3.3 Relaxation Step

During the formation of agglomerates, there are some residual stresses in the agglomerate due to existing overlaps between some particles, which might contribute to a higher degree of failure when the particles are impacted. In order to minimise this effect, the residual stresses should be reduced as much as possible.

The relaxation step has been applied by gradually decreasing the acceleration used to calculate the forces. The contact number as a function of time is regularly monitored. When the contact number reaches a steady state level, the acceleration is reduced to  $9 \text{ m/s}^2$ , and the new body force is applied to the particles. This procedure is continued until the acceleration is at its lowest value, close to zero. At the last part of the relaxation step, the body force is fully removed to make sure no further change takes place in the structure, and the velocity of particles are set to zero. This part should not be run for so long, in order to avoid the agglomerate disintegration as there is no adhesion force applied yet, and the particles are kept together just because of the centripetal force. The formed agglomerate has a diameter of 4.6 mm. The unbalanced force at the end of the relaxation step is then compared to the initial value after agglomerate formation. The values are shown in Table 7-4.

**Table 7-4. Comparison of different parameters before and after relaxation step**

<b>Condition</b>	<b>Unbalanced force (N)</b>	<b>Number of contacts</b>
After agglomerate formation	$4 \times 10^{-4}$	10822
After relaxation step	$9 \times 10^{-7}$	10821

The comparison of the results shows that the unbalanced force within the system has been dropped by three orders of magnitude, while the number of contacts remained almost the same. The mentioned number of contacts would result in a coordination number of between 5-6 on average.

### 7.3.4 Adhesive Bonding Model

On the conclusion of the stress relaxation step, the agglomerate formation is not yet complete and a bonding model needs to be applied to keep the particles together. Various types of bonding model with different specifications are available to be used such as the Hertz-Mindlin with bonding (DEM-Solutions, 2015), the JKR model (Johnson et al., 1971) and the Timoshenko Beam Bond model (Brown et al., 2014). For the first set of simulations, it is decided to use the JKR model. The principles of JKR theory have been described earlier. The level of the adhesion force is dependent on the surface energy defined in the model. Different levels of surface energy are used to produce agglomerates with different strengths, to explore its effect on the impact strength of agglomerates. The relation between surface energy and interface energy is defined based on the equation below.

$$\Gamma = \gamma_1 + \gamma_2 - \gamma_{12} \quad \text{Eq. (7-6)}$$

where  $\gamma$  is the surface energy, and subscripts indices 1 and 2 refer to type of the particles.  $\gamma_{12}$  is an interaction term between both surfaces.

If the materials of the two particles are the same, then  $\gamma_1 = \gamma_2 = \gamma$ , and the term corresponding to the interaction between two surfaces would be gone, therefore,

$$\Gamma = 2\gamma \quad \text{Eq. (7-7)}$$

This surface energy is then used to calculate the cohesive interparticle forces, according to the JKR model, as was shown in Eq. (5). Four different values of 0.5, 1, 3 and 5  $J/m^2$  are used in this work. After applying the JKR model and surface energies, the

agglomerate formation is complete. A final agglomerate formed using this approach after around 5 s is shown in Figure 7-2. The colour map is based on the volume of the primary particles. As mentioned before, the primary particles have been generated with a size distribution, and hence different volumes. Therefore, the primary particles with the same colour in Figure 7-2 have the same sizes.

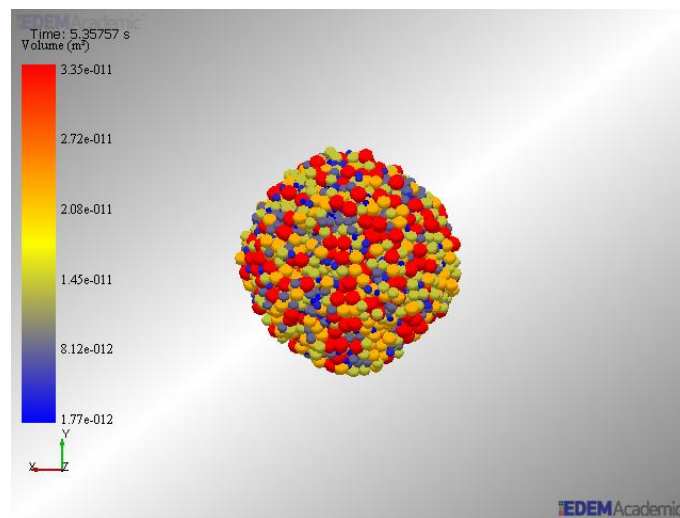


Figure 7-2. An agglomerate made by EDEM simulation

The formed agglomerate is referred to as the ‘reference agglomerate’ in this work, with a solid fraction of around 0.7.

### 7.3.5 Effect of Factory Geometry

As mentioned before, the primary particles are generated within a virtual space. By default, one of the three options can be used; box, cylinder and polygon. There is also the possibility to design other geometries and import them into the geometry options of EDEM. In order to explore the effect of factory geometry on the shape of the final simulated agglomerate, two different simulations were done under the same conditions.

The only different parameter is the shape of the geometry used to generate the primary particles. One of the simulations has been carried out using a box as geometry, and the other one spherical space. Interestingly, there is a slight difference in the shape of the final agglomerate generated between using the two different geometry types, although all the particles are brought to the centre under the same condition. The final simulated agglomerates under these two conditions are shown in Figure 7-3.

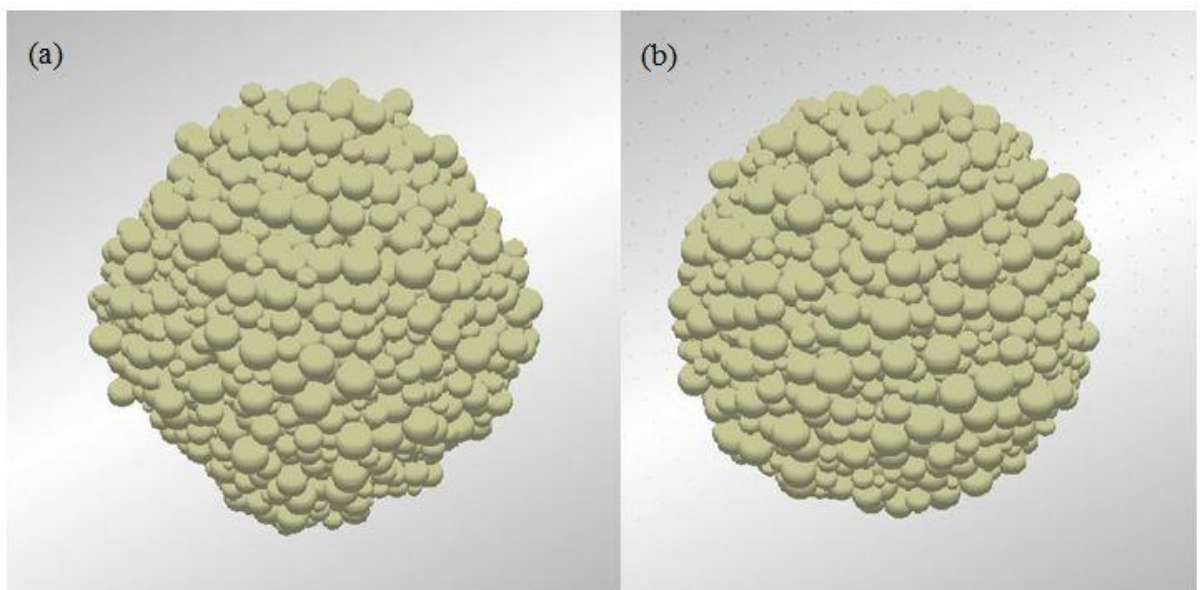


**Figure 7-3. Agglomerates made with primary particles generated using two different geometries; (a) box;  
(b) sphere**

A better-shaped spherical agglomerate is obtained using a spherical geometry, as shown in Figure 7-3b. However, the number of contacts for both agglomerates is exactly the same, which is 10822. The results reported in the next sections are based on the agglomerate shown in Figure 7-3a.

### **7.3.6 Effect of Factory Size**

There is no specific rule to choose the size of the geometry in which the primary particles are generated. However, a reasonable size of the geometry must be chosen based on the size and number of the primary particles. If the geometry is too small, the space would not be large enough for generation of all the primary particles. In the opposite case, if the geometry size is too large, it takes too long to bring all the particles towards the centre and form an agglomerate. In this work, the geometry used for primary particles generation is a 20 mm-diameter sphere.

## **7.4 Impact Strength of Agglomerates**

The impact breakage of simulated agglomerates is analysed under different conditions. The effects of impact velocity, interface energy, porosity and impact angle are studied in this section. The generated agglomerates with different levels of cohesive interparticle forces and different levels of porosity are impacted on both flat and inclined surfaces at different impact velocities (0.2, 0.5, 1, 5, 10 and 20 m/s) on a rigid target. The impact strength is then compared using the definition of damage ratio as described below.

### **7.4.1 Damage Ratio**

The concept of damage ratio has been used here to quantify the level of agglomerate breakage. This concept was proposed by Kafui and Thornton (1993) and Thornton et al. (1996) for the first time. The damage ratio is defined as the ratio of number of broken contacts during impact to the initial number of contacts.

It should be noted that one of the problems of using the JKR model in EDEM simulation is that after impacting the particles the cohesive force still exists. Therefore, there is a possibility of re-adhesion of broken bonds, which will clearly affect the obtained value for damage ratio. However, in order to minimise the effect of this issue in the reported results, the reported damage ratios in this work are calculated based on the data obtained after impact, and before any possible re-adhesion.

#### 7.4.2 Effect of Surface Energy on Agglomerate Impact Strength

As mentioned before, four different levels of surface energy are used to bond the contacts; 0.5, 1, 3 and 5  $J/m^2$ . The agglomerates are then impacted on a flat surface at six different impact velocities. The breakage ratio as a function of impact velocity for all the agglomerates is reported in Figure 7-4.

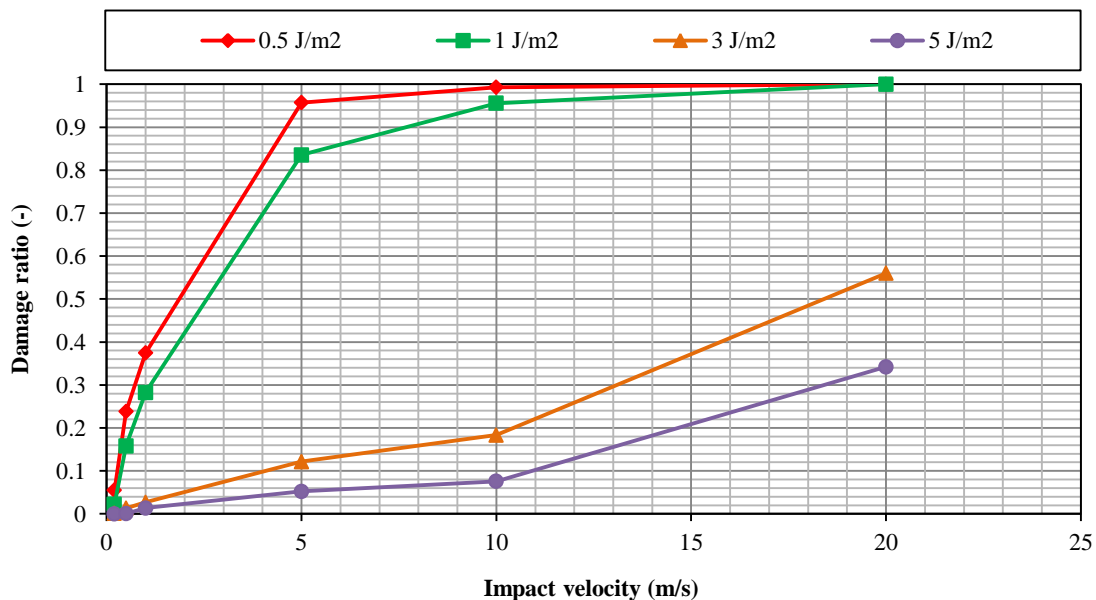


Figure 7-4. Damage ratio as a function of impact velocity for agglomerates with different cohesive interparticle forces

For a given surface energy, as the impact velocity is increased, the damage ratio increases. At a given impact velocity, the agglomerate with a lower surface energy breaks to a larger extent compared to the one with higher surface energy, which is as expected. However, two different trends are clearly observed, which are attributed to the pattern of breakage. Further analysis is presented in Section 7.6.

### 7.4.3 Effect of Impact Angle on Agglomerate Impact Strength

To explore the effect of impact angle on the extent of breakage, the agglomerates have been impacted at  $60^\circ$  and  $90^\circ$ . The impact angle is defined as the angle between agglomerate moving direction and the surface of the impact target, and is schematically shown in Figure 7-5.

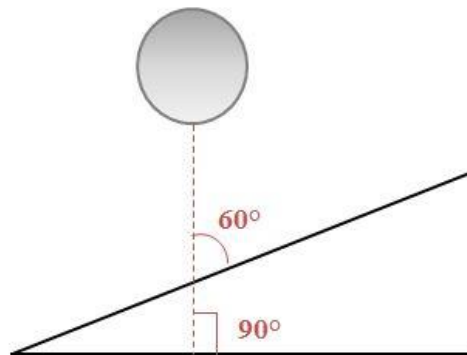
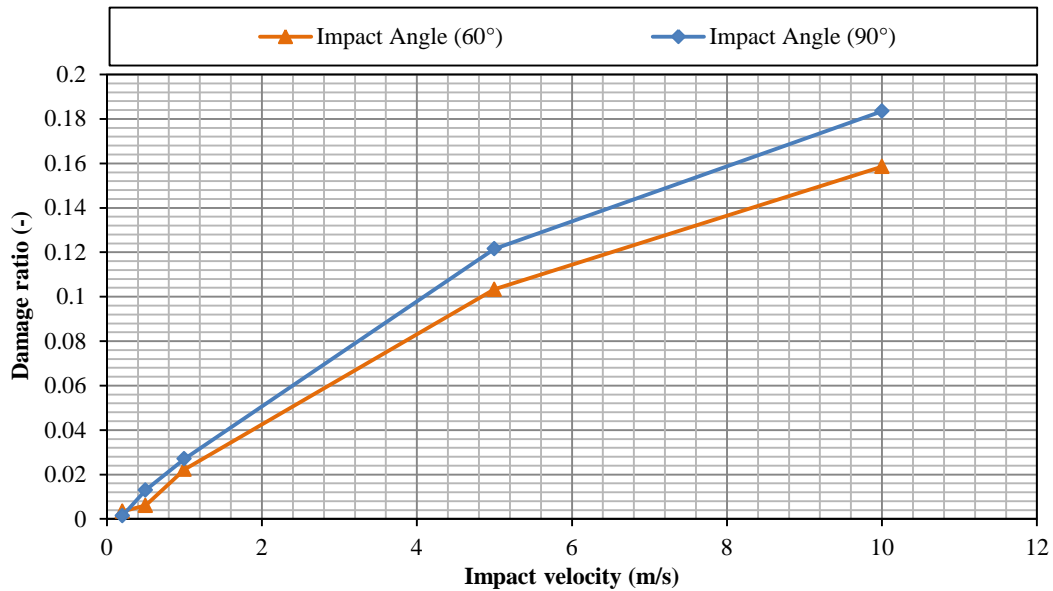


Figure 7-5. Schematic of different  
impact angles

As an example, the damage ratio as a function of impact velocity is shown in Figure 7-6 for impacting the agglomerate with  $3 \text{ J/m}^2$  surface energy at these two angles.



**Figure 7-6. Damage ratio as a function of impact velocity for the same agglomerates (surface energy of  $3 \text{ J/m}^2$ ) at different impact angles**

Normal impacting of the agglomerates at the same impact velocity results in more breakage compared to impacting of the same agglomerate at the inclined surface with the same impact velocity. The same case is observed for other surface energies such as  $0.5 \text{ J/m}^2$  and  $1 \text{ J/m}^2$ , as shown in Figures 7-7 and 7-8, respectively.

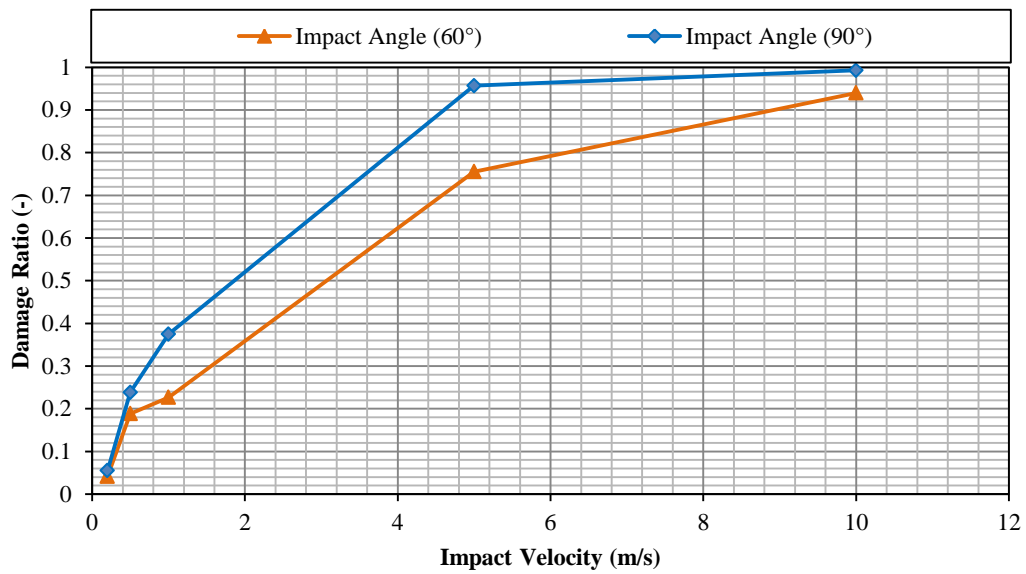


Figure 7-7. Damage ratio as a function of impact velocity for the same agglomerates (surface energy of  $0.5 \text{ J/m}^2$ ) at different impact angles

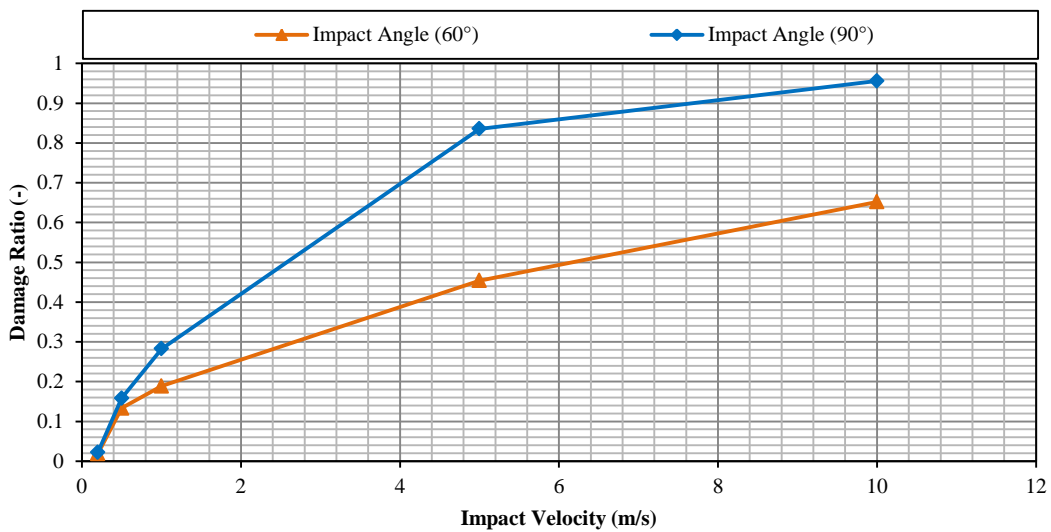
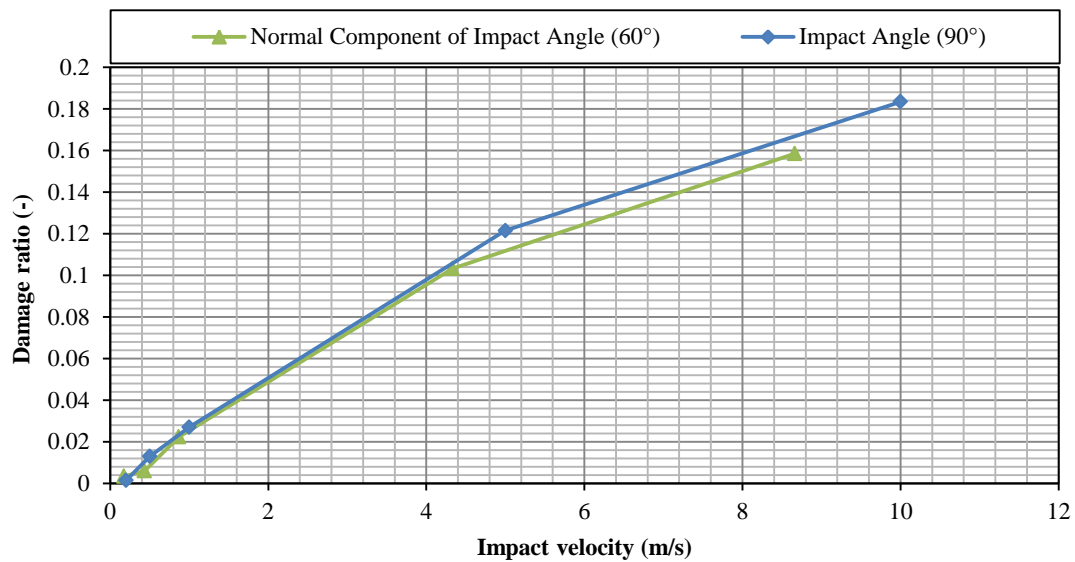


Figure 7-8. Damage ratio as a function of impact velocity for the same agglomerates (surface energy of  $1 \text{ J/m}^2$ ) at different impact angles

For both surface energies of  $0.5 \text{ J/m}^2$  and  $1 \text{ J/m}^2$ , impacting the agglomerates at normal target would result in more breakage compared to the inclined one.

The same comparison has been done considering the normal component of the impact velocity to explore the most influential component of the impact velocity on impact strength of the agglomerates, and it is shown in Figure 7-9.



**Figure 7-9. Damage ratio as a function of impact velocity for normal component of impact velocity, impacting the same agglomerates (surface energy of  $3 \text{ J/m}^2$ ) at different impact angles**

the normal velocity component of the inclined impact is taken into account, then the data overlap, indicating that the agglomerate breakage is mainly dependent on the normal component. The same analysis has been carried out on the data corresponding to the  $0.5 \text{ J/m}^2$  and  $1 \text{ J/m}^2$  surface energies. The results are shown in Figures 7-10 and 7-11, respectively.

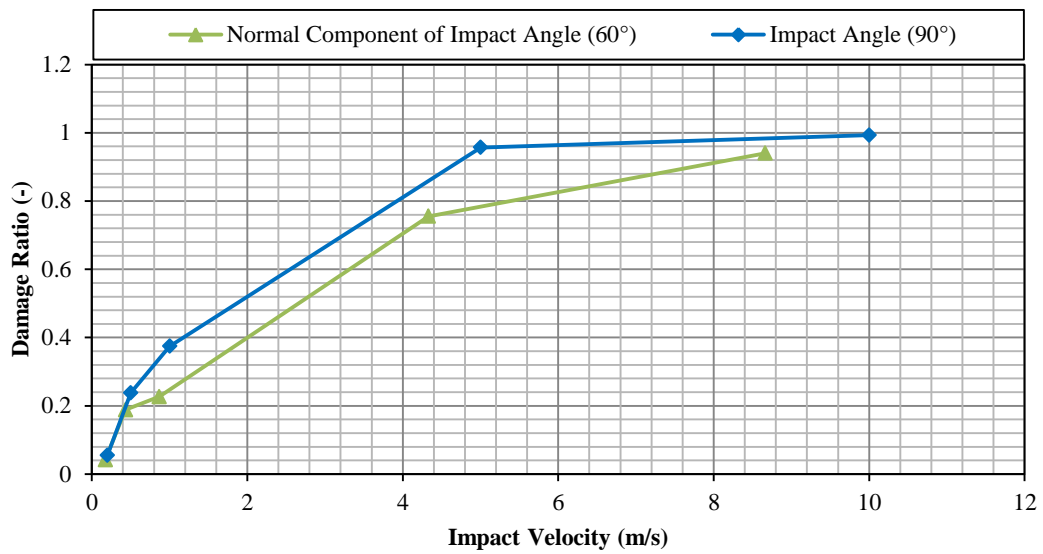


Figure 7-10. Damage ratio as a function of impact velocity for normal component of impact velocity, impacting the same agglomerates (surface energy of  $0.5 \text{ J/m}^2$ ) at different impact angles

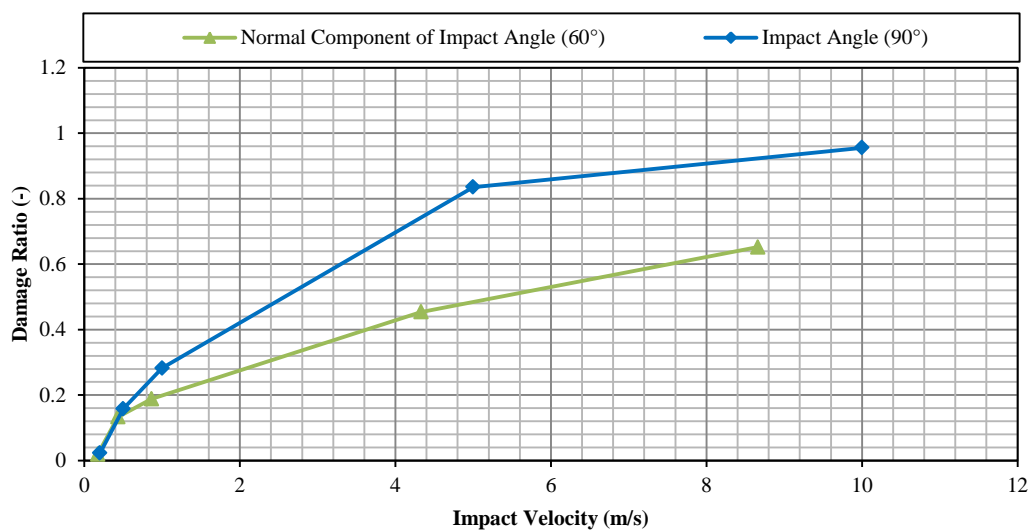


Figure 7-11. Damage ratio as a function of impact velocity for normal component of impact velocity, impacting the same agglomerates (surface energy of  $1 \text{ J/m}^2$ ) at different impact angles

Both Figures 7-10 and 7-11 show the data overlap at low impact velocities, indicating that the agglomerate breakage is mainly dependent on the normal component. However,

it is not the case for high impact velocities, showing that the tangential component is mainly causing breakage.

These results could vary based on the method used to form an agglomerate, i.e. the type of the bonding model used to keep the primary particles together might affect the results.

#### **7.4.4 Effect of Porosity on Agglomerate Impact Strength**

To make a porous agglomerate, some of the primary particles are removed from the structure. As mentioned before, the formed agglomerated has 30% porosity. At the start of the simulation work, the size and number of primary particles were chosen in a way that deleting a class or combination of particle classes could result in producing a defined porosity, e.g. by removing the particle types B and E, which are 30% of total particles, the porosity of the agglomerate is further increased. Therefore, the total porosity after removing the types B and E of the primary particles would increase to 51%. The two agglomerates (reference and 51% porosity) with a very low surface energy ( $0.5 \text{ J/m}^2$ ) have been impacted under the same impact conditions, and the damage ratio as a function of impact velocity has been compared for both cases, as shown in Figure 7-12.

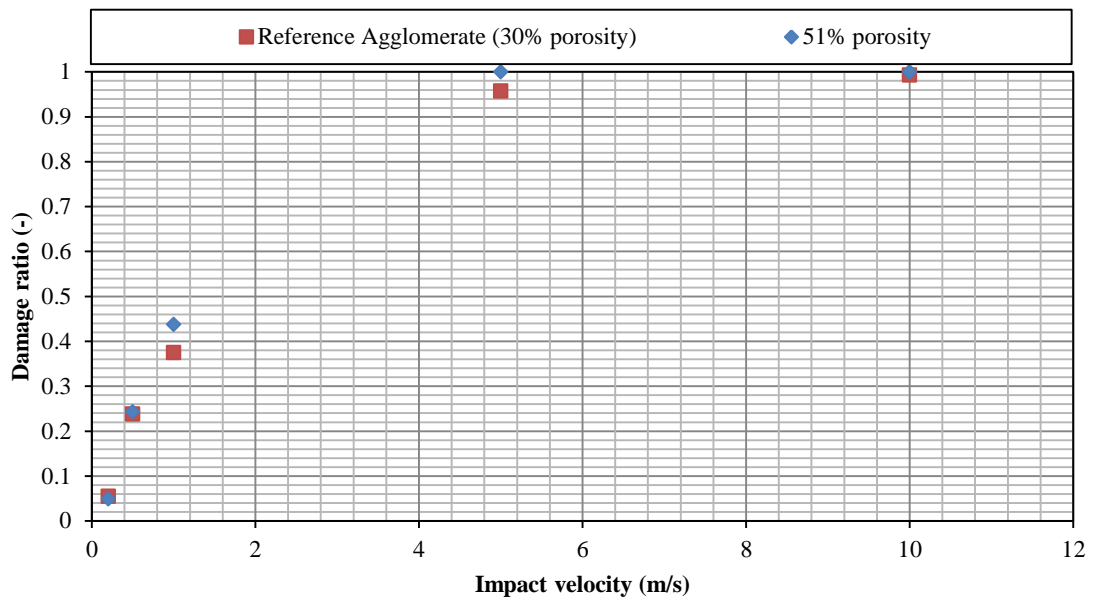


**Figure 7-12. Damage ratio as a function of impact velocity for two agglomerates with different levels of porosity and surface energy of  $0.5 \text{ J/m}^2$**

At low impact velocities (0.2 and 0.5 m/s), the two agglomerates break to almost the same extent. This is also the case at the high impact velocity of 10 m/s, as both particles are fully disintegrated and hence the damage ratio of 1 is obtained. For other impact velocities, the agglomerate with a higher porosity level breaks slightly more than the other agglomerate. However, a larger difference was expected to be observed. The same comparison has been carried out on the agglomerates with  $3 \text{ J/m}^2$  surface energy, and the results are shown in Figure 7-13.

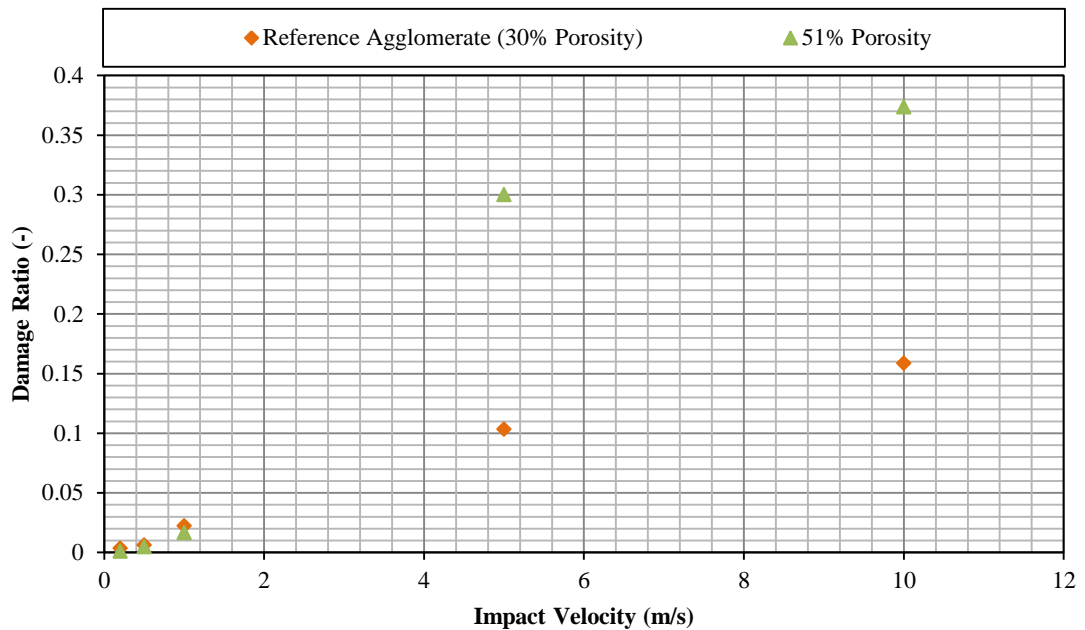


**Figure 7-13. Damage ratio as a function of impact velocity for two agglomerates with different levels of porosity and surface energy of  $3 \text{ J/m}^2$**

Based on the results shown in Figures 7-12 and 7-13, the agglomerates with two different porosity levels break to almost the same extent at low impact velocities. However, as the impact velocity is increased, the difference between the damage ratios for the two cases becomes larger to the extent that a significant difference is observed at 10 m/s impact velocity.

According to the simulation results, the difference between damage ratios of impacted agglomerates with different porosity levels is clearer for the agglomerates with higher surface energies. However, for very weak agglomerates with loose bonding the difference is not that significant.

## 7.5 Analysis of Impact Results

In previous sections, damage ratio was analysed as a function of impact velocity. However, the breakage of contacts can also be related to Weber Number ( $We$ ). Previously Kafui and Thornton (1993) used this approach to analyse the agglomerate breakage. Weber number is defined based on the equation below,

$$We = \frac{\rho D V^2}{\Gamma} \quad \text{Eq. (7-8)}$$

where  $D$  and  $\rho$  are particle diameter and density of the particles, respectively.  $V$  is the impact velocity.

However, the modified version of the Weber number ( $We'$ ) is more accurate (Thornton et al., 1996), as it considers the velocity below which there is no breakage ( $V_0$ ).

$$We' = \frac{\rho D (V - V_0)^2}{\Gamma} \quad \text{Eq. (7-9)}$$

Moreno-Atanasio and Ghadiri (2006b) did an extensive piece of work on impact breakage of spherical agglomerates using DEM simulation. Based on their model, the number of broken contacts is proportional to the incident kinetic energy, and by using an energy balance between the work required to break interparticle contacts and incident kinetic energy, the relationship between damage ratio ( $\Delta$ ) and the surface energy is presented as below,

$$\Delta \propto We' \left( \frac{ED}{\Gamma} \right)^{2/3} \quad \text{Eq. (7-10)}$$

where  $E$  is the primary particle elastic modulus. Therefore, the analysis has been carried out using Eq. (7-10) to explore the dependency of damage ratio on the surface energy, as shown in Figure 7-14.

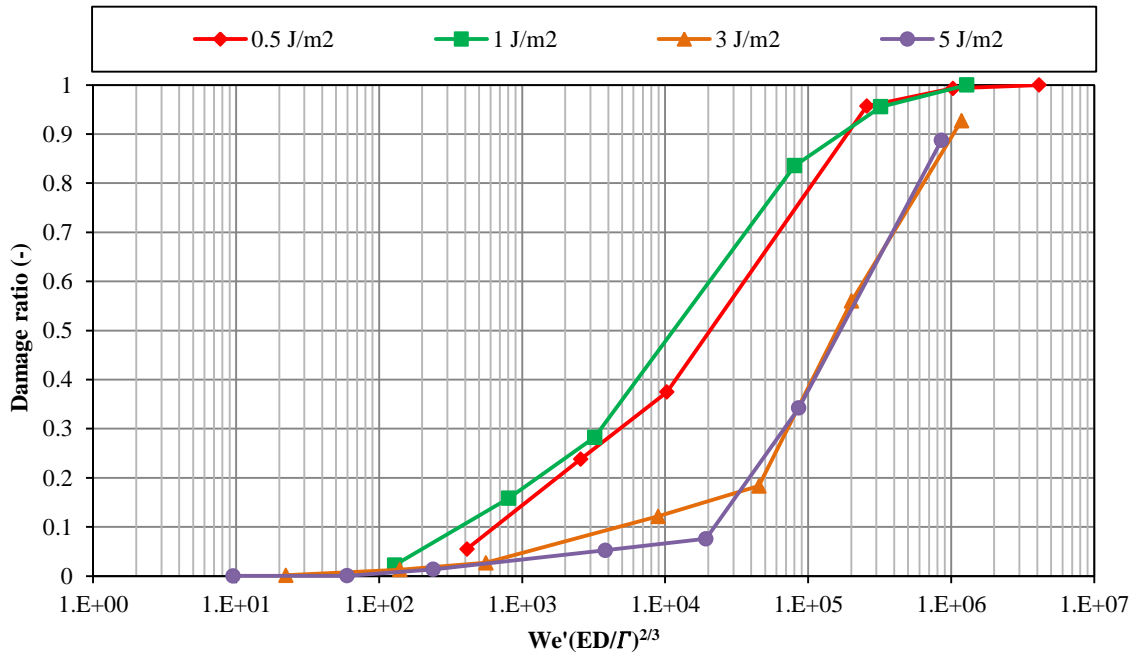
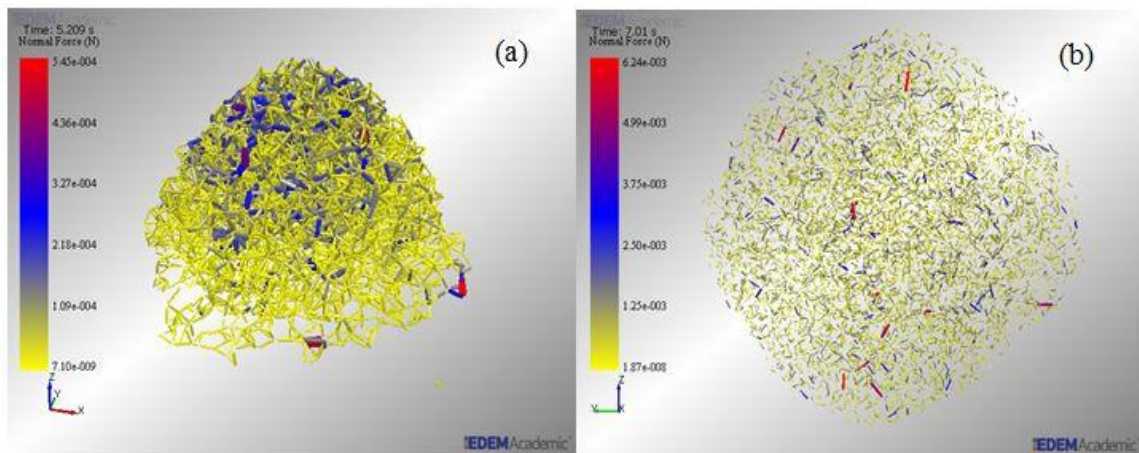


Figure 7-14. Damage ratio as a function of  $\Gamma^{-5/3}$  for agglomerates with different surface energies

Based on Moreno's model (Moreno-Atanasio and Ghadiri, 2006), a unification was expected when the damage ratio is plotted as a Weber-dependant group. However, this is not the case. The trend observed in Figure 7-14 is similar to that obtained from Figure 7-4. In both Figures, there are two clear trends, each trend being attributed to a different pattern of breakage. Based on the observation of the agglomerates after impact, impacting the agglomerates with low surface energies (0.5 and 1  $J/m^2$ ) would result in fragmentation and disintegration, whilst for agglomerates with high surface energies (3 and 5  $J/m^2$ ) the damage is localised and chipping is the main pattern of breakage for these range of velocities. As an example, the force distribution after

impact at 0.5 m/s shown in Figure 7-15 for agglomerates with 0.5 and 3  $J/m^2$  surface energy.



**Figure 7-15.** Side view of force distribution after impacting at 0.5 m/s for agglomerates with (a): 0.5  $J/m^2$ ;  
(b) 3  $J/m^2$

The force distributions are exported after impact at 0.5 m/s. Figures 7.15a and 7.15b show the side views of agglomerates with the surface energy of 0.5  $J/m^2$  and 1  $J/m^2$ , respectively. However, both of them have been exported at 0.01 s after impact, and the difference in the time shown in the Figure is due to the time taken for agglomerate generation and applying surface energy at previous steps before impact. The disintegration of the agglomerate with 0.5  $J/m^2$  surface energy is clearly seen, as the bottom part of the agglomerate (close to the impact zone) is completely deformed. The force has been also propagated within the agglomerate and reached to the top part, as shown in Figure 7-15a, causing breakage of the contacts. A different scenario is observed in Figure 7-15b for 3  $J/m^2$  surface energy. There is no clear deformation at the impact zone (bottom part of the agglomerate), and the force distribution is different compared to Figure 7-15a.

Based on these observations, it is not expected to achieve unification of breakage data in Figure 7-14, as there are different patterns of breakage. For tested agglomerates by Moreno, all of them failed through the same pattern of breakage, therefore unification was obtained as the damage ratio plotted as a function of  $\left(\frac{ED}{r}\right)^{2/3}$ .

Considering the definition of *We* Number, it is also expected that the damage ratio follows a square of velocity relationship. Therefore the damage ratio has been plotted as a function of  $V^2$  to see if such a dependency holds. The results are shown in Figure 7-16.

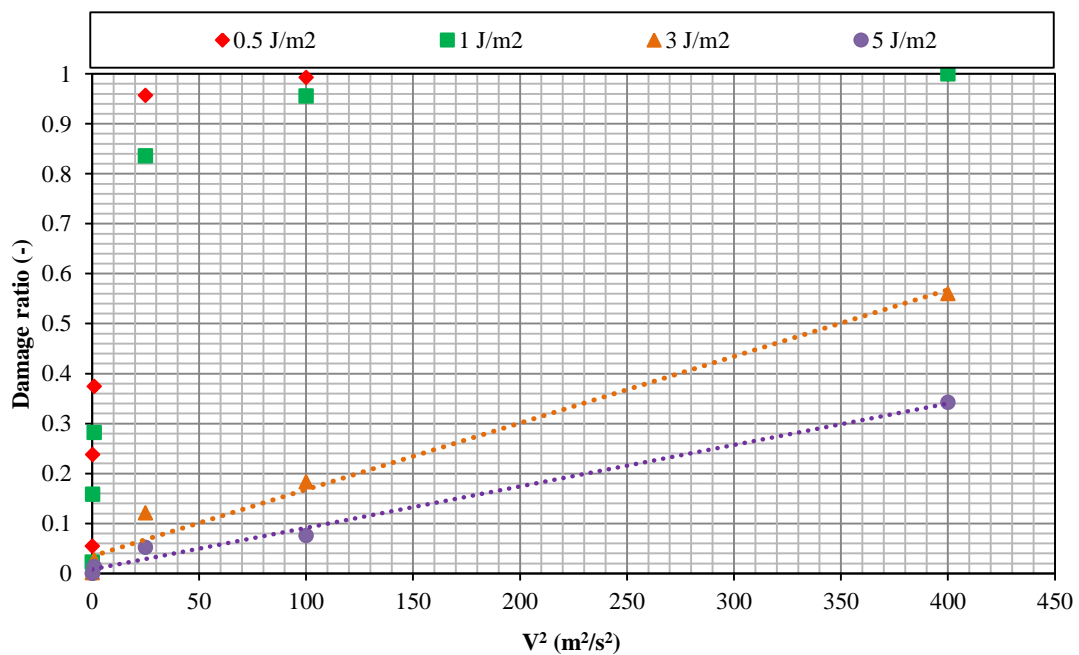


Figure 7-16. Damage ratio as a function of  $V^2$  for agglomerates with different surface energies

Based on the results, a linear relationship is only observed for impact results of high surface energy agglomerates, but there is no such a dependency for the low surface energy case.

## 7.6 Concluding Remarks

The structure of the agglomerates significantly affects properties such as strength. The impact simulation of different agglomerates has been carried out using EDEM simulation to explore the effects of impact velocity, impact angle, surface energy and porosity on the impact breakage of agglomerates. The agglomerates are bonded using the JKR model, using different levels of surface energy.

The concepts of damage ratio and Weber Number have been used to analyse the breakage results. Impacting the agglomerates with different surface energies for a range of impact velocities shows two different trends of breakage, which are attributed to different patterns of breakage. The agglomerates with high surface energies (3 and 5  $J/m^2$ ) undergo less breakage compared to the agglomerates with low surface energies (0.5 and 1  $J/m^2$ ). The damage ratio is a function of  $V^2$  for the high surface energies.

Based on the simulation results in this work, impacting the agglomerates at a flat surface would result in a larger number of broken contacts compared to impact at inclined surfaces. It has been found that the agglomerate failure is mainly dependent on the normal component of the impact velocity for the agglomerates used in this work.

Two different levels of porosity have been used to explore the effect of porosity on the impact strength of agglomerates; the reference agglomerate with the void fraction of 0.3 and the more porous agglomerate by removing 30% of primary particles to increase the porosity level to 51%. Generally, more porous agglomerates break to a higher extent compared to the agglomerates with a lower porosity. However, the difference is clearer for the agglomerates with a high surface energy.

The damage ratio has also been analysed using a Weber-related group. It has been shown that the breakage results are classified into different categories based on the pattern of breakage. The force distribution in the impacted agglomerates shows that the agglomerates with a low surface energy are deformed even at low impact velocities. The force is then propagated in to the agglomerate and reaches to the top surface of the agglomerate, causing more broken number of contacts, and hence disintegration. However, for agglomerates with a high surface energy, this is not the case, and only a small number of broken contacts are observed at the impact zone.

More studies are still needed to fully understand the breakage behaviour of agglomerates under impact. This work can be expanded by using more conditions, e.g. more porosity and surface energy levels, to provide more information on the dependency of the agglomerate strength on different parameters.

## **CHAPTER 8      OVERALL CONCLUSIONS AND FUTURE WORK**

### **8.1 Conclusions**

Understanding the breakage behaviour of particles is important for manufacturing plants handling particulate solids, particularly for weak and friable materials such as spray-dried powders. A combination of experimental and simulation work has been carried out in this study to understand the breakage of spray-dried burkeite particles, which have an agglomerate structure.

A comprehensive literature review has been undertaken on different topics such as mode of failure, test methods, patterns of breakage, agglomerates, computer simulation of agglomerates, etc. The breakage behaviour of single particles and agglomerates has been analysed. It has been found that the agglomerate breakage behaviour is more complex than single particles. Different pieces of work with the main aim of understanding the agglomerate breakage have been reviewed. DEM simulation has been found to be a fast method to explore the effects of different parameters of the agglomerate breakage.

In this work, spray-dried burkeite particles have been subjected to different levels of impact stresses using a single particle impact rig. Various patterns of breakage have been identified at each impact condition, and the breakage results have been analysed based on their patterns of breakage. The impact breakage results show that the burkeite particles are very weak, as they go through extensive breakage even at low impact

velocities. However, the clusters inside each single particle have been separated and subjected to different levels of impact stresses. The comparison of the impact breakage results obtained from impacting of the spray-dried burkeite particles and clusters shows that the clusters break less than the single particles. Therefore, clusters are clearly stronger than single particles.

It has been found that there are structural differences (envelope density variation) as a function of size; therefore different methods have been used to evaluate the envelope density of different particle sizes. Among all the methods described, X-ray microtomography has been chosen for the envelope density measurement method in this work. Using the obtained values of envelope density for different particle sizes along with the impact breakage results, the mechanical properties of the test materials have been estimated.

The single particle impact rig is not a commercially available device, so the Scirocco disperser of the Malvern Mastersizer 2000 has been used as an impact test device. Particles of different sizes accelerate to different velocities in the Scirocco disperser and break to different extents. Therefore, the impact velocities of different particle sizes in the Scirocco disperser have been obtained by CFD simulation by Ali et al. (2015). The same analysis as single particle impact testing has then been carried out by plotting the shift in specific surface area of the particles as a function of breakage propensity group. It has been found that a good unification is obtained by taking into account the impact velocity of different particle sizes in the Scirocco disperser.

The same approach has also been applied to three crystalline materials: aspirin, sucrose and  $\alpha$ -lactose monohydrate. Considering the mass required to be tested in the Scirocco,

it could be an attractive method where the quantity is an issue, e.g. pharmaceutical industries. The particles have been passed through the Scirocco disperser, and different sizes accelerate differently, and hence break to different extents. The relative increase in the specific surface area of the particles with respect to the initial value following impact in the Scirocco disperser shows a linear dependence on  $\rho_f \bar{d}_{f,v} V^2 \left( \frac{\rho_f \bar{d}_{f,v}}{\rho_a \bar{d}_{a,v}} \right)$ . The slope of the fitted line reflects particle breakage propensity and correlates well with  $\alpha H/K_c^2$  obtained by single particle impact testing. Therefore this method can be used to evaluate the grindability of powders and grains, provided the particle impact velocity is first determined.

DEM simulations have been carried out to obtain a better understanding of breakage of porous agglomerates. It has been found that the geometry in which the primary particles are generated has an effect on the final shape of the produced agglomerate, i.e. the cubical geometry would not result in a perfect spherical agglomerate, while in order to improve the spherical shape of the agglomerates a spherical geometry can be used. However, the total number of contacts would remain the same for both spherical and cubical geometries. The JKR model has been used to apply adhesive forces to make the primary particles sticky and form the agglomerates. There are some advantages with the JKR model, i.e. the problem of re-adhesion after agglomerate failure. More porous agglomerates have been produced by removing some of the primary particles. In EDEM, the removal of the particles is achieved based on the particle type and it is not easy to remove the particles based on their ID number. The agglomerates with two levels of porosities are then impacted at both normal and inclined impact targets for a range of impact velocities. The results show the effects of porosity, impact velocity,

impact target and surface energy on the impact breakage results of agglomerates. Plotting of the damage ratio as a function of Weber Number clearly shows two different trends for the impact results of the agglomerates with different interface energies. Based on observations, the agglomerates with interface energies of  $0.5 \text{ J/m}^2$  and  $1 \text{ J/m}^2$  undergo chipping and agglomerates with interface energies of  $3 \text{ J/m}^2$  and  $5 \text{ J/m}^2$  undergo disintegration after impacting at the range of  $0.2 \text{ m/s}$  to  $20 \text{ m/s}$ , which are in agreement with two observed trends.

The results obtained from this work provide a better understanding of the breakage of weak and porous agglomerates such as spray-dried burkeite particles. The information can also be used by related industries to improve their designs to avoid undesirable breakage under the studied conditions.

## 8.2 Future Work

A number of interesting lines of research work can be followed based on the work presented in this thesis. Much still needs to be done to understand the breakage of agglomerates. There are a number of improvements on the present work rather than new lines of research. In this respect, the data on fragmentation and disintegration patterns of breakage need to be improved by undertaking a full sieve analysis and obtaining the mass fraction of particles for all the size cuts below the feed size. It requires using a larger mass quantity for impact testing than that used in this work, in order to provide enough materials and avoid any mass loss during full sieve analysis. The particles are then impacted for a range of impact velocities. A full sieve analysis is used, the mass fraction in each sieve cut is measured and the data corresponding to

fragmentation and disintegration regimes are separated using Schuhman's graph (Schumann, 1940). The obtained information will then lead to develop breakage function.

Spray-dried burkeite particles are made from a number of clusters with a crystalline structure. The particles which undergo fragmentation and disintegration after impact, are disintegrated into the clusters, as they are loosely stuck to each other. However, clusters are much stronger than the particles based on the impact breakage results. Therefore, the strength of the particles can be improved by adding polymeric binders. However, it requires an extensive study to investigate where the binders will end up. This approach would be useful if the binders forge between the clusters.

The structure of spray-dried burkeite particles can be explored in more detailed studies. Information on porosity distribution as a function of particle size can be quite useful to understand the structural differences of particles as a function of size.

DEM simulations of impact breakage of agglomerates have been carried out by a good number of researchers. However, there is still a significant difference between simulation and experimental results. In order to make the simulation results closer to reality, the use of a realistic contact model is needed. This requires a better characterisation of bond failure. Hapgood's work (Hapgood, 2015), a collaborative project between Monash University and University of Leeds, provides for the first time an opportunity to precisely control the structure and interparticle bond properties in order to investigate their role in affecting the strength of complex structures and to help develop realistic models for simulations. A rigorous comparison with experimental work then needs to be undertaken to validate the results. In this project, the

agglomerates are produced by 3D printing. Different types of bonds, with different mechanical properties and thicknesses, are used to bond the primary particles together. The failure of the agglomerates is then tested under both quasi-static and dynamic conditions. The obtained information is used to develop a bonding model. The simulation results using the new contact model would be then compared to the experimental results to validate the bonding contact model.

In an ongoing project, a different bonding model is being used to bond the primary particles together to form the agglomerates. The breakage results would then be compared to those from the JKR model. The other issue is the distribution of porosities in the agglomerates. At the moment, the porosities have been made by randomly deleting the primary particles. However, in a more precise way the particles can be removed based on the porosity distribution of the actual agglomerates. Therefore, the results would be more comparable with the experimental work.

---

## REFERENCES

- Adams, M.J., Mullier, M.A. and Seville, J.P.K. 1994. Agglomerate strength measurement using a uniaxial confined compression test. *Powder Technology*. 78(1),pp.5–13.
- Adhikari, B., Howes, T., Bhandari, B.R. and Truong, V. 2000. Experimental studies and kinetics of single drop drying and their relevance in drying of sugar-rich foods: A review. *International Journal of Food Properties*. 3(3),pp.323–351.
- Aguilera, J.M. and Stanley, D.W. 1999. *Microstructural principles of food processing and engineering*.
- Ahmadian, H. 2008. Analysis of Enzyme Dust Formation in Detergent Manufacturing Plant.
- Ahmadian, H. and Ghadiri, M. 2007. Analysis of enzyme dust formation in detergent manufacturing plants. *Advanced Powder Technology*. 18(1).
- Alamilla-Beltrán, L., Chanona-Pérez, J.J., Jiménez-Aparicio, A.R. and Gutiérrez-Lopez, G.F. 2005. Description of morphological changes of particles along spray drying. *Journal of Food Engineering*. 67(1-2),pp.179–184.
- Ali, M., Bonakdar, T., Ghadiri, M. and Tinke, A. 2015. Particle Breakage in a Scirocco Disperser. *Powder Technology*. 285,pp.138–145.
- Allen, R.M. and Bakker, H.H.C. 1994. Spray Dryer Control based on Online Particle Size Analysis. *Trans IChemE*. 72, Part A.
- Allen, T. 1990. Particle Size Measurement. *Powder Technology Series*. 1.
- Analyzer, E.D. n.d. GeoPyc 1360. Available from: <http://www.micromeritics.com/Product-Showcase/GeoPyc-1360-Envelope-Density-Analyzer.aspx>.
- André, D., Iordanoff, I., Charles, J. and Néauport, J. 2012. Discrete element method to simulate continuous material by using the cohesive beam model. *Computer Methods in Applied Mechanics and Engineering*.
- Anon 2015. Burkeite. Available from: <http://www.mindat.org/min-805.html>.
- Antonyuk, S., Khanal, M., Tomas, J., Heinrich, S. and Mörl, L. 2006. Impact breakage of spherical granules: Experimental study and DEM simulation. *Chemical Engineering and Processing: Process Intensification*. 45(10),pp.838–856.
- Antonyuk, S., Khanal, M., Tomas, J., Heinrich, S. and Mörl, L. 2006. Impact breakage of spherical granules: Experimental study and DEM simulation. *Chemical*

- Engineering and Processing: Process Intensification*. 45(10),pp.838–856.
- Antonyuk, S., Tomas, J., Heinrich, S. and Mörl, L. 2005. Breakage behaviour of spherical granulates by compression. *Chemical Engineering Science*. 60(14),pp.4031–4044.
- Arbiter, N., Harris, C., C. and Stamboltzis, G., A. 1969. Single Fracture of Brittle Spheres. *Transactions of the Society of Mining Engineers of A.I.M.E.* 244,pp.118–133.
- Audu, T. and Jeffreys, G. 1975. The drying of drops of particulate slurries. *Chemical Engineering Research and Design*.,pp.165–172.
- Balakrishnan, A., Pizette, P., Martin, C.L., Joshi, S. V. and Saha, B.P. 2010. Effect of particle size in aggregated and agglomerated ceramic powders. *Acta Materialia*. 58(3),pp.802–812.
- Barth, J. 2013. *Personal Communication*.
- Bash, E. 2015. No Title No Title. *PhD Proposal*. [Online]. 1. Available from: <http://www.thm.de/ibva/images/stories/doku/mastersizer/mrk456-01.pdf>.
- Beekman, W.J. 2000. Measurement of the mechanical strength of granules and agglomerates. ,p.179.
- Beekman, W.J., Meesters, G.M.H., Becker, T., Gaertner, A., Gebert, M. and Scarlett, B. 2003. Failure mechanism determination for industrial granules using a repeated compression test. *Powder Technology*. 130(1-3),pp.367–376.
- Bemrose, C.R. and Bridgwater, J. 1987. A review of attrition and attrition test methods. *Powder Technology*. 49(2),pp.97–126.
- Bentham, A.C., Kwan, C.C., Boerefijn, R. and Ghadiri, M. 2004. Fluidised-bed jet milling of pharmaceutical powders. *Powder Technology*. 141(3),pp.233–238.
- Bika, D.G., Gentzler, M. and Michaels, J.N. 2001. Mechanical properties of agglomerates. *Powder Technology*. 117(1-2),pp.98–112.
- De Boer, A.H., Chan, H.K. and Price, R. 2012. A critical view on lactose-based drug formulation and device studies for dry powder inhalation: Which are relevant and what interactions to expect? *Advanced Drug Delivery Reviews*. 64(3),pp.257–274.
- Boerefijn, R., Gudde, N.J. and Ghadiri, M. 2000. A review of attrition of fluid cracking catalyst particles. *Advanced Powder Technology*. 11(2),pp.145–174.
- Boerefijn, R., Ning, Z. and Ghadiri, M. 1998. Disintegration of weak lactose agglomerates for inhalation applications. *International Journal of Pharmaceutics*. 172(1-2),pp.199–209.
- Briscoe, B. 1992. Tribology -- Friction and wear of engineering materials: I.M.

- Hutchings. *Tribology International*. 25(5),p.357.
- Brown, N.J., Chen, J.-F. and Ooi, J.Y. 2014. A bond model for DEM simulation of cementitious materials and deformable structures. *Granular Matter*. 16(3),pp.299–311.
- Calvert, G., Ghadiri, M., Dyson, M., Kippax, P. and McNeil-Watson, F. 2013. The flowability and aerodynamic dispersion of cohesive powders. *Powder Technology*. 240,pp.88–94.
- Calvert, G., Ghadiri, M. and Tweedie, R. 2009. Aerodynamic dispersion of cohesive powders: A review of understanding and technology. *Advanced Powder Technology*. 20(1),pp.4–16.
- Carmona, H., Wittel, F., Kun, F. and Herrmann, H. 2008. Fragmentation processes in impact of spheres. *Physical Review E*.
- Chapelle, P., Abou-Chakra, H., Christakis, N., Bridle, I., Patel, M.K., Baxter, J., Tuzun, U. and Cross, M. 2004. Numerical predictions of particle degradation in industrial-scale pneumatic conveyors. *Powder Technology*. 143-144,pp.321–330.
- Chaudhri, M.M. 2004. Impact breakage of semi-brittle spheres. *Powder Technology*. 143-144,pp.31–40.
- Chawla, J. 1994. Effect of the droplet agglomeration on the design of spray dryer towers. *Drying technology*.
- Cheong, Y.S., Adams, M.J., Routh, A.F., Hounslow, M.J. and Salman, A.D. 2005. The production of binderless granules and their mechanical characteristics. *Chemical Engineering Science*. 60(14),pp.4045–4053.
- Couroyer, C., Ning, Z., Ghadiri, M., Brunard, N., Kolenda, F., Bortzmeyer, D. and Laval, P. 1999. Breakage of macroporous alumina beads under compressive loading: Simulation and experimental validation. *Powder Technology*. 105(1-3),pp.57–65.
- Cundall, P. 1989. Numerical experiments on localization in frictional materials. *Ingenieur-archiv*.
- Cundall, P.A. and Strack, O.D.L. 1979. A discrete numerical model for granular assemblies. *Géotechnique*. 29(1),pp.47–65.
- D’addetta, G., Kun, F. and Ramm, E. 2002. On the application of a discrete model to the fracture process of cohesive granular materials. *Granular matter*.
- Daszykowski, M. and Walczak, B. 2010. Density-Based Clustering Methods. *Comprehensive Chemometrics*. 2,pp.635–654.
- DEM-Solutions 2015. *EDEM User Manual* (DEM-Solutions, ed.). DEM-Solutions.

- Dolinsky, A. 2001. High-temperature spray drying. *Drying Technology*.
- Dosta, M., Antonyuk, S. and Heinrich, S. 2013. Multiscale simulation of agglomerate breakage in fluidized beds. *Industrial and Engineering Chemistry Research*. 52(33),pp.11275–11281.
- Eggermont, P.P.B., Herman, G.T. and Lent, A. 1981. Iterative algorithms for large partitioned linear systems, with applications to image reconstruction. *Linear Algebra Appl.* 40,pp.37–67.
- Elwazri, A.M., Wanjara, P., Varano, R. and Stewart, G.R. 2009. Influence of Processing Conditions on Obtaining. *Powder Technology*. 48(3),pp.219–228.
- Ennis, B.J., Tardos, G. and Pfeffer, R. 1991. A microlevel-based characterization of granulation phenomena. *Powder Technology*. 65(1-3),pp.257–272.
- Evans, A.G. and Wilshaw, T.R. 1976. Quasi-static solid particle damage in brittle solids -- I. Observations, analysis and implications. *Acta Metallurgica*. 24(10),pp.939–956.
- Evans, A.G. and Wilshaw, T.R. 1976. Quasi-static solid particle damage in brittle solids-I. Observations analysis and implications. *Acta Metallurgica*. 24(10),pp.939–956.
- Ferrari, G., Meerdink, G. and Walstra, P. 1989. Drying kinetics for a single droplet of skim-milk. *Journal of Food Engineering*. 10(3),pp.215–230.
- Frye, L. and Peukert, W. 2005. Identification of material specific attrition mechanisms for polymers in dilute phase pneumatic conveying. *Chemical Engineering and Processing: Process Intensification*. 44(2),pp.175–185.
- Frye, L. and Peukert, W. 2004. Transfer of fracture mechanical concepts to bulk solids attrition in pneumatic conveying. *International Journal of Mineral Processing*. 74(SUPPL.).
- Fu, X., Dutt, M., Bentham, A.C., Hancock, B.C., Cameron, R.E. and Elliott, J.A. 2006. Investigation of particle packing in model pharmaceutical powders using X-ray microtomography and discrete element method. *Powder Technology*. 167(3),pp.134–140.
- Furuta, T., Hayashi, H. and Ohashi, T. 1994. Some Criteria of Spray Dryer Design for Food Liquid. *Drying Technology*. 12(1),pp.151–177.
- Gahn, C. and Mersmann, a 1997. Theoretical Prediction and Experimental Determination of Attrition Rates. *Chemical Engineering Research and Design*. 75(2),pp.125–131.
- Ge, X. and Schmauder, S. 1995. Micromechanism of fracture in Al/SiC composites. *Journal of Materials Science*. 30(1),pp.173–178.

- Ghadiri, M. 1997. Particle impact and attrition. *Powder Technology Handbook*.
- Ghadiri, M. and Moreno-Atanasio, R. 2007. Analysis of Agglomerate Breakage. *Handbook of Powder Technology*.
- Ghadiri, M., Ning, Z., Kenter, S. and Puik, E. 2000. Attrition of granular solids in a shear cell. *Chemical Engineering Science*. 55(22),pp.5445–5456.
- Ghadiri, M. and Zhang, Z. 1992. IFPRI Final Report, FRR 16-03. *University of Surrey, UK*.
- Ghadiri, M. and Zhang, Z. 2002. Impact attrition of particulate solids. Part 1: A theoretical model of chipping. *Chemical Engineering Science*. 57(17),pp.3659–3669.
- Golchert, D., Moreno, R., Ghadiri, M. and Litster, J. 2004. Effect of granule morphology on breakage behaviour during compression. *Powder Technology*. 143-144,pp.84–96.
- Grant, E. and Kalman, H. 2001. Fatigue analysis of particle attrition in a rotating drum. *Particle & particle systems characterization*. 18(2),pp.64–69.
- Gutsch, A., Pratsinis, S.E. and Löffler, F. 1995. Agglomerate structure and growth rate by trajectory calculations of monomer-cluster collisions. *Journal of Aerosol Science*. 26(2),pp.187–199.
- Hagan, J.T. 1981. Impossibility of fragmenting small particles: brittle-ductile transition. *Journal of Materials Science*. 16(10),pp.2909–2911.
- Hagan, J.T. and Swain, M. V 2001. The origin of median and lateral cracks around plastic indents in brittle materials. *Journal of Physics D: Applied Physics*. 11(15),pp.2091–2102.
- Hapgood, K. 2015. No Title.
- Hare, C.L., Ghadiri, M., Dennehy, R. and Collier, A. 2009. Particle breakage in agitated dryers. *AIP Conference Proceedings*. 1145.
- Hecht, J.P. and King, C.J. 2000. Spray Drying: Influence of Developing Drop Morphology on Drying Rates and Retention of Volatile Substances. 1. Single-Drop Experiments. *Industrial & Engineering Chemistry Research*. 39(1),pp.1756–1765.
- Hertz, H. 1882. On the contact of elastic solids. *Journal für die reine und angewandte Mathematik*. 91,pp.156–171.
- Hertz, H.R. 1882. Über die Berührung fester elastischer Körper. *Journal für die reine und angewandte Mathematik*. 92,pp.156–171.
- Huntington, D.H. 2004. The Influence of the Spray Drying Process on Product Properties. *Drying Technology*. 22(6),pp.1261–1287.

- Hutchings, I.M. 1993. Mechanisms of wear in powder technology: A review. *Powder Technology*. 76(1),pp.3–13.
- John, E., Germaine, A. V and Wiley, J. 2009. *Measurements for Engineers*.
- Johnson, K. 1987. *Contact mechanics*.
- Johnson, K.L., Kendall, K. and Roberts, a. D. 1971. Surface Energy and the Contact of Elastic Solids. *Proceedings of the Royal Society A: Mathematical, Physical and Engineering Sciences*. 324(1558),pp.301–313.
- Jones, M.D. and Price, R. 2006. The influence of fine excipient particles on the performance of carrier-based dry powder inhalation formulations. *Pharmaceutical Research*. 23(8),pp.1665–1674.
- JUSLIN, L. and YLIRUUSI, J. 1996. Granule growth kinetics and attrition of granules made of different materials in a fluidized bed granulator. *STP pharma sciences*. 6(5),pp.321–327.
- Kafui, K.D. and Thornton, C. 1993. Computer simulated impact of agglomerates. *Powders and Grains*. 93,pp.401–406.
- Kaláb, M., Allan-Wojtas, P. and Miller, S.S. 1995. Microscopy and other imaging techniques in food structure analysis. *Trends in Food Science & Technology*. 6(6),pp.177–186.
- Kalman, H. 2000. Attrition of powders and granules at various bends during pneumatic conveying. *Powder Technology*. 112(3),pp.244–250.
- Kalman, H. 2000. Particle breakage and gradation. *KONA Powder and Particle Journal*.
- Karihaloo, B.L. 1979. The impossibility of comminuting small particles by compression. *Nature*. 279(5709),pp.169–170.
- Kendall, K. 1988. AGGLOMERATE STRENGTH. *Powder Metallurgy*.
- Keningley, S.T., Knight, P.C. and Marson, A.D. 1997. An investigation into the effects of binder viscosity on agglomeration behaviour. *Powder Technology*. 91(2),pp.95–103.
- Khanal, M., Schubert, W. and Tomas, J. 2004. Ball Impact and Crack Propagation - Simulations of Particle Compound Material. *Granular Matter*. 5(4),pp.177–184.
- Ku, N., Hare, C., Ghadiri, M., Murtagh, M. and Haber, R.A. 2015. Effect of mechanical vibration on the size and microstructure of titania granules produced by auto-granulation. *Powder Technology*. 286,pp.223–229.
- Ku, N., Hare, C., Ghadiri, M., Murtagh, M., Oram, P. and Haber, R.A. 2015. Auto-granulation of Fine Cohesive Powder by Mechanical Vibration. *Procedia*

- Engineering*. 102,pp.72–80.
- Kwan, C.C., Chen, J.Q. and Ding, Y.L. 2004. Development of a novel approach towards predicting the milling. *European Journal of Pharmaceutical Sciences*. 23(4-5),pp.327–336.
- Lawn, B. and Wilshaw, R. 1975. Indentation fracture: principles and applications. *Journal of Materials Science*.
- Lecoq, O., Chouteau, N., Mebtoul, M., Large, J.F. and Guigon, P. 2003. Fragmentation by high velocity impact on a target: A material grindability test. *Powder Technology*. 133(1-3),pp.113–124.
- Litster, J., Iveson, S. and Hapgood, K. 1998. Predicting and controlling granule properties in granulation processes. *Proc. IChemE World Congr.*
- Mackin, L., Zanon, R., Park, J.M., Foster, K., Opalenik, H. and Demonte, M. 2002. Quantification of low levels (<10%) of amorphous content in micronised active batches using dynamic vapour sorption and isothermal microcalorimetry. *International Journal of Pharmaceutics*. 231(2),pp.227–236.
- Manegold, E., Hofmann, R. and Solf, K. 1931. Ueber Kapillarsysteme XII. I. Die mathematische Behandlung idealer Kugelpackungen und das Hohlraumvolumen realer Ger??ststrukturen. *Kolloid-Zeitschrift*. 56(2),pp.142–159.
- Masters, K. 1991. Handbook of Spray Drying. 5<sup>th</sup> edn, Longman, London.
- Meenan, P., Roberts, K., Knight, P. and Yuregir, K. 1997. The influence of spray drying conditions on the particle properties of recrystallized burkeite (Na<sub>2</sub>CO<sub>3</sub>·(Na<sub>2</sub>SO<sub>4</sub>)<sub>2</sub>). *Powder technology*.
- Meissner, H., Michaels, A. and Kaiser, R. 1964. Crushing strength of zinc oxide agglomerates. *Industrial & Engineering Chemistry Process Design and Development*. 3(3),pp.202–205.
- Metzger, M.J. and Glasser, B.J. 2012. Numerical investigation of the breakage of bonded agglomerates during impact. *Powder Technology*. 217,pp.304–314.
- Mindlin, R.D. and Deresiewicz, H. 1953. Elastic spheres in contact under varying oblique forces. *American Society of Mechanical Engineers -- Transactions -- Journal of Applied Mechanics*. 20(3),pp.327–344.
- Moreno, R., Ghadiri, M. and Antony, S. 2003. Moreno\_2003\_Effect of the impact angle on the breakage of agglomerates\_a numerical study using DEM.pdf. *Powder Technology*.
- Moreno-Atanasio, R. 2003. Computer simulation of impact behaviour of spherical agglomerates using Distinct Element Method.
- Moreno-Atanasio, R. and Ghadiri, M. 2006. Mechanistic analysis and computer

- simulation of impact breakage of agglomerates: Effect of surface energy. *Chemical Engineering Science*. 61(8),pp.2476–2481.
- Moreno-Atanasio, R., Williams, R.A. and Jia, X. 2010. Combining X-ray microtomography with computer simulation for analysis of granular and porous materials. *Particuology*. 8(2),pp.81–99.
- Müller, M. and Löffler, F. 1996. Development of agglomerate size and structure during spherical agglomeration in suspension. *Particle & particle systems characterization*.
- Mullier, M.A., Seville, J.P.K. and Adams, M.J. 1991. The effect of agglomerate. *Wear*. 65,pp.321–333.
- Nguyen, D., Rasmuson, A., Thalberg, K. and Niklasson Björn, I. 2015. A breakage and adhesion regime map for the normal impact of loose agglomerates with a spherical target. *AIChE Journal*. 61(12),pp.4059–4068.
- Ning, Z. 1995. Elasto-plastic impact of fine particles and fragmentation of small agglomerates.
- Ning, Z., Boerefijn, R., Ghadiri, M. and Thornton, C. 1997. Distinct element simulation of impact breakage of lactose agglomerates. *Advanced Powder Technology*. 8(1),pp.15–37.
- Ning, Z. and Ghadiri, M. 2006. Distinct element analysis of attrition of granular solids under shear deformation. *Chemical Engineering Science*. 61(18),pp.5991–6001.
- Oakley, D.E. 1994. Scale-Up of Spray Dryers With the Aid of Computational Fluid Dynamics. *Drying Technology*. 12(1-2),pp.217–233.
- Oliver, C. and Pharr, M. 1992. An improved technique for determining hardness and elastic modulus using load and displacement sensing indentation experiments. *Journal of Materials Research*. 7(11),pp.1564–1583.
- Papadopoulos, D.G. 1998. Impact breakage of particulate solids.
- Pietsch, W. 2008. *Agglomeration Processes: Phenomena, Technologies, Equipment*. John Wiley & Sons.
- Pitchumani, R., Strien, S.A., Meesters, G.M.H., Schaafsma, S.H. and Scarlett, B. 2004. Breakage of sodium benzoate granules under repeated impact conditions. *Powder Technology*. 140(3),pp.240–247.
- Potapov, A. V and Campbell, C.S. 1996. Computer Simulation of Particle Breakage. *Xxx*,p.Bab 19.2.
- Puttick, K.E. 1980. The correlation of fracture transitions. *Journal of Physics D: Applied Physics*. 13(12),p.2249.

- R.D. Mindlin 1949. Compliance of elastic bodies in contact. *Journal of applied mechanics*. 71,pp.259–268.
- Rahmanian, N., Ghadiri, M., Jia, X. and Stepanek, F. 2009. Characterisation of granule structure and strength made in a high shear granulator. *Powder Technology*. 192(2),pp.184–194.
- Reynolds, G.K., Fu, J.S., Cheong, Y.S., Hounslow, M.J. and Salman, A.D. 2005. Breakage in granulation: A review. *Chemical Engineering Science*. 60(14),pp.3969–3992.
- Rice, R.W. 1996. Grain size and porosity dependence of ceramic fracture energy and toughness at 22 °C. *Journal of Materials Science*. 31(8),pp.1969–1983.
- Rong, G., Liu, G., Hou, D. and Zhou, C.-B. 2013. Effect of particle shape on mechanical behaviors of rocks: a numerical study using clumped particle model. *TheScientificWorldJournal*. 2013,p.589215.
- Rumpf, H. 1958. Grundlagen und Methoden des Granulierens. *Chemie Ingenieur Technik*. 30(3),pp.144–158.
- Rumpf, H. 1962. The strength of granules and agglomerates *In: A. Interscience, ed. Agglomeration*. new york, pp. 379–418.
- Rumpf, H. and Schönert, K. 1972. Die Brucherscheinungen in Kugeln bei elastischen sowie plastischen Verformungen durch Druckbeanspruchung. *Dechema Monograph*.
- Salman, A.D., Fu, J., Gorham, D.A. and Hounslow, M.J. 2003. Impact breakage of fertiliser granules. *Powder Technology*. 130(1-3),pp.359–366.
- Salman, A.D. and Gorham, D.A. 2000. The fracture of glass spheres. *Powder Technology*. 107(1-2),pp.179–185.
- Salman, A.D., Gorham, D.A. and Verba, A. 1995. A study of solid particle failure under normal and oblique impact. *Wear*. 186-187(PART 1),pp.92–98.
- Salman, A.D., Hounslow, M.J. and Verba, A. 2002. Particle fragmentation in dilute phase pneumatic conveying. *Powder Technology*. 126(2),pp.109–115.
- Salman, A.D., Reynolds, G.K., Fu, J.S., Cheong, Y.S., Biggs, C.A., Adams, M.J., Gorham, D.A., Lukenics, J. and Hounslow, M.J. 2004. Descriptive classification of the impact failure modes of spherical particles. *Powder Technology*. 143-144,pp.19–30.
- Samimi, A., Ghadiri, M., Boerefijn, R., Groot, A. and Kohlus, R. 2003. Effect of structural characteristics on impact breakage of agglomerates. *Powder Technology*. 130(1-3),pp.428–435.
- Samimi, A., Moreno, R. and Ghadiri, M. 2004. Analysis of impact damage of

- agglomerates: Effect of impact angle. *Powder Technology*. 143-144,pp.97–109.
- Sano, Y. and Kee, R.B. 1982. The drying of a spherical containing colloidal material into a hollow sphere. *Chemical Engineering Science*. 37(6),pp.881–889.
- Schönert, K. 2004. Breakage of spheres and circular discs. *Powder Technology*. 143-144,pp.2–18.
- Schneider, B., Bischoff, M. and Ramm, E. 2010. Modeling of material failure by the discrete element method. *PAMM*.
- Schubert, W., Khanal, M. and Tomas, J. 2005. Impact crushing of particle-particle compounds - Experiment and simulation. *International Journal of Mineral Processing*. 75(1-2),pp.41–52.
- Schumann, R. 1940. Principles of comminution. *AIME Tech.* (TP 1189).
- Segovia-Torres, F. 2012. Understanding and Prediction of Particle Breakage during Handling, Mixing and Packing in Detergent Manufacturing.
- Shipway, P.H. and Hutchings, I.M. 1993a. Attrition of brittle spheres by fracture under compression and impact loading. *Powder Technology*. 76(1),pp.23–30.
- Shipway, P.H. and Hutchings, I.M. 1993b. Influence of nozzle roughness on conditions in a gas-blast erosion rig. *Wear*. 162-164(PART A),pp.148–158.
- Smith, W.E. and Dent, G. 2005. The Theory of Raman Spectroscopy. *Modern Raman spectroscopy - A practical approach*. [Online]. Available from: <http://www.horiba.com/scientific/products/raman-spectroscopy/raman-academy/raman-tutorial/the-theory-of-raman-spectroscopy/>.
- Smith, W.O., Foote, P.D. and Busang, P.F. 1930. Capillary Retention of Liquids in Assemblages of Homogeneous Spheres. *Physical Review*. 36.
- Sneddon, I.N. 1965. The relation between load and penetration in the axisymmetric boussinesq problem for a punch of arbitrary profile. *International Journal of Engineering Science*. 3(1),pp.47–57.
- Spetl, A., Dosta, M., Antonyuk, S., Heinrich, S. and Schmidt, V. 2015. Statistical investigation of agglomerate breakage based on combined stochastic microstructure modeling and DEM simulations. *Advanced Powder Technology*. 26(3),pp.1021–1030.
- Stock, S.R. 1999. X-ray microtomography of materials. *International Materials Reviews*. 44(4),pp.141–164.
- Subero, J. 2001a. Impact breakage of agglomerates. *International Journal of Mineral Processing*.
- Subero, J. 2001b. Impact breakage of agglomerates.

- Subero, J. and Ghadiri, M. 2001. Breakage patterns of agglomerates. *Powder Technology*. 120(3),pp.232–243.
- Subero, J., Ning, Z., Ghadiri, M. and Thornton, C. 1999. Effect of interface energy on the impact strength of agglomerates. *Powder Technology*. 105(1-3),pp.66–73.
- Subero-Couroyer, C., Ghadiri, M., Brunard, N. and Kolenda, F. 2005. Analysis of catalyst particle strength by impact testing: The effect of manufacturing process parameters on the particle strength. *Powder Technology*. 160(2),pp.67–80.
- T, H., A, L. and H, K. 2003. DEM Simulation for Attrition of Salt During Dilute Phase Pneumatic Conveying. *Powder Technology* 129.,pp.92–100.
- Tantawy, H. and Martinez-Guzman, A. 2014. Spray-dried detergent powder. *US Patent*.
- Thornton, C., Ciomocos, M.T. and Adams, M.J. 1999. Numerical simulations of agglomerate impact breakage. *Powder Technology*. 105(1-3),pp.74–82.
- Thornton, C., Ciomocos, M.T. and Adams, M.J. 2004. Numerical simulations of diametrical compression tests on agglomerates. *Powder Technology*. 140(3),pp.258–267.
- Thornton, C., Kafui, D. and Ciomocos, T. 1995. IFPRI Meeting Proceedings. *Urbana*.
- Thornton, C. and Liu, L. 2004. How do agglomerates break? *Powder Technology*. 143-144,pp.110–116.
- Thornton, C. and Ning, Z. 1998. A theoretical model for the stick/bounce behaviour of adhesive, elastic- plastic spheres. *Powder Technology*. 99(2),pp.154–162.
- Thornton, C. and Yin, K.K. 1991. Impact of elastic spheres with and without adhesion. *Powder Technology*. 65(1-3),pp.153–166.
- Thornton, C., Yin, K.K. and Adams, M.J. 1996. Numerical simulation of the impact fracture and fragmentation of agglomerates. *Journal of Physics D: Applied Physics*. 29,pp.424–435.
- Tomas, J., Schreier, M., Gr??ger, T. and Ehlers, S. 1999. Impact crushing of concrete for liberation and recycling. *Powder Technology*. 105(1-3),pp.39–51.
- Vogel, L. and Peukert, W. 2003. Breakage behaviour of different materials - Construction of a mastercurve for the breakage probability. *Powder Technology*. 129(1-3),pp.101–110.
- Vogel, L. and Peukert, W. 2005. From single particle impact behaviour to modelling of impact mills. *Chemical Engineering Science*. 60(18),pp.5164–5176.
- Walton, D. 2000. The morphology of spray-dried particles a qualitative view. *Drying Technology*.

- Weibull, W. 1951. Wide applicability. *Journal of applied mechanics*.
- Weichert, R. 1988. Correlation between probability of breakage and fragment size distribution of mineral particles. *International Journal of Mineral Processing*. 22(1-4),pp.1-8.
- Wolff, M.F.H., Salikov, V., Antonyuk, S., Heinrich, S. and Schneider, G.A. 2013. Three-dimensional discrete element modeling of micromechanical bending tests of ceramic-polymer composite materials. *Powder Technology*. 248,pp.77-83.
- Wu, S.Z., Chau, K.T. and Yu, T.X. 2004. Crushing and fragmentation of brittle spheres under double impact test. *Powder Technology*. 143-144,pp.41-55.
- Yangxin, Y. U., Zhao, J. and Bayly, A.E. 2008. Development of Surfactants and Builder in Detergent Formulations. *Chinese Journal of Chemical Engineering*. 16(4),pp.517-528.
- Yu, A., Tan, Y. and Yang, X. 2004. Machining characteristics of Ce-ZrO<sub>2</sub>/CePO<sub>4</sub> ceramics. *JOURNAL OF RARE EARTHS*. 22,pp.223-225.
- Yu, A., Zhong, L., Liu, J., Qiu, S. and Tian, X. 2003. Cutability evaluation of oxide ceramics containing rare earth phosphates. *JOURNAL OF RARE EARTHS*. 21,pp.93-98.
- Yuregir, K.R., Ghadiri, M. and Clift, R. 1987. Impact Attrition of Sodium Chloride Crystals. *Chemical engineering science*. 42(4),pp.843-853.
- Yuregir, K.R., Ghadiri, M. and Clift, R. 1986. Observations on impact attrition of granular solids. *Powder Technology*. 49(1),pp.53-57.
- Zhang, Z. and Ghadiri, M. 2002. Impact attrition of particulate solids. Part 2: Experimental work. *Chemical Engineering Science*. 57(17),pp.3671-3686.

## Appendix A

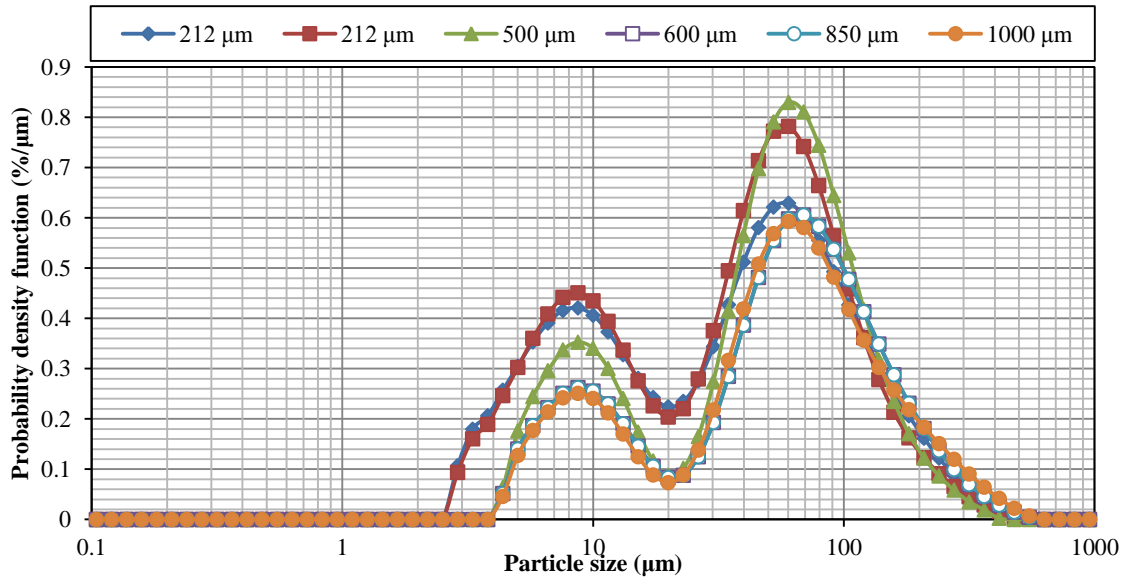


Figure a 1. Particle size distribution for different near-mesh particle sizes of burkeite at 100 kPa nozzle pressure

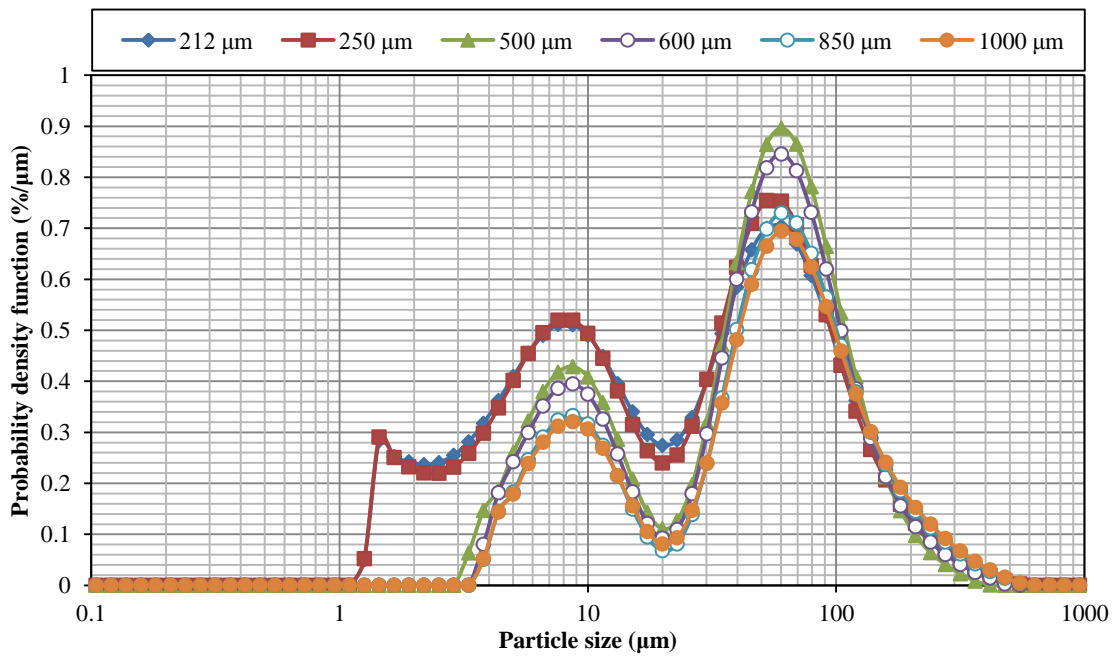


Figure a 2. Particle size distribution for different near-mesh particle sizes of burkeite at 150 kPa nozzle pressure

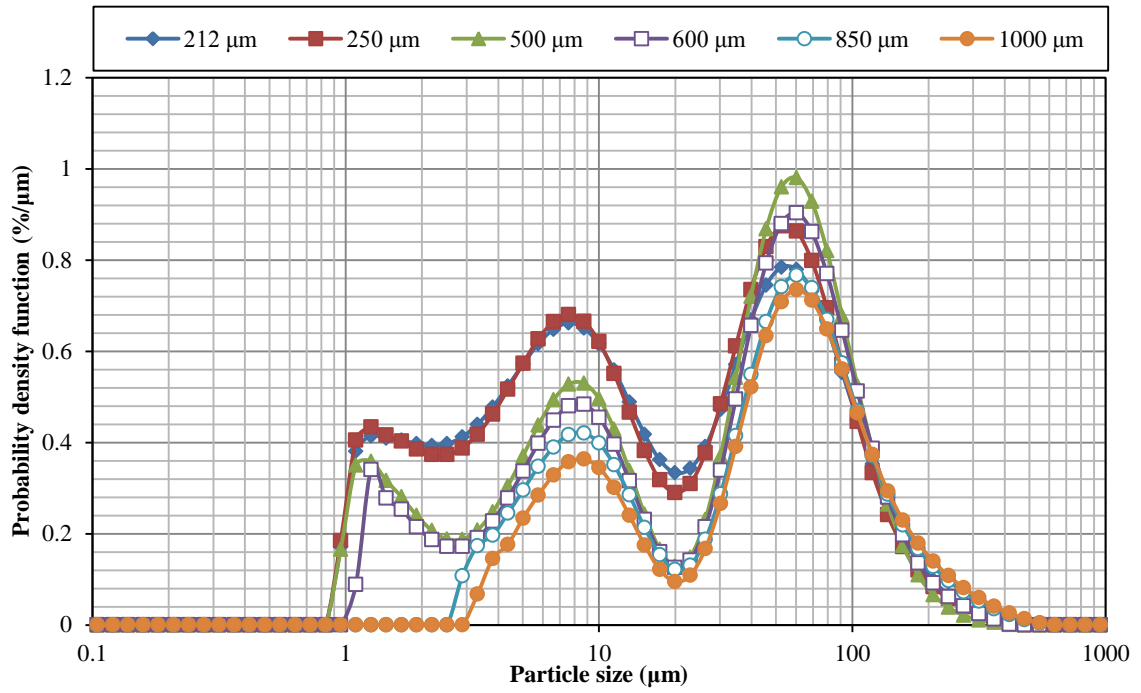


Figure a 3. Particle size distribution for different near-mesh particle sizes of burkeite at 200 kPa nozzle pressure

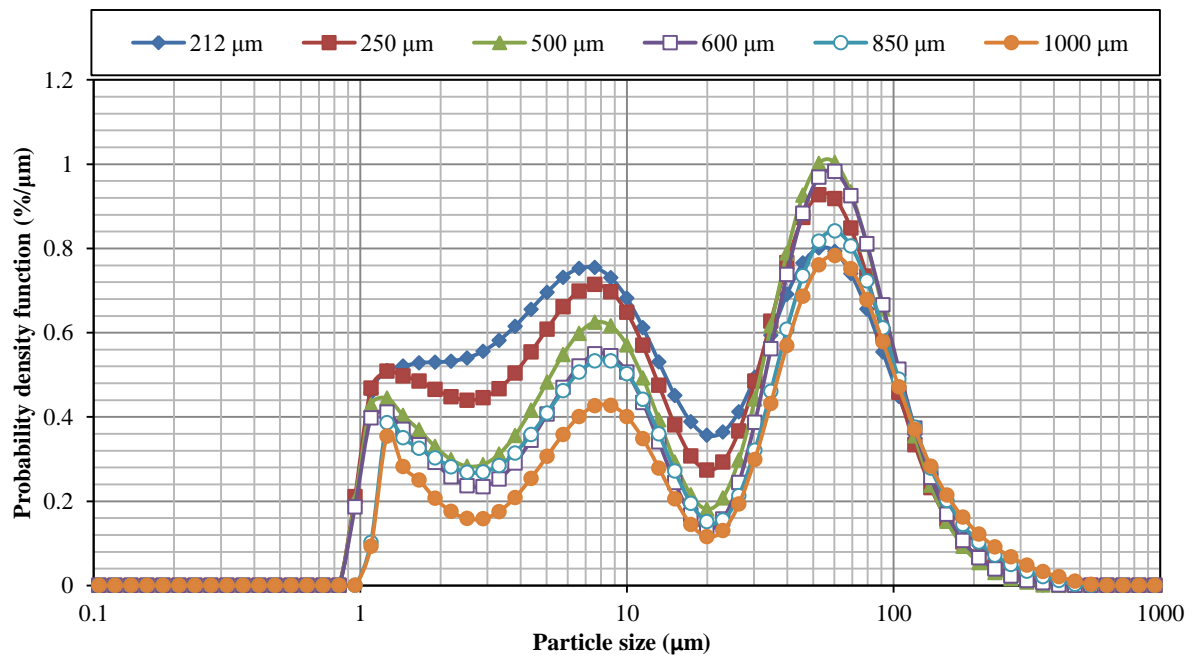


Figure a 4. Particle size distribution for different near-mesh particle sizes of burkeite at 250 kPa nozzle pressure

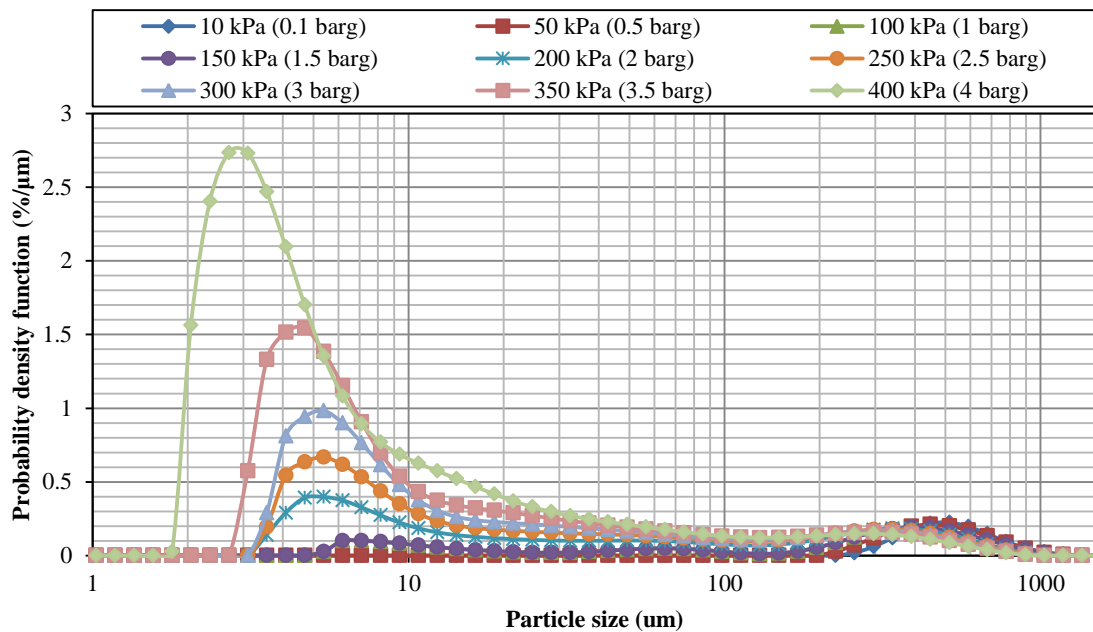


Figure a 5. Shift in size distribution of 400-425 μm of aspirin at different nozzle air pressures

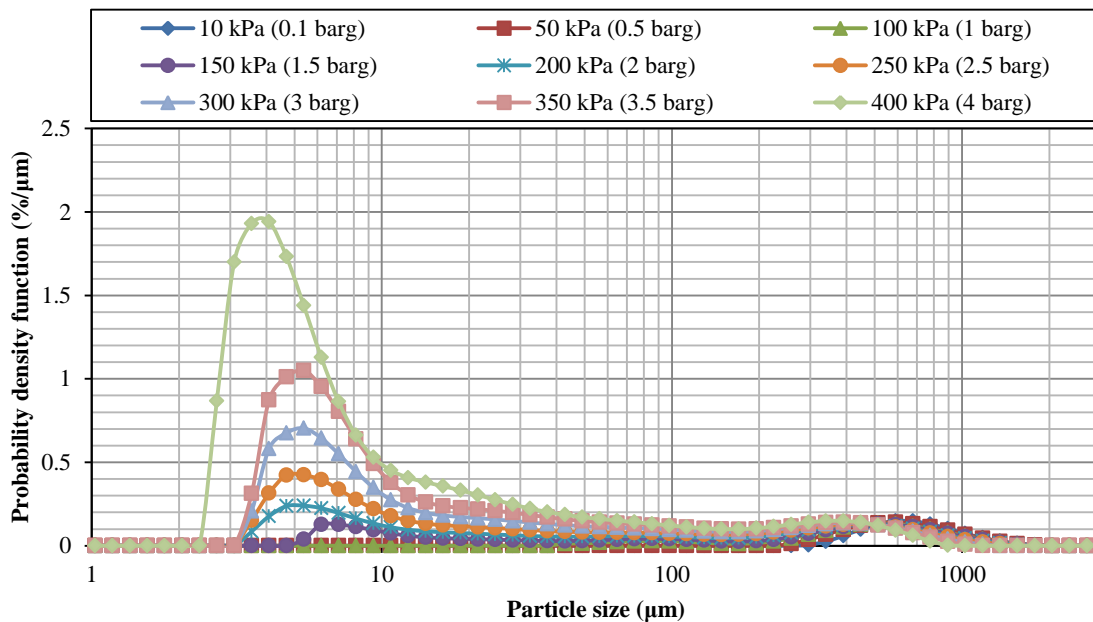


Figure a6: Shift in size distribution of 600-630 μm of aspirin at different nozzle air pressures

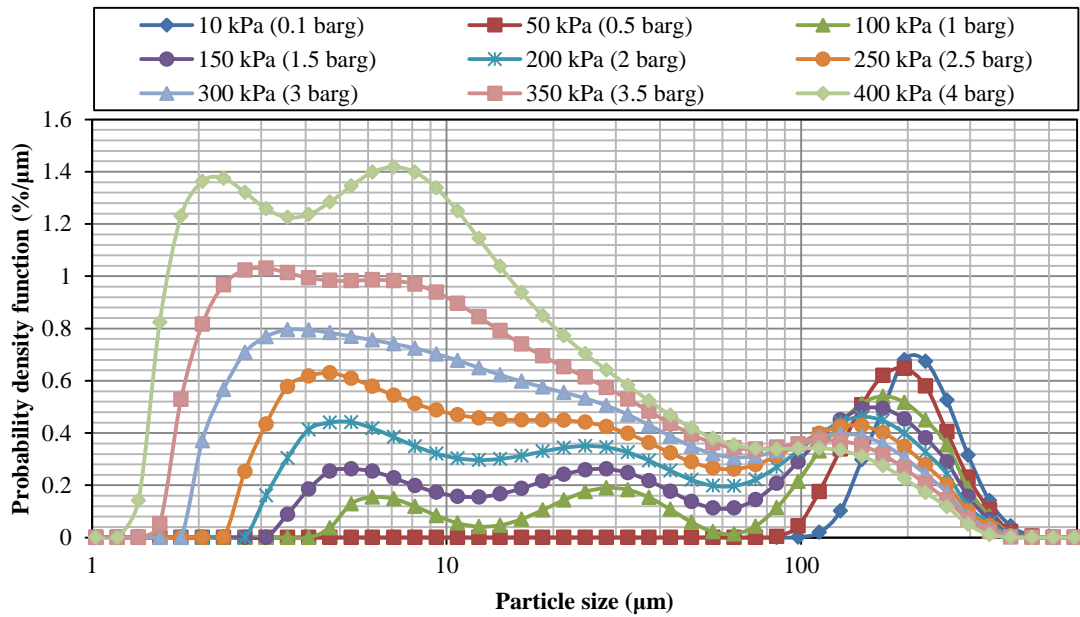


Figure a7: Shift in size distribution of 160-180 μm of sucrose at different nozzle air pressures

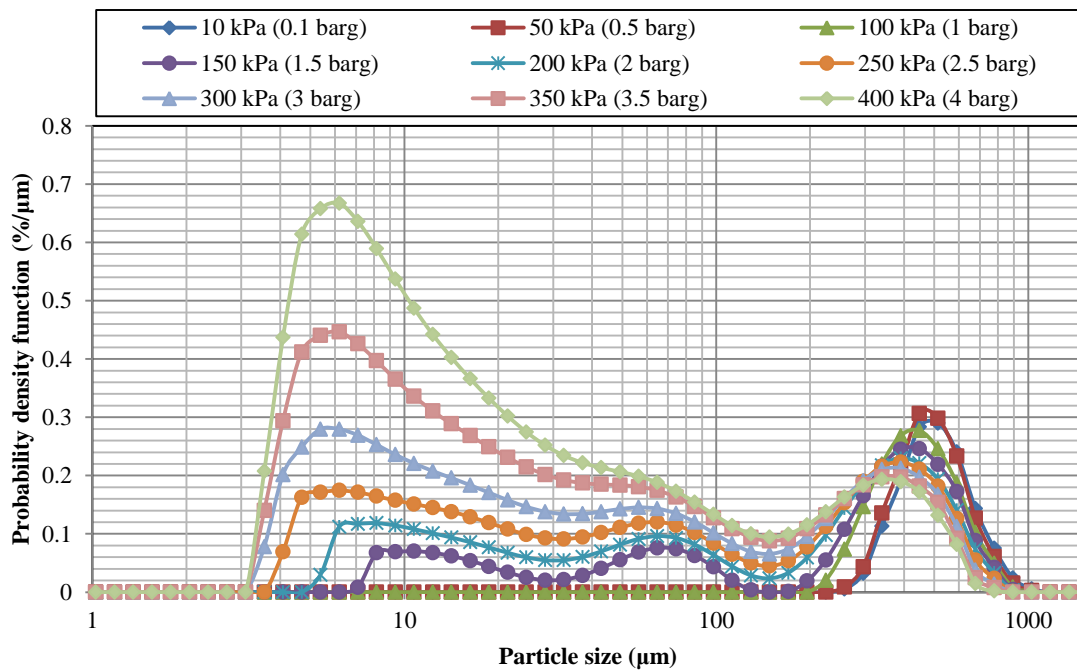


Figure a8: Shift in size distribution of 400-425 μm of sucrose at different nozzle air pressures

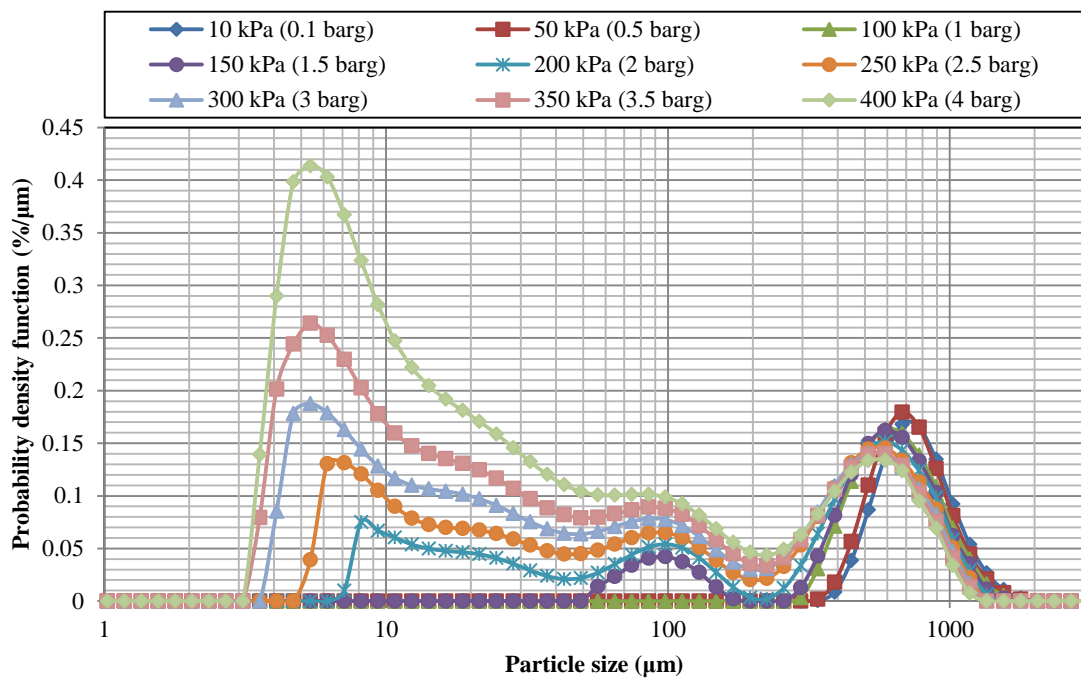


Figure a9: Shift in size distribution of 600-630  $\mu\text{m}$  of sucrose at different nozzle air pressures

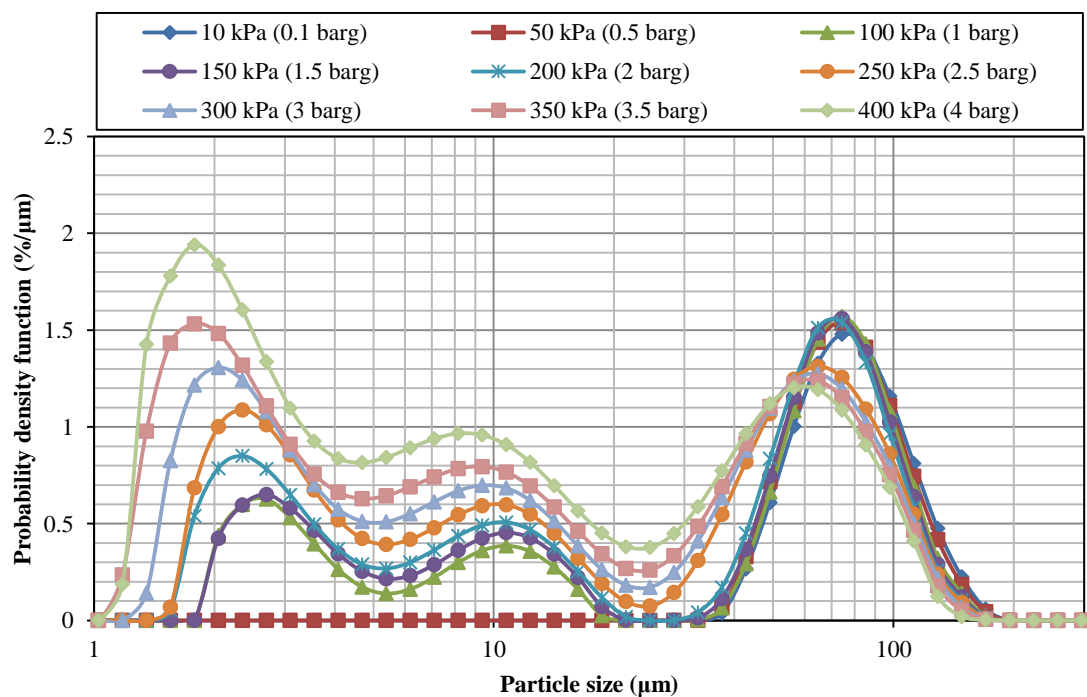


Figure a10: Shift in size distribution of 80-90  $\mu\text{m}$  of  $\alpha$ -lactose monohydrate at different nozzle air pressures

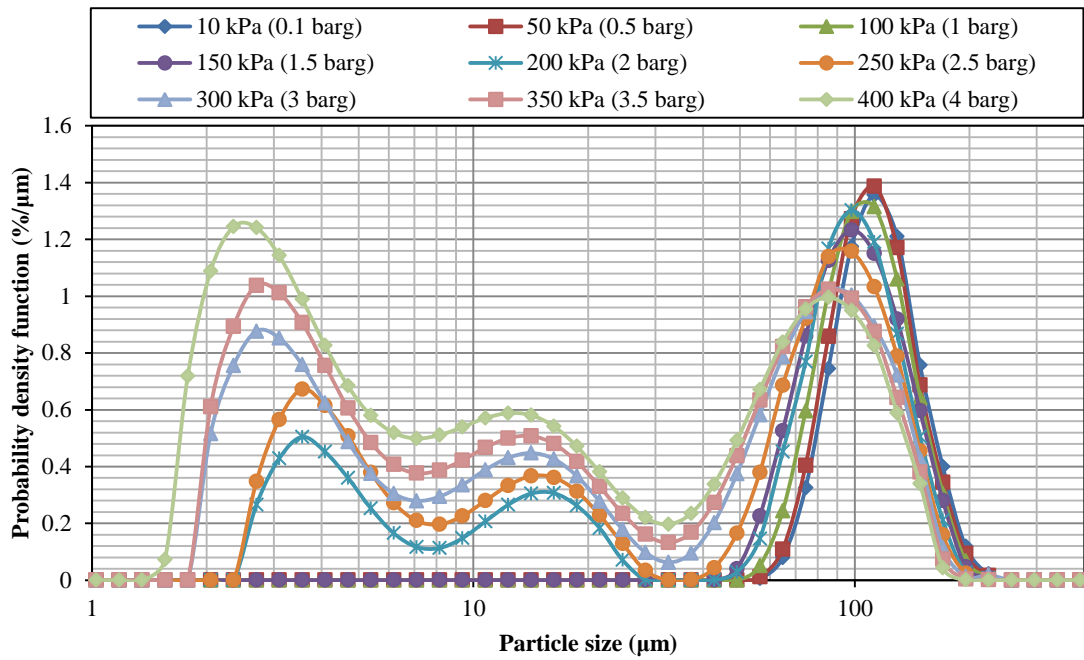


Figure a11: Shift in size distribution of 112-125  $\mu\text{m}$  of  $\alpha$ -lactose monohydrate at different nozzle air pressures

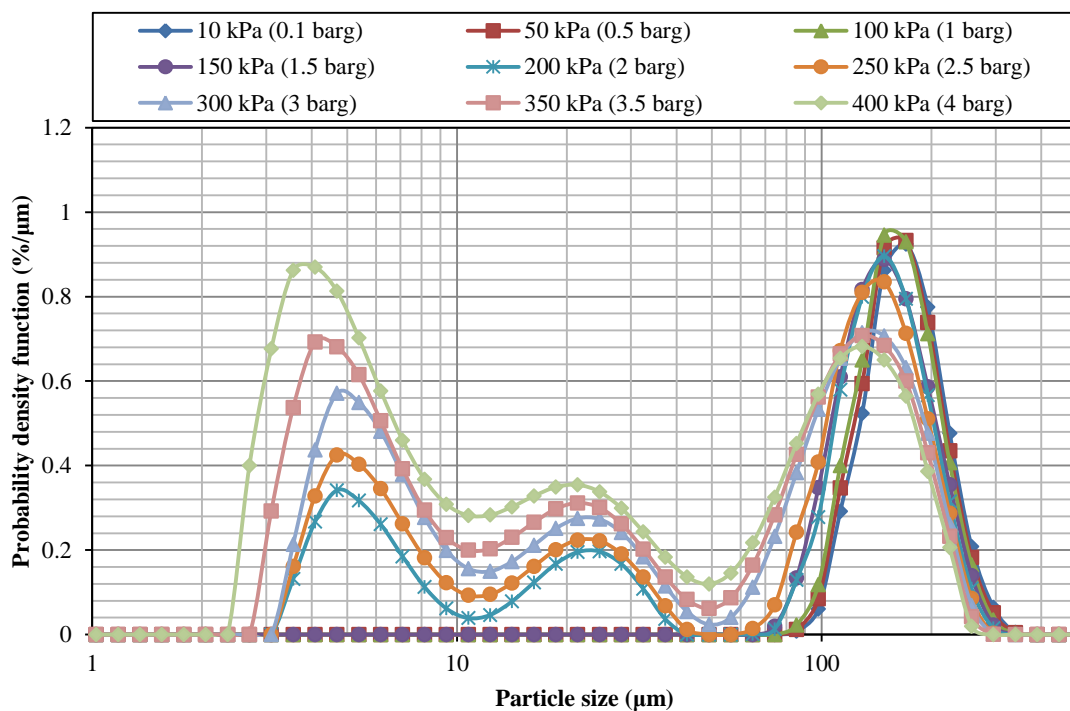


Figure a12: Shift in size distribution of 160-180  $\mu\text{m}$  of  $\alpha$ -lactose monohydrate at different nozzle air pressures

## Appendix B

### Body Force

```
#include "strs_body_force.h"
#include "Helpers.h"
#include <fstream>

using namespace NApiPbf;
using namespace NApi;
using namespace NApiCore;
using namespace std;

strs_body_force::strs_body_force()
{
    ;
}

strs_body_force::~strs_body_force()
{
    ;
}

void strs_body_force::getPreferenceFileName(char
prefFileName[NApi::FILE_PATH_MAX_LENGTH])
{
    ;
}

bool strs_body_force::isThreadSafe()
{
    return true;
}

bool strs_body_force::usesCustomProperties()
{
    return false;
}

bool strs_body_force::setup(NApiCore::IApiManager_1_0& apiManager,
                           const char prefFile[])
{
    return true;
}

bool strs_body_force::starting(NApiCore::IApiManager_1_0& apiManager)
```

```

{
    return true;
}

void strs_body_force::stopping(NApiCore::IApiManager_1_0& apiManager)
{
    ;
}

ECalculateResult strs_body_force::externalForce(
    double           time,
    double           timestep,
    int              id,
    const char       type[],
    double           mass,
    double           volume,
    double           posX,
    double           posY,
    double           posZ,
    double           velX,
    double           velY,
    double           velZ,
    double           angVelX,
    double           angVelY,
    double           angVelZ,
    double           charge,
    const double     orientation[9],

    NApiCore::ICustomPropertyDataApi_1_0* particlePropData,

    NApiCore::ICustomPropertyDataApi_1_0* simulationPropData,
    double&         calculatedForceX,
    double&         calculatedForceY,
    double&         calculatedForceZ,
    double&         calculatedTorqueX,
    double&         calculatedTorqueY,
    double&         calculatedTorqueZ)
{
    /*****Stress
    Calculations*****/
    double accel = 10;

    double C_x = 0.0;
    double C_y = 0.0;
    double C_z = 0.0;

    double AC_x = C_x - posX;
    double AC_y = C_y - posY;
    double AC_z = C_z - posZ;

    double mag_AC = sqrt( (AC_x * AC_x) + (AC_y * AC_y) + (AC_z * AC_z) );

    double norm_x = AC_x / mag_AC;
    double norm_y = AC_y / mag_AC;
    double norm_z = AC_z / mag_AC;

    calculatedForceX = mass * accel * norm_x;
    calculatedForceY = mass * accel * norm_y;

```

```
    calculatedForceZ = mass * accel * norm_z;

    /*****
    *****/

    return eSuccess;
}

unsigned int strs_body_force::getNumberOfRequiredProperties(
    const NApi::EPluginPropertyCategory
category)
{
    return 0;
}

bool strs_body_force::getDetailsForProperty(
    unsigned int                propertyIndex,
    NApi::EPluginPropertyCategory category,
    char
name[NApi::CUSTOM_PROP_MAX_NAME_LENGTH],
    NApi::EPluginPropertyDataTypes& dataType,
    unsigned int&                numberOfElements,
    NApi::EPluginPropertyUnitTypes& unitType)
{
    return false;
}
```